Fracture Mechanics of Bi-material Interfaces for Composite Pipe Repair

Johannes M. Linden

In fulfilment of the requirements for the degree of Doctor of Philosophy

Supervisors: Prof A Geoff Gibson
Dr George Kotsikos

School of Mechanical & Systems Engineering
Newcastle University
Newcastle upon Tyne, UK
July 2015

Abstract

Composite repairs evolved as popular choice for rehabilitation of oil and gas pipelines from corrosive material loss. However, corrosion can develop into local through-wall defects. In this case, fluid pressure acts directly on repairs, forms blisters and applies stresses on repair-pipe interface bonds. A practical model is needed to evaluate and design composite repairs against interface failure.

This study investigated fracture mechanics aspects of failure through crack propagation along the repair-pipe interface. Thick fibre-reinforced plates were examined as repairs for circular 'sharp-edged' through-holes in stiff metal substrates. Blister formation and propagation onset were analysed. Energy release rates were investigated as measure of interface failure.

Two types of blister tests were conducted; using fluid pressure and shaft-loading with different punch heads. A novel method of determining energy release rates in pressure blister tests was developed. Digital image correlation was used to track blister volumes, which are directly related to energy release rates.

Existing and newly derived analytical solutions for each test method were compared with measurements and simulations using the virtual crack closure technique. Energy release rates were found to be influenced differently by repair, defect and shaft geometries. Contrary, critical loads could be plotted as function of defect size to repair thickness ratio.

To reduce geometry dependence, 'volumetric' energy release rates were introduced by adjusting for defect and repair geometries. Similar to load curves, these are functions of defect size to repair thickness ratios, potentially simplifying fracture criteria. Shaft-loading could not be recommended as general fluid pressure replacement, because of differences between the test methods.

Design criteria against debonding by ISO/TS 24817 [1] and ASME PCC-2/4 [2] based on energy release rates were reviewed against results presented. An improvement to the formulation in the standards was suggested. An alternative process for qualification and dimensioning was proposed based on empirical formulations for volumetric energy release rates and critical loads as design criteria.

Declaration of own Work

I declare that this thesis is my own work and that I have correctly acknowledged the work of others. This submission is in accordance with University and School guidance on good academic conduct.

I certify that no part of the material offered has been previously submitted by me for a degree or other qualification in this or any other University.

I confirm that the word length is within the prescribed range as advised by my school and faculty

The thesis does not contain collaborative work.

List of Publications

J. M. Linden, G. Kotsikos and A. G. Gibson, „Design of composite repairs of steel pressure piping against leakage“, to be submitted in 2015

J. M. Linden, G. Kotsikos and A. G. Gibson, „Use of digital image correlation in blister tests to measure the energy release rate for composite repairs“, written, to be submitted in 2015

J. M. Linden, G. Kotsikos and A. G. Gibson, „Influence of the punch head geometry on the energy release rate in shaft-loaded blister tests“, written, to be submitted in 2015

J. M. Linden, M. Köpple, D. Elder and A. G. Gibson, Fracture mechanics of crack propagation in composite repairs of steel pressure piping, *Journal of Reinforced Plastics and Composites*, SI, Vol. 33, No. 6, p526-532, Mar 2014

A. G. Gibson, J. M. Linden, D. Elder and K. H. Leong, „Non-metallic pipe systems for use in oil and gas“, *Plastics Rubber and Composites*, Vol. 40, No. 10, p465-480, Dec 2011

Acknowledgements

This work was undertaken as part of a Cooperative Research Centre - Advanced Composite Structures (CRC-ACS) research programme, established and supported under the Australian Government's Cooperative Research Centres Programme. I would also like to acknowledge our other partners of the project, in particular PETRONAS Research Sdn. Bhd. Namely, I would like to acknowledge Dr Paul Falzon, Dr David Elder, Dr Luke Djukic and Dr Leong Kok Hoong for the good collaboration.

I would like to thank my supervisors, Prof Geoff Gibson and Dr George Kotsikos, for giving me this opportunity, their continuous support, professional discussions and good times.

Furthermore, I would like to thank Simon Frost from Walker Technical Resources Ltd. (WTR) for helpful advice, material, training and pictures. Our superintendent and technicians have to be mentioned for their excellent work and for their patience with us PhD students, in particular, Nicky Dafter, who manufactured most of the metal discs, and Bill Cragie, who allowed me into his lab, while our own was closed for refurbishments. I would like to acknowledge the EPSRC Engineering Instrument Pool for providing me with their DIC system.

A special thanks goes to my PhD colleagues Shukry, Tarek, Pietro, Harry, Sandra, Katerina, Maria, Sheila and James for their technical input, helpfulness, inspiring discussions and great banter; categories in which Karen must be mentioned as well.

Last not least I would like to thank my family for their unconditional love and support in all aspects, in particular Sophia for bearing most of the load and with a smile.

Contents

Lists

Figures

Tables

Abbreviations

Acronym	Description
2D/3D	2-/3-dimensional
BEM	Boundary element method
BIE	Boundary integral equation
B-K	Fracture criterion after Benzeggagh and Kenane
CBT	Constraint blister test
U/CCI/–LS	Universal / Crack closure integral / – local smoothing
C-ELS	Calibrated end loaded split (fracture energy test)
CLT	Classical laminate theory
G/L/C COS	Global / local / corner node coordinate system
CPT	Classical plate theory
CT	Crack tip
CZM	Cohesive zone model
DCB	Double cantilever beam (fracture energy test)
DDM	Displacement discontinuity method
DIC	Digital image correlation
DOF	Depth of field (optics)
ENF	End-notched flexure (fracture energy test)
ERR	Energy release rate
FE / FEA	Finite element analysis
FFM	Finite fracture mechanics
FMM	Fast multipole method
FSDT	First-order shear deformation theory
G/CFRP	Glass / carbon fibre-reinforced polymer
IQR	Interquartile range
LEFM	Linear elastic fracture mechanics
LM	Line method
LT	Linear transducer
MMB	Mixed mode bending test
NCC	Normalised cross-correlation
NCF	Non-crimp fabric
ODE	Ordinary differential equation
OT	Orthotropic
PBT	Pressure blister test
PDE	Partial differential equation
Prepreg	Pre-impregnated fabric
PT	Pressure transducer
PVM	Pressure volume method
QI	Quasi-isotropic
SEM	Scanning electron microscope
SIF	Stress intensity factor
SLB	Single leg bending (fracture energy test)
SLBT-F/H	Shaft-loaded blister test, flat/hemispherical punch head
STD	Standard deviation
TSDT	Third-order shear deformation theory
UV	Ultra violet
USTM	Universal strength testing machine
VCCT	Virtual crack closure technique
VCE	Virtual crack extension method
VERR	Volumetric energy release rate
XFEM	eXtended FEM
Z/N/SSD	Zero-/Normalised/Sum of squared differences

Nomenclature

List of important mathematical expressions and their meaning; unless otherwise stated at the time of introduction.

Symbol	Description
A, A_C	Area, Crack face area
$a, \Delta a$	Crack length, crack increment
b	Width / Distance point load to crack tip
C	Compliance
$C_{1...4}$	Polynomial constants
D	Flexural rigidity
D_{ij}, D_m	Material parameter, Damage parameter
$E, \mathbf{E}$	Young's modulus, Matrix
$e, f, g, h(x)$	General line functions
$F, G(x)$	Image set functions
G	Shear modulus
$\mathcal{G}$	Energy release rate
h	Height
I	Moment of inertia
$J/L/M/I$	$J/L/M/I$-Integral
K_s	Shear correction factor
$\mathcal{K}$	Stress intensity factor
M	Bending moment
N	Membrane stress
P	Pressure
P_C, P_S	Point on hexagon corner, sphere
p	Uniform load (area)
Q	Shear / transverse Force
q, q_0	Uniform load (line), annular line punch load
r, φ, z	polar coordinates
R, R_0, R'_0	Radius; Defect, Contact zone, Equivalent contact zone

Symbol	Description
S	Static moment
t	Repair thickness
u, v, w	Deflection in x, y, z direction
X, Y, Z	Nodal forces in x, y, z direction

Symbol	Description
α, β	Dundur's parameters
$\Gamma, \Gamma_{A,V}$	Contour (line), Contour (domain; area, volume)
γ	Volumetric ERR
γ_{rz}	Shear strain
Δ	Increment / Difference / Displacement
$\varepsilon, \varepsilon_{1,2}$	Strain, Principal strain
ϵ	Bi-material constant
ϑ	Phase angle, mode III vs I+II
κ	Stiffness factor / General factor
λ	Dimensionless (crack) length
ν	Poisson's ratio
Π	Energy
σ	Stress (normal)
τ	Stress (shear)
ϕ	Fibre volume fraction
φ	Crack tip angle, polar coordinates (r, φ, z)
$\chi_{b,m}$	Normalised ERR; bending, membrane
χ_{NSSD}	Correlation function
ψ	Phase angle, mode I vs II
Ω	Blister surface domain
ω	crack notch opening angle

Sub-/Super	Description	Sub-/Super	Description
$\overline{x}$	Average value	$x_{\mathrm{I,II,III}}$	Modes I, II, III
$\hat{x}$	Normalised value	$x_{i,j,k}$	Counting variables
x^{T}	Transposed value	x_{k}	Kinetic
$x^{+,-}$	Above, Below crack face	x_{lb}	Load based solution
$x_{\parallel}$	Fibre direction	x_{live}	Under live pressure
$x_{\perp}$	Transverse to fibre direction	x_{M}	Moment
x_0	Default value / Punch value (e. g. R_0)	x_{m}	Membrane / Measured / Matrix Material / Midside node
$x_{1,2,3}$	Local coordinate direction	$x_{\mathrm{max,min}}$	Maximum, Minimum value
x_{a}	Axial	x_{n}	Single mode nominal (net-section) failure
x_{an}	Annular	x_{np}	Near-point solution
$x_{\mathrm{aux}}, x^{aux}$	Auxiliary	x_{p}	Potential (strain) / Point load / Elastic-plastic zone
x_{b}	bending	x_{pun}	Punch
x_{C}	Central / Corner node	x_{Q}	Shear force
x_{c}	Critical / Elastic-plastic yield / Crack opening value	$x_{\mathrm{r},\varphi,\mathrm{z}}$	Polar coordinate direction
x_{CC}	Concave	x_{rep}	Repair
x_{CV}	Convex	x_{S}	Superimposed
x_{d}	Dissipative	x_{s}	Shear / Steel
x_{db}	Deformation based solution	$x_{\mathrm{t,T}}$	Total
x_{def}	Defect	x_{u}	Ultimate tensile strength
x_{ext}	External	$x_{\mathrm{x,y,z}}$	Global coordinate direction
x_{f}	Fibre	x_{y}	Elastic zone
x_{h}	Circumferential (Hoop)		

Chapter 1. Introduction and motivation

Production facilities in the oil and gas industry undergo a great amount of stress cycles, corrosion and wear. In particular pipelines, of which risers [3] are most stressed, have to be durable enough to withstand structural, thermal, abrasive and corrosive loads of both a static and a cyclic nature. Structural loads can be tensile, compressive, bending and pressure. While tensile forces are imposed from e. g. the pipe's own weight [4], wave movement [5] or tensioning platforms [6], bending moments originate from the shape in which a pipe is laid out [7]. The environment of a pipeline creates additional pressure loads, like soil weight [8] and water pressure. The predominant pressure load is in most cases the pressure of the transported medium (e. g. ca. 200 bar inside high pressure, long-distance, gas pipelines [9]). Furthermore, high gradients of temperature between transported media and environments as well as maximum and minimum temperature ranges can envelope a temperature difference of more than 200 °C. Failures could occur through excessive loads and fatigue.

Figure 1.1: Metal clamps ready for deployment to oil fields in Vietnam (courtesy of Merit Technologies Sdn Bhd)

However, this study focuses on failure through internal erosive and corrosive material deterioration and the external repair methods against this type of failure.

Design lifetimes of pipelines can span decades, typically 20 years and longer. Because failures of pipelines and pressure vessels in the hydrocarbon industry are dangerous and expensive, pipelines have to be protected from deterioration and, when a failure is imminent, must be repaired. Maintenance of oil and gas pipelines is subject to a number of limitations and challenges. Full replacements of damaged pipe sections would have to be done after a shut down of the production, although shut down times are time consuming and expensive.

Therefore, repair methods were developed to carry out pipeline rehabilitation alongside continuing production activities. Welding patches on defect areas is a

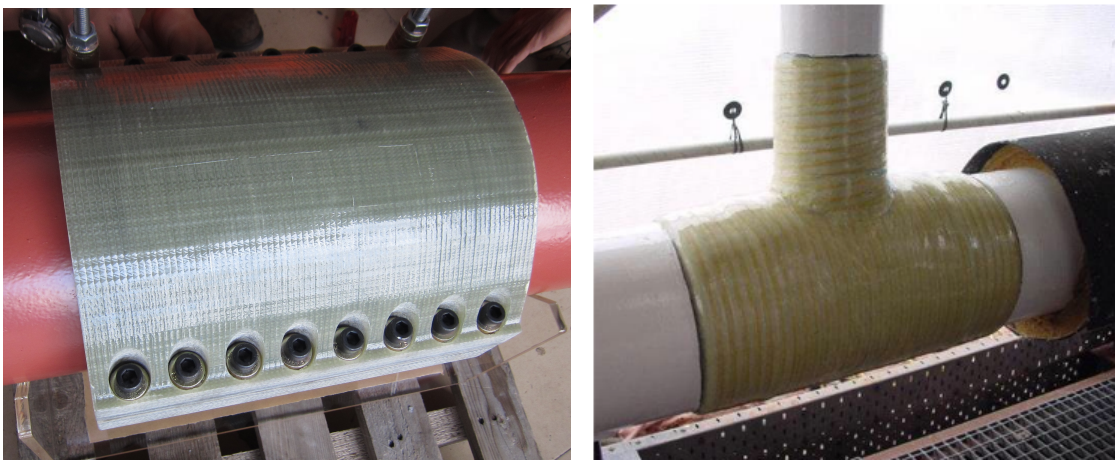

(a) **(b)**

Figure 1.2: (a) Composite shell clamp (courtesy ACS Australia Pty. Ltd. and Petronas Research Sdn. Bhd.), (b) WTR Technowrap 2K wet hand laminate on T-section (courtesy of WTR Ltd.)

standard measure for the repair of metals in many industries [10]. However, welding is less feasible as a repair technique for oil and gas pipework, as health and safety regulations do not permit any hot work next to flammable and explosive media. A typical repair for oil and gas pipelines is a metal clamp as presented in figure (1.1). Repair clamps are mainly built to contain leakages. Commonly custom built for a specific pipe or section of a pipe, metal clamps can be difficult to deploy, because of their size and weight.

1.1 Composite repair methods

Fibre-reinforced composite material repair applications have risen to be a strong competitor to the already established solutions, such as metal clamp repairs. The reasons are their potential advantages in corrosion resistance, fatigue performance, strength, stiffness, thermal insulation, damping and weight reduction [11] combined with often easier and faster deployment, which altogether lead to a reduction in costs.

Recently, a repair clamp, similar to the standard metal clamps, was invented made out of glass reinforced epoxy composites (fig. 1.2a) providing an improvement in weight, corrosion resistance and costs [12].

In contrast to repair systems that are produced in a factory and later assembled mechanically, other composite material repair techniques have emerged that are partly made at site. One of the leading composite repairs solutions is the Clock Spring© sleeve, providing a permanent repair for containment as well as structural reinforcement. Clock Spring© repairs are cylindrically precured glass fibre rein-

Product	Company	Country
A+ Wrap™	Pipes Wrap Inc	USA
Aquawrap®	Stork	Netherlands
Armor Plate®	Armor Plate Inc	USA
Black Diamond®	Citadel Technologies	USA
Bolder Wrap	Comptek Structural Composites Inc	USA
Carbon-Ply CRS	ITW Polymer Technologies	USA
Clock Spring©	Clock Spring Company LP	USA
CompoSol®	IMG Composites Ltd	UK
DiamondWrap©	Citadel Technologies	USA
DuraWrap®	ENECON Corporation	USA
Fortec™	PROKEM	France
Furmanite Composite Repair	Furmanite Corporation	UK
Hydrowrap®	Argosy International Inc	USA
Helicoid epoxy sleeve™	Merit Technologies Sdn Bhd	Malaysia
LOCTITE Composite Repair	Henkel AG & Co. KGaA	Germany
Perma-Wrap®	WrapMaster Inc	USA
Pipeassure®	PETRONAS	Malaysia
PowerSleeve®	Stork	Netherlands
Rapp-It	Alatas Singapore Ptd Ltd	Singapore
StrongBack®	Nixus International	USA
SuperWrap	Belzona Polymerics Ltd	UK
Tyfo® Fibrwrap® Systems	Fyfe Co LLC	USA
Technowrap 2k™	Walker Technical Resources Ltd	UK
Viper-Skin™	Neptune Research Inc	USA
Wrap Seal Plus™	SealXpert™ Products	Singapore
...	...	...

Table 1.1: List of some wrapped composite pipe repair sleeve products on the market.

forced polyester or vinyl ester resin composites, which are wound around a pipe with additional adhesive between the layers [13]. Another product was developed by Alexander [14], who used a combination of wet laminated carbon fibre cloth and precured carbon half shells.

Beside precured composite repair solutions, most common today are wet laminate composite repairs, although an unreinforced epoxy filler can be enough for some applications [15]. Typically, robust non-crimp fabric (NCF) cloth tapes are manually impregnated with high viscosity epoxy resins and wound around the damaged pipe section. An advantage of in situ laminated repairs over other repair methods is the

flexibility of application to any size and on complex shaped sections. An example of a complex shape (i. e. T-section) of a pipe repaired with an in situ laminate is shown in figure (1.2b).

Pre-impregnated ('prepreg') systems, such as Petronas' Pipeassure composite repair system (fig. 1.3), are available on the market to enhance quality assurance of impregnation and fibre volume fraction. Adversely to mixing resins for in situ impregnation, prepregs have to be cooled with, for example, dry ice until application to prevent premature curing.

Figure 1.3: Prepreg glass epoxy repair system Pipeassure® (courtesy of Petronas Research Sdn. Bhd.)

Glass fibre is predominantly used as the reinforcement, while carbon fibre [16] and aramid are more rare. Carbon fibre repairs always need an additional layer of glass as isolator to avoid galvanic corrosion. Mainly epoxy resins, but also vinyl ester [17] and urethane [18] are utilised as matrix material. Two component resin systems that react at ambient temperature are favoured for their reduced complexity of the repair process, but also activation by heat, UV light [19] or water [18] may be necessary. Some available composite repair products of the described types are listed in table (1.1).

1.2 Corrosion in oil and gas production

The general cases of corrosion (fig. 1.4) are distinguished in uniform, galvanic, crevice, pitting and erosion corrosion as well as dealloying and stress corrosion cracking [20]. Also microbes can be the cause for local material deterioration. Uniform corrosion is what is usually referred to as general corrosion of a metal across its surface. Chemical reactions can form a protective film on the surface, but also separate molecules from the solid metal. The latter process provides access to the pristine metal for further corrosive reactions and therefore leads to a degradation and thinning of the material.

In contrast to uniform corrosion, highly localised defects are the result of pitting corrosion as shown in figure (1.5a). A passivation layer on a metal surface can become damaged, which allows pitting corrosion to start and mitigate through the material. Pits grow, when a critical solution, mass-transport and electro potential

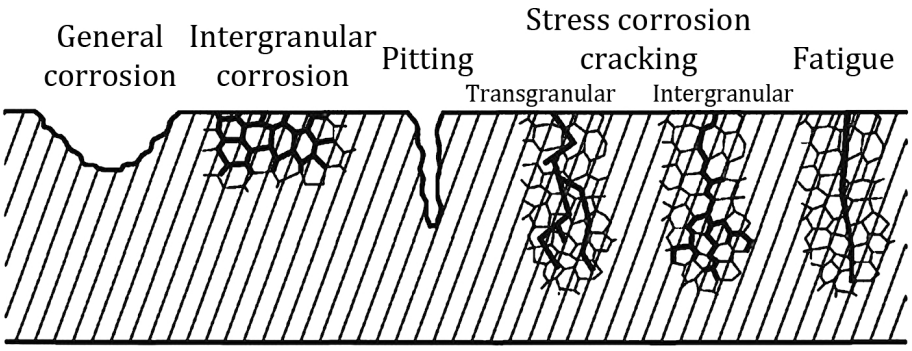

Figure 1.4: Overview off different types of corrosion; [23]

gradient between the surface and the bottom of the pit (fig. 1.5b) is reached in combination with the right material [21]. Otherwise the pit growth might not become autocatalytic and the pit surface repassivates. The general principle behind pitting corrosion can be described as related to galvanic corrosion by creating a very small anodic area (i. e. the pit bottom) in conjunction with a comparatively vast cathodic area (the majority of the solids surface). Pit shape and penetration rates vary strongly dependent on the material [22].

Closely related to the pitting corrosion is the crevice corrosion [24]. A small fissure between two materials, e. g. between a screw cap and its substrate or between a coating and a pipe wall, develops a complex chemical ambience that can be vastly different to the surroundings [21]. The complex chemical reactions of the crevice corrosion are based on a number of variables [25]. Yet, the mechanisms behind crevice corrosion are not fully understood and several mechanisms are likely to act together [26].

Galvanic corrosion occurs when an electrical contact between two dissimilar metals is established by an electrolyte. One metal becomes the cathode that takes

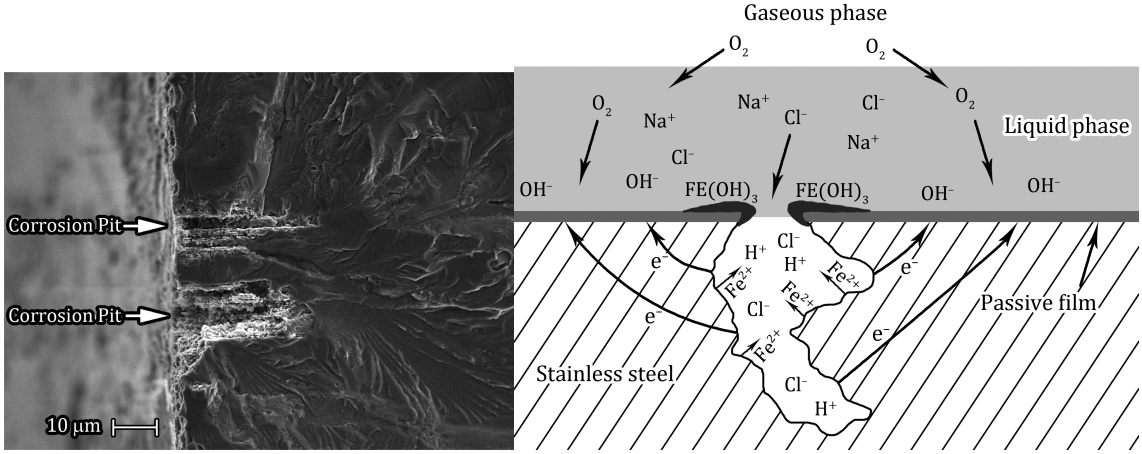

Figure 1.5: (a) SEM photograph of failure due to pitting corrosion, [27] (b) Diagram of pitting corrosion; [21]

electrons from the other metal that acts as the anode. Consequentally, the cathodes overall corrosion rate is lowered, while the anode's reduction rate is accelerated. Apart from the potential difference between both metals, the electrolytes solution constituents, the chemical reactions and metal characteristics are important as well as the surface conditions and geometry factors [28]. Dissimilar metals on pipelines can, for instance, be weld seams or fittings.

To summarise, the main cause for corrosion is the availability of specific chemicals (e. g. oxygen, sulphur, chloride) and compounds of those, in regards to corrosion promotion as well as prevention. The variation of the chemical mixtures of crude oils between reservoirs, as illustrated in table (1.2), imposes a challenge in corrosion prevention and repair. Additionally, physical factors impact the corrosion rates, in particular temperature, flow characteristics and solid particles. Furthermore, dissimilar materials acting as anode and cathode are essential for galvanic corrosion.

Crude Source	Parrafins [% vol.]	Naphthenes [% vol.]	Aromatics [% vol.]	Sulphur [% wt.]	API Gravity (° API)
Light Crudes					
Saudi Light	63	18	19	2.0	34
South Louisiana	79	45	19	0.0	35
Beryl	47	34	19	0.4	37
North Sea Brent	50	34	16	0.4	37
Lost Hills Light	50% Aliphatics	–	50	0.9	>38
Mid range Crudes					
Venezuela Light	52	34	14	1.5	30
Kuwait	63	20	24	2.4	31
USA West Texas sour	46	32	22	1.9	32
Heavy Crudes					
Prudhoe Bay	27	36	28	0.9	28
Saudi Heavy	60	20	15	2.1	28
Venezuela Heavy	35	53	12	2.3	24
Belridge Heavy	37% Aliphatics		63	1.1	14

Table 1.2: Properties of whole crude oils from world wide reservoirs; [29]

1.3 Failure in oil and gas pipes

The first design criterion for repairs of pressure vessels in general is the need to restore radial and axial strength. Loads on pipelines are created by the internal fluid pressure, the weight of the pipe and the curvature from its depositioning. Also the environment can impose stresses on the material through pressure from soil or water, but also from waves, currents, vortex induced vibrations and movements of connected vessels [30].

These influences lead to a stress combination of tension, compression, bending and pressure. Alexander and Ochoa [31] highlighted the importance of stress testing CFRP repaired steel risers not just on burst pressure, but also on tension and bending. Long life-times and cyclic loads from environmental influences and intentional and undesired production cycles, such as slugging [32], lead to fatigue failure. Particularly, welded joints of pipe segments near the touchdown point of risers are vulnerable to fatigue failure [33]. In the case of composite tubing and repairs, expedited by the elevated temperatures of transported products in oil and gas, creep becomes an additional factor in the long term design considerations [34].

The work presented focuses on loads induced by the internal pressure on the pipe. Possible failures due to excessive internal or external pressure are burst or collapse respectively, of which the latter is more common for flexible tubing and internal linings [35], but can also happen on the pipe underneath a repair [36].

Unreinforced polymer liners are rarely designed to take up structural loads, but rather for fluid containment [37] and protection of the structure from corrosive media. Accumulation of gases and fluids in-between the liner and the pipe wall can lead to corrosion on the surrounding metal pipe [38] or to the collapse of the liner in the event of a depressurisation of the pipeline, introducing potential damage to the liner [39].

Yet, only external repairs were under investigation for the study presented, which is why only burst failure is of interest. General burst failure safety of pipes under pressure is designed from the well known Barlow's formula equation (1.1). The circumferential hoop stress σ_h for a given pressure P is dependent on the radius R and the thickness t and is twice as large as the axial stress σ_a equation (1.2).

$$\sigma_\mathrm{h} = P\frac{R}{t} \tag{1.1}$$

$$\sigma_\mathrm{a} = P\frac{R}{2t} \tag{1.2}$$

The standards ISO 24817 [1] and ASME PCC2-4 [2] distinguish between the scenarios, whether a pipe wall contributes to the load bearing or not. In the event of the pipe wall's contribution becoming negligible, the wall thickness of a repair t_rep has to exceed the minimum for hoop and axial stress accordingly to equations (1.3)

and (1.4) respectively.

$$t_{\mathrm{min,h}} = \frac{1}{e_{\mathrm{h}} E_{\mathrm{h}}} \left(PR - \frac{\nu F}{\pi 2R} \right) \tag{1.3}$$

$$t_{\mathrm{min,a}} = \frac{1}{e_{\mathrm{a}}} \left(\frac{F}{\pi 2 R E_{\mathrm{a}}} - \frac{PR\nu}{E_{\mathrm{h}}} \right) \tag{1.4}$$

Often repairs are applied on a pipe with a wall thickness capable of bearing parts of the load. The required minimum repair thickness and the strain in the composite repair for a chosen repair thickness can be calculated with equations (1.5) to (1.7).

$$t_{\mathrm{min,h}} = \frac{R}{\sigma_{\max}} \cdot \frac{E_{\mathrm{s}}}{E_{\mathrm{h}}} \cdot (P - P_{\mathrm{s}}) \tag{1.5}$$

$$t_{\mathrm{min,a}} = \frac{R}{\sigma_{\max}} \cdot \frac{E_{\mathrm{s}}}{E_{\mathrm{h}}} \cdot \left(\frac{F}{\pi 2 R^2} - P_{\mathrm{s}} \right) \tag{1.6}$$

$$e_{\mathrm{h}} = \frac{PR}{E_{\mathrm{h}} t_{\mathrm{rep}}} - \frac{\sigma_{\max} t_{\mathrm{s}}}{E_{\mathrm{h}} t_{\mathrm{rep}}} - \frac{P_{\mathrm{live}} R}{(E_{\mathrm{h}} t_{\mathrm{rep}} + E_{\mathrm{s}} t_{\mathrm{s}})} \tag{1.7}$$

Here the subscripts denote steel '$_{\mathrm{s}}$' and the composite elastic moduli in axial '$_{\mathrm{a}}$' and hoop '$_{\mathrm{h}}$'. The maximum allowable working pressure P_{s} before repair, the internal pressure at the time of repair application P_{live}, the allowable stress $\sigma_{\max}$ and axial loads F are applied. Detailed explanations can be found in the standards. This study investigates external composite repairs for internally corroding pipes, in which the thinning of the pipe wall is assumed to continue until total loss of wall thickness. However, the loss of pipewall through corrosion can be a local problem as is shown in greater detail in chapter 1.2 and [40], so that a repair only has to take over parts of the loads although a leak could be present. Another important aspect of the repair design, therefore, is the capability to contain the transported fluids and gases.

Polymers are susceptible to permeation [41] with varying rates depending on the matrix material. Permeation cannot be avoided but reduced and has to be evaluated [37] to stay within permissible limits. Usually permeation rates need greater attention in the design of polymer or composite pipework and polymer liners rather than repairs, because of the large difference in exposed area.

Composite repairs are commonly rated 'safe fail' against excessive pressures. While the fibres bear the main loads, the matrix carries shear and out-of-plane loads, transfers loads between the fibres and keeps the fibres aligned. Consequentially, matrix cracking does not imply a burst failure, as the fibres may still be intact. Weepage through the repair is a clear sign of matrix cracking and the cracking itself can be detected, for instance, by acoustic emission [42]. Therefore, composite repairs offer a benign failure mode through matrix cracking occurring long before fibre breakage [43] in contrast to the catastrophic failure mode of a sudden rupture of pipes made from steel.

Composite repairs are less likely to fail through interlaminar debonding, but the adhesion of the repair to the substrate is a critical design criterion. When the bond strength is too low to withstand the crack opening forces, a crack in the interface between repair and pipe would form. Stresses around a crack tip may reduce through crack forming, if the opening force on the crack area remains constant. But because the internal pressure on a pipe would remain the same and thus even increase the force on the open crack surface, a crack would continue propagating depending on the load cycles of the pipe. Every time the crack surface increases, bond energy would be set free and have to be carried by the remaining, decreased adhesive area. Ultimately, a critical energy level would be reached when the remaining adhesive joint area is too small to absorb the released energy and the bond would fail catastrophically. As a result the fluid would leak out at the side of the repair. An investigation of the fracture mechanics of bonded repairs made from vinyl ester and glass fibre NCF was published by Mableson et al. [17].

The critical strain energy release rate (ERR) is the energy released from a new debonded crack area for a specific load and geometry. The standards of ISO 24817 [1] and ASME PCC2-4 [2] provide the engineer with an analytical solution to calculate the ERR needed for a repair-substrate bond with a repair of a particular thickness under working pressure. More detailed descriptions of the analytical solution of the standards are presented in chapter 2.4. Further explanations and the research undertaken for this study about the fracture mechanics of the bi-material interface adhesion of external composite repairs on pressurised steel pipes can be found in the following chapters.

Chapter 2. Fracture mechanics for blister tests

2.1 General fracture mechanics

Although fracture can be investigated on different levels up to atomic scales, the work presented is based on fracture mechanics of continuum mechanics. Two dimensional cross-section, perpendicular to the crack plane, are analysed. By examination of infinitesimally long sections of the crack front, the crack path of the section can be approximated as straight and the crack area as rectangular. Therefore, three dimensional crack curvatures can be analysed as two dimensional problems, reducing the complexity of analytical expressions used. Numerical methods are able to determine the change in fracture behaviour along a crack contour by discretisation into a large number of idealised two dimensional calculations with a small step width.

Two different, yet related values are a measure for the probability of crack propagation. One of which is the 'fracture toughness' or 'stress intensity factor' $\mathcal{K}$ in $\left[\mathrm{Pa}\sqrt{\mathrm{m}}\right]$, while the other is referred to as 'energy release rate' $\mathcal{G}$ in $\left[\mathrm{J}/\mathrm{m}^2\right]$. Both are related to each other through equations (2.1) and (2.2) for a single mode fracture as long as yielding around the crack tip remains on a small scale [44].

$$\mathcal{G} = \frac{\mathrm{d}}{\mathrm{d}A}\left[\Pi_{\mathrm{ext}} - \Pi_{\mathrm{p}} - \Pi_{\mathrm{d}} - \Pi_{\mathrm{k}}\right] \tag{2.1}$$

with Π_{ext} — external work
Π_{p} — potential/strain energy
Π_{k} — kinetic energy
Π_{d} — dissipated energy
and A — created crack area

$$\mathcal{G}_{\mathrm{I}} = \frac{\mathcal{K}_{\mathrm{I}}^2}{E'} \quad , \qquad \mathcal{G}_{\mathrm{II}} = \frac{\mathcal{K}_{\mathrm{II}}^2}{E'} \quad , \qquad \mathcal{G}_{\mathrm{III}} = \frac{\mathcal{K}_{\mathrm{III}}^2}{2G} \tag{2.2}$$

with
$$E' \begin{cases} E\ ; & \text{plane stress} \\ \dfrac{E}{1-\nu^2}\ ; & \text{plane strain} \end{cases} \tag{2.3}$$

In this study, materials were evaluated that are less ductile than necessary to result in large zones of yielding, such as fibre reinforced epoxy polymers and steel.

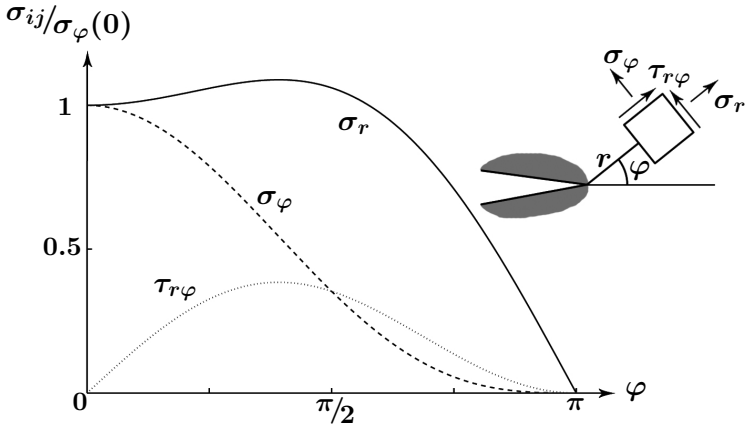

Figure 2.1: Mode I crack tip polar stress distribution; [45]

Thus the assumption of a small inelastic zone around the crack held. While the stress intensity factors are derived from the stresses and strains around a crack tip, the energy release rate $\mathcal{G}$ is defined as the released energy in relation to a crack opening. This energy criterion for crack propagation was published by Irwin and Kies [46] and is comparable to the energy criterion of Griffith [47] (cf. sec. 2.1.3). As $\mathcal{G}$ is dependent on the size of the crack opening, an infinitesimal small opening is assumed.

Similar to any other physical phenomena, cracks propagate along the path of smallest resistance or, in other words, seek to maximise the energy release rate in order to reach the lowest energy level. In a homogeneous, isotropic material the need to maximise the energy release rate leads to a change in crack propagation direction. The ratio of stresses in crack transverse tensile, in-plane and out-of plane shear is expressed as the fracture modes I, II and III respectively. For instance, a crack angled to the orientation of principal stress would start to propagate such that the crack path becomes perpendicular to the principal stress direction, thus, becoming a pure mode-I crack propagation [48]. However, in scenarios like interface cracks or delamination between layers in a composite material the crack path is confined. No change in direction of the crack growth occurs, as the propagation along an interface between two layers needs less energy than transverse through the layers. As a result, the crack propagation does not develop into a steady pure mode-I fracture, but continues as mixed-mode. The phase angles are a measure for the ratio of the fracture modes of the general form:

$$\psi = \arctan\left(\frac{\mathcal{K}_{\mathrm{II}}}{\mathcal{K}_{\mathrm{I}}}\right) \quad , \qquad \vartheta = \arctan\left[\frac{\mathcal{K}_{\mathrm{III}}}{\sqrt{\mathcal{K}_{\mathrm{I}}^2 + \mathcal{K}_{\mathrm{II}}^2}}\right] \tag{2.4}$$

Further details on the calculation of phase angles can be found among others in [48–50].

With the general formulation for the compliance C as the division of deflection over load, the energy Π can be written for a crack surface under fluid pressure P as

equation (2.5). Inserting the opened crack surface $\mathrm{d}A = 2\pi R\,\mathrm{d}R$ and equation (2.5) in equation (2.1) results in equation (2.6), which is explained in further detail in chapter 2.4. This solution is comparable to, for example, the solution for a DCB sample (2.7) of width b under load F with crack length a by Irwin and Kies [46].

$$\Pi = -\frac{P^2 C}{2} \tag{2.5}$$

$$\mathcal{G} = \frac{P^2}{4\pi R}\frac{\mathrm{d}C}{\mathrm{d}R} \tag{2.6}$$

$$\mathcal{G} = \frac{F^2}{2b}\frac{\mathrm{d}C}{\mathrm{d}a} \tag{2.7}$$

The compliance can be expressed as the ratio between deflection per force or volume per pressure.

$$C = \frac{y}{F} \tag{2.8}$$

$$C = \frac{V}{P} \tag{2.9}$$

2.1.1 *Stress field analysis of crack tips*

Williams [51], Westergaard [52], Irwin [53] and Sneddon [54] published fundamental solutions for calculation of stress fields and stress intensity factors in isotropic, linear elastic material. Anderson [55, tables 2.1–2.3] summarised general solutions for the stress intensity factors of all three fracture modes for which two different general approaches exist. Asymptotic near-crack tip stress fields can be examined as well as the full-field stress in the material around a crack. Zhender [44] presented a detailed overview over different solutions for both approaches.

Stress concentrations in the vicinity of cracks, first quantified for elliptical holes in

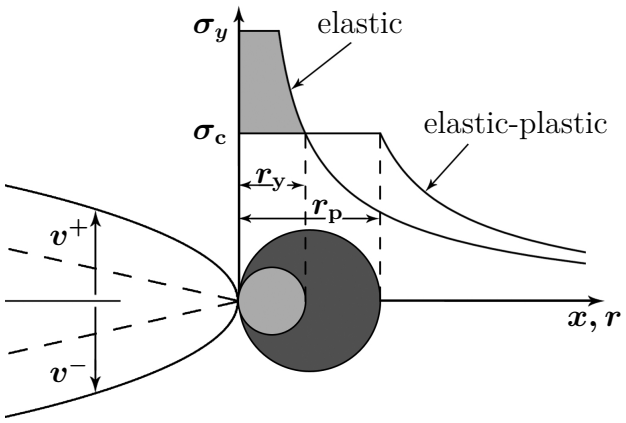

Figure 2.2: Difference between a theoretical sharp and actual blunt crack tip with $\frac{1}{\sqrt{r}}$ stress singularity, [45], shown together with the plastic zone of first (r_y) and second-order (r_p) approximations, [55]

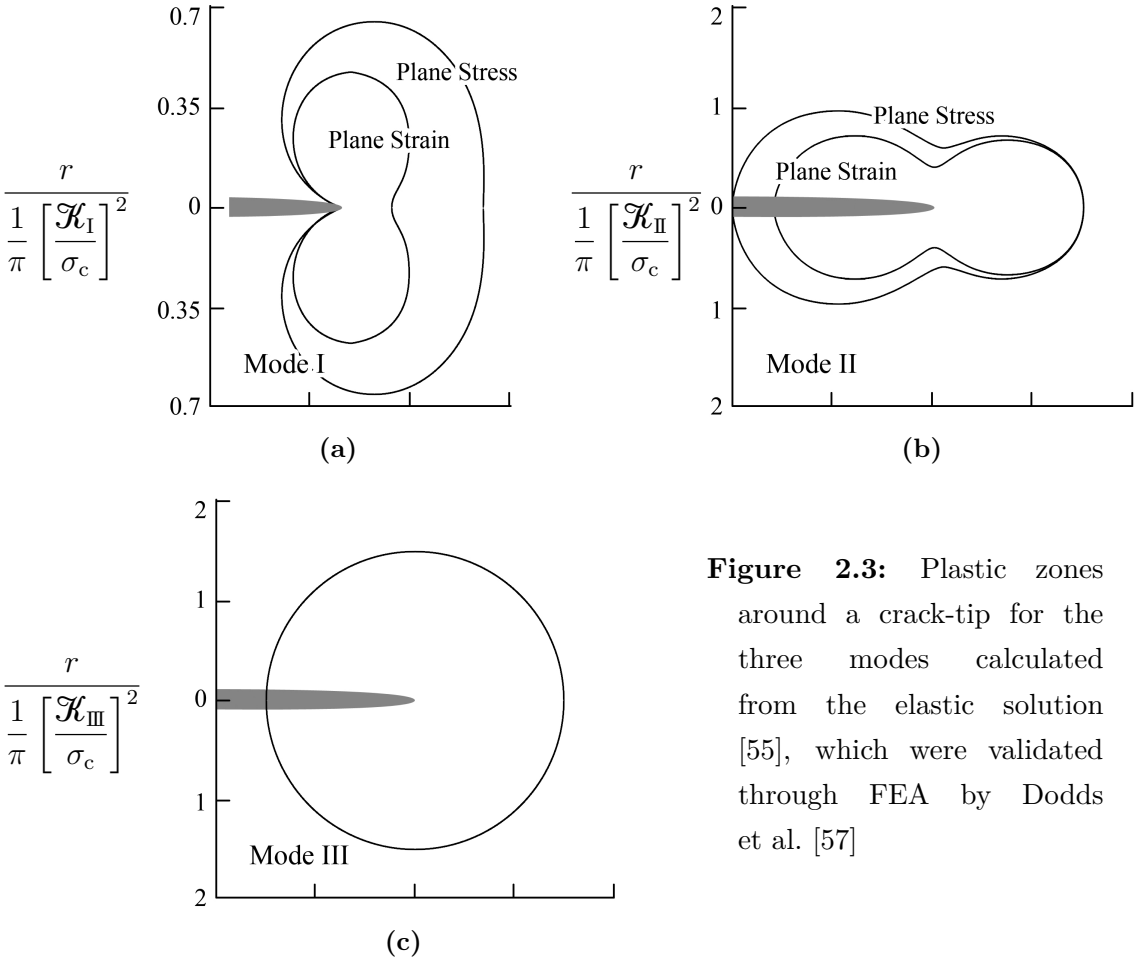

Figure 2.3: Plastic zones around a crack-tip for the three modes calculated from the elastic solution [55], which were validated through FEA by Dodds et al. [57]

flat plates by Inglis [56], show an asymptotic increasing behaviour towards the crack tip. At the crack tip the stress field is singular with $1/\sqrt{r}$, which was first shown as universal by Williams [51]. While a mathematical examination of an ideally sharp crack tip would therefore result in an infinitely high stress, actual material undergoes plastic deformation where the stress exceeds the critical stress level. Observing real crack tips reveals that plasticity at the crack tip yields in a blunt, rather than a sharp crack tip.

The plastic zone can be approximated as $r_\mathrm{p} \sim \mathcal{K}^2/\sigma_\mathrm{c}^2$. Irwin and Kies [46] approximated the plastic zone radius r_p equation (2.10) based on the critical yield stress σ_c. Presuming a degradation in load bearing capabilities within the plastic zone Irwin and Kies corrected the stress intensity factor through increasing the original crack length by the plastic zone correction length r_y.

$$r_\mathrm{p} = \frac{\mathcal{K}_\mathrm{I}^2}{\pi\sigma_\mathrm{c}^2} \tag{2.10}$$

$$r_\mathrm{y} = \frac{\mathcal{K}_\mathrm{I}^2}{6\pi\sigma_\mathrm{c}^2} \tag{2.11}$$

Another simplistic plastic zone correction for linear elastic fracture mechanics was

developed by Dugdale [58] and Barenblatt [59]. Known as yield strip model, a classical finite crack inside an infinite material under remote stress is superimposed with a crack with closure stresses at the crack tip. The crack length in the latter case is increased across the plastic zone at which the closure stresses are applied. Choosing the length of the plastic zone such that the stress intensity factors of both cracks are balanced yields equation (2.12).

$$r_{\mathrm{p}} = \frac{\pi^2 \sigma^2 a}{8\sigma_{\mathrm{c}}} = \frac{\pi \mathscr{K}_{\mathrm{I}}^2}{8\sigma_{\mathrm{c}}^2} \tag{2.12}$$

However, for a crack of length a the near-crack tip stress distribution in the elastic annulus in between $r_{\mathrm{p}} < r \ll a$ can be approximated as equation (2.13) with $f(\varphi)$ being a universal, dimensionless, polar coordinate function of φ. Replacing $\sigma_0 = \sigma_{\mathrm{xx}} = \sigma_{\mathrm{yy}}$, $\sigma_0 = \tau_{\mathrm{xy}}$ or $\sigma_0 = \tau_{\mathrm{yz}}$ in equation (2.13) results in $\mathscr{K}_0$ becoming $\mathscr{K}_{\mathrm{I}}$, $\mathscr{K}_{\mathrm{II}}$ or $\mathscr{K}_{\mathrm{III}}$ respectively.

$$\mathscr{K}_0 = \lim_{r \to 0} \sqrt{2\pi r}\ \sigma_0 f(\varphi = 0) \tag{2.13}$$

Correspondingly, the fracture toughness $\mathscr{K}_{\mathrm{I,II,III}}$ can be written as a function of the crack opening deflections at the crack tip v, u and w respectively with $\varphi = \pm\pi$ [45].

$$\mathscr{K}_{\mathrm{I}} = v \frac{2G}{k+1} \sqrt{\frac{2\pi}{r}} f(\varphi = \pm\pi) \tag{2.14}$$

$$\mathscr{K}_{\mathrm{II}} = u \frac{2G}{k+1} \sqrt{\frac{2\pi}{r}} f(\varphi = \pm\pi) \tag{2.15}$$

$$\mathscr{K}_{\mathrm{III}} = w \frac{G}{2} \sqrt{\frac{2\pi}{r}} f(\varphi = \pm\pi) \tag{2.16}$$

with plane strain: $k = 3 - 4\nu$

plane stress: $k = \dfrac{(3-\nu)}{(1+\nu)}$

The formulations above for the stress field around a crack tip can be developed into an expression of the stress intensity factors for a specific crack and solid geometry. The general form for cracks under a stress equation (2.17) or a point load equation (2.18) contain the variables for the crack size a or the distance between point load and crack tip b. The shape function Y changes depending on the load and solid geometry setup.

$$\begin{bmatrix} \mathscr{K}_{\mathrm{I}} \\ \mathscr{K}_{\mathrm{II}} \end{bmatrix} = \begin{bmatrix} \sigma \\ \tau \end{bmatrix} \sqrt{\pi a} Y \tag{2.17}$$

$$\begin{bmatrix} \mathscr{K}_{\mathrm{I}}^{\pm} \\ \mathscr{K}_{\mathrm{II}}^{\pm} \end{bmatrix} = \begin{bmatrix} P \\ Q \end{bmatrix} \sqrt{\pi b} Y \tag{2.18}$$

In the case of a single mode fracture scenario the critical stress intensity factors for crack propagation can be regarded as material properties (2.19). However, this does not apply for mixed-mode fracture scenarios and is discussed in more detail in section 2.1.3.

$$\mathscr{K}_{\mathrm{I}} = \mathscr{K}_{\mathrm{Ic}} \quad , \qquad \mathscr{K}_{\mathrm{II}} = \mathscr{K}_{\mathrm{IIc}} \quad , \qquad \mathscr{K}_{\mathrm{III}} = \mathscr{K}_{\mathrm{IIIc}} \tag{2.19}$$

2.1.2 *Interface fracture and delamination*

Bi-material interface cracks and delaminations of composites are different from crack growth in isotropic materials, which were discussed in the previous section, by the oscillatory singular stress field near a crack tip, which was first discovered by Williams [60] and continued by several research groups. Cherepanov [61] demonstrated the oscillatory behaviour for pure elastic assumptions. A Green's function solution was derived by Rice and Sih [62] for a finite interface crack. Cracks in a non-homogeneous plane were investigated by Erdogan [63] and an oscillatory area of the order of 10^{-6} of the crack size was determined. England [64] and Malyshev and Salganik [65] showed that the oscillatory behaviour leads to interpenetration of the crack faces, which is physically wrong, and the size of the contact zone was estimated in the order of 10^{-4}.

The assumption of a small frictionless contact zone of the order of $10^{-4 \leftrightarrow -7}$ between two crack faces in front of a crack tip was further investigated by Comninou et al. [67], who were also evaluating contact zones with friction [68]. Gautesen and Dundurs [69] build on [67], which was only solved for a Dundurs' parameter $\beta \approx 0.5$ [70], and derived exact solutions across the entire range of β. Dundurs discovered that for isotropic bi-materials the plane problem of the elasticity is dependent on the two dimensionless parameters α and β (2.20) with the bimaterial constant from [60] as a relation of both as shown in equation (2.22). The Dundurs' parameters can be explained as being the measure of the mismatch of the plane tensile moduli (α) and of the in-plane bulk moduli β. Dundurs' parameters α and β vanish, if both materials are of equal stiffness or incompressible respectively. The uniqueness of the contact zone shape problem was proven by Shield [71, 72].

$$\begin{aligned} \alpha &= \frac{G_1\,(\kappa_2+1) - G_2\,(\kappa_1+1)}{G_1\,(\kappa_2+1) + G_2\,(\kappa_1+1)} \\ \beta &= \frac{G_1\,(\kappa_2-1) - G_2\,(\kappa_1-1)}{G_1\,(\kappa_2+1) + G_2\,(\kappa_1+1)} \end{aligned} \tag{2.20}$$

$$\text{with} \qquad \kappa_k = \begin{cases} 3 - 4\nu_k \\ \dfrac{3-\nu_k}{1+\nu_k} \end{cases} \tag{2.21}$$

$$\epsilon = \frac{1}{2\pi} \ln\left(\frac{1+\beta}{1-\beta}\right) \tag{2.22}$$

Atkinson [73] introduced a circumventing solution to the oscillatory problem by creating a thin 'adhesion layer', so that either the crack can grow within this isotropic layer or that the crack can grow in the interface between the extra adhesive layer and the original material. Latter option would work under the assumption of anisotropic adhesive layer with a modulus that continuously varies between both materials in a way that at both boundaries the modulus of the interfacing material and adhesive layer are equal. A study on parameters recommended for this extra adhesive layer was presented in [74].

Although it is possible through the approaches by Comninou and Atkinson to avoid interpenetration problems, Aravas and Sharma [75] have proven that the problem of crack face overlap is irrelevant, when the contact zone is smaller than the process zone or the inelastic zone.

The singular form equation (2.23) of the near tip stress field at an interface crack tip between dissimilar isotropic materials was determined by Rice et al. [76]. The two singularity types combined are (a) the coupled oscillatory field scaled by a complex $\mathscr{K}$ and (b) the non-oscillatory field scaled by a real $\mathscr{K}_{\text{III}}$ [49].

$$\sigma_{ij}^{(k)} = \frac{1}{\sqrt{2\pi r}}\Big[\Re(\mathscr{K} r^{ie})\Sigma_{ij}^{(1)}(\varphi,\epsilon) + \Im(\mathscr{K} r^{ie})\Sigma_{ij}^{(2)}(\varphi,\epsilon) + \mathscr{K}_{\text{III}}\Sigma_{iz}^{(\text{III})}(\varphi,\epsilon)\Big] \tag{2.23}$$

$$\text{with} \quad (i,j = r,\varphi)$$

The angular functions $\Sigma_{ij}^{(1,2)}(\varphi,\epsilon)$ are listed in the appendix of [76] and $\Sigma_{ij}^{(\text{III})}(\varphi,\epsilon)$ in [77], containing the polar coordinates (r, φ), the bimaterial constant ϵ and k indicating the number (1, 2) of the upper and lower material. Arabic sub- and superscripts $\{1,2,3\}$ are used for the $\Re$ and $\Im$ parts in contrast to the Roman $\{\text{I},\text{II},\text{III}\}$ that indicate real values associated with stresses. For crack propagation along the interface (i. e. $\varphi = 0$) the dimensionless angular functions are equivalent to the tensile stress, in-plane shear and out-of-plane shear. Deng [77] also provided the functions $U_i(\varphi)$ for the asymptotic formulation of the displacement (2.24) [50].

$$u_i^{(k)} = \sqrt{\frac{r}{2\pi}}\Big[\Re(\mathscr{K} r^{ie})U_i^{(1)}(\varphi) + \Im(\mathscr{K} r^{ie})U_i^{(2)}(\varphi) + \mathscr{K}_{\text{III}}U_z^{(\text{III})}(\varphi)\Big]\,(i = r,\varphi) \tag{2.24}$$

The complex stress intensity factor (2.25) according to Banks-Sills [50] assembles from the real $\mathscr{K}_{1,2}$, which are not linked with the tension and shear stresses. The energy release rate of the interface ($_{\text{if}}$) is derived from Irwin in equation (2.26).

$$\mathscr{K} = \mathscr{K}_1 + \text{i}\mathscr{K}_2 \tag{2.25}$$

$$\mathscr{G}_{\text{T,if}} = \frac{1}{H_1}\left(\mathscr{K}_1^2 + \mathscr{K}_2^2\right) + \frac{1}{H_2}\mathscr{K}_{\text{III}}^2 \tag{2.26}$$

$$\frac{1}{H_1} = \frac{1}{2\cosh^2 \pi\epsilon}\left(\frac{1}{\overline{E_1}} + \frac{1}{\overline{E_2}}\right) \tag{2.27}$$

$$\frac{1}{H_2} = \frac{1}{4}\left(\frac{1}{G_1} + \frac{1}{G_2}\right) \tag{2.28}$$

$$\frac{1}{\overline{E}_k} = \begin{cases} \dfrac{1-\nu_k^2}{E_k} & \text{plane strain} \\ \dfrac{1}{E_k} & \text{generalised plane stress} \end{cases} \tag{2.29}$$

Phase angles are defined as a measure of the stress ratios and the stress intensity factor ratios. The phase angle ψ (2.30) is the ratio between in-plane shear and normal stress in interface direction and the phase angle ϑ (2.31) is the ratio of the out-of-plane shear to the in-plane shear and normal stresses. Here, $\hat{L}$ is an arbitrary length that is suggested to be comparable to the crack tip process zone [48] and the size of $\hat{L}$ was evaluated by [49] for its influence on the phase angle.

$$\psi = \arctan\left[\frac{\Im(\mathcal{K}\hat{L}^{\mathrm{i}\epsilon})}{\Re(\mathcal{K}\hat{L}^{\mathrm{i}\epsilon})}\right] = \arctan\left[\frac{\sigma_{12}}{\sigma_{22}}\right]_{\varphi=0, r=\hat{L}} \tag{2.30}$$

$$\vartheta = \arctan\left[\sqrt{\frac{H_1}{H_2}}\frac{\mathcal{K}_{\mathrm{III}}}{\sqrt{\mathcal{K}_1^2+\mathcal{K}_2^2}}\right] = \arctan\left[\sqrt{\frac{H_1}{H_2}}\frac{\sigma_{32}}{\sqrt{\sigma_{22}^2+\sigma_{12}^2}}\right]_{\varphi=0, r=\hat{L}} \tag{2.31}$$

Stress intensity factors in front of the crack tip ($\varphi = 0$) can be written as

$$\mathcal{K} = \frac{\sqrt{2\pi r}}{r^{\mathrm{i}\epsilon}}\left[\sqrt{\frac{D_{22}}{D_{11}}}\sigma_{22} + \mathrm{i}\sigma_{12}\right]_{\varphi=0} \tag{2.32}$$

Further details on the derivation and the material parameters D_{11}, D_{22} can be found in [78]. Accordingly, formulations for $\sigma_{ij}^{(k)}$, $u_i^{(k)}$, ψ, ϑ, $\mathcal{K}$ and $\mathcal{G}_{\mathrm{T,if}}$ were derived for anisotropic [79, 80] and other types of materials [81] that lead to the energy fracture criterion in equation (2.33) as recently summarised by Banks-Sills [50].

Additionally, Mohammed and Liechti [82] investigated into corner angles in bimaterial interfaces that can also contain stress free surfaces. Fleck et al. [83] summarised the crack path development in a brittle adhesive layer between substrates depending on residual stress, T-stress, $\mathcal{K}_{\mathrm{I}}/\mathcal{K}_{\mathrm{II}}$ and the stiffnesses of adhesive layer and substrates.

While the methods above are based on the *linear elastic fracture mechanics* (LEFM), Shih and Asaro [84] numerically obtained elastic-plastic results for small to large scale yielding based on the deformation theory. Yet, first to publish results on plastic deformation at a crack tip were Rice and Rosengren [85] and Hutchinson [86, 87] with an asymptotic field near a crack tip in a power-law hardening material, as later reviewed and analytically solved by Wang et al. [88]. The HRR solution

(named after Hutchinson, Rice and Rosengren) can be seen as the fundaments of non-linear fracture mechanics.

Yang et al. [89] presented a complete analytical solution of the first two terms of the HRR under mode-I (plane strain) or mode-II (plain stress) loading. Shih [49] compares different elastic and plastic methods and concludes that the domain of validity of *separable* asymptotic solutions of the HRR type appears to be too small to be of relevance. Østby et al. [90] highlighted the plastic hardening mismatch between dissimilar bi-material and its influence on the near tip stress field in small scale yielding. Lee and Kim [91] investigated into asymmetric J-integrals for plastic hardening mismatches. Recently, Belhouari et al. [92] published a study on the interaction between an interface and a crack that runs along, parallel or angled to an interface. A study was undertaken by Strom and Parmigiani [93] on the transition from penetration to deflection of a crack growing perpendicular towards an interface of dissimilar material.

Elastic-plastic analyses are less convenient in practice than LEFM approaches, which are mainly applicable to brittle materials. Composites and bi-materials with ductile behaviour need corrections for the plastic zone around the crack tip, when analysed by LEFM, as has been discussed for isotropic materials in section 2.1.1. Both plastic zone corrections by Irwin and Kies [46] as well as by Dugdale [58] and Barenblatt [59] apply for interface fracture mechanics. Yi et al. [94, 95] presented the effect of different loadings on the plastic zone size and the crack tip opening displacement with a mixed-mode Dugdale model [96] in comparison to FEA and the Irwin model. For the first time, Fan et al. [97] analysed most recently the elastic-plastic fracture behaviour of a curved interface crack and presented a solution based on the mixed-mode Dugdale model for the plastic zone size and the crack tip opening displacement.

Although oscillations due to changing fluid pressure in pipelines occur in long term, dynamic fracture mechanics of interface bonds lies outside the scope of this study. Further details on dynamic and other non-classical fracture mechanics problems, such as under compression along crack face, buckling or residual stresses, for interface cracks and extending literature were presented recently in [98].

2.1.3 *Energy fracture criteria*

The onset of an unstable crack growth defines the critical energy release rate, so that the released energy exceeds the energy bearing capability of the remaining material. This is known as the energy fracture criterion by Griffith [47] that was adjusted independently by Irwin [99] and Orowan [100] to extend the validity of Griffith's model beyond ideally brittle materials. This energy fracture criterion can also be

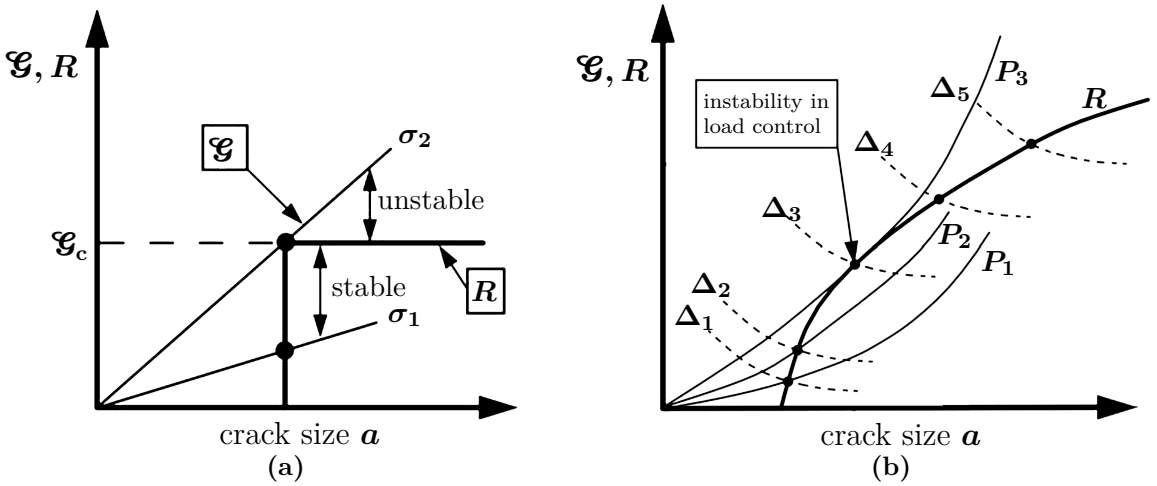

Figure 2.4: Driving force against resistance R curve for: (a) linear $\frac{\mathrm{d}\mathcal{G}}{\mathrm{d}a}$ with flat R curve, (b) non-linear $\frac{\mathrm{d}\mathcal{G}}{\mathrm{d}a}$ and R curve showing a comparison between displacement Δ and load P driven; [55]

explained as a crack becoming unstable, when the driving force exceeds the material resistance to crack extension [55].

An ideally brittle material would exhibit a flat resistance curve, which has a unique $\mathcal{G}_c$ as illustrated in figure (2.4a). For other materials the resistance curves vary as illustrated in figure (2.4b), where a rising R curve is plotted that can be observed for ductile materials. Similar, the ERR is typically not linearly related to the crack size; for instance, $\mathcal{G} \sim a^2$ for a DCB test and $\mathcal{G} \sim a^4$ for a PBT. Figure (2.4b) also demonstrates the difference between load and displacement controlled experiments. Load control leads to unstable crack growth, because the decreased intact material size has to bear continuously increasing loads. In contrast, under displacement control the load is relaxed with every increase in crack size.

In single mode fracture $\mathcal{G} \sim \mathcal{K}^2$ as illustrated in equation (2.2) and analogously $\mathcal{G}_{Ic}$ can be seen as a material property for pure mode-I fracture as is $\mathcal{K}_{Ic}$ [45]. Equivalent to equation (2.19), a critical energy release rate can be used as fracture criterion for single mode fracture. In particular composite materials and interface debonding undergo mode mixes during crack propagation. A simple correlation like equation (2.19), however, cannot describe mix-mode situations sufficiently. Many different fracture criteria have been developed, which in itself illustrates that the different hypotheses of those criteria cannot be applied on any type of material and load-geometry scenario.

One class of criteria is based on physical relationships, such as the maximum tangential (or hoop) stress criterion (Erdogan and Sih [101], Williams and Ewing [102] and for dynamic Yoffe [103]), the maximum tangential principal stress (Maiti and Smith [104–106]), the maximum tangential strain (Wu [107]), the minimum

strain energy density criterion (or S-criterion, Sih [108]), the maximum strain energy density criterion (or T-criterion, Theocaris et al. [109]) and the kinking crack model (Hussain et al. [110], extended for bi-material by Wang et al. [111]).

All those criteria do not account for the microscopic failure mechanism, which limits the spectrum of possible applications and the validity for scenarios of $|\mathscr{K}_{\mathrm{II}}| \gg \mathscr{K}_{\mathrm{I}}$ [45]. In the same way, all criteria yield similar results for small $|\mathscr{K}_{\mathrm{II}}|$ or pure mode-I as well as all are invalid for pure mode-II. Nevertheless, the angles of deflection of the crack direction that can be estimated from the fracture criteria listed above are usable, even in the case that the fracture criteria are not.

Differences between crack growth within isotropic homogeneous materials to crack growth along interfaces of dissimilar materials were previously discussed in sections 2.1.1 and 2.1.2. Banks-Sills and Ashkenazi [112] compared four fracture criteria for LEFM of interfaces and further developed one into the three dimensional energy fracture criterion [113, 114] of equation (2.33), which is dependent on the average, complex, critical mode-I ERR and the phase angles. The averaged $\overline{\mathscr{G}}_{\mathrm{Ic}}$ is evaluated from tests through equation (2.34).

$$\mathscr{G}_{\mathrm{if,c}} = \overline{\mathscr{G}}_{\mathrm{Ic}} \left(1 + \tan^2 \psi\right) \left(1 + \tan^2 \vartheta\right) \tag{2.33}$$

$$\mathscr{G}_{\mathrm{Ic}} = \frac{1}{H_1} \left[\Re(\mathscr{K} \hat{L}^{\mathrm{i}\epsilon})\right]^2 \tag{2.34}$$

Because no criterion was proven to be ideal across the range of possible materials and load-geometry configurations, a second class of 'non-local' criteria was proposed that utilise two parameters. As one of the first, Newman [115] proposed the two-parameter fracture criterion in equation (2.35). Newman's TPFC combines the fracture parameter m and the single mode fracture toughness with the nominal (net-section) failure stress σ_{n}, which must not be larger than the yield stress, and the nominal stress of the section at plastic deformation σ_{u}, which is equivalent to the ultimate tensile strength for tensioned plates or 1.15 times larger for pressurised cylinders.

$$\mathscr{K}_{\mathrm{c}} = \frac{\mathscr{K}_{\mathrm{Ic}}}{1 - m \left(\sigma_{\mathrm{n}} / \sigma_{\mathrm{u}}\right)} \quad , \quad (\sigma_{\mathrm{n}} \leq \sigma_c) \tag{2.35}$$

Leguillon [116] developed the 'coupled criterion' in equation (2.38) that combines the general critical energy release rate criterion (2.36) with critical stress criterion (2.37). Here, $C(\omega, \varphi_0)$ [117] is a scaling term dependent on the notch opening angle ω and the crack kinking angle φ_0. The singularity exponent $1/2 \leq \alpha \leq 1$ becomes $1/2$ for a crack ($\omega = 0$) and 1 for a straight edge ($\omega = \pi$). With $s_\varphi(\varphi_{\mathrm{c}}) = 1$ the general form of equation (2.38) can be simplified to equation (2.39). Applied on a corner of a rectangular geometry such as a lap joint interface [118], the critical stress

intensity factor can be expressed as equation (2.40).

It incorporates the dimensionless crack length $\lambda = l/t$ and the initial crack jump length λ_c, in contrast to the LEFM assumption of an infinitesimally small initial crack length. The *finite fracture mechanics* (FFM) [119] requires a minimum initial crack length $\Delta a > 0$ that acts as a material constant defined as $L = {}^{\Delta a}/_{2}$ [120].

$$\mathscr{G}_\mathrm{c} \leq \mathscr{G} = \frac{\mathrm{d}\Pi_\mathrm{p}}{\mathrm{d}A} \tag{2.36}$$

$$\sigma_\mathrm{c} \leq \sigma \qquad ((or)\ \tau_\mathrm{c} \leq \tau) \tag{2.37}$$

$$\mathscr{K} \geq \mathscr{K}_\mathrm{c} = \left(\frac{\mathscr{G}_\mathrm{c}}{C(\omega, \varphi_0)}\right)^{1-\alpha} \left(\frac{\sigma_\mathrm{c}}{s_\varphi(\varphi_0)}\right)^{2\alpha-1} \tag{2.38}$$

$$\mathscr{K} \geq \mathscr{K}_\mathrm{c} = \left(\frac{\mathscr{G}_\mathrm{c}}{C(\omega, \varphi_0)}\right)^{1-\alpha} \sigma_\mathrm{c}^{2\alpha-1} \tag{2.39}$$

$$\mathscr{K} \geq \mathscr{K}_\mathrm{c} = \left(\frac{\lambda_\mathrm{c}\mathscr{G}_\mathrm{c}}{C(\lambda_\mathrm{c}) - C(\lambda_0)}\right)^{1-\alpha} \left(\frac{\sigma_\mathrm{c}}{s_\varphi(-\lambda_\mathrm{c}, \varphi_0)}\right)^{2\alpha-1} \tag{2.40}$$

Similar to Leguillon, a coupled stress–energy criterion for FFM was presented by Cornetti et al. [121], which differs from the criterion of Leguillon, because it is not based on a point-wise stress criterion. The formulation by Cornetti et al. is similar to the *line method* (LM) that can be found in [122, 123]. The crack extension Δa and the failure load σ_f are the two unknowns for both necessary conditions of equation (2.41). A derivation for pull-push shear tests as single mode-II test can be found in [124] and mix-modes were discussed in [125].

$$\begin{cases} \displaystyle\int_a^{a+\Delta a} \sigma_\mathrm{y}(x)\,\mathrm{d}x & = \sigma_\mathrm{c}\Delta a \\ \displaystyle\int_a^{a+\Delta a} \mathscr{K}_\mathrm{Ic}^2(a)\,\mathrm{d}a & = \mathscr{K}_\mathrm{Ic}^2\Delta a \end{cases} \tag{2.41}$$

Weißgräber and Becker [126] continued on the work of Leguillon and Cornetti et al. and defined a criterion (2.42) for the failure load F_f. Its principle is to solve the functions for the stresses and the incremental (or average) energy release rate $\overline{\mathscr{G}}$ towards the smallest load where both conditions are satisfied and thus the crack lengths a of both criteria coincide. Recently, Perelmuter [127] extended the non-local criteria to large scale process zones.

$$F_\mathrm{f} = \min_{F,a} \left\{ F \| f(\sigma_{ij}(x_i)) \geq \sigma_\mathrm{c}\ , \qquad \forall x_i \in \Omega_\mathrm{c} \quad \wedge \quad \overline{\mathscr{G}}(A = \Delta A) \geq \mathscr{G}_\mathrm{c} \right\} \tag{2.42}$$

However, a lack of confidence exists in fracture criteria established on physical relationships. Therefore, a third type of criteria is based on simple mathematical formulations (2.43), whose variables are partly determined from experiments. The

critical total ERR criterion definition of $\mathcal{G}_{\mathrm{Tc}} = \mathcal{G}_{\mathrm{Ic}} + \mathcal{G}_{\mathrm{IIc}} + \mathcal{G}_{\mathrm{IIIc}}$ or a sole dependence on $\mathcal{G}_{\mathrm{Ic}}$ as in equation (2.44) are less complex, yet often not a good enough characterisation.

$$f(\mathcal{G}_{\mathrm{I}}, \mathcal{G}_{\mathrm{II}}, \mathcal{G}_{\mathrm{III}}, \mathcal{G}_{\mathrm{Ic}}, \mathcal{G}_{\mathrm{IIc}}, \mathcal{G}_{\mathrm{IIIc}}, \ldots) \geq f_c \tag{2.43}$$

$$f = \frac{\mathcal{G}_{\mathrm{T}}}{\mathcal{G}_{\mathrm{Ic}}} \geq 1 = f_c \quad , \qquad f = \frac{\mathcal{G}_{\mathrm{T}}}{\mathcal{G}_{\mathrm{Tc}}} \geq 1 = f_c \tag{2.44}$$

Some of the most common criteria were summarised by Shahverdi et al. [128] and can be found in proprietary FEA software [129]. Piece-wise linear fracture criteria compare each mode's ERR with its single mode critical (2.45).

A *quadratic polynomial criterion* is shown in equations (2.46) and (2.47) with the fitting parameters a, b and c determined through least square fit.

$$f = \frac{\mathcal{G}_{\mathrm{I}}}{\mathcal{G}_{\mathrm{Ic}}} + \frac{\mathcal{G}_{\mathrm{II}}}{\mathcal{G}_{\mathrm{IIc}}} + \frac{\mathcal{G}_{\mathrm{III}}}{\mathcal{G}_{\mathrm{IIIc}}} \tag{2.45}$$

$$f = a\frac{\mathcal{G}_{\mathrm{II}}^2}{\mathcal{G}_{\mathrm{I}}} + b\frac{\mathcal{G}_{\mathrm{II}}}{\mathcal{G}_{\mathrm{I}}} + c\frac{1}{\mathcal{G}_{\mathrm{I}}} \tag{2.46}$$

$$\mathcal{G}_{\mathrm{T}} = A\left(\frac{\mathcal{G}_{\mathrm{II}}}{\mathcal{G}_{\mathrm{T}}}\right)^2 + B\left(\frac{\mathcal{G}_{\mathrm{II}}}{\mathcal{G}_{\mathrm{T}}}\right) + C \tag{2.47}$$

The *bilinear fracture criterion* presented in equation (2.48) was invented by Reeder [130], which is the only type of fracture criterion that produces a discrete curve. The parameters ξ and ζ have to be determined as the best fit of the toughness against the mode mix data. To reduce the input parameters necessary and subsequently the tests to determine those, Davidson and Zhao [131] presented a derivation called the limited bilinear criterion.

$$f = \begin{cases} \dfrac{\mathcal{G}_{\mathrm{I}} - \xi\mathcal{G}_{\mathrm{II}}}{\mathcal{G}_{\mathrm{Ic}}} \ , & \text{for} \quad \dfrac{\mathcal{G}_{\mathrm{II}}}{\mathcal{G}_{\mathrm{I}}} < \dfrac{{}^{1}\!/_{\zeta}\mathcal{G}_{\mathrm{Ic}} - \mathcal{G}_{\mathrm{IIc}}}{\mathcal{G}_{\mathrm{I}} + \xi\mathcal{G}_{\mathrm{II}}} \\ \dfrac{\zeta\mathcal{G}_{\mathrm{II}} - \mathcal{G}_{\mathrm{I}}}{\mathcal{G}_{\mathrm{IIc}}} \ , & \text{for} \quad \dfrac{\mathcal{G}_{\mathrm{II}}}{\mathcal{G}_{\mathrm{I}}} > \dfrac{{}^{1}\!/_{\zeta}\mathcal{G}_{\mathrm{Ic}} - \mathcal{G}_{\mathrm{IIc}}}{\mathcal{G}_{\mathrm{I}} + \xi\mathcal{G}_{\mathrm{II}}} \end{cases} \tag{2.48}$$

An *exponential hackle criterion* [132], based on the hackle angle parameter N, can be written for the ERR as [130]

$$f = \frac{\mathcal{G}_{\mathrm{I}} + \mathcal{G}_{\mathrm{II}}}{(\mathcal{G}_{\mathrm{Ic}} - \mathcal{G}_{\mathrm{IIc}})\,\mathrm{e}^{\gamma(1-N)}} \tag{2.49}$$

$$N = \sqrt{1 + \frac{\mathcal{G}_{\mathrm{II}}}{\mathcal{G}_{\mathrm{I}}}\sqrt{\frac{E_{11}}{E_{22}}}} \tag{2.50}$$

Here, γ is arbitrarily adjustable to the model and geometry investigated. Another similar criterion presented in [130] is the *exponential stress intensity factor ratio*

criterion. This was translated to equation (2.51) to accommodate the ERR rate instead of the SIF and also contains the material parameter η.

$$f = \frac{\mathcal{G}_{\mathrm{I}} + \mathcal{G}_{\mathrm{II}}}{(\mathcal{G}_{\mathrm{Ic}} - \mathcal{G}_{\mathrm{IIc}})\, \mathrm{e}^{\sqrt[\eta]{\frac{\mathcal{G}_{\mathrm{I}}}{\mathcal{G}_{\mathrm{II}}}}}} \tag{2.51}$$

A criterion (2.52) based on the mode-I–mode-II interaction can be found in [130, 133]. In this criterion, the magnitude of i determines the interaction rate of both modes with each other.

$$0 = \left(\frac{\mathcal{G}_{\mathrm{I}}}{\mathcal{G}_{\mathrm{Ic}}} - 1\right)\left(\frac{\mathcal{G}_{\mathrm{II}}}{\mathcal{G}_{\mathrm{IIc}}} - 1\right) - i\left(\frac{\mathcal{G}_{\mathrm{I}}}{\mathcal{G}_{\mathrm{Ic}}}\right)\left(\frac{\mathcal{G}_{\mathrm{II}}}{\mathcal{G}_{\mathrm{IIc}}}\right) \tag{2.52}$$

$$i = \left[\kappa + \varphi\left(\frac{\mathcal{G}_{\mathrm{I}}}{\mathcal{G}_{\mathrm{I}} + \mathcal{G}_{\mathrm{II}}}\right)\right] \tag{2.53}$$

Benzeggagh and Kenane [134] developed the criterion in equation (2.54) that was later modified by Reeder [135] to the *modified B-K fracture criterion* in equation (2.55).

$$f = \frac{\mathcal{G}_{\mathrm{T}}}{\mathcal{G}_{\mathrm{Ic}} + (\mathcal{G}_{\mathrm{IIc}} - \mathcal{G}_{\mathrm{Ic}})\left(\dfrac{\mathcal{G}_{\mathrm{II}} + \mathcal{G}_{\mathrm{III}}}{\mathcal{G}_{\mathrm{T}}}\right)^{\eta}} \tag{2.54}$$

$$f = \frac{\mathcal{G}_{\mathrm{T}}}{\mathcal{G}_{\mathrm{Ic}} + \left((\mathcal{G}_{\mathrm{IIc}} - \mathcal{G}_{\mathrm{Ic}})\dfrac{\mathcal{G}_{\mathrm{II}}}{\mathcal{G}_{\mathrm{T}}} + (\mathcal{G}_{\mathrm{IIIc}} - \mathcal{G}_{\mathrm{Ic}})\dfrac{\mathcal{G}_{\mathrm{III}}}{\mathcal{G}_{\mathrm{T}}}\right)\left(\dfrac{\mathcal{G}_{\mathrm{II}} + \mathcal{G}_{\mathrm{III}}}{\mathcal{G}_{\mathrm{T}}}\right)^{\eta-1}} \tag{2.55}$$

One of the most common and versatile fracture criteria is the *power-law fracture criterion* [137] shown in equation (2.56). The three power exponents α, β and γ are

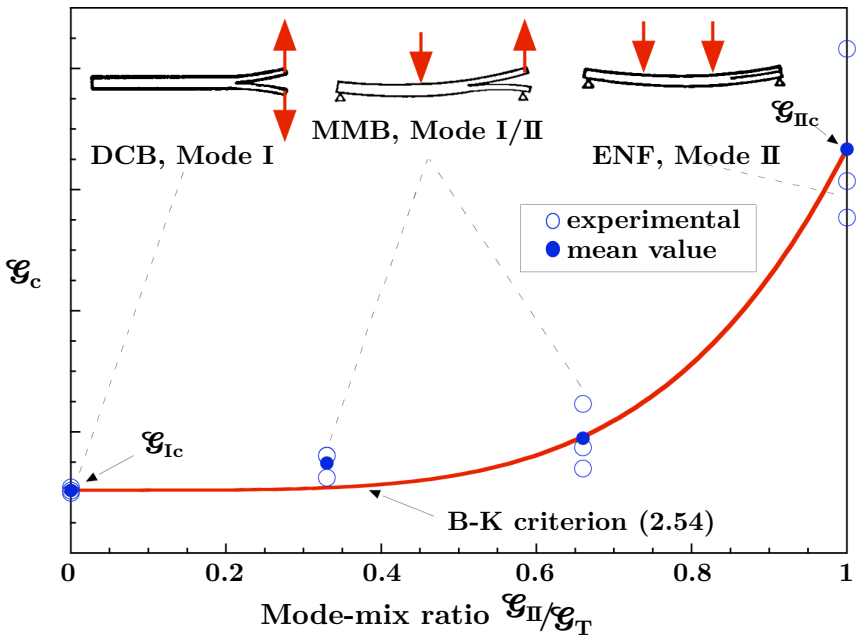

Figure 2.5: Determination of the B-K fracture criterion through DCB, MMB and ENF tests; from [136]

constants and have to be determined through a curve fit.

$$f = \left(\frac{\mathcal{G}_{\mathrm{I}}}{\mathcal{G}_{\mathrm{Ic}}}\right)^{\alpha} + \left(\frac{\mathcal{G}_{\mathrm{II}}}{\mathcal{G}_{\mathrm{IIc}}}\right)^{\beta} + \left(\frac{\mathcal{G}_{\mathrm{III}}}{\mathcal{G}_{\mathrm{IIIc}}}\right)^{\gamma} \tag{2.56}$$

It becomes obvious from the number and variety of fracture criteria as well as the fact that no criterion developed into a dominant position over the other criteria, that one simple, universal fracture criterion does not exist. Every criterion needs a number of different tests conducted with several specimens tested, in order to determine different parameters such as single mode fracture toughness and curve fits as illustrated in figure (2.5). The standard test procedures to obtain single and mixed-mode fracture toughness are described in the following chapter.

2.2 Interlaminar fracture energy tests

The standardised test procedures for interface or interlaminar fracture energy were developed to determine the critical single mode fracture toughness $\mathcal{K}_{\mathrm{Ic..IIIc}}$ and critical ERRs accordingly. Typically, a *double cantilever beam* (DCB) test is undertaken to measure $\mathcal{K}_{\mathrm{Ic}}$. In a DCB test (fig. 2.6) as recommended by the BS ISO 15024 [138] and other standards [139–141], the load pulls the upper and lower side of the pre-cracked edge of the beam apart, while the other edge remains free, which results in a pure crack tip opening displacement. Results can be obtained through the modified beam theory or the compliance calibration method [44].

The most common method to determine the mode-II fracture toughness is an

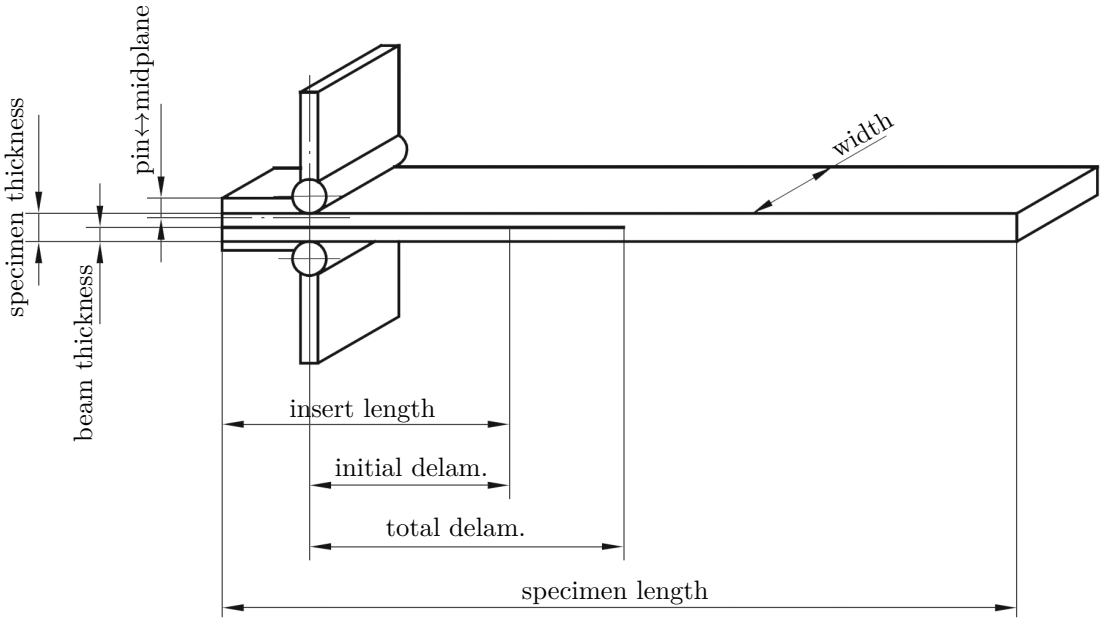

Figure 2.6: Double cantilever beam (DCB) with pre-crack and piano hinges for load application; from BS ISO 15024 [138]

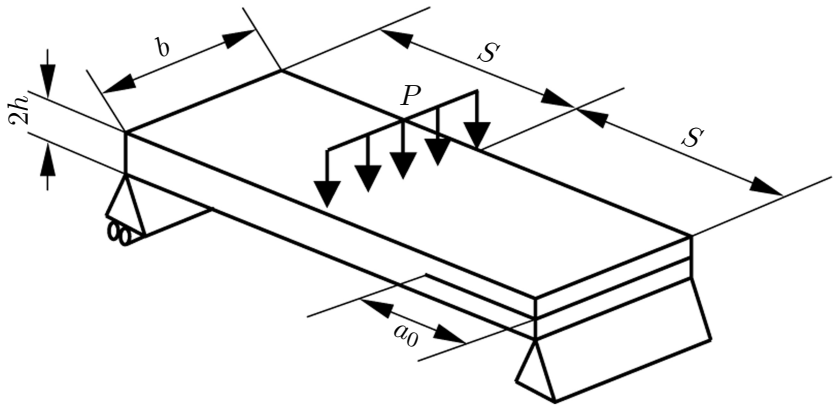

Figure 2.7: End notched flexure (ENF) test; [44]

end notch flexure (ENF) test [142] or the *calibrated end-loaded split* (C-ELS) as the proclaimed equivalent from the BS ISO 15114 [143] standard. The latter performs an initial calibration by inversing the test setup when clamping the cracked and loading the intact end of the beam. The actual mode-II test has the intact end fixed and the cracked end displaced. The ENF test is the same apart from that the test setup is identical to a 3-point bend test. The result in both cases is an in-plane shear stress on the crack tip.

Often knowledge about the critical ERR for single mode loading is not sufficient to evaluate the fracture potential in a mixed mode situation. Data for the development of a fracture criterion valid across a range of mode-mixity can be obtained from a *mixed mode bending* (MMB) test as standardised in ASTM D6671 [144]. The specimen is put under a combined DCB and ENF loading through an eccentrically pin-jointed lever arm, which imposes a central point load on the beam through the bending load applied at the cracked end. This complex setup is illustrated in figure (2.9).

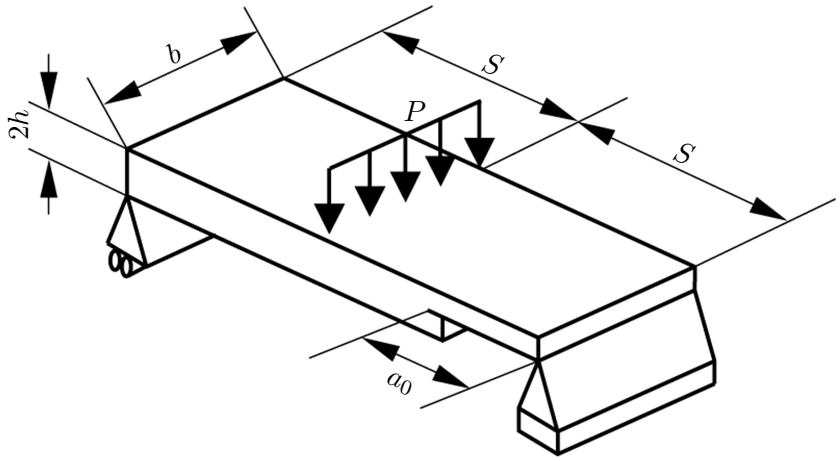

Figure 2.8: Single leg bending (SLB) test; [44]

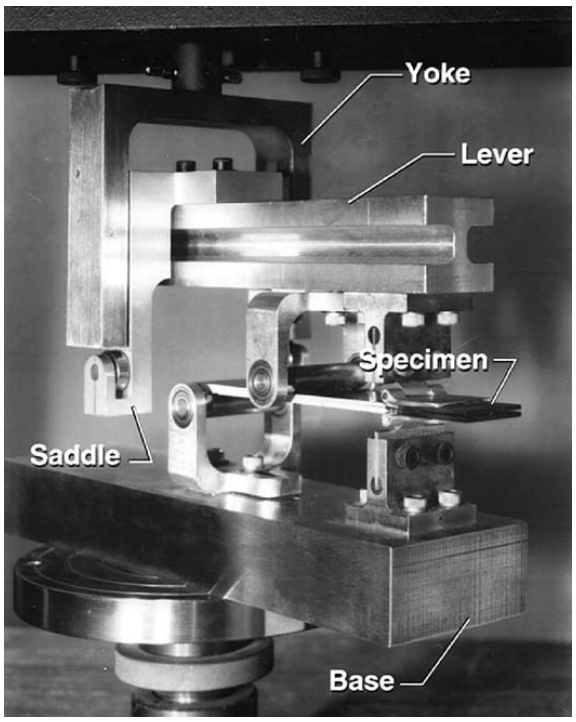

Figure 2.9: Mixed mode bending (MMB) specimen in test rig; from ASTM D6671 [144]

Less complex than the MMB is a *single leg bending* (SLB) test [145]. An SLB test setup is comparable with an ENF apart from the lower half of the pre-cracked end is missing and the load is applied solely on the top half. However, it is not possible to investigate a variety of mode mixes with an SLB, because its limitation to a single mode mix of $\mathcal{G}_{\mathrm{II}}/\mathcal{G}_{\mathrm{T}} \approx 0.4$ [44].

The three tests of DCB, CELS and SLB are sufficient to determine the mix-mode ERR fracture criterion as presented in [131]. All test methods need to be pre-cracked first, in order to create a more natural crack tip. The specimen width must be $w \gg t$ to obtain a central region wide enough under plane strain condition. In contrast, the crack tip edge is stress free, followed by a small region of parabolic stress increase. A wider specimen provides a larger area of constant stress and therefore the influence of the edge can be marginalised. As the discussed tests and their respective calculations are based on the classical beam theory, the specimen length must be large compared to the beam thickness. Further explanations and detailed mathematical formulation about standard fracture test methods can be found in the respective standards or the literature [44, 55].

The fundamental solutions for peel tests were summarised by Thouless and Jensen [146]. The resilience of an adhesive bonding to peel stress is lower than against any other load scenario. However, peel is mainly a problem for thin, elastic or very low modulus materials. Kinloch et al. [147] corrected ERR formulations for the energy dissipation through plastic bending of the peeling arm and developed a model that considers root rotation of the peel front. Specimens under peel load can additionally

undergo a large range of mode phase angles [146].

2.3 Analytical Determination of Fracture Energy of SLBTs

In the following sections 2.3.1 and 2.3.2 different analytical solutions for circular plates are discussed. Fixed edges are assumed as boundary conditions along the crack contour. The plates are under load by a single central force or circular surface load with near-zero radius as well as annular line loads for investigation of shaft-loaded blister tests. Different load setups were investigated, because of the differences in punch geometries used. First descriptions of the contact mechanics of elastic solids were published by Heinrich Hertz [148]. Sneddon [149] presented formulae for the determination of the penetration of a punch with arbitrary profile. Solutions for pressure loads across the full crack surface in the case of a pressurised blister test are discussed in chapter 2.4.

2.3.1 *Point loading*

Malyshev and Salganik [65] studied plexiglass lapjoints and circular plexiglass plates on rigid substrates bonded by epoxy adhesives. They solved the determination of the energy release rate from the law of energy conservation (2.57). Alteration of their own fracture energy solution for cantilever beams bonded to a rigid substrate, towards circular plates yielded a solution for circular bending plates under stress by a central point load. The energy release rate can be derived accordingly as equation (2.62) dependent on the load F and the flexural rigidity D (2.107) of the plate and is labelled with '$_{\mathrm{lb}}$'. Neither the deformation nor the crack opening influences this solution.

$$\mathcal{G} = \frac{F\partial w - \partial\Pi}{\partial A} \tag{2.57}$$

$$\text{with} \quad \partial\Pi \quad — \quad \text{stored potential energy} \tag{2.58}$$

$$w_0 = \frac{FR^2}{16\pi D} \tag{2.59}$$

$$\Pi = \frac{8\pi D w^2}{R^2} \tag{2.60}$$

$$\text{from Malyshev and Salganik} \qquad \mathcal{G}_{\mathrm{lb}} = \frac{F^2}{32\pi D} = \frac{3\left(1-\nu^2\right)F^2}{8\pi E t^3} \tag{2.61}$$

$$\text{from O'Brien et al.} \qquad \mathcal{G}_{\mathrm{lb}} = \frac{3\left(1-\nu^2\right)F^2}{8\pi^2 E t^3} \tag{2.62}$$

Equation (2.62) originates from equation (2.61) by Malyshev and Salganik, but was corrected to the presented version through O'Brien et al. [150]. In contrast to the 'load dependent' equation (2.62), Malyshev and Salganik also derived a solution (2.63), which is dependent on the deformation w and crack radius R instead of the load (label: '$_{\mathrm{db}}$').

$$\mathcal{G}_{\mathrm{db}} = \frac{8Dw^2}{a^4} = \frac{2Et^3w^2}{3\left(1-\nu^2\right)a^4} \tag{2.63}$$

The combination of 'load based' equation (2.62) and 'displacement based' equation (2.63) in equation (2.64) is labelled as '$_{\mathrm{cb}}$' and does not contain the flexural rigidity as separate factor. The same result can be found in [151, 152] with a more detailed description of its deduction.

$$\mathcal{G}_{\mathrm{cb}} = \frac{Fw}{2\pi R^2} \tag{2.64}$$

Sheplak and Dugundji [153] observed that a transition between plate bending and membrane stretching occurs within the range of $1 < \beta < 20$ of the non-dimensional, normalised membrane stress. Komaragiri et al. [154] proposed a similar dimensionless parameter λ (cf. eq. 2.69). While [153] studied pressurised blister tests, Wan [151] investigated the transition behaviour for shaft-loaded blister tests. In accordance with [153], Wan introduced the dimensionless parameters for normalised radius, deflection slope, membrane stress and applied load of equations (2.65) to (2.68) respectively.

$$\hat{r} = \frac{r}{R} \tag{2.65}$$

$$\hat{\varphi} = \frac{\mathrm{d}W}{\mathrm{d}\hat{r}} = \frac{R}{t}\frac{\mathrm{d}w}{\mathrm{d}r} \tag{2.66}$$

$$\hat{N} = \sqrt{\frac{NR}{D}} \tag{2.67}$$

$$\hat{p} = \frac{FR^2}{2\pi D} \tag{2.68}$$

$$\lambda = \sqrt{\left[12\left(1-\nu^2\right)\right]^3}\,\frac{FR^2}{Et^4} \tag{2.69}$$

The membrane stress N is determined as shown in equation (2.70), [151]. For pure plate bending the membrane stress N becomes negligible and $\hat{N} \to 0$. The result is the classical solution of equation (2.59) for a clamped plate over the radius in equation (2.73) or equivalent in the normalised form of equation (2.74). Wan deduced this solution through the slope (2.72), which was build from modified bessel

functions of the first and second kind.

$$N = \frac{Et}{2R^2\left(1-\nu^2\right)} \int_0^R \left(\frac{\mathrm{d}w}{\mathrm{d}r}\right)^2 r\,\mathrm{d}r = \frac{Et^3}{2R^3\left(1-\nu^2\right)} \int_0^1 \hat{\varphi}^2 \hat{r}\,\mathrm{d}\hat{r} \tag{2.70}$$

$$\hat{\varphi}\left(\hat{r}\right) = \frac{\hat{p}}{\hat{N}^2}\left[\left(\frac{1-\hat{N}K_1\left(\hat{N}\right)}{I_1\left(\hat{N}\right)}\right) I_1\left(\hat{N}\hat{r}\right) + \hat{N}K_1\left(\hat{N}\hat{r}\right) - \frac{1}{\hat{r}}\right] \tag{2.71}$$

$$\hat{\varphi}_\mathrm{b} = \frac{\hat{p}\hat{r}}{2}\ln\hat{r}^2 \tag{2.72}$$

$$w\left(r\right) = \frac{FR^2}{16\pi D}\left[1-\left(\frac{r}{R}\right)^2 + \left(\frac{r}{R}\right)^2 \ln\left(\frac{r}{R}\right)^2\right] \tag{2.73}$$

$$\hat{\Phi}\left(\hat{r}\right) = \int_0^1 \hat{\varphi}\,\mathrm{d}\hat{r} = \frac{\hat{p}}{8}\left[1-\hat{r}^2+\hat{r}^2\ln\hat{r}^2\right] \tag{2.74}$$

Williams [152] was first to show the elastic solution for membrane stretching. In the case of membrane stretching as sole deformation, $\hat{N} \to \infty$. The slope's maximum moves towards the centre and approaches infinity, though being zero at the plate centre.

$$\hat{\varphi}_\mathrm{m} = -\frac{\hat{p}}{\hat{N}^2\hat{r}} \tag{2.75}$$

$$\hat{\Phi}\left(\hat{r}\right) = -\frac{\hat{p}}{\hat{N}^2}\ln\hat{r} \tag{2.76}$$

Based on the relations of equation (2.1) and equation (2.6), Wan [151] also gives an expression for a normalised ERR, χ, for point loaded blisters as shown in equation (2.77). The pure bending energy release rate $\mathcal{G}_\mathrm{b}$ is the same as in equation (2.64). In this case with $\hat{N} \to 0$, the normalised ERR $\chi_\mathrm{b} = 1/2$, while for $\hat{N} \to \infty$ under pure membrane stretching $\chi_\mathrm{m} = 1/4$.

$$\chi = \frac{\mathcal{G}A}{Fw_0} \tag{2.77}$$

$$\chi = \chi_\mathrm{b} + \chi_\mathrm{m} = \frac{\hat{\varphi}'^2}{4\hat{p}\hat{\Phi}_0} + \frac{\hat{N}^4}{24\hat{p}\hat{\Phi}_0} \tag{2.78}$$

$$\mathcal{G} = \mathcal{G}_\mathrm{b} + \mathcal{G}_\mathrm{m} = \frac{M^2}{2D} + \frac{N^2\left(1-\nu\right)}{Et} \tag{2.79}$$

$$\text{for pure bending:} \qquad \mathcal{G}_\mathrm{b} = \frac{1}{2}\frac{Fw_0}{\pi R^2} \quad \Rightarrow \quad \chi_\mathrm{b} = \frac{1}{2} \tag{2.80}$$

$$\text{for pure membrane:} \qquad \mathcal{G}_\mathrm{m} = \frac{1}{4}\frac{Fw_0}{\pi R^2} \quad \Rightarrow \quad \chi_\mathrm{m} = \frac{1}{4} \tag{2.81}$$

Pressure across a minimised surface is another approach for an analytical plate bending solution under a central point load as shown in figure (2.10), which was deduced by Al-Maskari [155]. Within the same assumptions as described in the preceded paragraphs, a plate deformation under bending from a central surface load p_0 with near-zero radius R_0 can be aproximated according to Young and Budynas [156, tab. 11.2., case 17]. An uniform load (2.82) over a very small, circular, central area with radius R_0 (2.83) is assumed instead of an ideal point load F. Concentrated loads or loads across a very small area result analytically in very high stress concentrations. It was shown that replacing the actual radius R_0 of the area with an 'equivalent radius' R_0' aproximates the actual stress concentration more precisely [157].

$$F = p_0 \pi R_0^2 \tag{2.82}$$

$$\text{for} \qquad r > R_0' \qquad \text{and} \qquad R_0 \begin{cases} \geqslant \dfrac{t}{2}\,; & R_0' = R_0 \\ < \dfrac{t}{2}\,; & R_0' = \sqrt{1.6R_0^2 + t^2} - 0.675t \end{cases} \tag{2.83}$$

The deflection curve is calculated from equation (2.84) with the maximum deflection in the centre at $r = 0$ yielding equation (2.85).

$$w_{\mathrm{b,np}} = \frac{F}{16\pi D}\left[R^2 - r^2\left(1 + 2\ln\left(\frac{R}{r}\right)\right)\right] \tag{2.84}$$

$$w_{\mathrm{b,np,max}} = \frac{F R^2}{16\pi D} \tag{2.85}$$

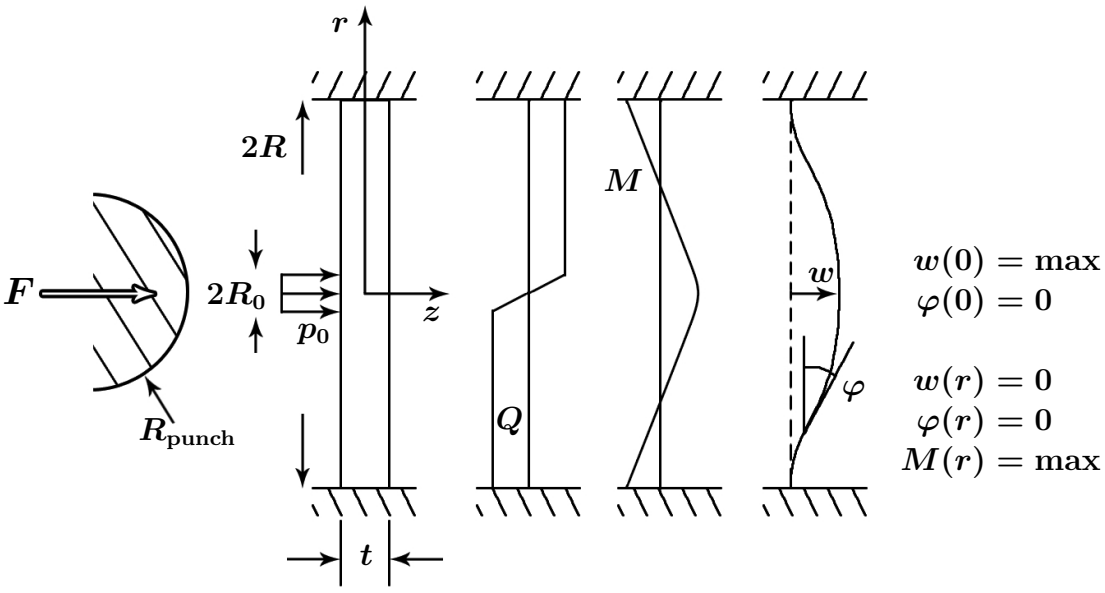

Figure 2.10: Circular plate under a near point load by a hemispherical punch

The opened crack area $\mathrm{d}A$ is derived from equation (2.86).

$$\frac{\mathrm{d}A}{\mathrm{d}R} = \frac{\mathrm{d}\pi R^2}{\mathrm{d}R} = 2\pi R \qquad \Rightarrow \qquad \mathrm{d}A = 2\pi R\,\mathrm{d}R \tag{2.86}$$

Inserting equation (2.84) in equation (2.6) produces the energy release rate as equation (2.87) within the limits of the classical plate bending theory.

$$\mathscr{G}_\mathrm{b} = \frac{F^2}{4\pi R} \cdot \frac{\partial C}{\partial R} = \frac{F^2}{4\pi R} \frac{2\,(R^2 - r^2)}{16\pi D R} \tag{2.87}$$

Shear can not be omitted [158], because of the small R/t ratio that usually has to be assumed for corrosion repairs. The deflection due to shear can be found from Castigliano's theorem of equation (2.88). The strain energy as result of shear stress is the integral of the shear force over the radius in combination with the area, shear modulus and the shear correction factor K_s. Young and Budynas [156, chap. 8.10] listed shear correction factors for various cross-sections. Their derivation is presented in section 2.4.2.

$$w_\mathrm{s,np} = \frac{\partial U_\mathrm{s}}{\partial P} \tag{2.88}$$

$$\Pi_\mathrm{s,np} = \frac{K_\mathrm{s}}{2AG} \int_0^R Q^2\,\mathrm{d}r \tag{2.89}$$

$$\text{with} \qquad K_\mathrm{s} = \frac{6}{5} \qquad \text{for rectangular cross-sections} \tag{2.90}$$

The difference in shear deflection for central surface loads with small radii can be assumed to be similar to the shear deflection of central annular line loads with small radius. The derivation of the shear deflection for the near-point solution can be calculated under this assumption from equation (2.99).

$$\begin{aligned} w_\mathrm{s,np}(r) &= \frac{6}{5}\left(\frac{r}{R}\right)^2 \ln\left(\frac{R}{r}\right) \frac{p_0 R^2}{2tG} = \frac{6Fr^2R^2}{10\pi R_0^2 R^2 tG} \ln\left(\frac{R}{r}\right) \\ &= \frac{6Fr^2}{10\pi R_0^2 tG} \ln\left(\frac{R}{r}\right) \end{aligned} \tag{2.91}$$

The total deflection due to bending and shear is summed up in equation (2.92). Inserting equation (2.92) in equation (2.8) yields the compliance.

$$w_\mathrm{t,np} = w_\mathrm{b,np} + w_\mathrm{s,np} = \frac{F}{16\pi D}\left[R^2 - r^2\left(1 + 2\ln\left(\frac{R}{r}\right)\right)\right] + \frac{6Fr^2}{10\pi R_0^2 tG} \ln\left(\frac{R}{r}\right) \tag{2.92}$$

The energy release rate for the 'near-point' loading solution '$_\mathrm{np}$' is obtained from the partial derivative of the compliance C with respect to R as shown in

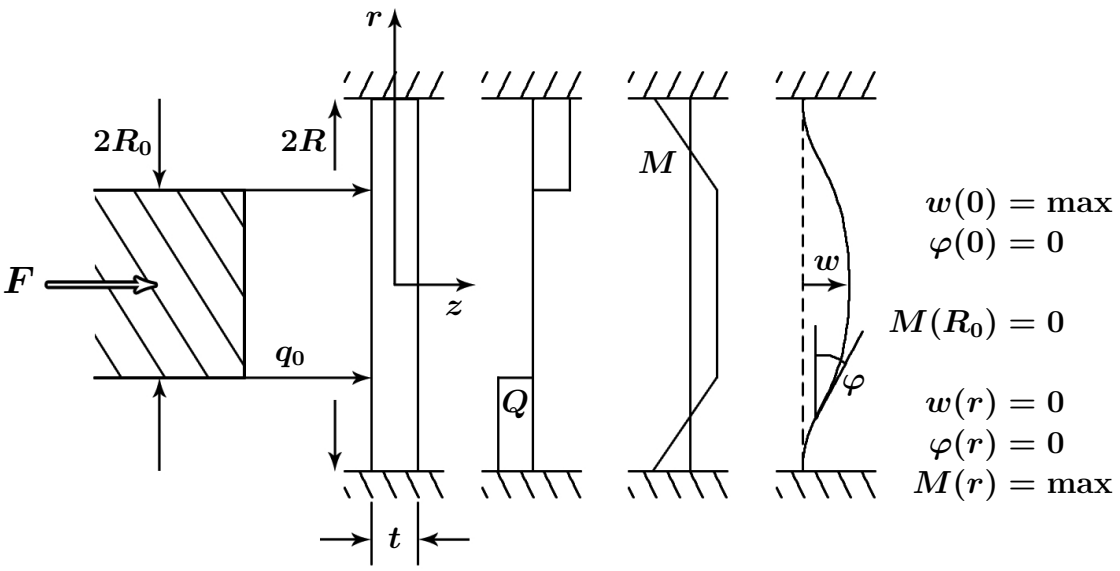

Figure 2.11: Circular plate under annular load by a flat punch

equation (2.6).

$$\mathcal{G}_{\mathrm{np}} = \frac{F^2}{4\pi R} \cdot \frac{\partial C}{\partial R} = \frac{F^2}{4\pi^2 R^2} \left(\frac{2\left(R^2 - r^2\right)}{16D} + \frac{6r^2}{10R_0^2 tG} \right) \Bigg|_{r=R_0}$$

$$= \frac{F^2}{4\pi^2 R^2} \left(\frac{3\left(1 - \nu_{\mathrm{xy}}^2\right)\left(R^2 - R_0^2\right)}{2E_{\mathrm{x}} t^3} + \frac{3}{5tG} \right) \tag{2.93}$$

2.3.2 *Annular line load*

In contrast to a hemispherically capped punch, the load distribution of a flat punch can be assumed to be a surface load across the full punch head. However, experiments and FE analysis proves that, due to the plate bending stiffness of reinforced polymers, the plate lifts of the flat punch head's main surface area. The plate remains rested on the edge of the punch. The gap becomes more pronounced with an increase in punch diameter. Therefore, a new solution based on plate bending due to an annular line load, illustrated in figure (2.11), was derived from Young and Budynas [156, tab. 11.2, case 9b]. Assumptions about the contact area and congruently the applied load case can be simpler than those made for the contact area of a hemispherically capped punch as outlined in studies of [148, 149] and others. The resulting deflection curve of equation (2.100) and it's derivation is described in the following section.

For a general formulation the plate bending deflection under an annular load can be written as equation (2.95) with separate summands for the central deflection $w_{\mathrm{C,an}}$, the deformation due to moments $w_{\mathrm{M,an}}$ and transverse shear force $w_{\mathrm{Q,an}}$. The load F is defined as line load q_0 around the circle of the punch radius R_0. The

deformation in the centre of the plate, where $r = 0$, is shown in equation (2.96). It is clear that after substitution of the two different variants of force load of equation (2.94) and equation (2.82) the central deflection $w_{\mathrm{C,an}}$ in equation (2.96) of an annular load is identical to the deflection of a central point load $w_{\mathrm{b,np}}$, which was derived in equation (2.84) in the previous paragraph.

$$F = q_0 2\pi R_0 \tag{2.94}$$

$$w_{\mathrm{b,an}} = w_{\mathrm{C,an}} + w_{\mathrm{M,an}} + w_{\mathrm{Q,an}} \tag{2.95}$$

$$w_{\mathrm{C,an}} = \frac{F}{16\pi D}\left[R^2 - R_0^2\left(1 + 2\ln\left(\frac{R}{R_0}\right)\right)\right] \tag{2.96}$$

Another term is introduced to describe the deflection $w_{\mathrm{M,an}}$ under influence of the moment in the plate centre M_{C} resulting in equation (2.97). Finally, the transverse shear force Q is considered through equation (2.98). The transverse shear influences the total deflection for a radial coordinate r within the annular section of the plate between punch contour and plate edge, thus $R > r > R_0$.

$$w_{\mathrm{M,an}} = \frac{M_{\mathrm{C}} r^2}{2D\,(1+\nu)} = -\frac{F r^2}{16\pi D}\left[\left(\frac{R_0}{R}\right)^2 - 1 + 2\ln\left(\frac{R}{R_0}\right)\right] \tag{2.97}$$

$$w_{\mathrm{Q,an}} = \frac{Q r^3}{4D}\left\{\left[\left(\frac{R_0}{r}\right)^2 + 1\right]\ln\left(\frac{r}{R_0}\right) + \left(\frac{R_0}{r}\right)^2 - 1\right\}\langle r - R_0\rangle \tag{2.98}$$

$$\langle r - R_0\rangle \begin{cases} > 0\ ; & w_{\mathrm{Q,an}} = \dfrac{F r^2}{8\pi D}\left\{\left[\left(\dfrac{R_0}{r}\right)^2 + 1\right]\ln\left(\dfrac{r}{R_0}\right) + \left(\dfrac{R_0}{r}\right)^2 - 1\right\}(r - R_0) \\ \leqslant 0\ ; & w_{\mathrm{Q,an}} = 0 \end{cases}$$

Shear needs to be taken into account similar to the solutions of point loaded plate bending (cf. eq. 2.91). Again, the total deformation $w_{\mathrm{t,an}}$ in equation (2.100) consists of both, a bending and shear term.

$$\begin{aligned} w_{\mathrm{s,an}} &= \frac{6r}{5R}\ln\left(\frac{R}{r}\right)\frac{q_0 R}{tG} = \frac{6FRr}{5\,(2\pi R_0)\,RtG}\ln\left(\frac{R}{r}\right) \\ &= \frac{6Fr}{10\pi R_0 tG}\ln\left(\frac{R}{r}\right) \end{aligned} \tag{2.99}$$

$$
\begin{aligned}
w_{\mathrm{t,an}}(r) &= w_{\mathrm{b,an}}(r) + w_{\mathrm{s,an}}(r) \\
&= \frac{Fr^2}{16\pi D}\Bigg\{ \left[\frac{R^2}{r^2} - \frac{R_0^2}{r^2}\left(1 + 2\ln\left(\frac{R}{R_0}\right)\right)\right] - \\
&\qquad \left[\left(\frac{R_0}{R}\right)^2 - 1 + 2\ln\left(\frac{R}{R_0}\right)\right] + \\
&\qquad 2\left(\left[\left(\frac{R_0}{r}\right)^2 + 1\right]\ln\left(\frac{r}{R_0}\right) + \left(\frac{R_0}{r}\right)^2 - 1\right)\Bigg\} + \\
&\quad \frac{6Fr}{10\pi R_0 tG}\ln\left(\frac{R}{r}\right)
\end{aligned}
\tag{2.100}
$$

The energy release rate for plates bending under an annular load is deduced as presented above from the compliance C. The compliance is differentiated with respect to the radius R. Comparison of the newly derived solution from the work presented of equation (2.101) with the formerly used point load expression in equation (2.93) reveals the difference between both, which is the factor $\left(1 - R_0^2/R^2\right)$ on the bending deflection.

$$
\begin{aligned}
\mathcal{G}_{\mathrm{an}} &= \frac{F^2}{4\pi R}\cdot\frac{\partial C}{\partial R} \\
&= \frac{F^2}{4\pi R}\left(\frac{r^2}{16\pi D}\left[\frac{2\left(R^2 - R_0^2\right)}{r^2 R} - \frac{2\left(R^2 - R_0^2\right)}{R^3} + 0\right] + \frac{6r}{10\pi R_0 tGR}\right) \\
&= \frac{F^2}{2\pi^2 R^2}\left(\frac{1}{16D}\left[\left(R^2 - R_0^2\right) - r^2\left(1 - \frac{R_0^2}{R^2}\right)\right] + \frac{3r}{10R_0 tG}\right)\Bigg|_{r=R_0} \\
&= \frac{F^2}{4\pi^2 R^2}\left(\frac{3\left(1-\nu_{\mathrm{xy}}^2\right)}{2E_{\mathrm{x}}t^3}\left(R^2 - R_0^2\right)\left(1 - \frac{R_0^2}{R^2}\right) + \frac{3}{5tG}\right)
\end{aligned}
\tag{2.101}
$$

2.4 Analytical formulation for pressure blister tests

The standards of ASME [2] and ISO [1] provide the user with engineering formulations to design repairs against the different types of failures, which were pointed out in chapter 1. The present study is focussed on the interface fracture energy release rate of circular defects. In the following chapter, the equation for repairs of circular defects is derived and compared to the formulation (2.102) given in the standards,

which originates from Mableson et al. [17]. Limitations of the analytical formulations are highlighted at the end leading to the common test method of pressure blister tests.

$$\mathcal{G} = \frac{1}{\left(f_\mathrm{t} f\right)^2} P^2 \left[\frac{(1-\nu^2)}{E} \frac{3}{32 t_\mathrm{min}^3} R^4 + \frac{3}{16 G t_\mathrm{min}} R^2 + \frac{(1-\nu^2)}{\pi E} R \right] \tag{2.102}$$

The strain energy release rate $\mathcal{G}$ (ERR) is the energy released $\mathrm{d}\Pi$ over a corresponding opened crack area $\mathrm{d}A$, which is assumed to be a ring. The released energy can be expressed through the pressure P acting from underneath on the repair and the compliance C of the repair. The compliance is dependent on the pressure as well as the volume of the blister, which is generated underneath the repair by the pressure.

$$\mathcal{G} = -\frac{\mathrm{d}\Pi}{\mathrm{d}A} \quad \text{with} \quad \Pi = -\frac{P^2 C}{2} \quad \text{and} \quad \mathrm{d}A = 2\pi R \, \mathrm{d}R \tag{2.103}$$

$$\mathcal{G} = \frac{1}{4\pi R} P^2 \frac{\mathrm{d}C}{\mathrm{d}R} \quad \text{replacing} \quad C = V/P \tag{2.104}$$

$$\mathcal{G} = \frac{1}{4\pi R} P \frac{\mathrm{d}V}{\mathrm{d}R} \tag{2.105}$$

Consequently, knowledge of the blister volume is the key to calculate the ERR. For an analytical derivation of the volume it is necessary to define the formulation for the deflection of the blister. The *classical plate bending theory* of thin plates, also known as *Kirchhoff–Love* plate theory, was extended from the *Euler-Bernoulli* beam theory and therefore has to comply with the same assumptions [159]:

1. Elastic, homogeneous and isotropic material
2. Initially the plate is flat
3. Small deflections of the midplane compared to the thickness
4. Normals of the midplane stay straight and normal to the midplane after deformation
5. Stress normal to the midplane is small enough to be negligible $\sigma_\mathrm{z} \ll \sigma_\mathrm{x}, \sigma_\mathrm{y}$ (*plane stress* condition)
6. The midplane is free of stress and strain

This leads to the restraint that the influence of shear is omitted. As a result, the CPT applies only for thin plates ($10 \leq {}^{R}\!/_{t} \leq 100$). To overcome this limitation several higher order solutions were proposed of which the earliest and most well-known came from Reissner [161, 162] and Mindlin [163]. Both appear similar, yet they are distinctively different, which was summarised by Wang et al. [164]. Reissner's theory assumes a linear bending stress distribution superimposed by a parabolic

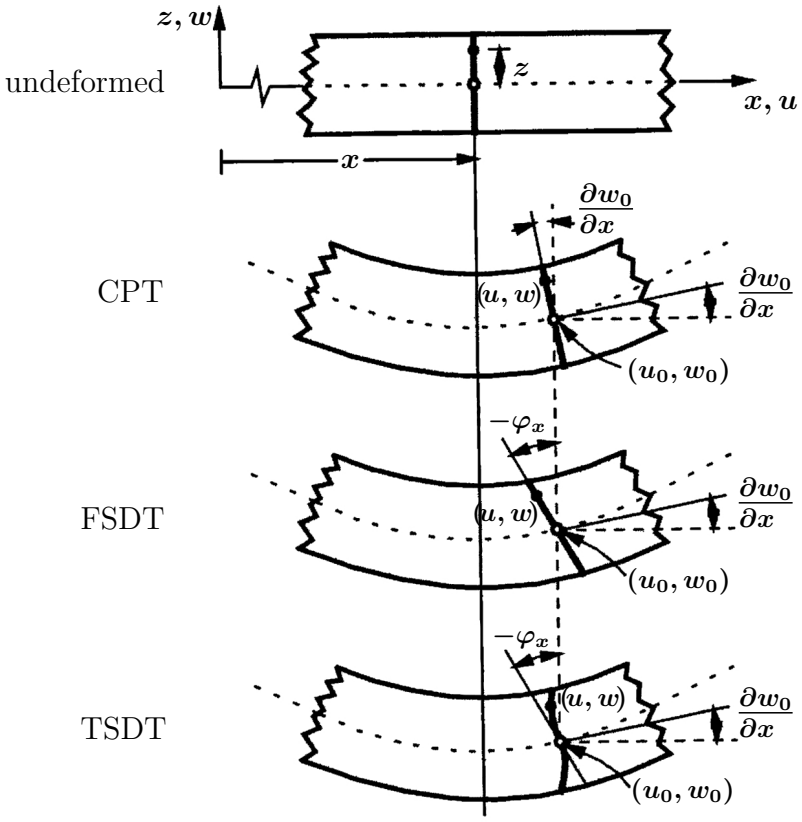

Figure 2.12: Difference in shear deformation between different order plate theories; [160]

shear stress distribution. His theory permits a non-linear transversal displacement variation and a variation of the thickness itself. In contrast, Mindlin's approach assumes a linear variation of displacements in out of plane direction in combination with inextensibility of the thickness. As another consequence Mindlin, contrary to Reissner, ignores the normal stress σ_z. Therefore, Reissner's theory cannot be categorised as *first-order shear deformation* plate theory (FSDT). Figure (2.12) displays the differences in shear deformation of the different plate theories.

ASME PCC2-4 and ISO 24817 both present the same equations based on an FSDT approach. The FSDT is merged from the CPT and from an additional correction term for shear. The main difference between CPT and FSDT is the abandoning of the constraint of normal lines to stay orthogonal to the midplane after deformation, although the restriction of lines to stay rectilinear and inextensible remains.

2.4.1 *Classical plate theory*

The general CPT formulation (2.106) for an axisymmetric thin plate under uniform load p_0, shown by Timoshenko and Woinowsky-Krieger [165, chap. 3], has to be solved for the particular boundary conditions of a clamped edge. Ventsel and Krauthammer [159, chap. 4.3] summarised the derivation (2.106). For a fixed edge the assumptions of a zero-slope ($\psi(r) = 0$) of surface deflection around the edge

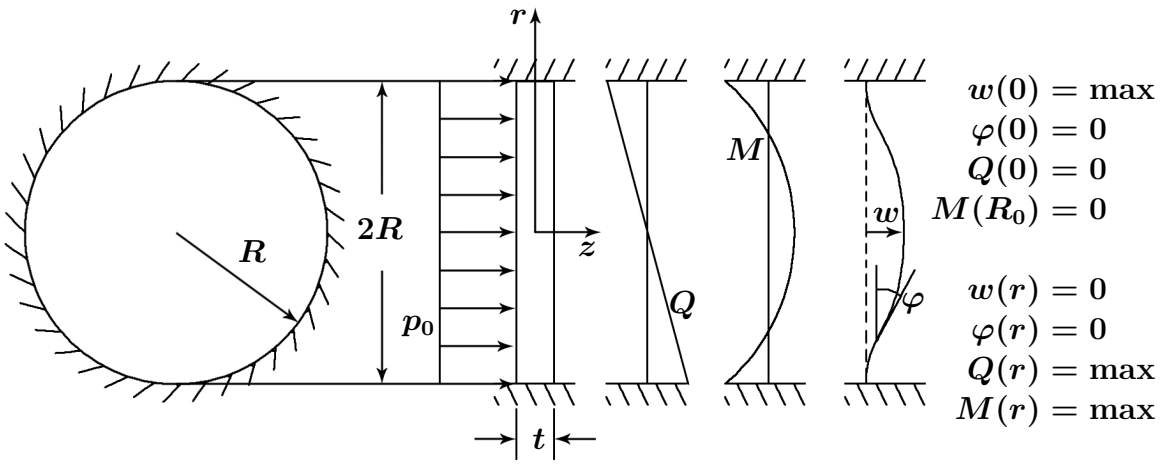

Figure 2.13: Circular plate under uniform load

($r = R$) and in the centre ($r = 0$) lead to the equation (2.108). The bending deflection without shear influence is labelled as w_b.

$$w(r) = \frac{p_0 r^4}{64D} + C_3 r^2 + C_4 \tag{2.106}$$

$$\text{with} \quad D = \frac{Et^3}{12\,(1-\nu^2)} \tag{2.107}$$

$$w_\mathrm{b}(r) = \frac{p_0}{64D}\left(R^2 - r^2\right)^2 \tag{2.108}$$

$$\text{with} \quad w_\mathrm{max} = \frac{p_0 R^4}{64D} \quad \text{maximum deflection in the centre} \tag{2.109}$$

2.4.2 *CPT extension to FSDT*

Transverse normal and shear stresses are neglected in the CPT, but the FSDT can overcome limitations of the CPT. Through allowing the cross-section of the plate to become angled to the normal of the plate as illustrated in figure (2.13), the angle of the cross-section φ_r changes with the shear strain γ_rz. In the following paragraphs all terms dependent on the tangential coordinate ϑ are omitted under the assumption of a quasi-isotropic material. The radial shear strain for an axi-symmetric plate can be derived from [166, chap. 10.]

$$\gamma_\mathrm{rz} = \frac{\partial w_0}{\partial r} + \varphi_r \tag{2.110}$$

Here, φ_r is the total angle, which is composed of the angle known from the CPT $\psi_r = \frac{\partial w_0}{\partial r}$ and the shear strain induced angle (cf. fig. 2.12). In accordance with [159], a *potential function* is introduced of the form

$$\varphi_r = \frac{\partial \omega(r)}{\partial r} \tag{2.111}$$

The new potential function $\omega(r)$ is closely related to the bending deflection $w(r)$ through

$$w(r) = \omega(r) - \frac{D}{Gt}\nabla^2\omega(r) \tag{2.112}$$

$$\text{with} \qquad \nabla^2 f = \frac{\partial^2 f}{\partial r^2} + \frac{1}{r}\frac{\partial f}{\partial r} \qquad \text{under negligance of } \vartheta \tag{2.113}$$

Because of the change of the cross-section angle, the boundary conditions of the angle ψ_r need to be applied to the new angle φ_r equivalently. Assuming a zero-slope around the fixed edge $r = R$ of the plate bending equation (2.109) as boundary condition yields

$$\varphi_r(R) = \gamma_{\mathrm{rz}}(R) - \frac{\partial w_0(R)}{\partial r} = 0 \tag{2.114}$$

$$\text{with} \qquad \gamma_{\mathrm{rz}}(R) = 0 \tag{2.115}$$

$$\Rightarrow \qquad 0 = \frac{\partial w_0(R)}{\partial r} = \frac{p_0 R^3}{32D} + C_3 R \tag{2.116}$$

$$\Rightarrow \qquad C_3 = -\frac{p_0 R^2}{32D} \tag{2.117}$$

In order to solve equation (2.112) the remaining unknown constant C_4 must be determined. Firstly, $\nabla^2\omega(r)$ has do be derived

$$\nabla^2\omega(r) = \frac{p_0 R^2}{4D} + 4C_3 \tag{2.118}$$

The plate bending equation (2.112) can be written as equation (2.119) and solved for the constant C_4 through the boundary condition of no deflection $w(R) = 0$ at the fixed edge along the crack tip.

$$w(r) = \frac{p_0 r^4}{64D} - \frac{p_0 R^2}{32D} r^2 + C_4 - \frac{p_0}{4Gt}\left(r^2 - \frac{R^2}{2}\right) \tag{2.119}$$

$$C_4 = \frac{p_0 R^4}{64D} + \frac{p_0 R^2}{8Gt} \tag{2.120}$$

$$w(r) = \frac{p_0}{64D}\left(R^2 - r^2\right)^2 + \frac{p_0}{4Gt}\left(R^2 - r^2\right) \tag{2.121}$$

In equation (2.121) it becomes obvious that the first part is equal to equation (2.108), while the second part derives from the FSDT. It can be referred to as deflection due to shear w_{s}^*.

$$w_{\mathrm{s}}^*(r) = \frac{p_0}{4Gt}\left(R^2 - r^2\right) \tag{2.122}$$

The simple stress formulation for shear ($\tau^u = \frac{Q}{A}$) yields in a uniform load across the face and differs from the actual, parabolic stress distribution τ^p of a transverse shear

stress. Shear correction factors can account for the difference and thus were applied on w_s. In general, transverse shear can be calculated, as presented by [167] and in equation (2.123), as a function of the bending moment M, the static moment S, the moment of inertia I_xx and the width b. In the case of a transverse load instead of a bending moment, $\frac{\mathrm{d}M}{\mathrm{d}z}$ is replaced by a single load Q or a pressure q.

$$\tau = \frac{\mathrm{d}M}{\mathrm{d}z}\frac{S}{bI_\mathrm{xx}} \tag{2.123}$$

$$S = Az = b\left(\frac{t}{2} - z\right)\frac{z + \frac{t}{2}}{2} = \left(\frac{t^2}{4} - z^2\right)\frac{b}{2} \tag{2.124}$$

$$I_\mathrm{xx} = \frac{bt^3}{12} \tag{2.125}$$

Equations (2.123) to (2.125) in combination with $\tau^u = \frac{Q}{A}$ leads to the actual shear stress distribution, which can be written as

$$\tau^p_\mathrm{rz}(z) = \frac{3q_r}{2t}\left[1 - \left(\frac{z}{t}\right)^2\right] = \frac{3}{2}\tau^u_\mathrm{rz}\left[1 - \left(\frac{z}{t}\right)^2\right], \qquad -\frac{t}{2} \le z \le \frac{t}{2} \tag{2.126}$$

The ratio of the strain energies for linear and parabolic stress distributions [166] gives the shear correction factor K_s.

$$\Pi^u_\mathrm{s} = \frac{1}{2G}\int_A (\tau^u_\mathrm{rz})^2 \,\mathrm{d}A = \frac{q_r^2}{2Gt} \tag{2.127}$$

$$\Pi^p_\mathrm{s} = \frac{1}{2G}\int_A (\tau^p_\mathrm{rz})^2 \,\mathrm{d}A = \frac{3q_r^2}{5Gt} \tag{2.128}$$

$$K_\mathrm{s} = \frac{\Pi^p_\mathrm{s}}{\Pi^u_\mathrm{s}} = \frac{6}{5} \tag{2.129}$$

Applying equation (2.129) on equation (2.122) results in the corrected shear deflection w_s.

$$w_\mathrm{s}(r) = K_\mathrm{s} w^*_\mathrm{s}(r) = \frac{3p_0}{10Gt}\left(R^2 - r^2\right) \tag{2.130}$$

2.4.3 *FSDT extension for crack opening by material compressibility*

Finally, a third correction term is introduced for a 'penny-shaped' crack (fig. 2.14) inside an infinite thick elastic solid, i. e. an equivalent of the plane strain condition. The crack is opened by an internal pressure acting along both surfaces of the crack. Sneddon [54] derived this theory from the previous work of Griffith [47, 168] and Orowan [169]. For a constant internal pressure over the full circular crack area in a three dimensional crack, Sneddon [54, eq. 3.3.2] developed an expression for the

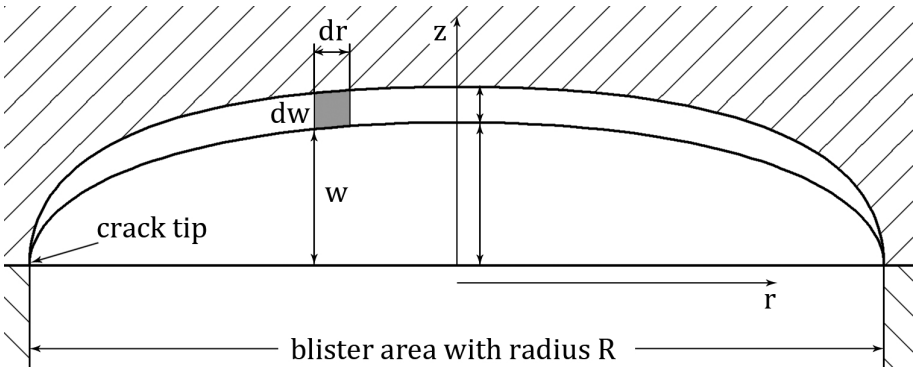

Figure 2.14: Orthogonal deflection of surface of 'penny-shaped' crack in semi-infinite material.

crack surface displacement in radial (2.131) and orthogonal direction (2.132). The radial deflection vanishes for incompressible material (Poisson's ratio $\nu = 0.5$). The standards only consider crack opening deflections orthogonal to the plane of the crack, because the assumption of a clamped edge is similar to infinitely stiff and incompressible material behaviour in radial direction.

$$u_{\mathrm{c}}(r) = \frac{-2\,(1+\nu)\,(1-2\nu)}{3\pi E} R I_r \tag{2.131}$$

$$w_{\mathrm{c}}(r) = \frac{4\,(1-\nu_{13}\nu_{31})}{\pi E} p_0 \sqrt{R^2 - r^2} \tag{2.132}$$

2.4.4 *Energy release rate determination from extended FSDT*

All three deflections for bending w_{b} (2.108), shear w_{s} (2.130) and crack opening w_{c} (2.132) have to be integrated over the area of the crack as presented in the general form in equation (2.133). Their sum yields the total volume in equation (2.137).

$$V(r) = 2\pi \int_{r=0}^{r=R} w(r) r \,\mathrm{d}r \tag{2.133}$$

$$V_{\mathrm{b}}(r) = \frac{(1-\nu_{12}^2)\,\pi}{16 \bar{E} t^3} P R^6 \tag{2.134}$$

$$V_{\mathrm{s}}(r) = \frac{3\pi}{20 G_{13} t} P R^4 \tag{2.135}$$

$$
\begin{aligned}
V_{\mathrm{c}}(r) &= 2\pi \int_{r=0}^{r=R} P \frac{4\left(1-\nu_{13}\nu_{31}\right)}{\pi E_{33}} \sqrt{R^2-r^2}\, r \,\mathrm{d}r \\
&= P \frac{8\left(1-\nu_{13}\nu_{31}\right)}{E_{33}} \left[-\frac{1}{3}\sqrt{R^2-r^2}^3\right]_{r=0}^{r=R} \\
&= \frac{8\left(1-\nu_{13}\nu_{31}\right)}{3E_{33}} P R^3 \qquad (2.136)
\end{aligned}
$$

$$
\begin{aligned}
V_{\mathrm{total}} &= V_{\mathrm{b}} + V_{\mathrm{s}} + V_{\mathrm{c}} \\
&= 2\pi P \left[\frac{\left(1-\nu_{12}^2\right)}{32\overline{E}t^3} R^6 + \frac{3}{40 G_{13} t} R^4 + \frac{4\left(1-\nu_{13}\nu_{31}\right)}{3\pi E_{33}} R^3\right] \qquad (2.137)
\end{aligned}
$$

Substituting equation (2.137) in equation (2.105) yields a result similar to the earlier presented equation (2.102) of the standards. Identical to the standard and Williams [170] is the bending term I with $\overline{E} = \sqrt{E_{11}E_{22}}$ under the assumption of quasi-isotropic material behaviour. The shear term II was altered by applying the transverse shear modulus G_{13}, which was not specified in the standard. Additionally, the shear correction factor has been applied as described in section 2.4.2. Finally, the compression crack opening term III is adjusted through application of the transverse Poisson's ratios and Young's modulus, in contrast to the standards that use the in-plane values.

$$
\mathcal{G} = \frac{1}{2R} P^2 \frac{\mathrm{d}}{\mathrm{d}R} \left[\frac{\left(1-\nu_{12}^2\right)}{32\overline{E}t^3} R^6 + \frac{3}{40 G_{13} t} R^4 + \frac{4\left(1-\nu_{13}\nu_{31}\right)}{3\pi E_{33}} R^3\right] \qquad (2.138)
$$

$$
\mathcal{G} = P^2 \left[\overbrace{\frac{3\left(1-\nu_{12}^2\right)}{32\overline{E}t^3} R^4}^{\mathrm{I}} + \overbrace{\frac{3}{20 G_{13} t} R^2}^{\mathrm{II}} + \overbrace{\frac{2\left(1-\nu_{13}\nu_{31}\right)}{\pi E_{33}} R}^{\mathrm{III}}\right] \qquad (2.139)
$$

Understanding of the derivation of equation (2.102) and equation (2.139) is also necessary to recognise its limitations. These are partially equivalent with those known from the CPT, the shear correction term and the compression crack opening correction. However, a few additional limitations are imposed and a summary of all assumptions of the analytical solution is listed below:

1. Repair material:
   - Linear-elastic, homogeneous, isotropic
2. Substrate material:
   - Infinitely stiff for V_{b} and V_{s}
   - V_{c} assumes symmetry about the crack plane, i. e. equal to repair material

3. Geometry

    - Initially the repair and substrate disks are assumed to be 'flat' plates and consequently, the area of the pipe, affected by the defect, is assumed to be small compared to the circumference
    - The crack defect is an axis-symmetric through-hole with sharp edges at the bond interface

4. Blister forming

    - Small deflections of the midplane compared to the thickness
    - Normals of the midplane stay straight and are inextended after deformation
    - Stress normal to the midplane is small enough to be negligible $\sigma_z \ll \sigma_x, \sigma_y$ (*plane stress* condition)
    - The midplane is free of stress and strain
    - 'Clamped edge' results in a zero deflection slope around the edge for the CPT expression and a zero deflection for the shear correction.
    - Constant pressure over the full crack area

It becomes obvious that the assumptions made for the analytical solution are partly oversimplifications of the problem or even contradictory to composite materials. This illustrates the need to investigate into the validity and quality of the analytically made estimates.

Chapter 3. Numerical simulation of fractures

3.1 Overview of fracture simulation methods

In chapter 2 an overview across different analytical ways of energy release rate and stress intensity factor calculations was given. Typically, multiple simulation approaches are possible to solve a problem and, consequently, a large number of different FE techniques to obtain $\mathcal{G}$ or $\mathcal{K}$ were developed. The following chapter provides a summary of available methods and explains the applied 'virtual crack closure technique' in greater detail in 3.3.

Apart from the VCCT, ANSYS supplies the option based on a domain integral method after [171, 172] for a conservation law J-integral simulation, which is one of the most important parameters for fracture characterisation. Closed contour integrals (or surface integral in 3D) are equivalent to $\mathcal{G}$ and $\mathcal{K}$ for elastic material, but in contrast to other methods closed contour integrals may be applied for elastic-plastic fracture behaviour [45, 173]. However, only total ERRs and SIFs can be calculated and fracture of interfaces between dissimilar media cannot be evaluated.

The J-integral, invented by Rice [174], was shown to be a valid approximation of the stress field around a crack-tip by Hutchinson [86] and Rice and Rosengren [85]. A contour around a crack tip can describe the difference in potential energy from a crack propagation. Closed contour integrals are independent of the path of the contour for stationary cracks or cracks with $\Delta a \ll r_p$ (cf. fig. 2.2). They vanish when the contours envelope homogeneous material without singularities, discontinuities or flaws [175].

The same rules apply for the domain integral method, which computes the area or volume instead of the line or surface for 2D or 3D simulations respectively. Due to its higher compatibility with the solution process of FEA, domain integrals are numerically more efficient than line integrals, in particular for 3D simulations. The J-integral calculation with the domain integral equation (3.1) consists of the strain energy density U with the Kronecker delta, the displacement vector u with the stress σ within the domain Γ_A and traction t acting on the crack face area A_C [175, 176].

$$J = \mathcal{G} = \int_{\Gamma_\mathrm{A}} \left(\sigma_{ij} \frac{\partial u_{i1}}{\partial x_1} - U\delta_{1i} \right) \frac{\partial q_1}{\partial x_i} \,\mathrm{d}\Gamma_\mathrm{A} - \int_{A_\mathrm{C}} t_j u_{j1} q_1 \,\mathrm{d}s \tag{3.1}$$

ANSYS uses interaction integrals to calculate stress intensity factors. Interaction

integrals (known as M-integral or I-integral), initially developed by Chen and Shield [177], are another extension of the J-integrals capable of computing the mixed mode stress intensity factors through the work of Stern et al. [178] and Yau et al. [179]. Two equilibrium states are superpositioned in the interaction integral method; the actual boundary value problem and an auxiliary solution of the asymptotic crack tip displacement. A concise summary of the history of interaction integrals can be found in Daimon and Okada [180] together with an improvement to employ quadratic tetrahedral elements. The superposition can be expressed analytically as equations (3.2) to (3.8) [181, 182]

$$u^{(0)} = u^{(1)} + u^{(2)} \tag{3.2}$$

$$\sigma^{(0)} = \sigma^{(1)} + \sigma^{(2)} \tag{3.3}$$

$$\vec{\mathscr{K}}^{(0)} = \vec{\mathscr{K}}^{(1)} + \vec{\mathscr{K}}^{(2)} \tag{3.4}$$

$$\mathscr{G}^{(0)} - \mathscr{G}^{(1)} - \mathscr{G}^{(2)} = \frac{1}{4}\left[\vec{\mathscr{K}}^{(1)\mathrm{T}}\mathbf{E}\vec{\mathscr{K}}^{(2)} + \vec{\mathscr{K}}^{(2)\mathrm{T}}\mathbf{E}\vec{\mathscr{K}}^{(1)}\right] \tag{3.5}$$

with the asymptotic solutions for

a) $[\mathscr{K}_{\mathrm{I}} = 0, \mathscr{K}_{\mathrm{II}} = 1, \mathscr{K}_{\mathrm{III}} = 0]$
b) $[\mathscr{K}_{\mathrm{I}} = 1, \mathscr{K}_{\mathrm{II}} = 0, \mathscr{K}_{\mathrm{III}} = 0]$
c) $[\mathscr{K}_{\mathrm{I}} = 0, \mathscr{K}_{\mathrm{II}} = 0, \mathscr{K}_{\mathrm{III}} = 1]$

the SIFS can be separated to:

$$\begin{bmatrix} E_{11} & E_{12} & E_{13} \\ E_{21} & E_{22} & E_{23} \\ E_{31} & E_{32} & E_{33} \end{bmatrix} \begin{bmatrix} \mathscr{K}_{\mathrm{II}}^{(1)} \\ \mathscr{K}_{\mathrm{I}}^{(1)} \\ \mathscr{K}_{\mathrm{III}}^{(1)} \end{bmatrix} = 2 \cdot \begin{bmatrix} \mathscr{G}_{\mathrm{a}}^{(0)} - \mathscr{G}^{(1)} - \mathscr{G}_{\mathrm{a}}^{(2)} \\ \mathscr{G}_{\mathrm{b}}^{(0)} - \mathscr{G}^{(1)} - \mathscr{G}_{\mathrm{b}}^{(2)} \\ \mathscr{G}_{\mathrm{c}}^{(0)} - \mathscr{G}^{(1)} - \mathscr{G}_{\mathrm{c}}^{(2)} \end{bmatrix} \tag{3.6}$$

and the equivalent expression for the domain integral of the superpositioned state (J_{S}); a sum of the actual (J) and the auxiliary (J_{aux}) domain integral as well as the interaction integral (M).

$$J_{\mathrm{S}} = J + J_{\mathrm{aux}} + M \tag{3.7}$$

The interaction integral M is derived as [181]

$$\begin{aligned} M = &\int_{\Gamma_{\mathrm{V}}} \left[\sigma_{ij} u_{j1}^{\mathrm{aux}} + \sigma_{ij}^{\mathrm{aux}} u_{j1} - \frac{1}{2}\left(\sigma_{jk}\varepsilon_{jk}^{\mathrm{aux}} + \sigma_{jk}^{\mathrm{aux}}\varepsilon_{jk}\right)\delta_{1i}\right] q_i \,\mathrm{d}\Gamma_{\mathrm{V}} \\ &+ \int_{\Gamma_{\mathrm{V}}} \left[\sigma_{ij} u_{j1}^{\mathrm{aux}} + \sigma_{ij}^{\mathrm{aux}} u_{j1} - \frac{1}{2}\left(\sigma_{jk}\varepsilon_{jk}^{\mathrm{aux}} + \sigma_{jk}^{\mathrm{aux}}\varepsilon_{jk}\right)\delta_{1i}\right]_i q \,\mathrm{d}\Gamma_{\mathrm{V}} \\ &- \int_{A_{\mathrm{C}}} \left(\tau_j u_{j1}^{\mathrm{aux}} + \tau_j^{\mathrm{aux}} u_{j1}\right) q \,\mathrm{d}s \end{aligned} \tag{3.8}$$

Other integrals noteworthy are the L-integral [183] and the mutual work difference integral [184]. The conservation law integrals J, L and M were interpreted by [185] as the ERRs for a translational, rotational or expanding crack growths. Paluszny and Zimmerman [186] published a meshing approach applicable with integral methods to automatically adapt arbitrary mesh geometries for mesh-independent crack fronts and propagations.

The *virtual crack extension method* (VCE) (3.9) was simultaneously developed by Parks [187] and by Hellen and Blackburn [188] and is another way of calculating single mode SIFs. Shifting the position of the nodes at and next to the crack tip, instead of opening node connections, results in a change of the master stiffness matrix per crack unit length $\mathrm{d}\mathbf{K}_i/\mathrm{d}a$ in-between the two contours Γ_0 and Γ_1. No change can be found inside Γ_0 or outside Γ_1 because the elements remain unchanged, if they are not within the band between the contours. All stiffness matrices $\mathbf{K}_i^{\mathrm{c}}$ of the elements N_{c} between both contours are summed up and multiplied with the vector of the nodal displacements $\vec{u}$. Parks [189] and Hellen [190] showed a VCE solution for non-linear materials, Matos et al. [191] were first to publish the VCE for bi-material interface fracture and Ikeda et al. [182] added anisotropy.

$$\mathcal{G} \approx -\frac{1}{2}\vec{u}^{\mathrm{T}} \sum_{i=1}^{N_{\mathrm{c}}} \frac{\mathrm{d}\mathbf{K}_i^{\mathrm{c}}}{\mathrm{d}a}\vec{u} \tag{3.9}$$

The *eXtended Finite Element Method* (XFEM) was introduced by Belytschko and Black [192] and Moës et al. [193] and offers the advantage of crack growth through an arbitrary FEM mesh independent of a potential crack path. Based on the partition-of-unity the nodes next to the crack path become enriched with additional near-tip asymptotic shape functions and a discontinuity field using generalised Heaviside step functions and singular functions [194]. Belytschko and Black summarised the advantages over alternative mesh-independent crack propagation methods as the compatibility with FE technology and software, being applicable to non-linear problems and fewer computational expense compared to continuous FEM remeshing operations. Although XFEM is most efficient for elastic 2D problems, because the singular function can be determined analytically, the XFEM was applied for 3D problems [195] and non-linear materials undergoing strain hardening, thermal softening, visco-plasticity and ductile damage [194].

Other mesh-geometry based FEM models are the nodal-force method [196], the body force method [197] and the extrapolation or displacement correlation technique [198].

Cohesive zone models (CZM) use an additional set of elements at the crack interface, which do not inherit material but rather can be understood as the coh-

ive forces acting between the material elements under load. ANSYS supplies the INTER202→205 elements for 2D, 3D, lower- and higher-order elements. Because the elements are only 'inserted' in the interface, CZM interface elements are line elements for 2D and surface elements for 3D simulations.

The approach taken by the CZM is the equivalent of the analytical modelling of the crack tip zone by Dugdale [58] and Barenblatt [59] and therefore an option to simulate non-linear material behaviour. Additionally, no initial crack has to be present and an initial crack may have a vanishing ERR [199]. Traction-separation laws are the measure for the separation, where the area under the traction over separation curve is equivalent to the energy required for the crack separation. Models based on the exponential model by Xu and Needleman [200] are most common, but for instance bilinear CZM laws can be found as well [201]. A comprehensive review of different traction-separation laws was published by Park and Paulino [202] together with a general overview of publications on the topic of CZM.

Originally, crack propagation with the CZM was confined to the mesh geometry and arbitrary crack propagation was achieved with a fine mesh and interface elements between all continuum elements [200]. This limitation was partly overcome through application of a smeared CZM with embedded discontinuities, a standard discrete CZM with adaptive discontinuities [203] and the partition-of-unity method [204], better known from the XFEM, as has been reviewed by [205]. A comprehensive comparison between LEFM and nonlinear FM using J-integral methods and CZM was conducted by Bittencourt [206].

ANSYS offers the functionality of exponential (equations (3.10) to (3.11)) and bilinear (equations (3.12) to (3.13)) traction laws that need additional input of material constants such as maximum stresses and separation, but also provides the option to utilise the VCCT with a fracture criterion instead. Xie and Biggers investigated using interface elements in conjunction with VCCT for 2D [207] and 3D [208, 209] with arbitrarily shaped crack fronts.

$$\sigma = e\sigma_{\max}\ \frac{v}{v_{\mathrm{I}}}\ e^{-\frac{v}{v_{\mathrm{I}}}}\ e^{-\left(\frac{u}{u_{\mathrm{II}}}\right)^2} \tag{3.10}$$

$$\tau = 2e\sigma_{\max}\ v_{\mathrm{I}}\frac{u}{u_{\mathrm{II}}^2}\left(1+\frac{v}{v_{\mathrm{I}}}\right)e^{-\frac{v}{v_{\mathrm{I}}}}\ e^{-\left(\frac{u}{u_{\mathrm{II}}}\right)^2} \tag{3.11}$$

$$\begin{aligned} \text{with} \quad & v_{\mathrm{I}} \quad \text{at } \sigma_{\max} \text{ for no shear separation} \\ \text{and} \quad & u_{\mathrm{II}} = \sqrt{2}u \quad \text{at } \tau_{\max} \text{ for no normal separation} \end{aligned}$$

$$\sigma = K_{\mathrm{n}} v\,(1 - D_{\mathrm{m}}(\lambda)) \tag{3.12}$$

$$\tau = K_{\mathrm{t}} u\,(1 - D_{\mathrm{m}}(\lambda)) \tag{3.13}$$

with $K_{\mathrm{n,t}}$ as the normal and tangential cohesive stiffness

λ as the non-dimensional effective displacement jump
and D_{m} as a damage parameter

The *boundary element method* (BEM), also known as *displacement discontinuity method* (DDM) [210], meshes the surface of a volume and employs boundary integral equation (BIE) formulations. Compared to FEM in which the full volume is meshed and differential equation (ODE/PDE) formulations are employed, using BEM with the *fast multipole method* (FMM) leads to the number of nodes being smaller by a magnitude and consequentially faster computation time. In exchange, BEM memory requirements are larger, because matrices are fully populated and non-symmetrical. Hypersingular (traction) BIE [211] and dual BIE formulations are common methods today to simulate cracks [210] and with several approaches to evaluate SIFs in 2D, 3D and for anisotropic bi-material interface problems [212].

An arbitrary crack propagation imposes difficulties to structurally meshed simulations. The advantage of no mesh employment is offered by a third class of simulation techniques that envelopes meshless methods with (a) predefined background mesh for integration, (b) realtime local cells for integration or (c) no mesh at all. Generally, 'meshless' methods are more stable and accurate to solve with increasing support from a mesh [213]. This behaviour is mainly due to the integration schemes, which affect convergence behaviour, and the number of integration points needed.

Meshless methods are more computationally expensive in defining the shape and weight functions and are more complex in the application of boundary conditions compared to FEM. In contrast, the preprocessing of a standard mesh generation is more complex than a meshless discretisation that only requires nodal informations. Furthermore, the adaptation to a change in geometry is more computationally expensive for a geometry based mesh since meshless methods only need randomly distributed nodes without element connectivity. Other advantages are a smooth, higher-order field approximation and therefore, in contrast to FEM, the stress field obtained does not need additional smoothing. Originating from the smoothed particle hydrodynamics method (SPH) [214], a number of different meshless methods have been developed since the early '90s such as the reproducing kernel particle method [215], the $h-p$ cloud method [216] and the meshless local boundary equation [217] amongst others that were summarised by [213, 218, 219].

Important additions are the moving least square approximations and the partition of unity [220] into the Galerkin weak form yielding the element-free Galerkin method (EFGM) by Belytschko et al. [222] and the Petrov-Galerkin weak form yielding the meshless local Petrov-Galerkin approach (MLPG) by Atluri and Zhu [223]. In contrast to the EFGM, the MLPG does not use any form of mesh, takes the trial and test functions from different spaces and evaluates a local symmetric weak form

within a local subdomain [217]. Another approach to overcome weaknesses in FEM and meshless methods is a coupling of both in order to use the strengths of each. For instance, finite elements are used for the main volume and the boundaries, while meshless methods are used for areas of changing geometries [224, 225].

A nonlocal continuum model, called *Peridynamics*, was proposed by Silling [226] that integrates forces per unit reference volume in an equation of motion as an interaction between 'material particles' [227] in a nonlocal region (the 'horizon') around every material particle individually [228]. Peridynamics was shown to be powerful in modelling the damage and fracture beyond the limitations of standard continuum mechanics and in particular the modelling of composite materials has gained attention over the past decade, following the work of Xu et al. [229] (for a brief review see Hu et al. [230]).

A novel approach of describing crack fronts with a *level set model* (LSM) was developed [231] and first applied for XFEM by Stolarska et al. [232]. Further developments for meshless methods were conducted by Zhuang [213] and an LSM adaptation was published in [233] for mesh independent arbitrary crack growth across geometry-meshes under avoidance of stress singularities and CZM. The LSM can be visualised as two surfaces (i. e. the 'sets') of which the intersection (where one set is 'level' to the other) represents the crack front.

3.2 Pressure Volume Method (PVM)

A simple method to calculate the ERR for PBTs was developed and published in Linden et al. [234]. This method utilises the principle of the compliance expression of the ERR as described in chapter 2.1. The difference in volume $\mathrm{d}V$ per new crack face area $\mathrm{d}A$ for a given pressure P yields the ERR (3.14).

$$\mathcal{G} = \frac{P}{2} \cdot \frac{\mathrm{d}V}{\mathrm{d}A} \tag{3.14}$$

A mechanical structural FE analysis has to be employed to obtain the deflection of the blister under pressure. The volume may be calculated separately after the FE simulation from the deflected x-, y- and z-coordinates of the nodes or within its postprocessor using 'soft' elements for the volume to expand. In the specific case of ANSYS APDL the second option would involve saving the deformed geometry with the UPGEOM command, followed by the line *GET,par,ELEM,n,VOLU to obtain the new volume of the elements (for detailed information regarding the programming see [129, 235, 236]).

The advantage of this method is its simplicity, that it can be applied for dissimilar materials and that no extra fracture mechanics simulation method of those shown

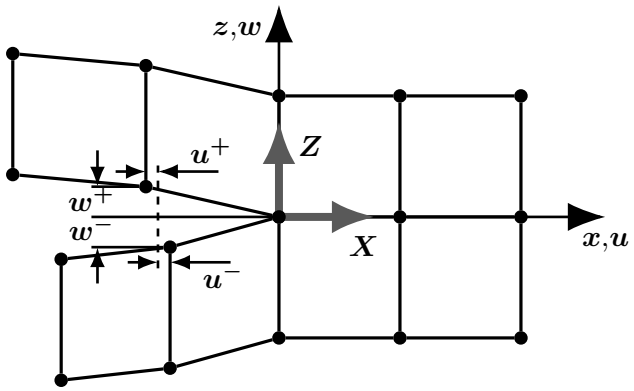

Figure 3.1: Crack tip opening displacement for a 4-noded, linear, rectangular element

in chapter 3.1 has to be implemented, which makes it easy to use with any FEA package. Disadvantageous is the limitation to PBTs and that no distinction between fracture modes can be achieved. While the PVM was used in the early stage of this project, the majority of the results were obtained through the VCCT in order to evaluate the mode mixity.

3.3 Virtual Crack Closure Technique (VCCT)

The *modified* or *virtual crack closure technique* was first published by Rybicki and Kanninen [237] in 1977. Later, Raju [238] proved the validity of the equations and its applicability on a collapsed crack tip mesh. The VCCT originates from the related crack closure integral method [239]. Both are based on the assumption by Irwin and Kies [46] that the released energy per extension of a crack is equivalent to the energy required to close the opened crack (cf. chap. 2).

In the case of the crack closure method, the opening of the crack is performed throughout two simulation steps. The second step differs from the first by the disconnection of the first pair of facing elements after the crack tip, resulting in a larger crack area for the second step. Equation (3.15) shows the relation between the released energy ΔE and the forces (X, Z) and deflections (u, w), with step indices $_1$ and $_2$.

$$\Delta E = \tfrac{1}{2}\left[X_1 \Delta u_2 + Z_1 \Delta w_2\right] \tag{3.15}$$

Other methods of solving the crack closure integral are the crack closure integral with local smoothing (CCI-LS) [240] and the universal crack closure integral (UCCI) [241], yet the focus of the following section is on the VCCT as the method applied in this study. In contrast to the CCI, the virtual crack closure technique does not require a second step, because it is assumed that for small crack extensions Δa the loads and displacements at and around the crack tip stay almost constant. Analogous, the released energy for a crack extension $a + \Delta a$ is identical to $a + 2\Delta a$, although the VCCT is not crack length independent. Therefore, it is possible to

utilise the forces at the crack tip node and the deflections of the nodes in front of the tip from the same simulation step.

The type of force needed from FEA for the equations in this section are the global nodal forces [242], unless extra highlighted otherwise. In general FEA three types of forces can be obtained: element forces and nodal reaction forces. The latter can be examined locally or globally, i. e. under sole contribution to the node's force by one element or by several elements of the node, respectively. In a crack opening simulation the global nodal reaction force is calculated from the upper or lower half of the total number of elements connected to the node in question. The global nodal reaction force vanishes, when both halves contribute to the calculation.

While some of the earlier described fracture mechanic approaches for FEA yield solely the total energy release rate, the VCCT allows the total energy release rate to be split into the three different modes. The calculations for a three-dimensional, linear (4-noded) element are shown in equations (3.16) to (3.18). Examples and equations for different types of elements were summarised by Krüger [239] and are listed in the following paragraphs for completeness. Deflections from nodes on the upper face are labelled '$^+$' and on the lower face '$^-$'. For a two-dimensional model unit thickness 1 is assumed and $\mathcal{G}_{\text{III}}$ is disregarded.

$$\mathcal{G}_{\text{I}} = -\frac{1}{2\Delta a} Z \left(w^+ - w^-\right) \tag{3.16}$$

$$\mathcal{G}_{\text{II}} = -\frac{1}{2\Delta a} X \left(u^+ - u^-\right) \tag{3.17}$$

$$\mathcal{G}_{\text{III}} = -\frac{1}{2\Delta a} Y \left(v^+ - v^-\right) \tag{3.18}$$

$$\mathcal{G}_{\text{T}} = \mathcal{G}_{\text{I}} + \mathcal{G}_{\text{II}} + \mathcal{G}_{\text{III}} \tag{3.19}$$

Linear elements are in most cases less desirable than higher order elements, because of the necessity for an increased number of elements and thus higher calculation time in order to achieve the same accuracy of higher-order elements.

Quadratic shape function elements are commonly used instead, which incorporate a midside node between the corner nodes yielding an 8-noded element for 2D applications. The VCCT calculation of the linear elements is extended for the additional set of midside nodes as shown in equations (3.20) to (3.21). In this case the deflection of the corner nodes (c) of the open faces are combined with the force on the corner node of the crack tip. Equivalent, the midside nodes' (m) deflection of the open face is multiplied with the force at the midside node of the closed face in front of the crack tip.

$$\mathcal{G}_{\text{I}} = -\frac{1}{2\Delta a} \left[Z_c \left(w_c^+ - w_c^-\right) + Z_m \left(w_m^+ - w_m^-\right)\right] \tag{3.20}$$

$$\mathcal{G}_{\text{II}} = -\frac{1}{2\Delta a}\left[X_c\left(u_c^+ - u_c^-\right) + X_m\left(u_m^+ - u_m^-\right)\right] \tag{3.21}$$

In chapter 2.1 the singular stress distribution near a crack tip was discussed. Midside node elements can be improved for the particular use in crack opening simulation as 'singularity elements' by derivation to quarter-point elements [238, 243, 244]. Singularity elements are more capable of accurately simulating the $1/\sqrt{r}$ stress field singularity. In quarter-point elements the midside nodes are at $1/4$ of the distance from the crack tip node to its next corner node, contrary to midside nodes at $1/2$. In ANSYS, this can be achieved by 'manually' moving the adjacent midside nodes of the crack tip corner node to the quarter position or with the KSCON command for a collapsed mesh of singular elements (cf. sec. 3.3.2). The latter method yielding triangular elements involves the collapse of three nodes on the crack tip first or the utilisation of six-noded singular elements, which were presented by [245, 246]. Raju [238] gives the solution for the ERR calculation applicable to rectangular and triangular 8-noded singularity elements.

$$\begin{aligned}\mathcal{G}_{\text{I}} = -\frac{1}{2\Delta a}\Big[&Z_c\left\{t_{11}\left(w_c^+ - w_c^-\right) + t_{12}\left(w_m^+ - w_m^-\right)\right\} + \\ &Z_m\left\{t_{21}\left(w_c^+ - w_c^-\right) + t_{22}\left(w_m^+ - w_m^-\right)\right\}\Big]\end{aligned} \tag{3.22}$$

$$\begin{aligned}\mathcal{G}_{\text{II}} = -\frac{1}{2\Delta a}\Big[&X_c\left\{t_{11}\left(u_c^+ - u_c^-\right) + t_{12}\left(u_m^+ - u_m^-\right)\right\} + \\ &X_m\left\{t_{21}\left(u_c^+ - u_c^-\right) + t_{22}\left(u_m^+ - u_m^-\right)\right\}\Big]\end{aligned} \tag{3.23}$$

$$\text{with} \quad t_{11} = 6 - \frac{3\pi}{2}\,, \quad t_{12} = 6\pi - 20\,, \quad t_{21} = \frac{1}{2}\,, \quad t_{22} = 1 \tag{3.24}$$

De Roeck and Abdel Wahab [247] presented formulations for the use of collapsed 3D

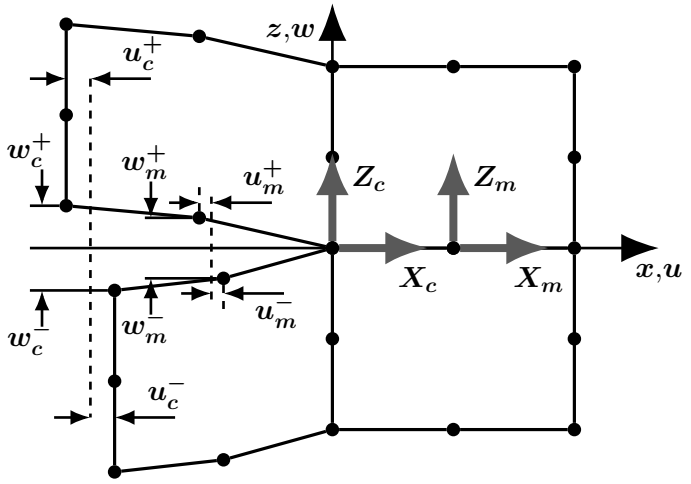

Figure 3.2: Crack tip opening displacement for an 8-noded, quadratic, rectangular element

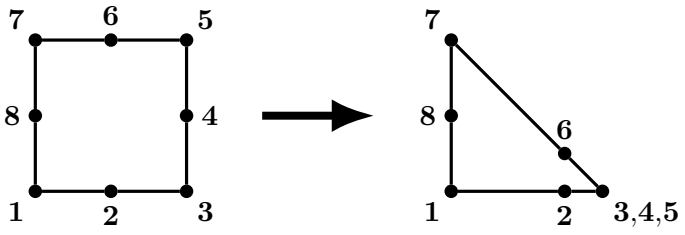

Figure 3.3: Derivation of singular element for crack tip at node 3 from 8-noded quadratic rectangular yielding quadratic singular

prism shaped singular elements among other types of elements. Using prisms for 3D VCCT simulations would significantly reduce the complexity of the mesh generation, as automatic meshing algorithms would be sufficient. The element formulations were adopted by Chiu and Lin [248] and extended for crack tip faces under pressure.

Nairn [242] described a generalised version of the VCCT that allows the side-nodes to be placed arbitrarily and mixed. Additionally, Nairn's method corrects an error in [238] for the application of traction forces on the crack faces. The formulation for $\mathcal{G}_{\text{II}}$ is obtained by replacement of $\mathbf{Z}$, w and σ_0 with $\mathbf{X}$, u and τ_0. For midside node elements equation (3.25) is equal to equation (3.20) with the additional traction term of $-\sigma_0/3\left(w_m + w_c/2\right)$.

$$\begin{aligned}\mathcal{G}_{\text{I}} = \frac{1}{2t\Delta a}\Bigg[&\left(\Delta w_c \begin{bmatrix} -R \\ 1-2R \\ 1-R \end{bmatrix} - R\mathbf{N}\mathbf{M}^{-1}\mathbf{K}\right)\cdot\mathbf{Z} \\ &+\left(\Delta w_m \begin{bmatrix} 1 \\ 1 \\ 1 \end{bmatrix} - \mathbf{N}\mathbf{M}^{-1}\mathbf{K}\right)\cdot\mathbf{Z}\Bigg] \\ &-\frac{\sigma_0}{3}\left(\frac{3-4R}{4}\Delta w_c + \Delta w_m\right)\end{aligned} \tag{3.25}$$

Nairn introduced new vectors and matrices for geometry, shape and fitting functions for equation (3.25). Also the nodal edge forces in z direction as the vector $\mathbf{Z}$ were introduced. More details about the terms and specific solutions for quarter-point elements and for axisymmetric problems can be found in [242]. Recently, Muthu et al. [249] published a method that employs the VCCT in an element-free Galerkin calculation.

3.3.1 *Aspects of VCCT simulations*

Mesh generation is the main disadvantage of the VCCT, which is labour intensive in the standard way of application. The mesh has to have a line of element edges aligned along the desired crack tip. The elements have to be rectangular

or hexahedral elements of the types discussed above. Research was undertaken to overcome limitations emerging from the required highly controlled mesh generation. Xie and Biggers [208, 209] published an approximating VCCT method to simulate an arbitrary crack front across a mesh of rectangular elements that is unaligned to the crack front, which was similarly approached and validated by Liu et al. [250]. Okada et al. [251] applied an averaging VCCT calculation that allows for a generic automatic meshing with triangular or tetrahedral elements along the crack tip.

Agrawal and Karlsson [252] showed a study about the influence of the crack tip element size on the ERR and mode mixity in particular. The crack tip element size is important, because the ERR is dependent on the crack size and simultaneously the crack size can change with the element size along the tip. This problem occurs whenever the crack is not embedded within material, but starts at a plane face or any form of edge geometry, such as a V-notched specimen, a lap joint or the investigated rectangular geometry of the defect edge between repair and metal substrate as shown in diagram (5.1). In this case minimising the crack tip element size affects the resulting ERR with two superimposing factors. The ERR changes with the change in crack size and with the larger stresses on the elements, which alter with the $1/\sqrt{r}$ stress singularity discussed in section 2.1.1. Therefore, a range of different element sizes have to be simulated to converge the ERR result for a single datum. Venkatesha et al. [253] published a 'generalized modified crack closure' method that allows to obtain the converged value within one simulation.

Additionally, the oscillatory behaviour of interface cracks of dissimilar materials (cf. sec. 2.1.2) must be avoided by a sufficiently large element size [254].

The VCCT was applied in interface crack investigation in numerous cases [252, 255–261]. Kattamis et al. [262] simulated the ERR of laser induced blister formation with linear rectangular 2D elements. Guo et al. [263] utilised the VCCT with axisymmetric shell elements to investigate into the delamination of thin polymeric films under pressure or point loads. Residual stresses were considered and the bending to stretching transition documented for an arbitrary interface failure ERR of $\mathcal{G} = 100\,\mathrm{J/m^2}$. Guo et al. did not obtain bending and stretching values for different specimen thicknesses, but in regards to the state of bending or stretching of thin films during an increase in load. The VCCT formulation for shell elements (3.26) was extended with the moment M and the rotation angle ϑ.

The VCCT applied for dynamic loading can be found in [264] and with utilisation of interface elements in [265].

$$\mathcal{G} = \frac{1}{2\Delta a}\left(Z_c \Delta w_c + X_c \Delta u_c + M_c \Delta \vartheta_c\right) \tag{3.26}$$

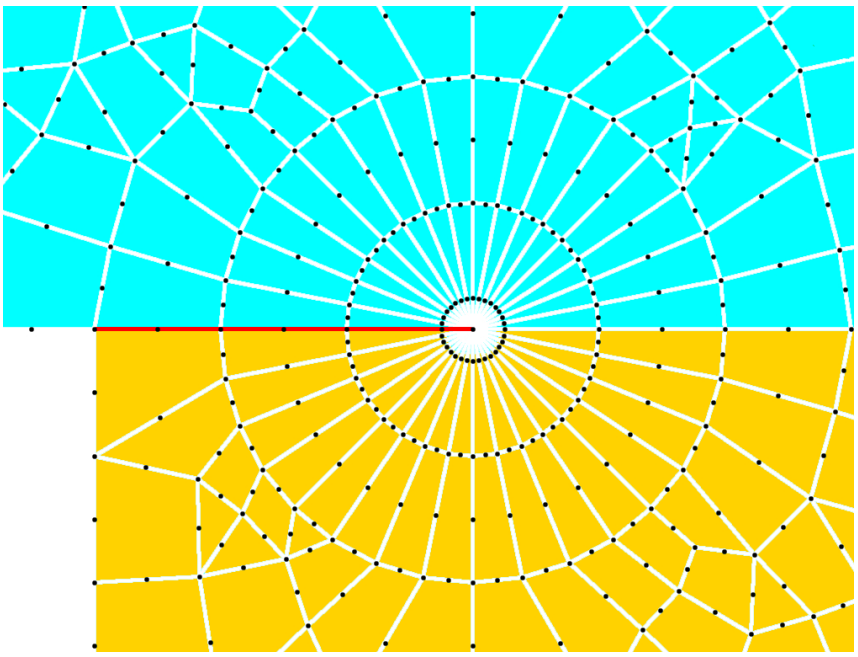

Figure 3.4: Collapsed mesh of 32 quarter-point elements around crack tip

3.3.2 *Application of the VCCT*

ANSYS® does not supply the user with methods to overcome limitations concerning the mesh generation, nor are elements other than rectangular linear (PLANE182, SOLID185) and midside node elements (PLANE183, SOLID186) supported for VCCT calculations. For automatic quarter-point element meshing, ANSYS provides the option of generating a collapsed mesh around a central node by the command KSCON, yielding a circular pattern of elements as shown in figure (3.4). The calculation of the ERR presented from equation (3.22) onwards has to be implemented manually. A comparison between the manually implemented calculations and ANSYS integrated routines was undertaken with linear and quadratic midside node elements and has proven that both yield identical results.

For plane strain or plane stress models typically the areas of the crack opening are identical for symmetric meshes, irrespective of the area investigated being the area of the element faces in front, behind or an average of both. Although, as explained before, the impact of a small change in crack length (i. e. a crack opening) is regarded negligible, an axisymmetric model also results in different area sizes depending on the radius. For this reason the ERR might vary noticeably with a change in crack length and through the element faces chosen as new crack area, in contrast to plane strain and stress models. To obtain the same result for the ERRs in the axisymmetric case by manual calculation and through ANSYS, the area of the crack opening has to be calculated from the average of the lengths of the element before and after the crack tip node.

For the simulation of flat punches (cf. fig. 4.2) it is necessary to apply an edge

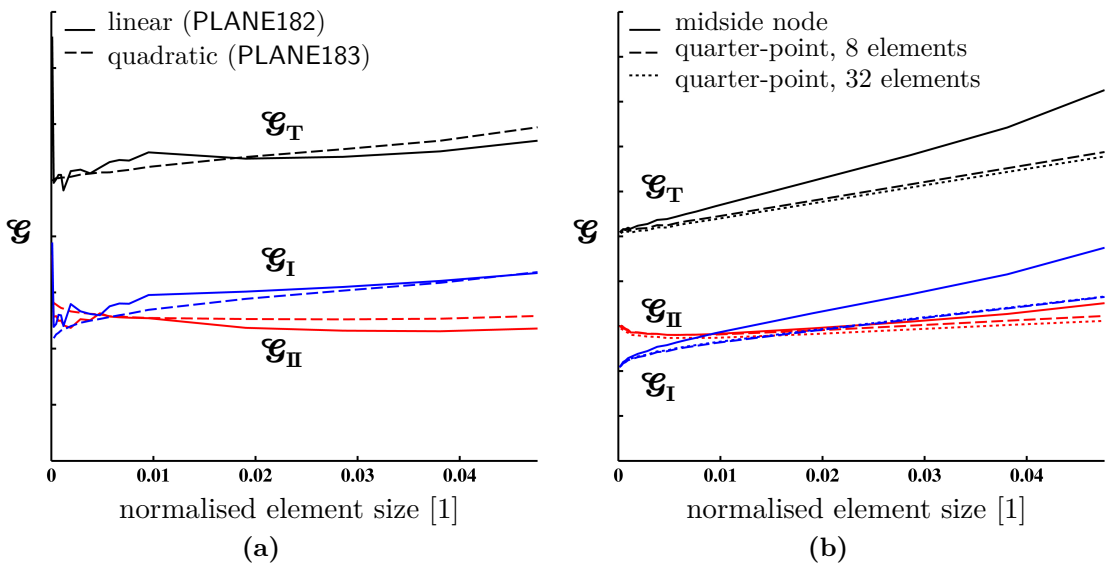

Figure 3.5: Influence of the element type and size; Size of elements normalised over defect radius; b) shows Plane183 elements with midside and quarter-point nodes from a collapsed mesh with 8 and 32 elements around the crack tip

fillet of the size of at least three elements. A sharp edge would lead to a single node applying force on a single element, leading to unnaturally high distortion and convergence problems for the simulation.

The effects of the different element types were analysed and are presented in figure (3.5). Element sizes in form of the length l_{elem} of the element faces at the crack interface were normalised against the critical length, the radius R, as l_{elem}/R. Figure (3.5a) illustrates the advantage of quadratic formulations over linear equation elements. In particular, the oscillatory behaviour of small linear elements is undesirable. Figure (3.5b) shows that midside node elements and quarter-point elements are different for large size elements, but converge towards the same result. An increase in elements for a collapsed mesh does not further improve the result. It was concluded, that midside node elements are sufficient for fracture simulations and the additional effort for the manual implementation of a quarter-point element mesh generation and ERR calculation in the ANSYS code was not justified. Similarly, Shivakumar et al. [266] showed that the VCCT yields accurate results without the need to employ singularity elements.

Therefore, calculations were conducted with PLANE183 elements for axisymmetric 2D modelling of the tests described in chapters 4 and 5. Since analytical solutions solely account for quasi-isotropic materials and because the ERR results of anisotropic and orthotropic materials were evaluated in an early PVM study and considered to be similar enough to quasi-isotropic materials, axisymmetric 2D models were chosen over 3D models for the lower computational effort. Consequentially, repair laminates were approximated as quasi-isotropic with mixed moduli as shown

in section 5.3.2.

For the studies presented a convergence was achieved by solving the models with varying crack tip element sizes similar to figure (3.5). In order to reduce computation time, the minimisation of the elements was kept within reason. In exchange, an extrapolation with a second order polynomial fit was applied to obtain the ERRs for an infinitesimally small initial crack under consideration of the stresses at the elastic-plastic zone (fig. 2.2).

Not only the tested specimens were simulated, but also an array of input variables investigated, such as different geometries. As a consequence, it was necessary to run a number of simulations too large to be undertaken individually and manually. An automation of the full process was realised through a MatLab programme steering the input variables, writing the ANSYS input file, calling ANSYS in batch mode and ultimately managing the output. For this purpose, a general ANSYS input file was written manually and later modified within MatLab according to the respective variables of the current run. A database file was constructed and extended with every simulation. Subsequently, it was fed into a second MatLab based programme dedicated to the analysis of the data, the calculation of the extrapolation and the generation of graphical outputs.

Chapter 4. Shaft-loaded blister test (SLBT)

4.1 Introduction to shaft-loaded blister test

Most of the established fracture toughness tests focus on fracture in isotropic material [267–270], adhesion between two solids [139, 271, 272], interlaminar fracture of composites [138, 143] or bi-material fracture of thin films on substrates (see chapters 4.2 and 5.1 and [146, 147]). With increasing use of composites in various applications and a greater variety of material combinations, the research on bi-material, interface fracture behaviour between composites and metals has intensified over the past two decades.

The particular application of an external composite repair on a corroded pipe wall needs to take the general geometry of the defect into account. Circular and slotted defects were assumed to simplify the problem. Standard test methods for mode I, II or mixed mode fractures, often applied for general determination of a materials fracture toughness, evaluate rectangular plates and beams of which a summary is given in chapter 2.2. In the case investigated throughout this study, the geometry of a repair across a circular defect is better described as an axisymmetric plate with a fixed end around the edge. Alternatively, the repair of a slotted defect may be represented by a plate with fixed ends and plane strain condition along the length of the slot.

To simulate a corrosion defect more accurately, a circular blister test can be conducted. In general, a blister test comprises of a top layer bonded onto a substrate. The term 'repair plate' will be used throughout this work instead of 'top layer', which is typically found in the literature. The substrate is stiffer than the repair, but contains an artificial defect. Circular shapes are the most widely used, but other defect shapes such as straight and U-shaped slots can also be found. Defects could be machined through-holes or pre-delaminations by using, for instance, Teflon tape. The repair plate covers the defect and is detached from the substrate throughout the course of the test.

The force needed to detach the repair from the substrate can be a fluid pressure or a mechanical force from a punch, driven into the centre of the defect. Shaft-loaded blister tests (SLBT) simplify the test and measurement procedure, compared to pressurised blister tests, with the drawback of dissimilar loading. In contrast to fluid pressure, a punch produces a more localised, central force on the repair. Changes in

the load situation are reflected by the deflection curve of the blister. SLBTs have the advantage of non-catastrophic crack propagation in the interface between substrate and repair, hence allowing the measurement of a number of data points along the continuous crack growth path. Finally, the mechanical properties of the repair can be determined [273, 274].

Many applications for blister tests are fracture toughness evaluations of coatings and thin films, ranging from protective coatings of large metal structures to mechanics of microelectronics. Membrane plate theories are the predominant analytical solutions for these types of applications. Instead, specimens for standard single and mixed mode fracture toughness tests are dimensioned as thin plates in accordance with the classical plate theory. However, corrosion defects can be highly localised (cf. chap. 1.2) and thus the ratio of the thickness of a repair per defect radius can be outside the limits of the classical plate theory.

The work presented analyses thick fibre reinforced polymer laminates as repair plates. Shaft-loaded blister tests were performed using punches with flat and hemispherical heads. The following chapter provides a review of SLBT research, outlines analytical solutions and compares 1) experimental measurements, 2) analytical results and 3) FEA results. Finally, the fracture toughness evaluation through SLBT is compared with the pressurised blister tests, presented in chapter 5, to validate SLBTs for pressure applications.

4.2 Review of shaft-loaded blister test research

Malyshev and Salganik [65] were the first to develop a shaft-loaded blister test by debonding a thin plexiglass plate from a metal substrate with a punch. Several types of SLBTs can be found, but one of the most common is conducted with a hemispherically capped cylinder as punch [273, 275, 276]. Depending on the investigated material and the radius of the hemisphere, the contact zone can change throughout the loading and plastic deformations can occur. Both contact zone and plastic deformation need to be taken into account for the analytical calculation [150, 277, 278].

Flat capped punches are typically used in an 'inverted' blister test [279, 280], in which the investigated film debonds from the punch. The punch is bonded to the film and pulls, while the film is clamped around the edge. Relatively little work is published that uses a flat punch pushing against a repair plate in a standard blister test [281, 282]. Hemispherical heads are favoured to avoid high accumulations of stress at the sharp edges of flat capped punches, which would result in yielding and rupture of the film. Axisymmetric flat punch and plate shapes are often used, but rectangular shapes may also be found for plane strain models [283, 284].

Theoretical and numerical studies were conducted on different punch and repair plate geometries, leading to different boundary conditions for the analytical solu-

tions at the centre of the plate [285–287].

Since most of the work investigated thin films, coatings and membranes, the strength of interfacial adherence could reach the structural strength of the investigated material. Consequently, research for SLBTs focussed on topics such as non-linear material behaviour [288], transitions between plate and membrane states [288], transition from bending to stretching [275, 289, 290], plastic deformation in the punch/film contact zone [150, 291] and residual stresses in the specimen [279, 292, 293]. The listed topics are less critical for thick and reinforced repair plates, as the material behaviour in general remains linear-elastic. Plastic material deformation can be expected in localised zones of high stress concentration. A typical example are the small punch/plate contact areas of hemispherical punches, which can lead to matrix cracking of FRP composite plates.

By constraining the specimen in radial direction, i. e. clamping the repair plate around the defect edge, it is possible to determine material properties with SLBTs. This test is also known as the clamped blister test (CLBT), where no crack growth occurs and the blister deflection due to the loading leads to the elastic modulus of the specimen [294, 295].

Different constraints are also used to control the blister shape and propagation. However, constraints are only applicable for pressurised blister tests. An overview of constraint pressurised blister tests is given in chapter 5.1.

4.3 SLBT evaluation process through experiments and simulations

Experimental testing of fracture energy with the shaft-loaded blister test was performed to obtain load and displacement data and material properties. Obtained data was used for comparison between and as input for analytical calculations and FE simulations.

The SLBT conducted in the present study was a circular blister test of a simply supported disk. No additional boundary conditions on the blister formation were applied. The tested disk specimens consisted of a metal substrate containing a central defect with a composite 'repair' laminate bonded on top. The defect was a circular through-hole with sharp edges at the repair interface. Three different hole diameters were investigated.

Geometries and materials were used in accordance with the pressurised blister test presented in chapter 5. However, only the bi-axial, non-crimp, E-Glass fabric was evaluated in combination with WTR Technowrap 2K epoxy resin. In order to measure crack growth by optical means from a change in translucency at the debonded area as shown in figure (4.1), it is essential to manufacture repair layers that are translucent to some extent. Glass fibre reinforced epoxy laminates provide a translucency, which is dependent on the fibre orientation, residual air in the poly-

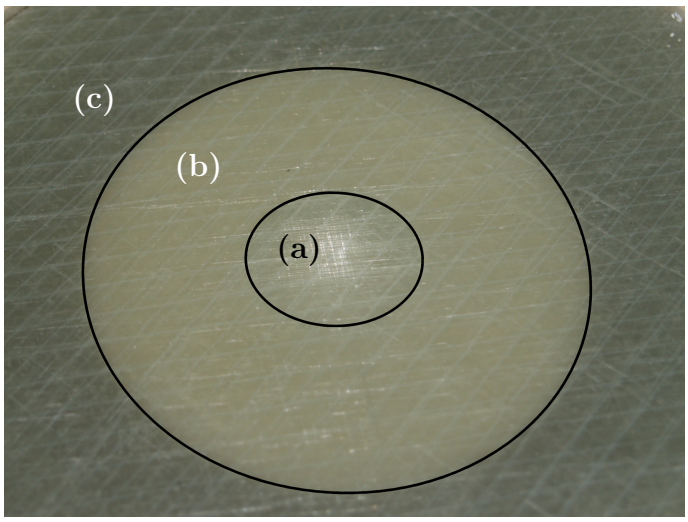

Figure 4.1: Top side view of SLBT specimen with glass epoxy repair after test with (a) the artifical defect area, (b) the debonded crack area and (c) the remaining intact bond area

mer matrix, the resin type and additives, and can range to full opaqueness. Carbon and aramid fibre laminates are always opaque and were not included in the study in order to retain the option to measure crack growths. The laminates were reduced to quasi-isotropic stack-ups. Test specimens were prepared as described in chapter 5.3, which also contains a description of the determination of the material properties.

Punches with a hemispherical and flat cap were used to push through the hole in the substrate against the repair plate (fig. 4.2). For every hole diameter one specific punch was manufactured, in order to harmonise the punch/plate contact area ratio between all specimens. The punch radii were 1 mm smaller than the radii of the holes.

A universal strength testing machine (USTM) drove the punch and the force was recorded from the USTM's load cell. Cross-head displacements were recorded from the USTM and from a linear transducer. The cross-head displacement speed was 2 kN/min and the total displacements were 2 and 3 mm.

Finite element simulations were carried out for the purpose of

a) investigation of the validity of the previously presented analytical solutions in chapter 2.3 for the determination of the energy release rate across a range of variables

and

b) determination of the energy release rates of every actual test under use of the respective material properties, geometries, displacements and shaft-loads; to be compared with the virtual equivalent loading from a fluid

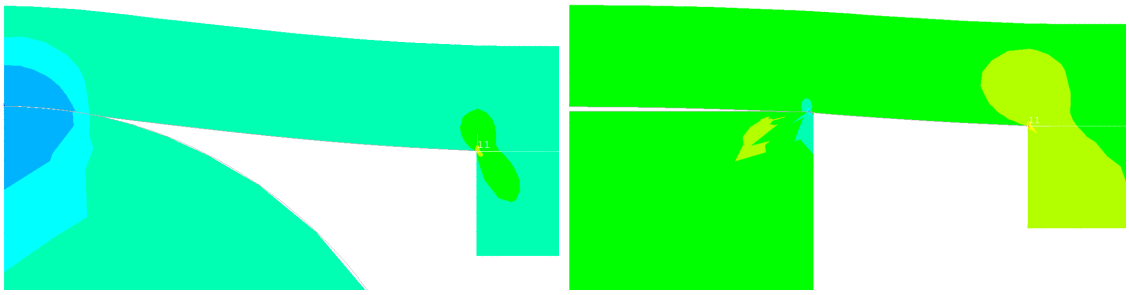

(a) (b)

Figure 4.2: Example of contact areas of an (a) hemispherical and (b) flat punch, obtained from FE simulation

pressure.

The FEA simulations were undertaken with ANSYS 14.5 Mechanical APDL and energy release rates were obtained from virtual crack closure technique simulations. More detailed descriptions of the finite element techniques are presented in chapter 3.3.

The two main variables investigated are the punch geometry and the repair plate under load. Commonly, flat capped and hemispherical punch heads are found, both of which were studied for various radii. Minimum sizes were smaller than 10 % of the defect radius, while the maximum punch radius reached about 95 %. Thus, almost point loads were achieved as well as nearly all of the defect area was filled out by the punch in order to mimic a surface load.

The dimensions of an investigated repair plate are one of the most important measures for the applicability of a plate theory, which are typically only valid for a number of assumptions (cf. chap. 2.4). For reasons of simplification, all analytical solutions presented are based on the classical plate theory. When a radius to thickness ratio of less than 10 is present, solutions derived from the CPT yield increasingly less acceptable results, as made assumptions do not apply. Therefore, R/t ratios of the repairs are studied from within the lower boundary of CPT validity to thicknesses of 4.5 times the defect radius.

By applying the material properties, specimen and punch geometries as well as failure loads and displacements as inputs for FE simulations, it was possible to obtain the mode I, II and the total energy release rate for each test. Furthermore, every test was simulated another time with an equivalent surface pressure replacing the shaft-loading. This study enabled a comparison between SLBTs and PBTs to evaluate, if SLBTs can provide an alternative test to the more complex PBT.

4.4 SLBT results

The shaft-loaded blister study contained two parts. Firstly, the analytical solutions described in chapter 2.3 were validated over a range of changing variables. Results obtained are presented in section 4.4.1. Secondly, a number of disk specimens were tested in order to obtain actual material properties, failure loads and displacements. Test results are displayed and explained in section 4.4.2 before the results are discussed in chapter 4.5 and the analytical expression that yields the best fit is highlighted.

4.4.1 *Comparison of analytical solutions against FEA*

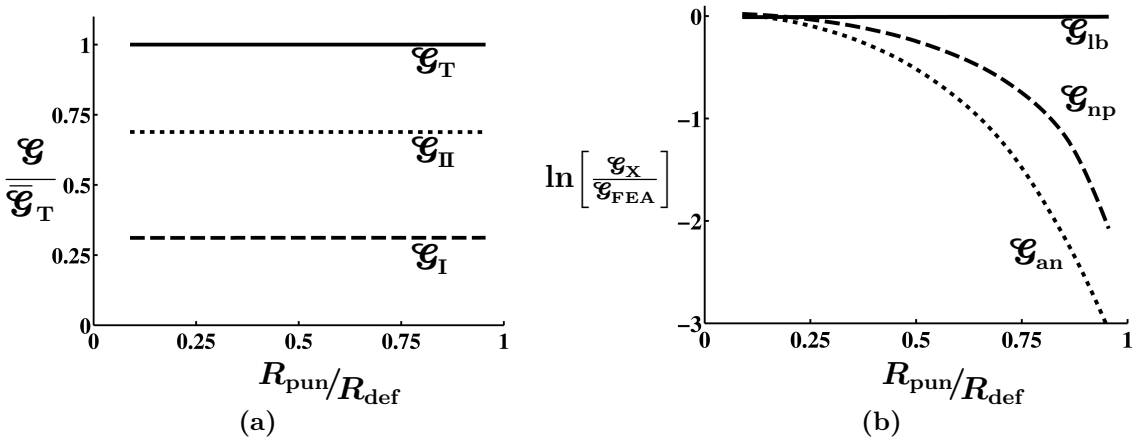

Figure 4.3: (a) $\mathcal{G}_{\mathrm{FEA}}$ of mode I, II and total from SLBT with hemispherical punch for varying punch radius in relation to the size of the defect (normalised over the mean of $\mathcal{G}_{\mathrm{T}}$),
(b) Difference between the analytical solutions of point load based, near-point load and annular line load to $\mathcal{G}_{\mathrm{T}}$, obtained by FEA

Hemispherical punch heads show almost no change in energy release rate over a change in radius of the punch head. The energy release rate mode ratio remains constant. Both are displayed in figure (4.3a). Here, the energy release rate is plotted against the punch head radius R_{pun}, which is normalised against the defect radius R_{def}. The energy release rates (mode I, II and total) are normalised against the average of $\mathcal{G}_{\mathrm{T}}$.

Because a change in punch head radius does not significantly alter $\mathcal{G}$, a further study across a range of different defect radius to repair thickness ratios was undertaken for a constant $R_{\mathrm{pun}}/R_{\mathrm{def}}$ ratio.

Furthermore, figure (4.3b) compares three analytical solutions previously described in chapter 2.3 for a punch radius variation. Only the point load based (*lb*, cf. equation (2.62)), the near-point load (*np*, cf. equation (2.93)) and the annu-

lar line load (*an*, cf. equation (2.101)) solutions are shown, because the displacement based (*db*, cf. equation (2.63)) and the combination (*cb*, cf. equation (2.64)) solutions strongly disagree with the FEA results.

It becomes clear that all three formulations yield similar results for loads, which converge towards a point. Simultaneously, the difference between the analytical solutions and the FEA simulation minimises towards point loads. As $\mathcal{G}_{\mathrm{lb}}$ is independent from defect or punch radii, it stays constant.

Investigating the variation of the radius to thickness ratio for a small diameter punch, figure (4.4a) reveals that the mode II energy release rate remains constant. The total energy release rate changes with $\mathcal{G}_{\mathrm{I}}$, but the change appears shallower for increased R/t.

Again, examining the same analytical formulations in figure (4.4b) as above, it can be observed that $\mathcal{G}_{\mathrm{lb}}$ is most valid for R/t within the limits of the classical plate theory. For a small hemispherical punch, both $\mathcal{G}_{\mathrm{np}}$ and $\mathcal{G}_{\mathrm{an}}$ are applicable over a wider range of R/t than $\mathcal{G}_{\mathrm{lb}}$, with a small advantage for $\mathcal{G}_{\mathrm{an}}$.

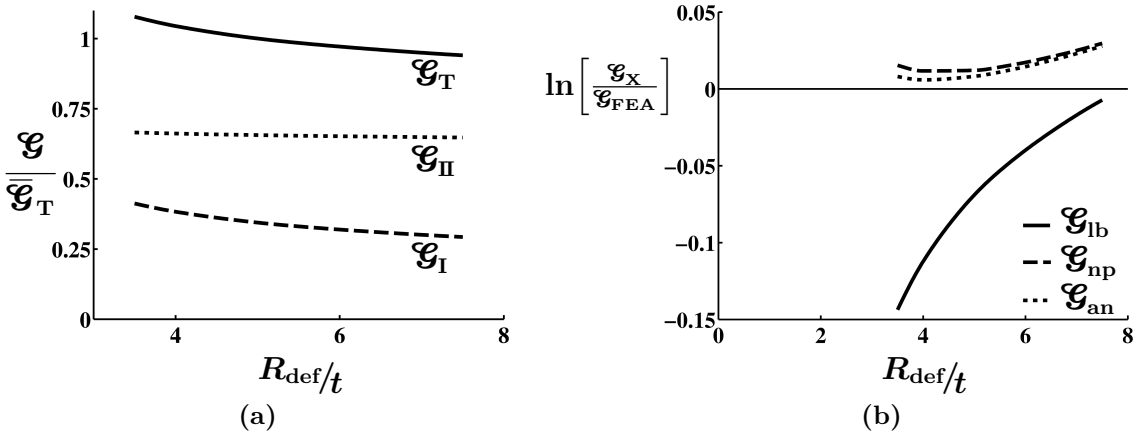

Figure 4.4: (a) $\mathcal{G}_{\mathrm{FEA}}$ of mode I, II and total from SLBT with hemispherical punch for varying plate radius to thickness ratio (normalised over the mean of $\mathcal{G}_{\mathrm{T}}$), (b) Difference between the analytical solutions of point load based, near-point load and annular line load to $\mathcal{G}_{\mathrm{T}}$, obtained by FEA

Flat punch heads yield a variation in energy release rate over a change in punch radius, in contrast to hemispherical punch heads. An example of this change is illustrated in figure (4.5). While the load and geometry remains constant, apart from the punch radius, it becomes obvious that the total energy release rate reduces. Mode I and II ratios converge with larger punch radii and switch for radius ratios near to 1.

To evaluate the quality of the presented analytical solutions, FE simulations were carried out along a matrix of two variables. The first variables of defect radius

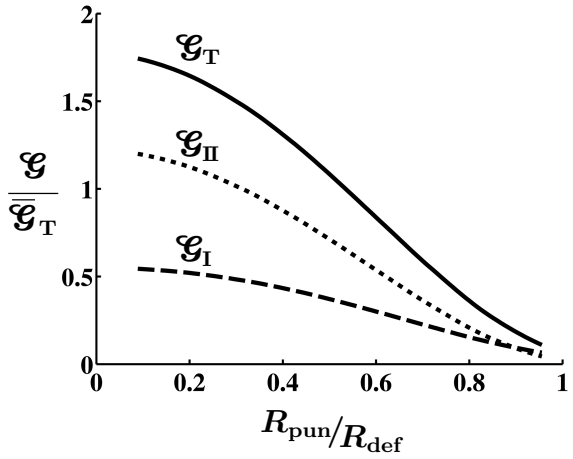

Figure 4.5: Energy release rate changes with variation of radius of flat punch head in relation to the defect radius.

to thickness ratio R_{def}/t is a measure of the general validity of plate theories. For instance, a 'thin plate' as known from classical plate bending theories (cf. chapter 2.4) would be applied within the limits of $10 \leq R/t \leq 100$. The second variable is the variation of the punch radius set in relation to the defect radius, $R_{\mathrm{pun}}/R_{\mathrm{def}}$.

When evaluating the mode mix of the simulated energy release rates over the array of variables, the results from figure (4.5) are confirmed in figure (4.6). Additionally, it can be observed that mode I is not just the dominant mode for large punches, but is also increasingly important with the relative 'thickening' of the repair plate before dropping off again close to reaching a nearly infinitely thick plate. In reverse, mode II becomes more dominant when approaching classical plate theory limits and a point loading.

The results showing the respective analytically obtained result for the energy release rate $\mathcal{G}_{\mathrm{X}}$ (with X: *lb*, *db*, *cb*, *np* or *an*) in comparison to the FE simulated total energy release rate $\mathcal{G}_{\mathrm{FEA}}$ are presented in 3D surface plots.

As some analytical solutions yield large variations to the simulated results, the natural logarithm was applied on the energy release rate comparison $\mathcal{G}_{\mathrm{X}}/\mathcal{G}_{\mathrm{FEA}}$. Thus, large deviations of analytical results to FE are 'compressed', yet unsuitable for the particular case. In contrast, differences within acceptable limits of $\pm 10\,\%$ $\widehat{=}\ \ln\left[\mathcal{G}_{\mathrm{X}}/\mathcal{G}_{\mathrm{FEA}}\right] = \pm 0.1$ are nearly linear after taking the logarithm.

Another advantage of the logarithmic fraction is the equal weighting of over and under estimation of the analytical result in terms of visual evaluation. In other words, a ten times larger analytical value would yield $\mathcal{G}_{\mathrm{X}}/\mathcal{G}_{\mathrm{FEA}} = 10$, while 0.1 would be the result of a ten times smaller value. Therefore, normal graphs appear to the eye biased. On the contrary, the natural logarithm of the ideal scenario when $\mathcal{G}_{\mathrm{X}} = \mathcal{G}_{\mathrm{FEA}}$ is 0. Both, $\mathcal{G}_{\mathrm{X}}/\mathcal{G}_{\mathrm{FEA}}$ values that are larger and smaller than 1, appear with the same magnitude, although remaining distinguishable through a positive or negative sign.

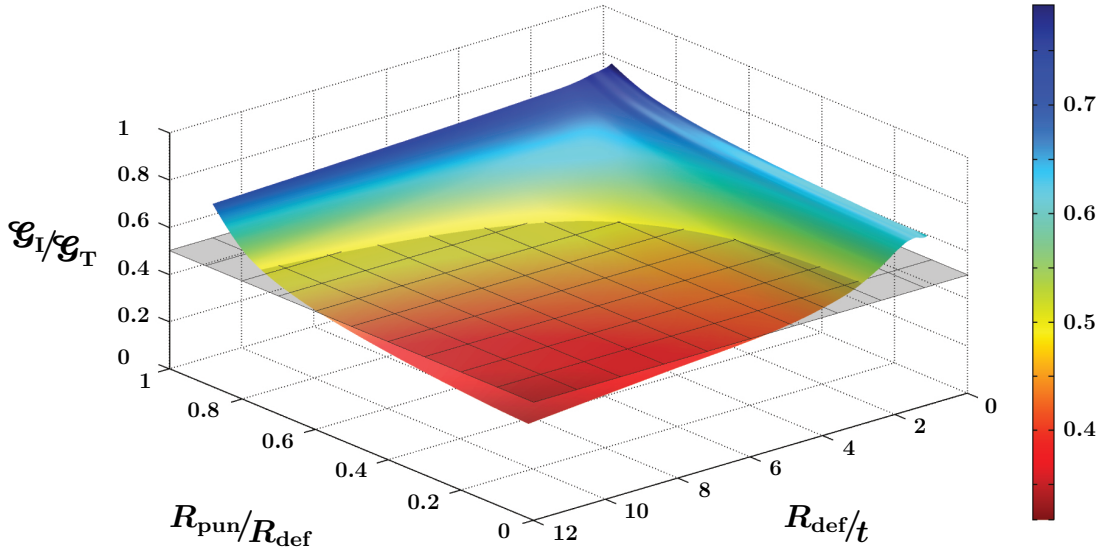

Figure 4.6: Change in fracture mode mix for an SLBT with flat capped punch. The grey plane indicates the 50 % $\mathcal{G}_{I,II}$ division of $\mathcal{G}_T$. (n. b.: maximum of R_{def}/t at front corner of coordinate system)

For further simplification of the interpretation of the graphs, a grey plane is displayed at the zero–level as an additional visual aid, indicating an ideal fit. Closer fits are highlighted by the colour green, though, the colour scaling of the plots across the full range of results are skewed. For a higher comparability, another set of plots is presented only displaying results within the limits of ± 0.4 and thus all resulting in the same colour scale. Finally, those reduced plots are also displayed in 2D with the intention to provide the reader with another overview to clarify the range of validity.

It must be noted that only the 2D plots are presented with unified axes. The other plots show axes directions that are adjusted for the best possible view of a 3D surface on paper.

Results from the **load based** formulation for point loads (cf. eq. 2.62) are shown in figure (4.7)ff. Best agreement between the energy release rate obtained through FEA and the load based solution can be found for small punch to defect radii. Closer to the lower boundary of $R_{\text{def}}/t = 10$ for the classical plate theory the load based solution provides a wider area of validity, which is best displayed in figure (4.8b). Thus, the load based analytical solution is the most robust for determination of the energy release rate when loading a 'thin plate' with a 'small' punch.

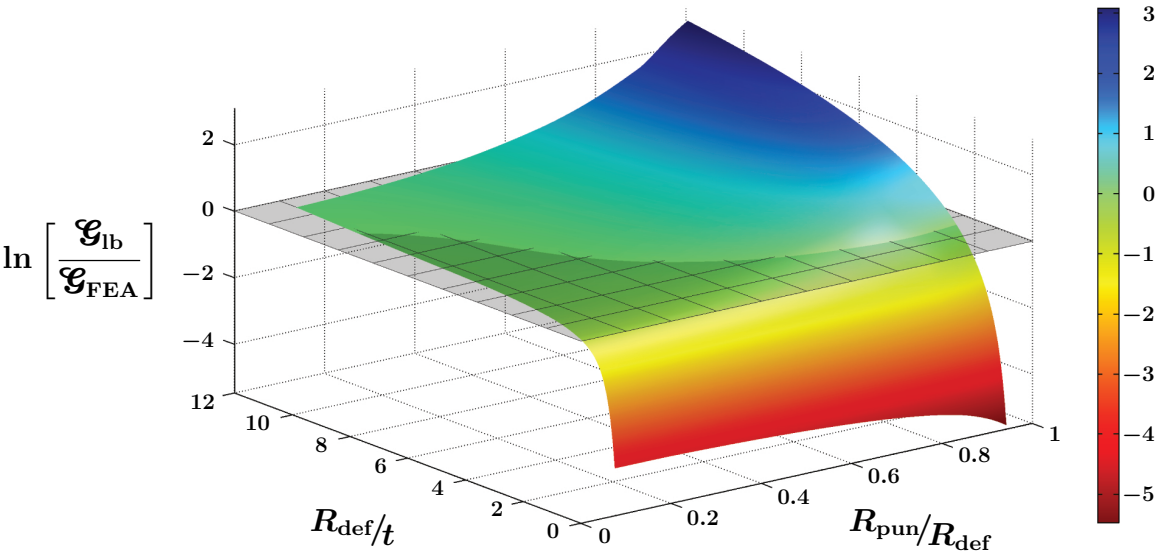

Figure 4.7: Range of validity of the analytical point load based solution, as shown in equation (2.62), for an SLBT with flat punch along the variables of punch to defect radius ratio and defect radius to thickness ratio. Compared to FEA results.

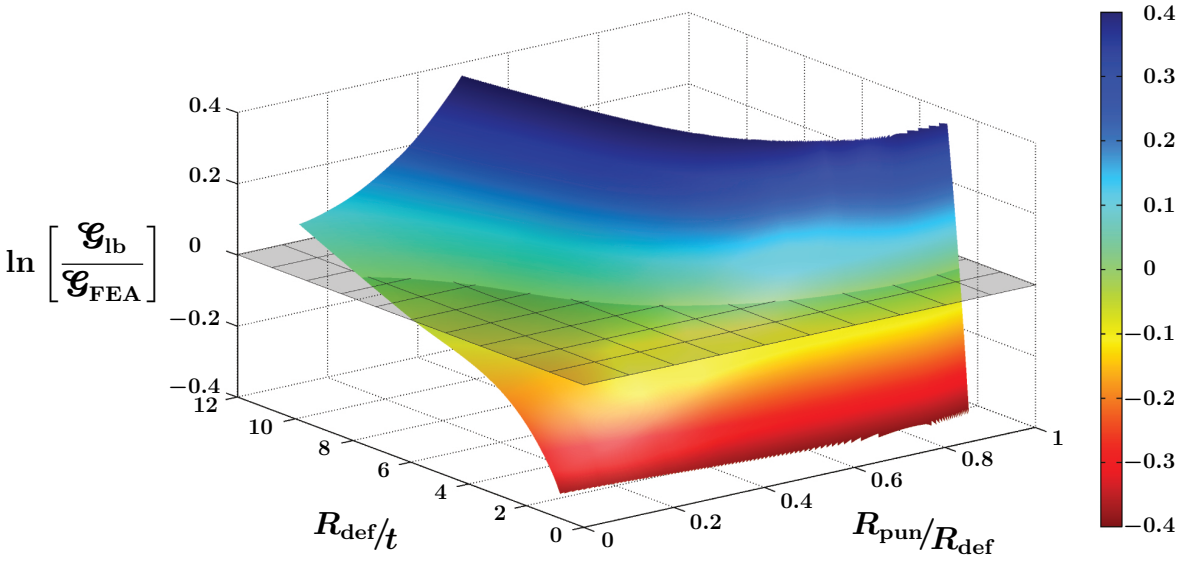

(a)

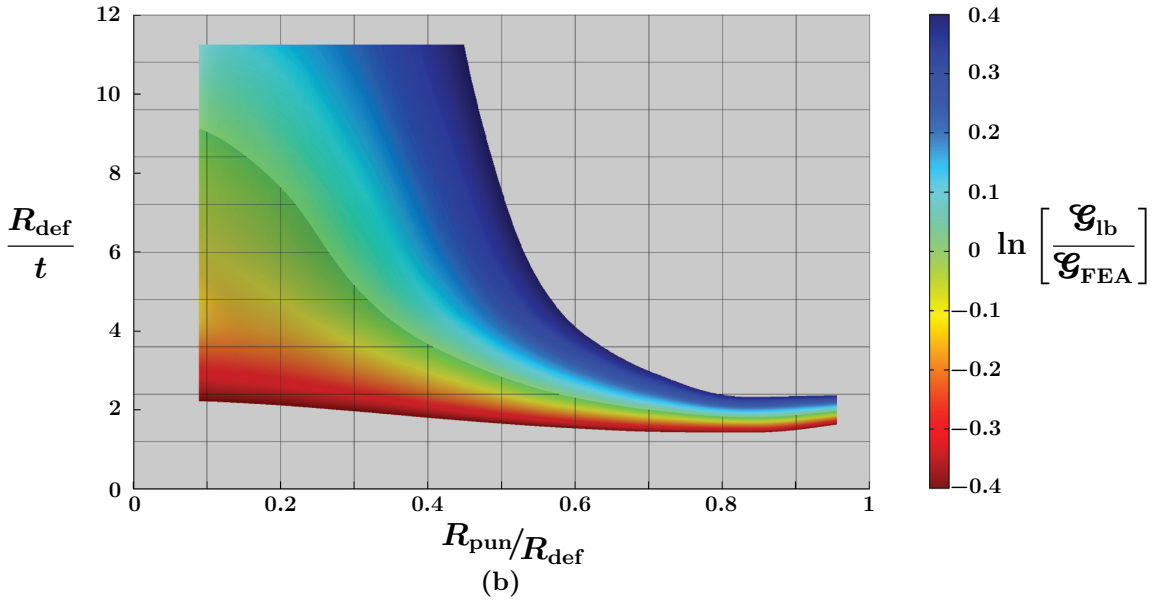

(b)

Figure 4.8: Range of validity of the analytical point load based solution,
(a) Magnification of figure (4.7) to z-axis limits $-0.4 \leq z \leq 0.4$
(b) 2D visualisation of figure (4.8a)

Results from the **displacement based** analytical equation (cf. eq. 2.63) are similar to the load based equation results in terms of the most reliable results, which can be achieved for a 'small' punch loading a 'thin' plate. When comparing figure (4.7) with figure (4.9) it can be observed that the maximum absolute values of the displacement based solution are about e^8 times larger than the results of the load based solution. The area across the investigated variables, which is in close agreement with the results obtained by simulation as shown in figure (4.10b), is smaller than the equivalent of the load based expression as well.

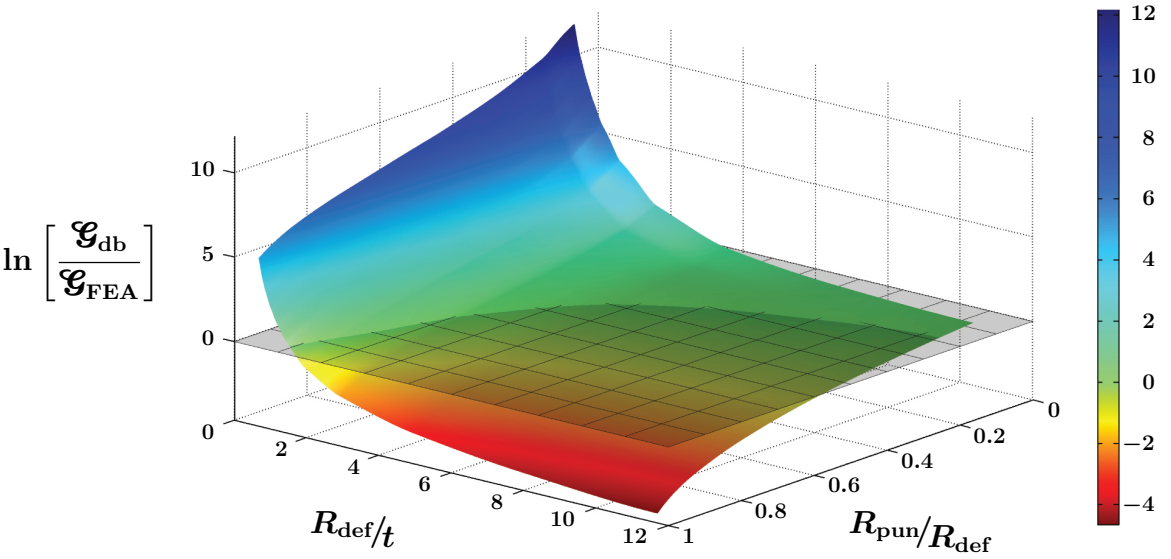

Figure 4.9: Range of validity of the analytical displacement based solution, as shown in equation (2.63), for an SLBT with flat punch along the variables of punch to defect radius ratio and defect radius to thickness ratio. Compared to FEA results. (n. b.: x- and y-axis maximum at front corner of coordinate system)

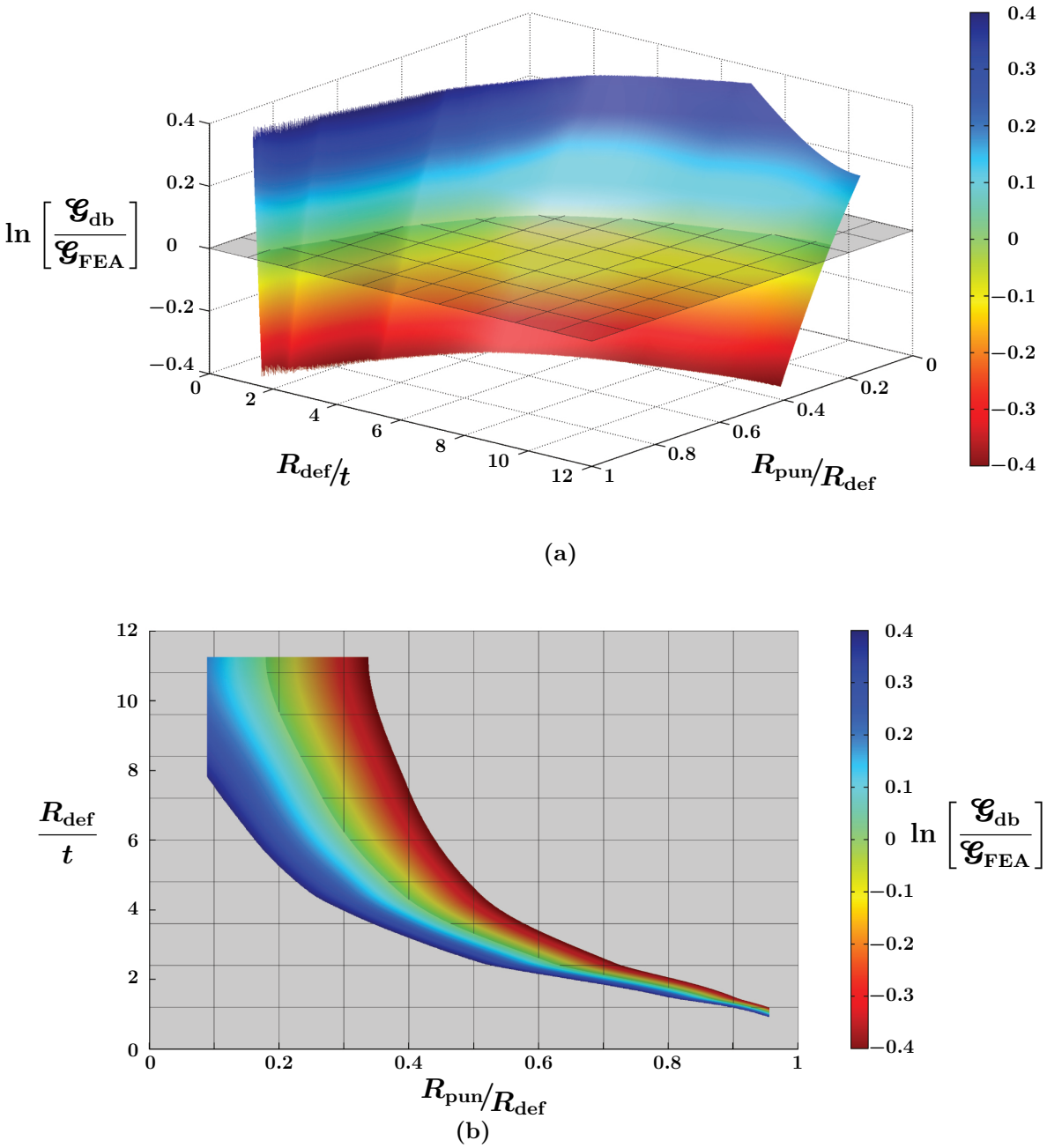

Figure 4.10: Range of validity of the analytical displacement based solution,
(a) Magnification of figure (4.9) to z-axis limits $-0.4 \leq z \leq 0.4$ (n. b.: x- and y-axis maximum at front corner of coordinate system)
(b) 2D visualisation of figure (4.10a)

Dependent on both, displacement and load, is the analytical **combination** solution of equation (2.64). As expected, elements of both previously presented results reflect in the results of the combination equation. For instance, a similar, yet smaller, characteristic spike can be found at $(x, y) = (0, 0)$ analogous to the displacement based equation results. The average magnitude is more similar to the load based equation results, which also yields a closer fit for punch sizes that converge to a point load. However, the combination formulation results appear valid along a larger range of punch to defect size ratios.

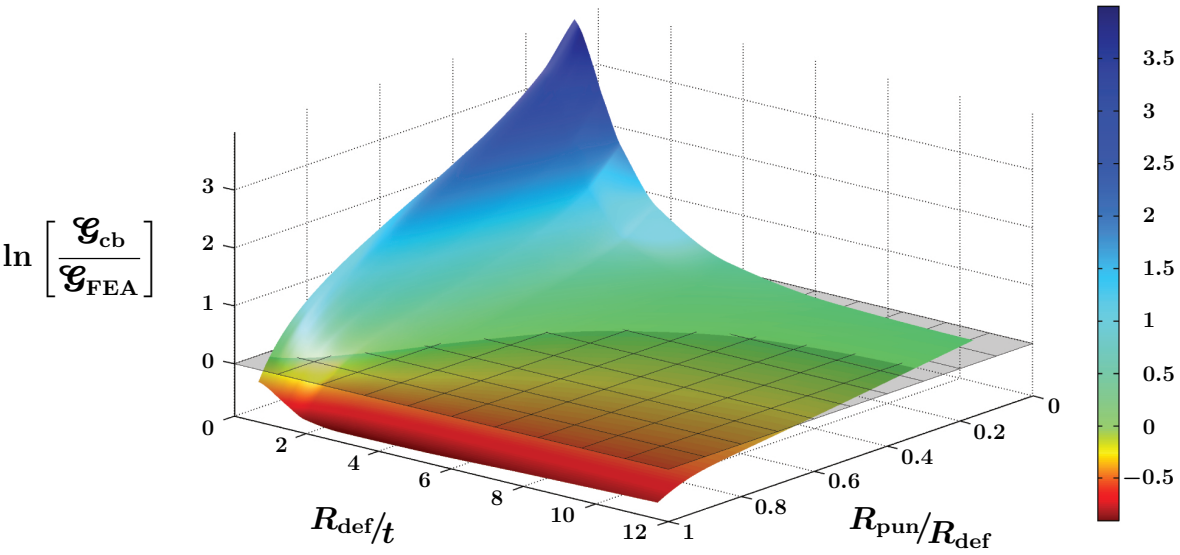

Figure 4.11: Range of validity of the analytical combination solution, as shown in equation (2.64), for an SLBT with flat punch along the variables of punch to defect radius ratio and defect radius to thickness ratio. Compared to FEA results. (n. b.: x- and y-axis maximum at front corner of coordinate system)

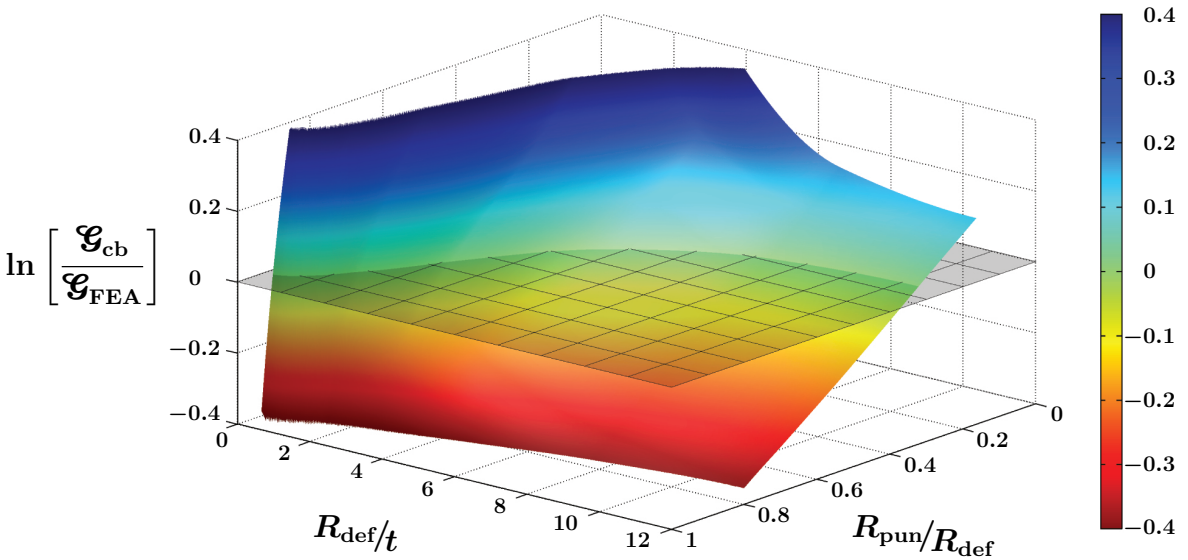

(a)

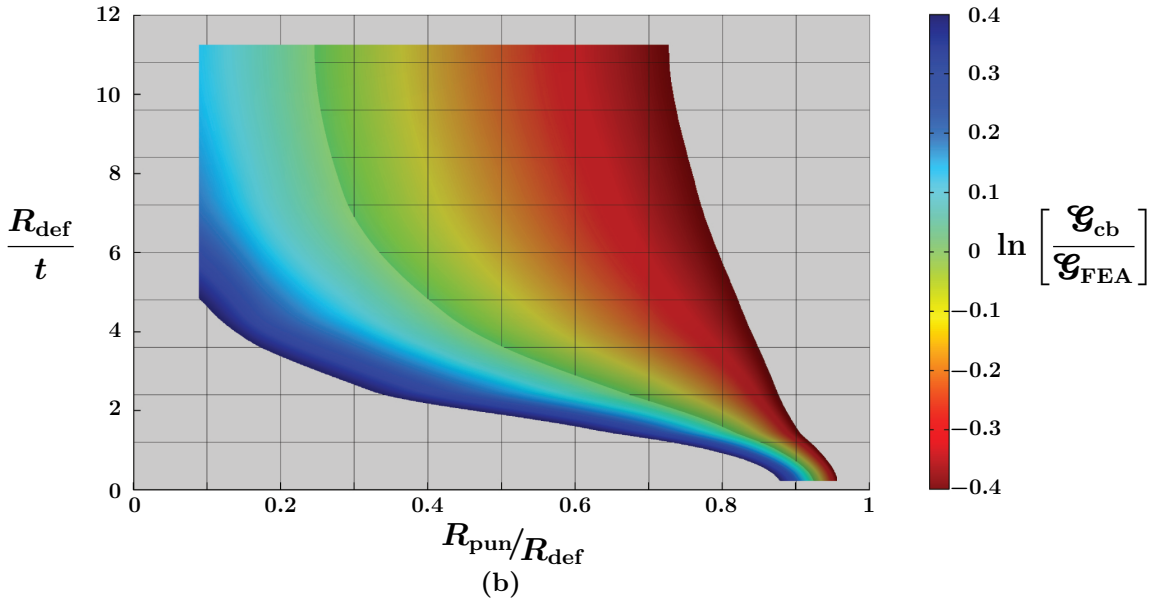

(b)

Figure 4.12: Range of validity of the analytical combination solution,
(a) Magnification of figure (4.11) to z-axis limits $-0.4 \leq z \leq 0.4$ (n. b.: x- and y-axis maximum at front corner of coordinate system)
(b) 2D visualisation of figure (4.12a)

The **near-point load** analytical solution from equation (2.87) shows a comparatively small magnitude of difference to the FEA simulation results in figure (4.13). Almost the full range of investigated variables yield results that are within ±0.4 and thus plotted in figure (4.14a). The best fit can be expected from small punch to defect size ratios. Good agreement can be found within the investigated area of approximately:

$$1.75 \leq \frac{R_{\text{def}}}{t} \leq 11$$

$$0.1 \leq \frac{R_{\text{pun}}}{R_{\text{def}}} \leq 0.4$$

Two different effects, described in more detail in chapter 4.5, result in the invalid areas of 'large' punch diameter and small defect size against plate thickness ratios. Because both effects counterbalance each other for some combinations of the two variables, the analytical near-point load solution yields acceptable results around $R_{\text{def}}/t = 2$.

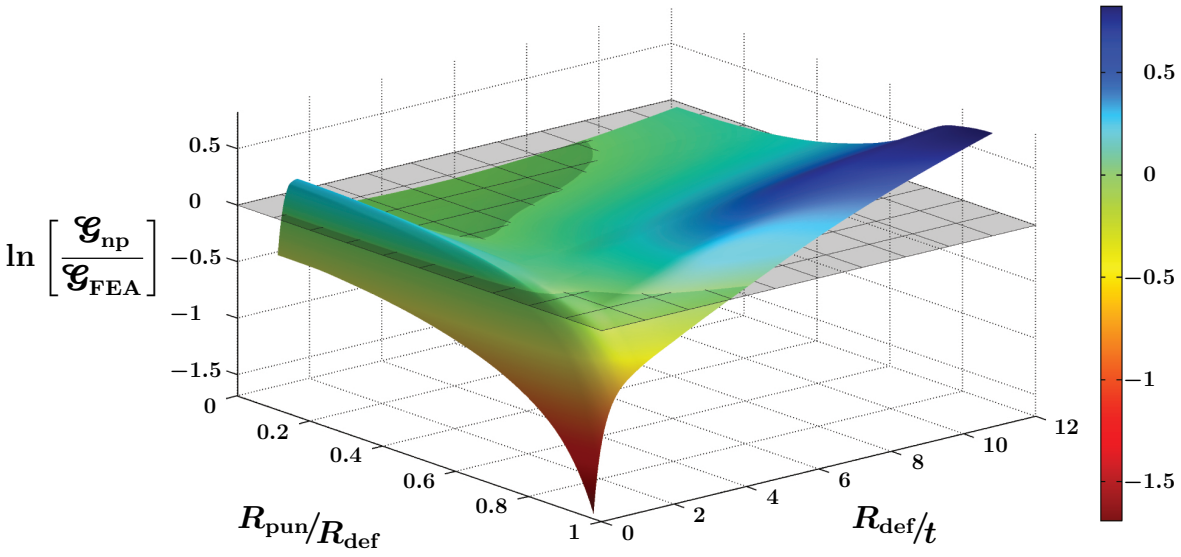

Figure 4.13: Range of validity of the analytical near-point load solution, as shown in equation (2.93), for an SLBT with flat punch along the variables of punch to defect radius ratio and defect radius to thickness ratio. Compared to FEA results. (n. b.: $\frac{R_{\text{pun}}}{R_{\text{def}}}$ maximum at front corner of coordinate system)

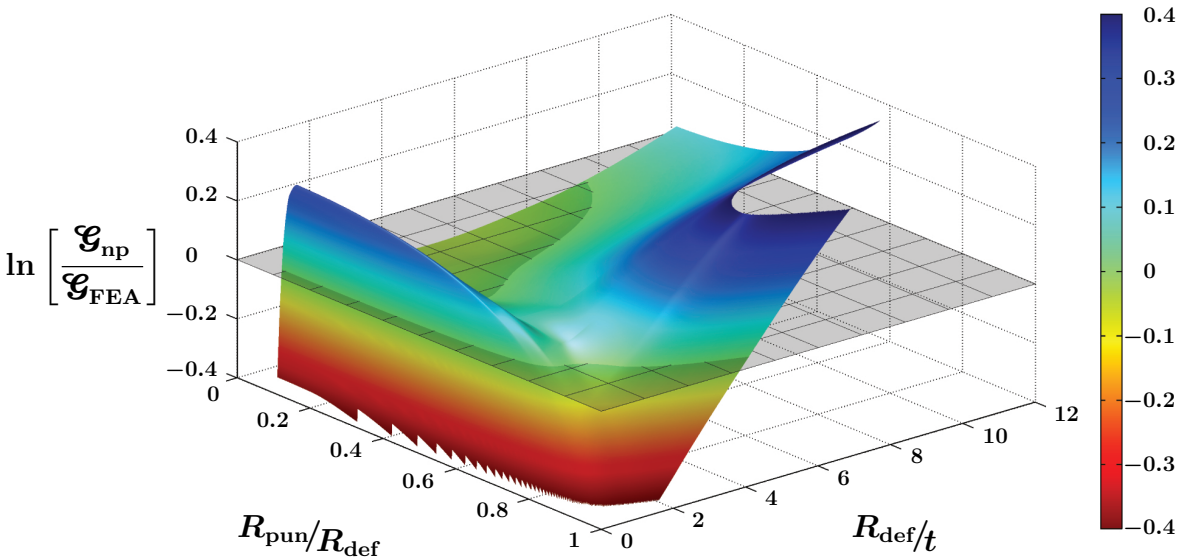

(a)

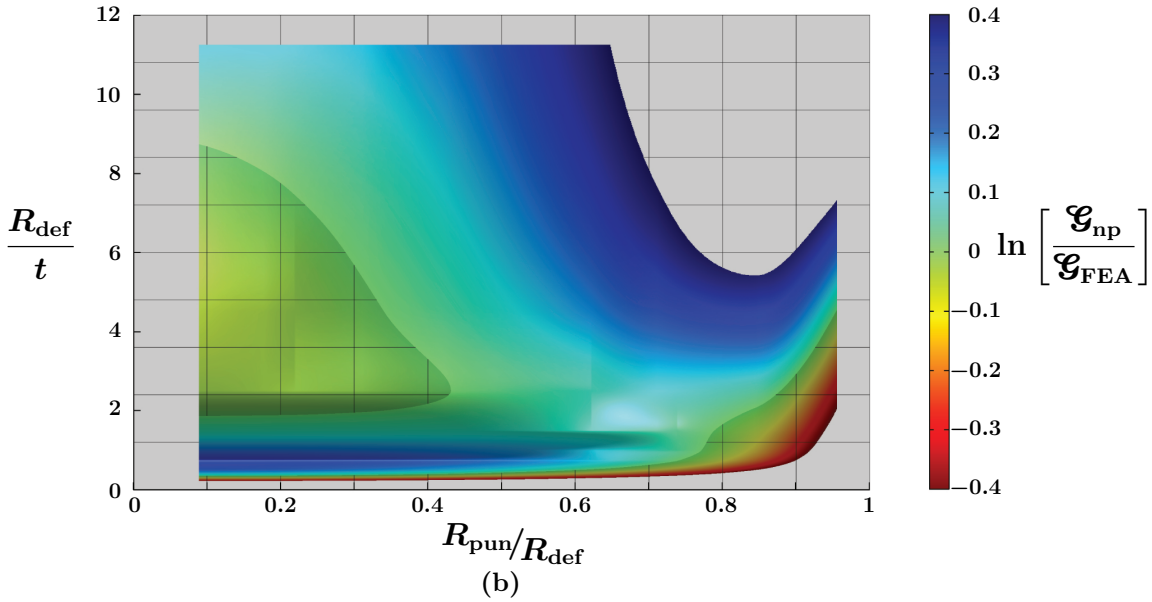

(b)

Figure 4.14: Range of validity of the analytical near-point load solution,
(a) Magnification of figure (4.13) to z-axis limits $-0.4 \leq z \leq 0.4$ (n. b.: $\frac{R_{\text{pun}}}{R_{\text{def}}}$ maximum at front corner of coordinate system)
(b) 2D visualisation of figure (4.14a)

The new proposed **annular line load** solution provides the largest region that yields valid results. Analytically related to the near-point load solution figure (4.15) shows a similar, yet closer fitting result compared to figure (4.13). The effect of large punch diameters that create problems in the near-point solution appears to be solved. The annular line load formulation predominantly underestimates the energy release rate, although on a small scale compared to the other analytical solutions presented. The valid range of variables can be read from figure (4.16b) and can be summarised as:

$$\begin{array}{ccc} \frac{R_{\text{def}}}{t} & & \frac{R_{\text{pun}}}{R_{\text{def}}} \\ 2 & & 0.1 \quad \cdots \quad 0.5 \\ \vdots & \leftrightarrow & \vdots \\ 11 & & 0.1 \quad \cdots \quad 0.7 \end{array}$$

In analogy to the near-point analytical solution, the annular line load expression loses validity for 'thick' plates with approximately $R_{\text{def}}/t < 1.7$.

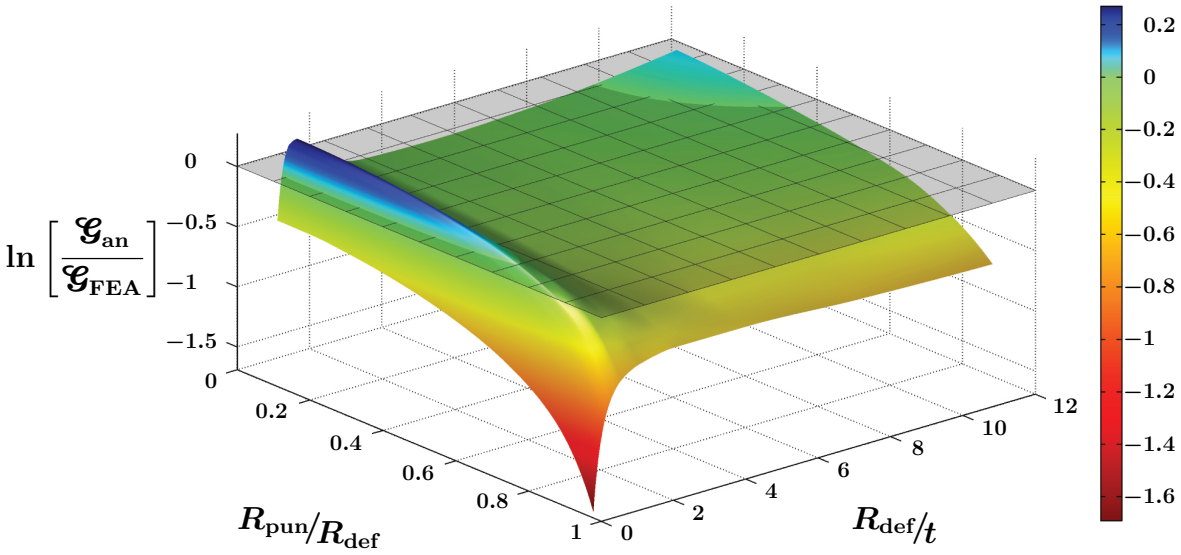

Figure 4.15: Range of validity of the analytical annular line load solution, as shown in equation (2.101), for an SLBT with flat punch along the variables of punch to defect radius ratio and defect radius to thickness ratio. Compared to FEA results. (n. b.: $\frac{R_{\text{pun}}}{R_{\text{def}}}$ maximum at front corner of coordinate system)

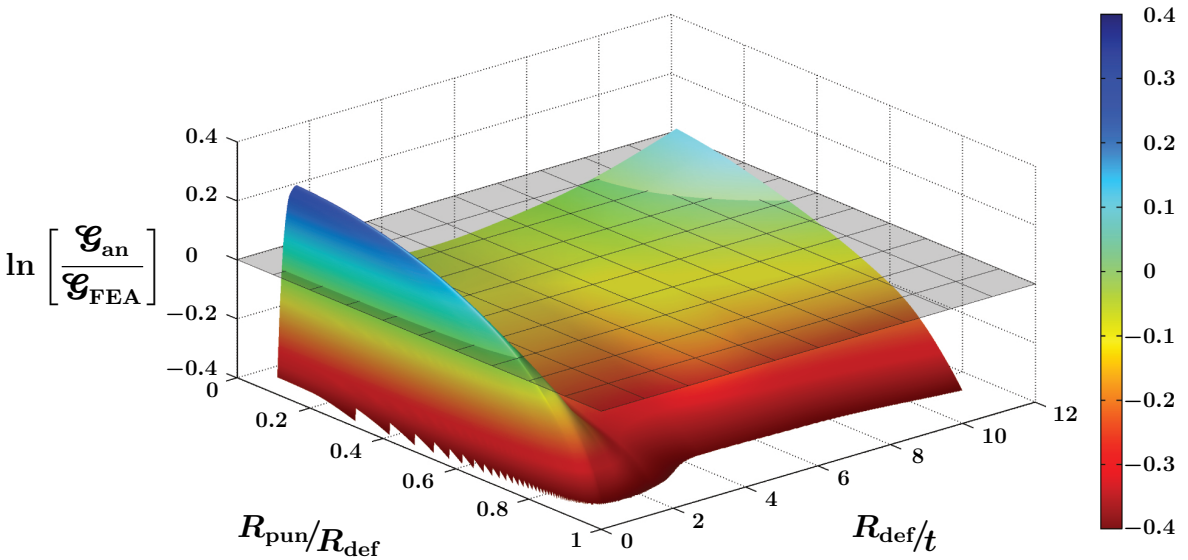

(a)

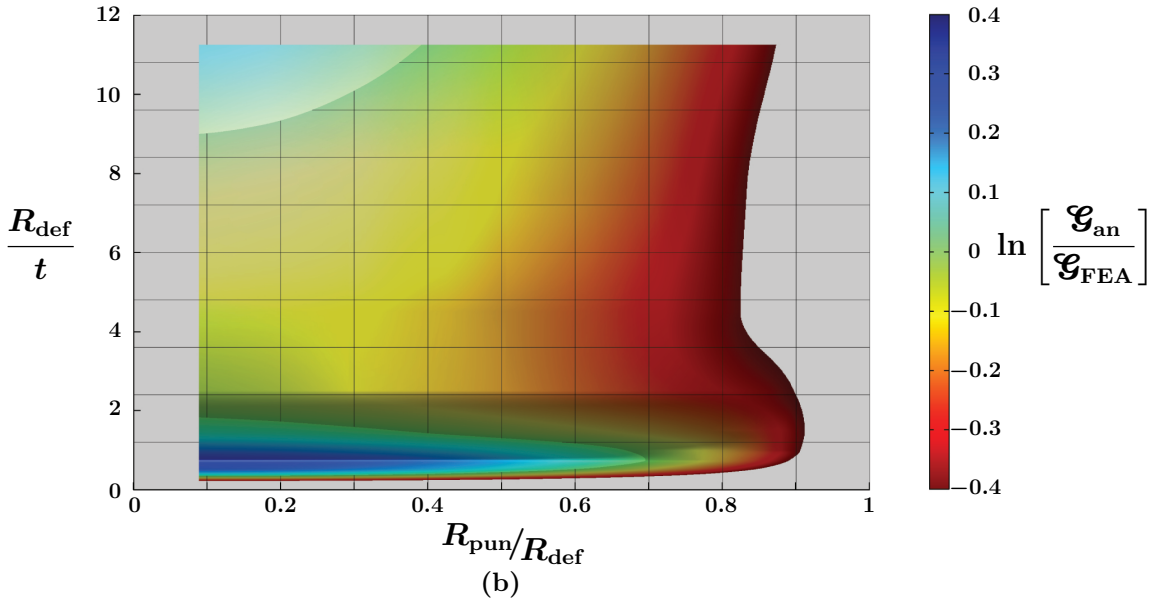

(b)

Figure 4.16: Range of validity of the analytical annular line load solution,
(a) Magnification of figure (4.15) to z-axis limits $-0.4 \leq z \leq 0.4$ (n. b.: $\frac{R_{pun}}{R_{def}}$ maximum at front corner of coordinate system)
(b) 2D visualisation of figure (4.16a)

4.4.2 *Experimental evaluation*

Diagrams with load against displacement curves are shown in figure (4.17) with two different radius to thickness ratios between (a) and (b). Measured pressures of four specimens are displayed as an example with each diagram containing two curves, one for each punch type. From figure (4.17a) and figure (4.17b) it becomes obvious, that a steeper increase in load and, at the point of failure, a sharper transition from linear-elastic bending to crack propagation is forced by a flat relative to a hemispherical punch head. After the crack initiation phase, both punch types result in nearly identical propagation in terms of propagation speed, load increase per propagation length and critical load.

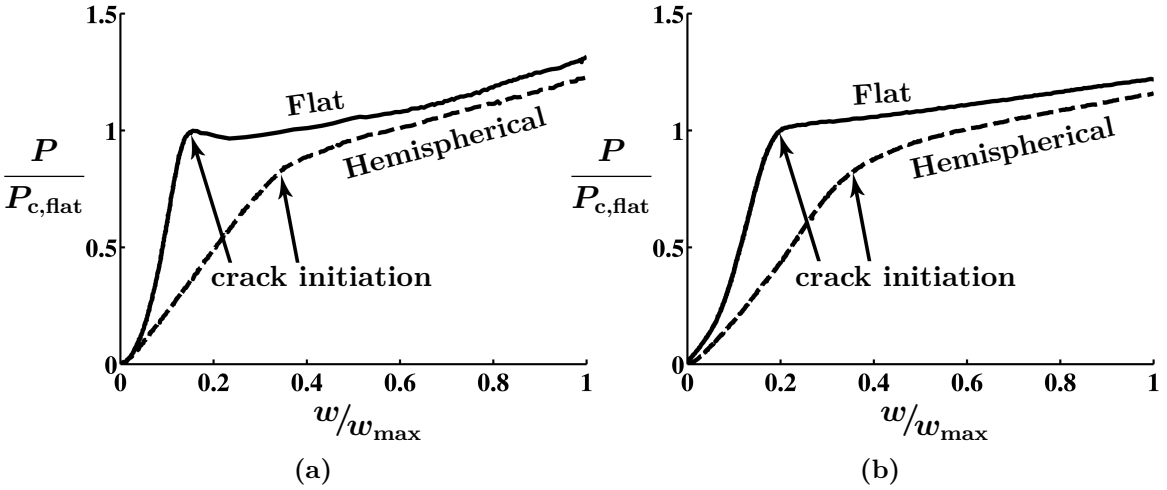

Figure 4.17: Measured load over displacement curves for SLBT specimens. Here, w is the displacement of the punch head and normalised over the maximum displacement of the test. The load P normalised over the critical crack initiation load of the specimen tested under load of a flat punch. While (a) and (b) are different in geometry, the graphs within each are the same geometry, but tested with a different type of punch.

Another distinction between flat and hemispherically capped punch heads is revealed in figure (4.18). The figures (4.18a) to (4.18d) are a comparison of specimens tested with hemispherical and flat punch heads with the respective 'virtual' equivalent of a fluid pressure blister test. Figure (4.18a) illustrates, that a hemispherical punch yields circa two times larger total energy release rates than the same amount of surface pressure. In contrast, flat punch loaded specimens, as shown in figure (4.18c), produce about a third of $\mathcal{G}_{\mathrm{T}}$ compared to the respective pressurised test configuration.

Differences can also be found in the proportion of mode I and mode-II fracture energy. Specimens of this study, which were tested with a hemispherical punch, yielded on average a 35 % $\mathcal{G}_{\mathrm{I}}$ fraction of $\mathcal{G}_{\mathrm{T}}$ (cf. fig. 4.18b). Pressure tested virtual

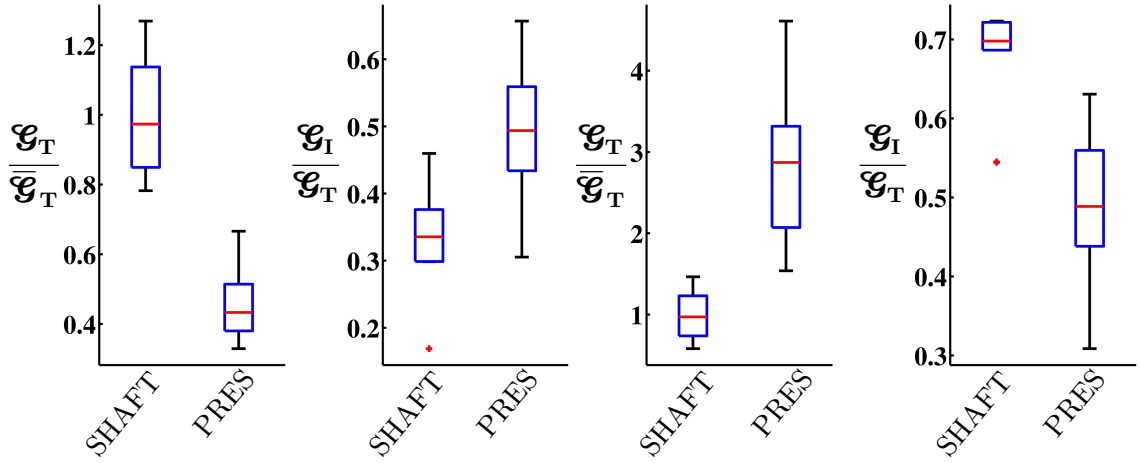

(a) Hemispherical **(b)** Hemispherical **(c)** Flat **(d)** Flat

Figure 4.18: $\mathcal{G}_T$ normalised over the mean $\overline{\mathcal{G}}_T$ of the SLBT (a, c) and the $\frac{\mathcal{G}_I}{\mathcal{G}_T}$ ratio between mode-I and $\mathcal{G}_T$ of the corresponding simulation (b, d) are plotted as comparison of actual shaft-loaded blister tests for hemispherical punch heads (a, b) and flat punch heads (d, c) against pressurised blister tests, obtained through FEA

specimens show a more even division into $\mathcal{G}_I$ and $\mathcal{G}_{II}$. Flat punch driven specimens, however, exhibit roughly the opposite ratio of the hemispherical punch tests. Here in figure (4.18d), $\mathcal{G}_I$ is on average 70 % of the total energy release rate.

4.5 SLBT discussion

The work presented showed substantial discrepancies in strain energy release rates between the two types of punch geometries and the pressurised blister tests. One reason for those discrepancies could be the ratio of $\mathcal{G}_{\mathrm{I}}$ and $\mathcal{G}_{\mathrm{II}}$. Inherent differences in the loading scenarios are likely to be the cause.

If assuming uniform surface pressure, the applied plate bending of the circular repair plate results in an additional membrane stretching or shear stress, depending on the plate thickness. The resulting deformations at the crack tip are similar in normal as well as tangential direction to the crack plane.

The load of a flat punch is applied through its edge onto the repair plate, because the bend repair plate rests on the punch head's edge, while lifting off from the punch head's top surface (cf. fig. 4.2b). With increasing punch diameter the load becomes increasingly dissimilar to a point load. Because the plate is mainly in contact with the punch head's edge, the loading is ideally mimicked by an annular line load.

For decreasing punch diameters, the energy release rate and its mode mix converges towards the expected result of an ideal point load. In this case the total energy release rate can be accurately determined through the 'load based' and the 'near-point' analytical solutions.

For larger size flat punches only the annular line load solution, which was developed throughout the study presented, approximates $\mathcal{G}_{\mathrm{T}}$ sufficiently. Increasing the radius leads to an increasingly dominant deflection normal to the crack plane at the crack tip, while the overall bending is comparatively moderate. Hence, the in-plane shear mode-II fracture energy is twice as large as $\mathcal{G}_{\mathrm{I}}$ for a small flat punch radius, but decreases non-linearly with increasing the radius. $\mathcal{G}_{\mathrm{I}}$ becomes larger than $\mathcal{G}_{\mathrm{II}}$ at a ratio of $R_{\mathrm{pun}}/R_{\mathrm{def}} > 0.9$.

Changing R_{def}/t affects the mode mix of specimens tested with a flat punch in a similar way to hemispherical punch heads. As expected 'thinner' repair plates lead to less transverse shear and higher normal in-plane loads and thus the $\mathcal{G}_{\mathrm{II}}$ proportion is larger.

Hemispherical punch heads are almost unaffected by a change in punch radius, which is assumed to be partly due to two effects. Loading a repair plate with a hemisphere results in a contact zone, which is dependent on the hemisphere's radius and the elasticity of the plate.

Apart from the theoretical case of infinitely stiff materials, a hemisphere allows the plate to mould around the hemisphere's contour. Therefore, a continuous 'surface pressure' is applied across the contact zone (cf. fig. 4.2a) and no part of the plate can lift off the punch as observed for a flat punch. However, this contact zone spreads over only a fraction of the punch area, so that an increasing punch radius

still results in a much smaller area under load. It can be assumed that with further increase of the radius of the hemisphere, the behaviour is going to match the flat punch results more closely as the punch heads' geometries are more similar.

Larger R_{def}/t ratios show the expected change in mode mix. The theoretical maximum defect radius over an infinitesimally small thickness would be described as a 'membrane' and thus only provide an in-plane normal load. As this load acts tangentially to the crack plane, the consequence would be a pure mode II fracture and $\mathcal{G}_{\text{I}}$ would vanish.

In general, the loading of a hemispherical punch is rather more similar to a pressurised repair plate than a flat punch loading. Despite the overall similarity, a fluid pressure acts on the whole surface including the crack tip and its vicinity. In reverse, a hemispherical punch head produces more tangential and less normal stress at the crack tip than a pressure. As a consequence, the differences in mode mix and $\mathcal{G}_{\text{T}}$ occur.

The fundamental dissimilarities in loading scenarios between the two types of punch heads as well as a fluid pressure are the root cause for the discrepancies presented, in terms of the magnitude of $\mathcal{G}_{\text{T}}$ and the mode mix ratio of $\mathcal{G}_{\text{I,II}}$.

Results presented in chapter 4.4 question the interchangeability of SLBTs for PBTs. At least the assumption of a direct compatibility for the total strain energy release rate between SLBTs and PBTs does not seem to be correct. Thus, a simple fracture criterion does not appear to be sufficient to compare SLBT fracture behaviour with PBTs. Further investigation in complex fracture criteria could overcome those limitations.

However, complex fracture criteria typically need to employ more precise information about critical stresses and critical fracture toughness or energy release rates for single mode fractures as well as knowledge about the stress field and the energy release rates of the mix mode failure of the actual test. This seems challenging for an SLBT, which is applied as a simplifying replacement for the PBT.

The investigated analytical solutions yield diverging results. For instance, the load based equation fits for small punch radii, and in particular for hemispherical punch head results. Since equation (2.62) does not contain any information about the displacement and radii, it is limited to application on scenarios similar to those of point loads on CPT type plates.

While the displacement based solution seems difficult to apply, the combination formulation of equation (2.64) has a wider field of application. However, because the influence of the displacement based exceeds the load based at nearly point load scenarios, its fit is inferior to the load based at small $R_{\text{pun}}/R_{\text{def}}$.

The near-point load analytical solution provides a comparatively good fit. Yet, it was possible to improve the solution through the annular line load formulation.

Its limitations are the least narrow of all other solutions, while providing a similar quality in areas where the other formulations show their best fits.

Chapter 5. Pressurised blister test (PBT)

5.1 Review of pressurised blister test research

Several techniques are commonly used to measure strain energy release rates (ERR). The interlaminar tension mode-I ERR, $\mathcal{G}_{\mathrm{I}}$, can be measured with a double cantilever beam (DCB) test, the interlaminar sliding shear mode-II, $\mathcal{G}_{\mathrm{II}}$, with an end notched flexure (ENF) test and combinations of both modes can be obtained through a single leg bending (SLB) or a mixed-mode bending (MMB) test (cf. chap. 2.2). All these methods test long, flat, rectangular specimens.

In contrast, this study proposes a way of measuring the mixed-mode ERR for an axis-symmetric specimen, in order to mimic actual corrosion defects more closely. For the evaluation of FRP-metal bi-material specimens, a pressurised blister test (PBT) was chosen in this study.

First introduced by Dannenberg [296], different pressure blister tests were developed, which differ substantially from each other. The Dannenberg [296] test comprised a slot defect in order to obtain an oblong shape blister, while using mercury to pressurise the film. Williams [170] presented the first circular pressurised blister test, developed an analytical expression for plane stress/strain and axisymmetric blister forming and set them in relation to the 'penny-shaped' crack of Sneddon [54]. Williams and his colleagues extended the work by proposing a model considering the energy stored in the adhesive layer [297], described an approximate analysis for estimation of cohesive-adhesive failure [298] and an investigation in the transition between different plate thickness types [299]. Another study on adhesive and cohesive failure for thick epoxy plates under plain strain condition was carried out by Andrews and Stevenson [300] presenting analytical solutions for both cases. Cotterell and Chen [301] conducted an investigation in the transition zone between membrane and plate material elastic behaviour [302]. Jensen [303] investigated into the effect of the mode mixity for pressurised blister tests of thin-films and plates around the transition zone from membrane to plate behaviour.

Most publications investigated thin films, membranes and coatings, which was amongst others shown by [304, 305], who reviewed existing analytical solutions. For this reason, work was conducted on specification of non-linearities, plasticity [306], transitions between plate-membrane and bending-stretching [302] as well as resid-

ual stresses [263, 292]. For instance, Juss and Mertiny [307] assessed the adhesion between a polyurethane liner top layer on an epoxy resin substrate applying an elastic stretching analysis.

One typical challenge in PBTs is the unstable crack growth which allows for only one measurement [301]. Constrained blister tests (CBT) increase the control over the blister shape and the crack growth, although only applicable when testing thin films, membranes and coatings. Already Dannenberg [296] used a slotted groove to guide the propagation resulting in an oblong blister shape. Similar are island blister tests, first proposed by Allen and Senturia [308] and altered by Dillard and Bao [309] to a peninsula test. In an island or peninsula test cracks grow in a defined radial or longitudinal direction respectively. Both tests benefit from a reduced stress level in the film and therefore less plastic deformation throughout the test [310]. Another variant of a CBT comprises a vertical constraint of the blister deflection [311, 312]. The major advantages of this type of CBT are again a lower stress peak in the film as well as non-catastrophic crack growth. As CBTs require a more complex manufacturing process [313] and plastic deformation is no concern for thick and reinforced materials, additional constraints were assessed not to be required for the tests throughout the study presented.

An unconventional pressurised blister test was developed by Wan and Mai [314]. To achieve a stable crack growth the blister was pressurised by encapsulating a working gas of specific volume and pressure underneath the thin film. Lowering the external pressure allowed the blister to form and propagate. Figiel and Lauke [315] showed the difference in propagation between a stiff and a compliant polymer film for a PBT. Laser-induced blister tests were simulated with VCCT by [262] and measured with DIC by [316]. Little work was published on thick films [317]. Gent and Lewandowski [318] analysed the impact of different thicknesses, while later Briscoe and Panesar [319] summarised solutions for the ERR determination of infinitely thick to thin top layers.

A gap in the published research of blister tests seems to exists on the topic of thick and reinforced layers. This study aims to minimise this gap by investigating into pressure blister tests of composite repairs for steel substrates.

5.2 Pressurised blister test setup

The specimens were made by laminating a fibre reinforced polymer (FRP) composite as repair on top of a steel substrate with a defect (cf. chap. 5.3). Load was applied by water pressure from the substrate side. The data obtained was used for comparison against the analytical solution provided by the standard. The key for the ERR analysis is the volume, which grows underneath the specimen. Analytically this is shown in chapter 2 and chapter 2.4. Studies were published on the meas-

urement of blister deformation and propagation, but the majority of these studies investigated in unreinforced thin films and membranes. A review of shaft-loaded blister tests was carried out and is presented in chapter 4.2. The published research on pressurised blister tests was reviewed and a summary is given in chapter 5.1. Analogous to the DCB, ENF, SLB and MMB tests the measurements were often carried out with a single camera recording the crack propagation. The thin films, therefore, had to be translucent enough for the crack propagation to be visualised.

Compared to the proposed method of uniform fluid pressure on an opaque, thick, FRP plate, the published research differs substantially in methodology, analysis and results as shown in chapters 4.2 and 5.1. Consequently, a novel method to measure the ERR had to be developed. A single camera recording the crack propagation was considered insufficient, because (a) the composite repairs are often too opaque to see the crack propagating and (b) the compliance of the total system in combination with the brittle behaviour lead to an abrupt and catastrophic failure. As a result, crack propagation could not be utilised and instead the deflection and volume of the blister was chosen. The critical ERR was assumed to be a function of the maximum load and maximum volume before failure. To the best of our knowledge, this study is the first to measure the critical ERR for this combination of specimen type and loading.

The water pressure was applied by a piston-cylinder rig. A standard strength testing machine was driving the piston to compress the water in the cylinder, connected through a short pipe with the rig holding the specimen. A more detailed description of the test setup is given in chapter 5.4.

Several challenges were associated with the actual volume measurement. Trials to measure the blister volume from the displacement of the piston proved difficult, because of the compliance of the overall system and the comparatively small magnitude of the blister volume. Furthermore, the repair's bottom surface could not be accessed, due to the design of the pressure application. Hence, an assumption had

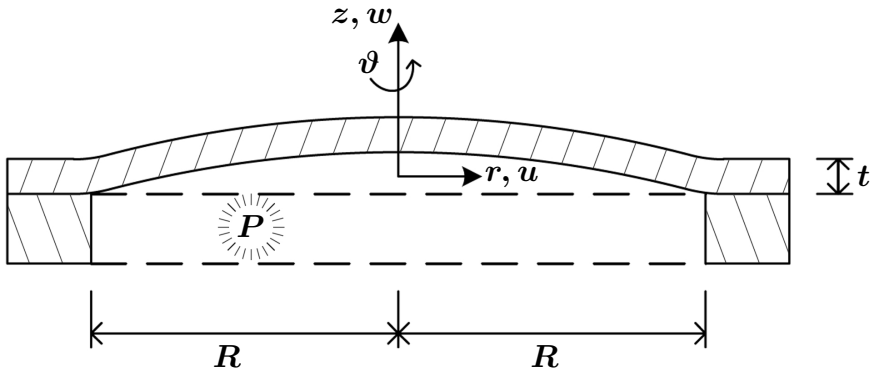

Figure 5.1: Diagram of blister formation under fluid pressure

to be made that the outer surface sufficiently reflects the deformation of the inner, pressurised surface. Otherwise, measuring the maximum deflection of the blister, without further knowledge of the blister shape, would have required the calculation of the ERR through an analytical solution. This would have led to matching two dependent variables, when comparing the results of measurement and analytical solution. Hence, a different method to measure the volume of the blister was required.

The non-contact deformation and strain measurement method of 3 dimensional digital image correlation (3D DIC) was identified as a suitable alternative to measure the deflection of the repairs top surface, which was linked to the blister volume. Few studies have applied DIC on blister measurements and one study was identified, which evaluated the ERR [320]. Hailesilassie and Partl [320] evaluated the ERR of a pressurised blister under a orthotropic, polymer modified, bitumen membrane with 3D DIC. Despite using the volume and pressure to determine the ERR, the volume was only derived analytically through measuring the blister radii and maximum height. Grohs et al. [321] applied 3D DIC on a proton exchange membrane under pressure to measure applied stress. Fedorov et al. [316] created pressure in-between a metal substrate and a polymer coating with an infrared pulsed LASER until delamination occurred. Fedorov et al. monitored the stress-fields and relaxation of the ridge shaped blister with DIC.

The presented work was carried out using the Correlated Solutions software VIC-Snap for image capturing purposes and VIC-3D™ 2012 for the digital image correlation calculation.

5.3 Specimen manufacturing and material property evaluation

5.3.1 *Manufacturing Process*

Bi-material specimens used in the described test series were made of a composite repair bonded on top of circular metal substrates, which were made of ASTM A36 type steel. With a diameter of 170 mm and a thickness of 15 mm the steel substrates were designed to accommodate enough space for a blister above defects of various sizes and to withstand the applied pressure with little elastic deformation. Artificial defects were machined into the centre of the substrates. For through-hole defects an additional metal plug was necessary to seal the defect against penetrating resin throughout the repair manufacturing.

Surface preparation is important to improve the quality of a bond. In the present study the surface preparation was done in accordance with BS EN ISO 8501 [322] and SSPC–SP10/NACE No.2 [323]. The metal substrate was grid blas-

ted to a roughness of $R_z \geq 65\,\mu m$ to increase the bonding area. Grid blasting was followed by a thorough cleaning of the surface with compressed air and acetone. An additional treatment with silane was abandoned in order to reduce the number of variables in the test. However, surface treatments with primers or adhesion promoters, such as titanate, chlorinated polyolefin, silane or silica-coatings, can improve the quality of the bond, as it was shown in a number of studies [324–326]. An overview of coupling agents is provided by Abel [327] and Petrie [328].

Materials used for the repair were E-Glass, Kevlar 49 Aramid and Carbon HT fibres. Both, E-Glass and Kevlar 49, were available as bi-axial, non-crimp fabric, while Carbon HT was supplied as bi-axial, woven fabric. Cutouts of the fabric were made with a laser cutter. Quasi-isotropic (QI) and orthotropic (OT) layups were manufactured with WTR's Technowrap 2K epoxy resin system used as the polymer matrix. After a hand lamination process the repairs were compressed and left for a 24 h cure at room temperature, followed by 150 °C for 3 h to reach the full strength of the material. Excess resin was removed before the application of a speckle pattern.

White spray paint was applied in a thin layer as prime coating. Using a different type of nozzle, black speckles were carefully sprayed on. Figure (5.2) shows an example of a speckle pattern applied to a specimen in the top image. The middle figure presents the same speckle pattern in a magnified view of the pixel level and the binary image thereof shown below. Other methods of applying speckle patterns are powdering [329], stamping, lithography [329], printing [330] or painting [331]. It is without implication for the correlation, if black speckles are applied on a white background or vice versa.

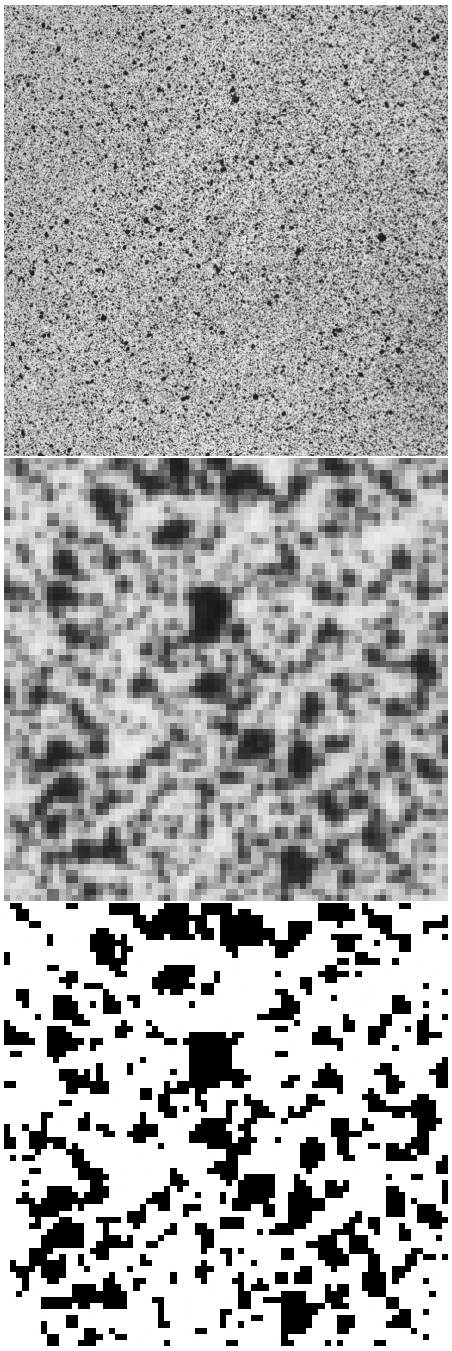

Figure 5.2: Speckle pattern applied on specimen (*top*), magnified to pixel level (*middle*) and reduced to binary (*bottom*)

More important for a good speckle pattern quality for DIC is a matt finish and a random speckle distribution with a high uniqueness in terms of size and shape. An increase in unique-

ness can be achieved by a higher contrast and larger speckles in relation to the subset size and therefore more pixel per speckle. However, more pixel representing larger speckles decreases the resolution as does a larger subset size. An increase in speckles in the pattern and a great variation in shape would result in a quality improvement [332].

Additionally, the recording situation determines the contrast and resolution and thereby also the ideal speckle size. Distance, zoom and aperture are important for the depth of field (DOF) (cf. chap. 5.4). Furthermore, the light situation in combination with the sensor type (here: 8-bit CCD) influences the ultimate quality of a speckle pattern. Insufficient or excessive light would result in an under- or over-exposed image. Due to this loss of information, measurement uncertainty of the correlation and errors would increase [333], while the accuracy would decrease.

Several statistical methods for speckle quality assessment were proposed over the past decade [334–338]. In this study the speckle quality was assessed through the intensity histogram and the confidence margin during test preparation. An adjustment of correlation and interpolation methods was carried out by means of a convergence study regarding the yielded volume during post-processing to evaluate the ideal calculation configuration. As an example figure (5.14) shows the convergence of the volume over an increasing subset size for different interpolation 'stiffnesses' in the volume calculation (cf. chap. 5.6).

5.3.2 *Material Analysis*

After testing, the composite repairs were analysed for their individual material properties. The fibre content and orientation of the laminate were known from the manufacturing process. In contrast, the amount of polymer varied for each repair plate according to the thickness. Consequentially, after a specimen was tested, the repair was fully detached to measure its thickness and weight. Knowledge of the repair dimensions was necessary for the derivation of the fibre volume fractions (ϕ).

Assuming standard properties for the employed fibre material, it was possible to calculate the properties of every single uni-directional (UD) ply with the rule of mixture (5.1) for fibre ($_\mathrm{f}$) and matrix ($_\mathrm{m}$). Within this rule it is assumed that fibre and matrix contribute to the overall modulus by mixing the individual moduli ($E_{\mathrm{f}\parallel}$, E_m) depending on ϕ [339, chap. 8]. The single ply's Young's modulus parallel to the fibre orientation ($E_\parallel$) can be approached as a parallel arrangement of springs (fibres and matrix) with different stiffnesses. On the contrary, the single ply's Young's modulus orthogonal to the fibre direction ($E_\perp$) can be seen as a serial alignment of springs.

Because the theoretical analytical solution of mixed transverse and shear moduli increasingly differs with higher fibre volume fractions compared to empirically ob-

tained material properties, the theoretical solutions were altered. The semi-empirical equations for the transverse Young's modulus (5.2) was adjusted according to Puck and Schürmann [340] and for the shear modulus (5.3) following the work of Förster and Knappe [341]. From the work of Foye [342], the single ply transverse Poisson's ratio ($\nu_{\perp\perp}$) for composites is corrected for the strain constraint of the matrix through the fibres (5.7).

$$E_{\parallel} = E_{\mathrm{f}\parallel} \cdot \phi + E_{\mathrm{m}} \cdot (1 - \phi) \tag{5.1}$$

$$E_{\perp} = \frac{E_{\mathrm{m}}}{1 - \nu_{\mathrm{m}}^2} \cdot \frac{1 + 0.85 \cdot \phi^2}{(1 - \phi)^{1.25} + \frac{E_{\mathrm{m}}}{(1 - \nu_{\mathrm{m}}^2) \cdot E_{\mathrm{f}\perp}}} \tag{5.2}$$

$$G_{\perp\parallel} = G_{\mathrm{m}} \cdot \frac{1 + 0.4 \cdot \phi^{0.5}}{(1 - \phi)^{1.45} + \frac{G_{\mathrm{m}}}{G_{\mathrm{f}\perp\parallel}}} \cdot \phi \tag{5.3}$$

$$G_{\perp\perp} = \frac{E_{\perp}}{2\,(1 + \nu_{\perp\perp})} \tag{5.4}$$

$$\frac{\nu_{\parallel\perp}}{E_{\perp}} = \frac{\nu_{\perp\parallel}}{E_{\parallel}} \tag{5.5}$$

$$\nu_{\perp\parallel} = \phi \cdot \nu_{\mathrm{f}\perp\parallel} + (1 - \phi) \cdot \nu_{\mathrm{m}} \tag{5.6}$$

$$\nu_{\perp\perp} = \phi \cdot \nu_{\mathrm{f},\perp\perp} + (1 - \phi)\, \nu_{\mathrm{m}} \left[\frac{1 + \nu_{\mathrm{m}} - \nu_{\perp\parallel} \frac{E_{\mathrm{m}}}{E_{\parallel}}}{1 - \nu_{\mathrm{m}}^2 + \nu_{\mathrm{m}} \cdot \nu_{\perp\parallel} \frac{E_{\mathrm{m}}}{E_{\parallel}}} \right] \tag{5.7}$$

This again leads into the calculation of the laminate properties through the *classical laminate theory*. The CLT combines the stiffness of all layers with respect to the layer's orientation into one global laminate stiffness matrix ($[A]$), by assuming the layer stackup as a parallel arrangement. The engineering constants were derived (5.8) from the compliance matrix ($[A]^{-1}$).

Gibson [343] presented an extension of the CLT for the calculation of the through-thickness elastic constants of laminates. This novel method overcomes the CLT's weakness in estimating the material properties of thick laminates and laminates with transverse anisotropic plies. The solutions for orthotropic (OT) and quasi-isotropic (QI) under the assumption of transverse isotropy of the single UD ply were applied in this study and are shown in equations (5.9) to (5.15). In this study the CLT was not employed to calculate failure. The engineering moduli and Poisson's ratios were needed for the analytical solution of the volumes and the ERRs (as described

in chapter 2.4) as well as the FE analysis.

$$E_{\mathrm{x}} = \frac{1}{(A^{-1})_{11} \cdot t} \; ; \qquad E_{\mathrm{y}} = \frac{1}{(A^{-1})_{22} \cdot t} \; ; \qquad G_{\mathrm{xy}} = \frac{1}{(A^{-1})_{66} \cdot t}$$
$$\nu_{\mathrm{xy}} = \frac{-(A^{-1})_{12}}{(A^{-1})_{22}} \; ; \qquad \nu_{\mathrm{yx}} = \frac{-(A^{-1})_{12}}{(A^{-1})_{11}} \tag{5.8}$$

Orthotropic laminates:

$$\begin{aligned} \nu_{\mathrm{xz,OT}} = \quad & \phi_0 \frac{\nu_{\parallel\perp}\left(1-\nu_{\perp\parallel}\nu_{\mathrm{xy}}\right)+\nu_{\perp\perp}\left(\nu_{\parallel\perp}-\nu_{\mathrm{xy}}\right)}{1-\nu_{\parallel\perp}\nu_{\perp\parallel}} \\ & + \phi_{90} \frac{\nu_{\parallel\perp}\left(\nu_{\perp\parallel}-\nu_{\mathrm{xy}}\right)+\nu_{\perp\perp}\left(1-\nu_{\parallel\perp}\nu_{\mathrm{xy}}\right)}{1-\nu_{\parallel\perp}\nu_{\perp\parallel}} \end{aligned} \tag{5.9}$$

$$\begin{aligned} \nu_{\mathrm{yz,OT}} = \quad & \phi_0 \frac{\nu_{\parallel\perp}\left(\nu_{\perp\parallel}-\nu_{\mathrm{yx}}\right)+\nu_{\perp\perp}\left(1-\nu_{\parallel\perp}\nu_{\mathrm{yx}}\right)}{1-\nu_{\parallel\perp}\nu_{\perp\parallel}} \\ & + \phi_{90} \frac{\nu_{\parallel\perp}\left(1-\nu_{\perp\parallel}\nu_{\mathrm{yx}}\right)+\nu_{\perp\perp}\left(\nu_{\parallel\perp}-\nu_{\mathrm{yx}}\right)}{1-\nu_{\parallel\perp}\nu_{\perp\parallel}} \end{aligned} \tag{5.10}$$

$$\begin{aligned} E_{\mathrm{z,OT}} = \Bigg[& \frac{1}{E_\perp} - \frac{\nu_{\parallel\perp}^2}{E_\parallel} - \frac{\nu_{\perp\perp}^2}{E_\perp} + \phi_0 \left(\frac{\nu_{\parallel\perp}\nu_{\mathrm{xz}}}{E_{\mathrm{x}}} + \frac{\nu_{\perp\perp}\nu_{\mathrm{yz}}}{E_{\mathrm{y}}} \right) \\ & + \phi_{90} \left(\frac{\nu_{\parallel\perp}\nu_{\mathrm{yz}}}{E_{\mathrm{y}}} + \frac{\nu_{\perp\perp}\nu_{\mathrm{xz}}}{E_{\mathrm{x}}} \right) \Bigg]^{-1} \end{aligned} \tag{5.11}$$

$$G_{\mathrm{xz,OT}} = \left(\frac{\phi_0}{G_{\parallel\perp}} + \frac{\phi_{90}}{G_{\perp\perp}} \right)^{-1} \qquad G_{\mathrm{yz,OT}} = \left(\frac{\phi_0}{G_{\perp\perp}} + \frac{\phi_{90}}{G_{\parallel\perp}} \right)^{-1} \tag{5.12}$$

Quasi-isotropic laminates:

$$\nu_{\mathrm{xz,QI}} = \frac{(1-\nu_{\mathrm{xy}})\left[\nu_{\parallel\perp}\left(1+\nu_{\perp\parallel}\right)+\nu_{\perp\perp}\left(1+\nu_{\parallel\perp}\right)\right]}{1-\nu_{\parallel\perp}\nu_{\perp\parallel}} \tag{5.13}$$

$$E_{\mathrm{z,QI}} = \left(\frac{1}{E_\perp} - \frac{\nu_{\parallel\perp}^2}{E_\parallel} - \frac{\nu_{\perp\perp}^2}{E_\perp} + \frac{\nu_{\mathrm{xz}}}{2E_{\mathrm{x}}}\left(\nu_{\parallel\perp}+\nu_{\perp\perp}\right) \right)^{-1} \tag{5.14}$$

$$G_{\mathrm{xz,OT}} = G_{\mathrm{yz,OT}} = 2\left(\frac{1}{G_{\parallel\perp}} + \frac{1}{G_{\perp\perp}} \right)^{-1} \tag{5.15}$$

5.4 DIC test setup

For the DIC composite repair blow-off test a specimen, which was prepared as described in chapter 5.3, was clamped in a test rig. While the top side of the

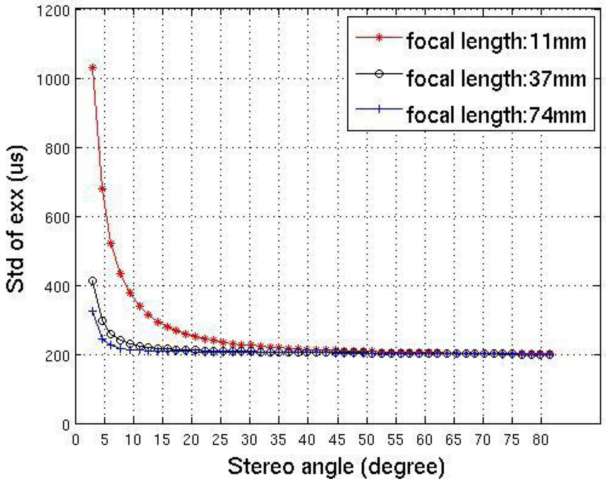

Figure 5.3: Dependence of the magnitude of error on the stereo angle for three different lenses; [344]

rig was open to allow for stereo imaging, the bottom side was connected to water pressure. Additionally, a vent was integrated to allow for breathing trapped air out of the system. The water pressure was applied by a piston-cylinder compressor, which was driven by a standard strength testing machine. Because a single camera is limited to detecting 2 dimensional in-plane deformations, a stereo system had to be set up.

It is possible to build a single camera stereo system through complex optical instruments, such as a combination of rotating and/or fixed mirrors [345]. Because of the increased complexity of a single-lens stereo system and ultimately the decrease in resolution, a conventional two-camera stereo system was chosen. A pressure transducer recorded the load acting on the repair. The chosen camera, AVT Pike F-421B [346], featured a CCD progressive sensor with a resolution of 2048×2048 px and a maximum frame rate of 16 Hz with a maximum bit depth of 14 bit for A/D conversion.

The cameras were operated at an aperture size of $f12$ and an exposure time of around 20 ms with a recording speed of 5 Hz. The sensor was set to an 8 bit digitisation. As one test took several minutes until failure, this recording speed was considered fast enough to gain a sufficient resolution over time. The load increase of the strength testing machine varied between 2.5–5 kN/min, depending on the thickness of the laminate. The system was set up with a 30° angle between the cameras and at a distance of approximately 200 mm to the specimen. With an angle of 25° as lower limit for 3D measurements (fig. 5.3), an increase in angle reduces the width b_{DOF} of the focused area [347].

In photography, the area of acceptable sharpness is denominated as depth of field (DOF). The combination of the DOFs of two cameras with an angle $180° > \gamma > 0°$ results in a rhombus. The depth d_{c} of a single camera depends on the lens, the

sensor, the aperture and the focal length. The width b_{DOF} and the depth d_{DOF} of the combined DOF is explained in figure (5.4) and equations (5.16) to (5.19). While the width b_{DOF} is important to focus on an area sufficiently large to record the full diameter of the blister, the deflection of the blister must lie within the depth d_{DOF}.

$$\lim_{\gamma \to 180°} d_{\mathrm{DOF}} \nearrow \infty \quad \Rightarrow \quad b_{\mathrm{DOF}} \searrow d_{\mathrm{c}} \tag{5.16}$$

$$\lim_{\gamma \to 0°} d_{\mathrm{DOF}} \searrow d_{\mathrm{c}} \quad \Rightarrow \quad b_{\mathrm{DOF}} \nearrow \infty \tag{5.17}$$

$$d_{\mathrm{DOF}} = d_{\mathrm{c}} \cos(\alpha)^{-1} \tag{5.18}$$

$$b_{\mathrm{DOF}} = d_{\mathrm{DOF}} \frac{\sin(\beta)}{\cos(\alpha)} \tag{5.19}$$

Two computers collected the data simultaneously. Computer one was dedicated to operate the cameras and save the images, using the software VIC-Snap. The software from Correlated Solutions features calibration, camera control and image recording capabilities as well as external analogue signal reading. One signal channel was interpreted as an analogue trigger.

Computer two read the pressure and the cross head displacement. It also sent out an analogue trigger and ramp signal to computer one, while reading the signals by itself. A rectangular function built the analogue trigger signal, which was translated by computer one in a trigger signal for the cameras. A sawtooth wave with 1.5 V/min increase running from $-10\,\mathrm{V} \rightarrow +10\,\mathrm{V}$ was used as ramp signal. All operations of

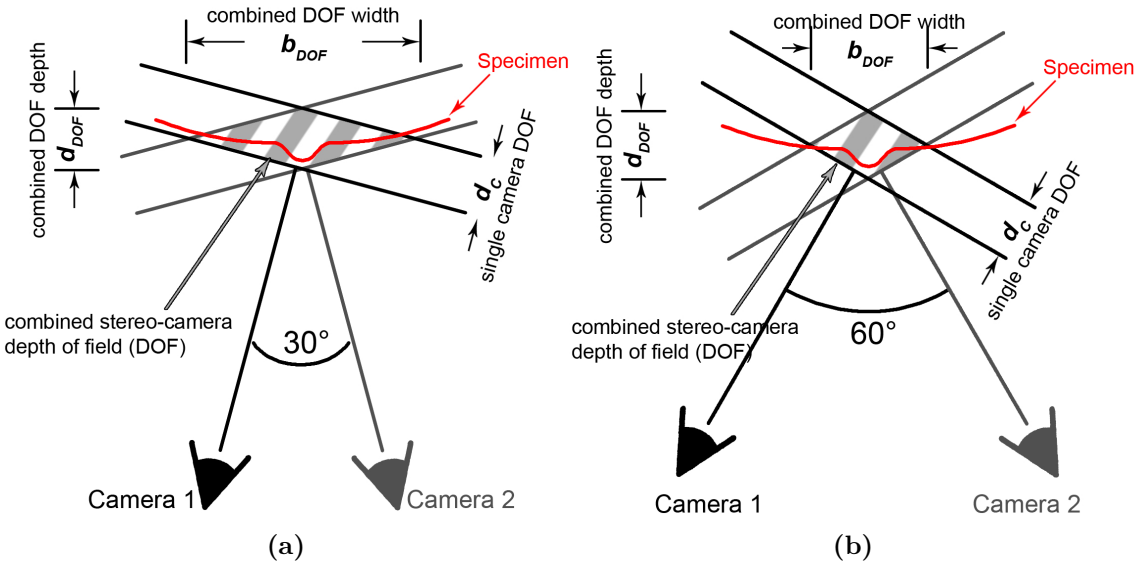

Figure 5.4: DOFs of two single cameras and the combination thereof resulting in the rhombus shaped DOF of the stereo-camera system for (a) 30° and (b) 60° stereo angle

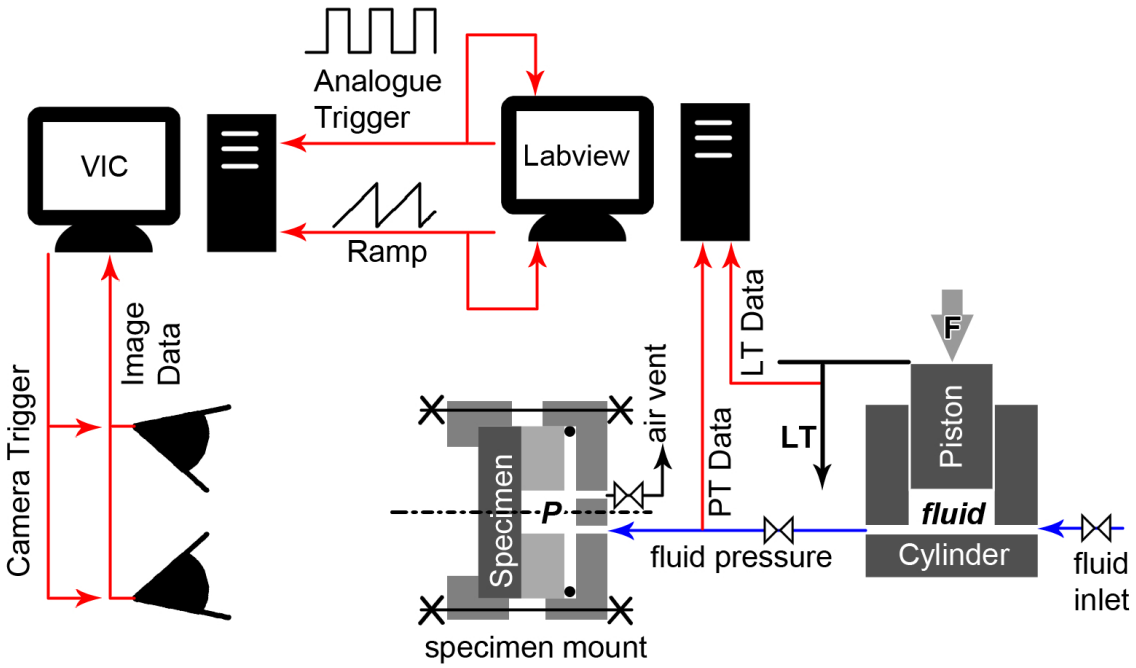

Figure 5.5: Diagram of test setup, (PT: pressure transducer, LT: linear transducer for cross-head displacement measurement)

computer two (i. e. reading and sending signals, timing and data management) were controlled by a LabView programme, which was developed for this study. Computer two was equipped for use with LabView with an NI cDAQ-9172 compact data acquisition system with two NI 9219 analogue input modules and one NI 9264 analogue output module from National Instruments.

Every image pair was automatically linked with a time stamp and all readings from the analogue signal inputs. Therefore, the ramp signal, recorded by both computers, connected the applied pressure with the corresponding images. Their speckle distribution were correlated to the first pair of images, which were made in a stress free state. Computation of deformation and strains from the images was done during postprocessing, described in chapter 5.6, after the test was finished.

5.5 Fundamentals of Digital Image Correlation

Digital image correlation (DIC) is a widely used method to measure deformation and strain [348, 349]. In a first of two assumptions for DIC the deformation of the material correlates to the change of a pattern of light intensity (i. e. grey scale values of a black and white speckle pattern) between two images, taken at different stress levels. Secondly a sufficient variation of contrast across each subregion is presumed to be achieved, in order to be able to identify point-pairs on the reference image and its dependent image to evaluate local deformations [350, chap. 20.2].

Digital images of CCD cameras supply one grey scale value for every discrete

pixel of the sensor matrix. However, in order to compare the reference image with a deformed image, a non-digital grey scale distribution over the pixel array is required. Typical methods to approximate values between the full integer coordinates are bi-linear, polynomial [351] and cubic b-spline interpolations [352]. Any interpolation introduces an error into the results. Similarly, an interpolation over the grey values between the known pixels imposes a phase error on the measured strain [353, chap. 5.6.1.]. The cubic b-spline is the least affected of the stated algorithms, though b-splines need to be corrected as well.

As interpolation filters can improve the error, optimised recursive pre-filters based on the b-spline transformation are applied on the b-spline interpolation [354]. Increasing the number of coefficients of the filter improves the interpolation at the expense of calculation effort. The present study utilised a cubic b-spline interpolation with an optimised 8-tap filter for minimal phase errors. Another benefit of higher-order b-spline filters is the improved amplitude attenuation of interpolations across noise [353, chap. 5.6.2.]. Recently, Crammond et al. [332] applied an edge detection detection, combining a Gaussian filter to reduce noise and a calculation of the second spatial derivative with the Laplacian operator followed by 2D alpha shape technique, that results in closed contours around detected speckles. This morphometric method improves the control of the recognition of patterns that otherwise can be difficult to analyse, for instance, because of little contrast in the grey levels.

Corresponding pixels in both images can be identified by comparison of a random pattern on the specimen, but the pattern must contain speckles of a high uniqueness. For an enhanced uniqueness an increased size, isotropic alignment, non repetitive, high contrast and random form of the speckles are important. Speckle areas of about $4 \times 4\,\mathrm{px}$ are a reasonable size, as speckles that are smaller require increased subset sizes in order to identify unique patterns. A description of the pattern application, which was employed throughout this study, is given in section 5.3.1.

Images are split in subsets to perform local searches for matching points between the pictures. Every subset correlation yields one data point. Therefore, being comparable to averaging over the subset area, an enlarged subset size decreases the spatial resolution. Smaller subsets are capable of detecting larger strain gradients, but can result in higher inaccuracies dependent on the speckle pattern [330, 336, 338] (cf. chap. 5.6). It is assumed that the deformation field in every subset is continuous [350, chap. 20.6]. A novel approach by Poissant and Barthelat [355] avoids discontinuities by automatic subset splitting, for instance enabling an easier measurement of crack openings.

Subsets are shifted in x- and y-direction along the image by the step width. Therefore, the total number of data points is dependent on the step width. The step width must be smaller than the subset dimensions for a sufficient overlap of the adjacent subsets.

Two subsets are compared through a cross-correlation (5.20), which is a standard measure to compare two signals at different points in time. In this case the two signals to correlate are the grey scale values of the images before (F) and after (G) deformation (fig. 5.6). VIC-3D provides three different correlation criteria: sum of squared differences (SSD), normalised sum of squared differences (NSSD) and zero-normalised sum of squared differences (ZNSSD). An overview of the different optimisation criteria can be found in Sutton et al. [353, chap. 5.4 and tab. 5.1] and Tong [356]. In this study the NSSD criterion was chosen (eq. 5.21), as it is unaffected by scale of light intensity and provides a higher convergence rate than the ZNSSD. The cost function $\chi_{\mathrm{NSSD}} = 1$ for perfectly matching patterns and $\chi_{\mathrm{NSSD}} = 0$ for mismatching patterns. Correlations are considered to be a match, if the cost function $\chi_{\mathrm{NSSD}} > 0.999$, while $\chi_{\mathrm{NSSD}} < 0.990$ are valued as a low quality match [350, chap. 20.6.1].

$$\chi^2_{\mathrm{NCC}} = \frac{\sum FG}{\sqrt{\sum F^2 \sum G^2}} \tag{5.20}$$

$$\chi^2_{\mathrm{NSSD}} = \sum \left(\frac{\sum FG}{\sum G^2} G - F \right)^2 \tag{5.21}$$

Several algorithms are commonly used to solve non-linear minimization problems, such as steepest descent (gradient search) [357, 358], Newton-Raphson [359, 360], coarse-fine [361] and more recently the Levenberg-Marquardt [362, 363] algorithms. To assist the iterative algorithms, a seed point has to be set by the user. The more accurate the initial guess of the unknown parameters of the algorithms, the faster and more accurate the algorithms will converge. The outdated integer displacement search for the initialisation of the parameters [364] was replaced by the more recent method of using optimised correlation coefficients [365]. However, the later developed method also assumes neighbouring points to be similar. Therefore, a seed point should be chosen in an area of little deformation to obtain an accurate set of initial parameters. A novel, automated, feature extraction method with usage of scale-invariant feature transformation (SIFT) could overcome those limitations in

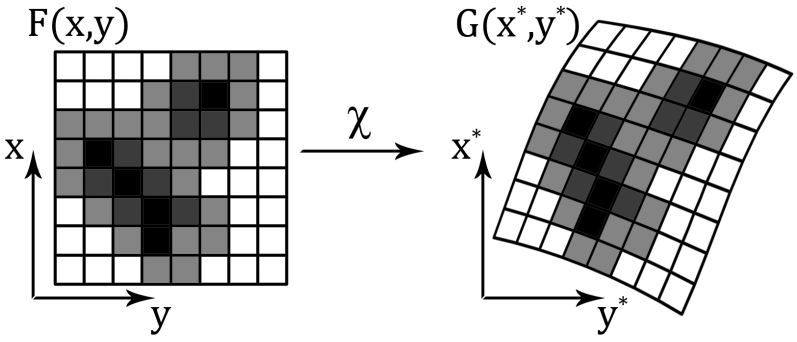

Figure 5.6: Mapping through correlation χ between speckle pattern before $F(x, y)$ and after $G(x^*, y^*)$ deformation.

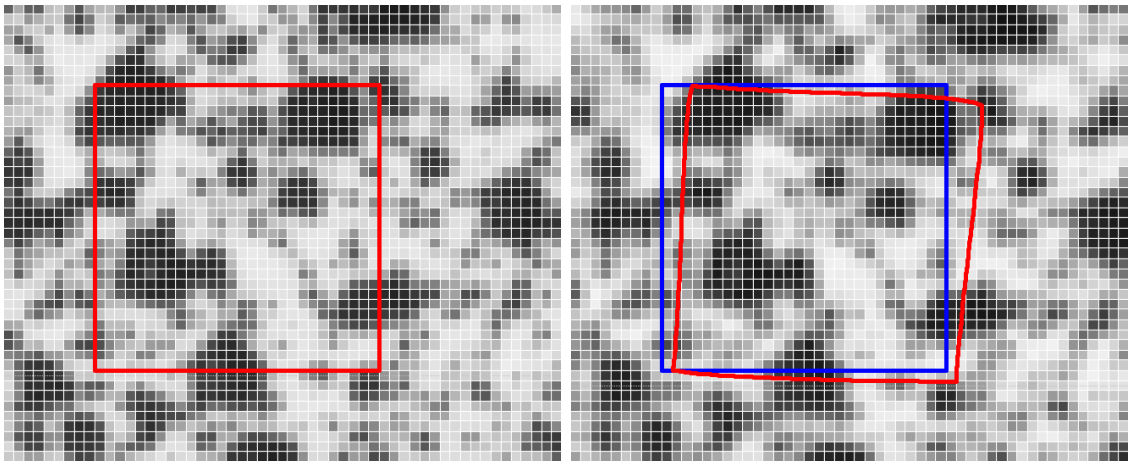

(a) **(b)**

Figure 5.7: a) Subset on image before deformation, b) Subset corrected with shape function (*red*) on image after deformation; image of actual applied speckles, numerical deformation for magnified illustration

the future [366].

Furthermore, the coordinate vector of the deformed subset has to be replaced by a shape function. Deformations can be composed of extension, compression, shear and rotation in all three dimensions. Consequentially, the specimen can undergo out-of-plane deformations as well as a level of general distortion, which leads to high residuals of the sum of squares χ for simple mapping algorithms. Applying subset shape functions, such as affine linear, polynomial (e. g. quadratic) for 2D or homographic for 3D DIC, into the matching algorithm adjusts the deformed subset's shape for a better match with the distorted image [367, 368]. Instead of copying the simple square of the reference subset, the deformed subset can become a complex distorted shape (fig. 5.7). An error from decorrelation can therefore be eliminated.

Additional smoothing can become necessary, if the data is superimposed by a high level of noise. The method applied was a 90 % centre-weighted Gaussian filter as decay filter over both; the locations z of the points and the displacements w. A smoothing algorithm is always applied on the result of the correlation and therefore on the data points of the subsets. Respectively, the diameter of the smoothing in pixels is the product of step size $\times$ filter size.

Sutton et al. [369] showed that out-of-plane translation and rotation can be measured with a stereo system without introducing measurable, full-field, strain errors. A two camera stereo-system was used for 3D DIC (cf. chap. 5.4). Instead of an independent camera calibration the full stereo-system was calibrated [350, chap. 20.9.1]. This leads to one camera being defined as the master and the other as the slave.

Cross-camera image matching is supported by the implementation of the 'epipolar constraint'. Any object point projected on the image planes in a stereo-vision is con-

strained through the epipolar constraint as shown in the diagram of figure (5.8). The epipolar lines are constructed by an intersection plane, which is spun between the object point and the two camera coordinate system origins, and the image planes. Hence, the cross-camera matching problem is reduced to a search along the epipolar baseline [353, chap. 4.2.2]. For the extension of 2D DIC to the third dimension the subsets of both cameras are matched with the same correlation processes as used for conventional 2D DIC. The utilised software VIC-3D 2012 first correlates the reference images of master and slave. Afterwards images from the master camera are matched with the master reference image and images from the slave camera are matched with the slave reference image. Later no further correlations between the cameras are made throughout the process.

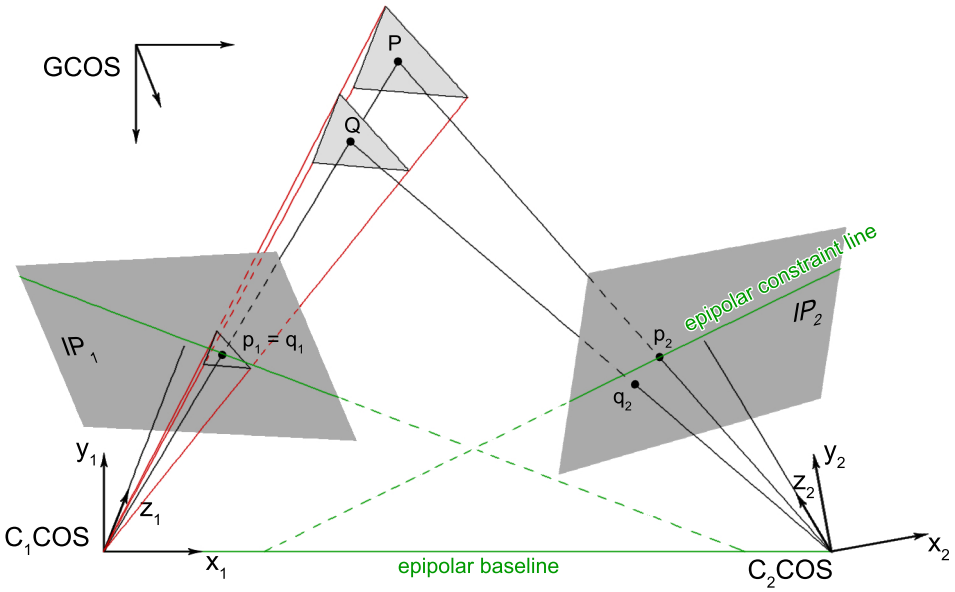

Figure 5.8: Two-camera stereo-system with global (GCOS) and camera coordinate systems ($C_{1,2}COS$), object (P, Q) and projection points ($p_{1,2}$, $q_{1,2}$) on image planes ($IP_{1,2}$) with epipolar baseline and constraint lines for point P

5.6 Postprocessing of DIC data

As a result of the measurement, two sets of image pairs had to be analysed per test. One of which was recorded for the calibration of the camera system, while the other one was generated throughout the test run. An excel file linked the images with their respective time and analogue channel readings. Correlated Solutions' VIC-3D software processed the camera calibration, calculated the deformations and strains before writing the results in MatLab output files. The post-processing of the x-, y- and z-deformation data of the stressed and unstressed situations was programmed in MatLab for this study and is described in the following paragraphs.

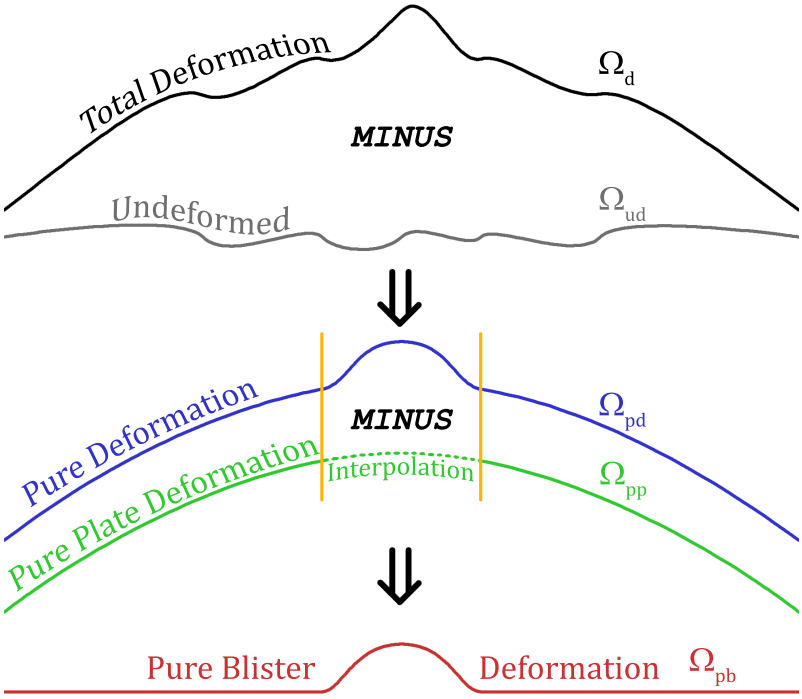

Figure 5.9: Process of determination of pure blister deformation from the total deformation.

During testing the repair plate surface is generally not ideally transverse to the axis of the camera system. Therefore, the deformation data of a plate contains a substantial proportion of deformation in x- and y-direction. Because it was required that the deflection was mainly described by a deformation in z-direction, the data set (Ω) was initially rotated around the x- and y-axis into the x–y plane (horizontal). Hereby, it was possible to reduce the deformed ($_d$, figure (5.11a)) with the undeformed state ($_{ud}$) to the pure deformation data ($_{pd}$, equation (5.22), figure (5.11b)) solely based on the deflection in z-direction. Disregarding surface asperities as a result allows for the main step, which is the separation of the pure deformation data into the pure plate bending displacement ($_{pp}$, figure (5.12b)) and the pure blister displacement ($_{pb}$, equation (5.23), figure (5.13)). This process is illustrated in figure (5.9).

$$\Omega_{pd} = \Omega_d - \Omega_{ud} \tag{5.22}$$

$$\Omega_{pb} = \Omega_{pd} - \Omega_{pp} \tag{5.23}$$

An automated iterative rotation was programmed to achieve a near-horizontal plane of the repair plate. The unstressed plate was the reference for the evaluation of the rotation angle for both data sets. Kurtosis and standard deviation of the z-value of the undeformed plate were the critical measure for the iteration. It was assumed that an ideally flat plate after rotation would lie perfectly in the x–y plane and therefore all z-values would be zero.

For the rotation's assessment, the kurtosis (γ) was used as a measure of the peakedness of the frequency distribution of z-values around a mean of zero (i. e. $\gamma \gg 0 \Rightarrow$ repair plate surface $\approx$ x–y plane). The standard deviation (STD, μ) was used as a complementary measure to summarise the variation of the z-values around a mean of zero with $\mu = 0$ indicating no variation (see histogram in figure (5.10)). Because errors occur around the edges of the measured surface, the STD was replaced with the inter-quartile range (IQR) to avoid their influence on the rotation.

The rotation angle, obtained by the iteration, was applied on both the deformed and undeformed plate. Another translational displacement of the pure deformation data was applied after rotation. The data was moved horizontally until the point of maximum blister deflection coincided with the centre of the investigated area. The most reliable method to determine the point of maximum blister deflection in the Ω_{pd} data set was the search for the maximum of the first principal strain (ε_1) of the blister. The point of maximum blister deflection became the new origin of the x–y plane, which guaranteed the blister to be sufficiently central inside the investigated blister area. The plate was then moved vertically, so that the z-mean of the full range of data points (subsequently referred to as 'nodes') coincided with the x–y plane.

Because of the limitation, that the cameras can only measure the outer surface of the repair, no direct data about the pure plate deformation was available. However, the repair plate deformation outside the defect area was assumed to cohere closely with the substrate deformation underneath. Furthermore, to obtain the blister volume the virtual substrate surface across the defect area had to be known. The virtual substrate deformation data was obtained by interpolating across the un-

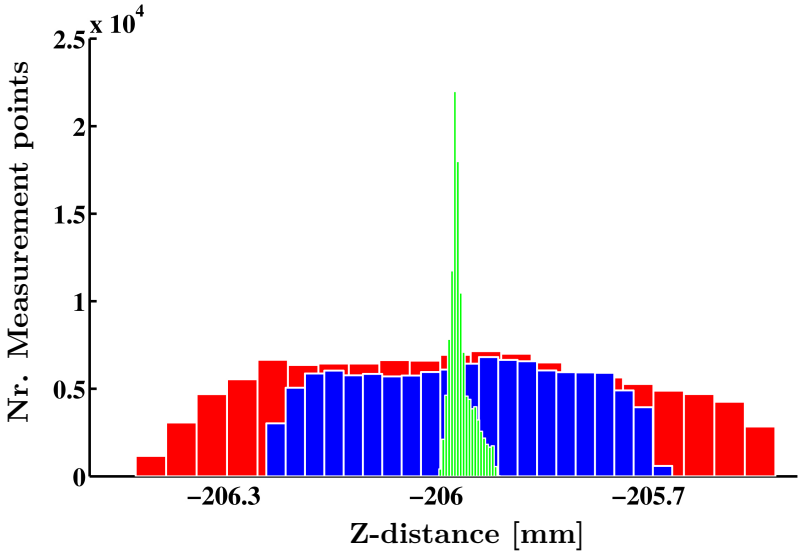

Figure 5.10: Change of distribution of z-distance between the measured points and the camera origin of one plate; (*red*) original, (*blue*) rotated around x-axis, then (*green*) rotated around y-axis

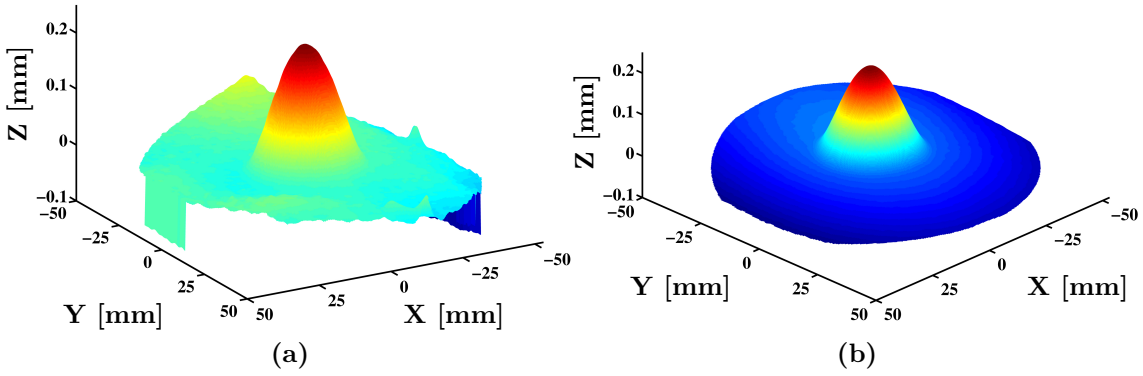

Figure 5.11: (a) Rotated and translated, (b) Deformed plate after subtraction of the undeformed state

known defect area with utilization of the deformation data outside the defect area as supporting points.

Hence, at first all of the data was disregarded across an area above the defect, which was chosen slightly wider than the defect area itself. Subsequently, numerical errors and measurement artefacts, in particular around the edges, were disregarded to increase the interpolation quality. All missing nodes were obtained by interpolating over the remaining ring shaped data set plotted in figure (5.12a) using the MatLab function 'gridfit' by D'Errico [370]. This function is based on the idea of an interpolating surface in the form of a plate with a certain stiffness and a force pulling the plate towards the nodes. The programme's description [370] of the interpolation is in parts adopted for this thesis to provide the reader with a brief overview of the interpolation algorithm.

The function applies a bi-linear method (also known as linear tensor product), which is widely used in digital image interpolation (e. g. [371, 372]). Bi-linear interpolations are the product of two linear functions and therefore non-linear themselves. An arbitrary point between four known points was interpolated by initially calcu-

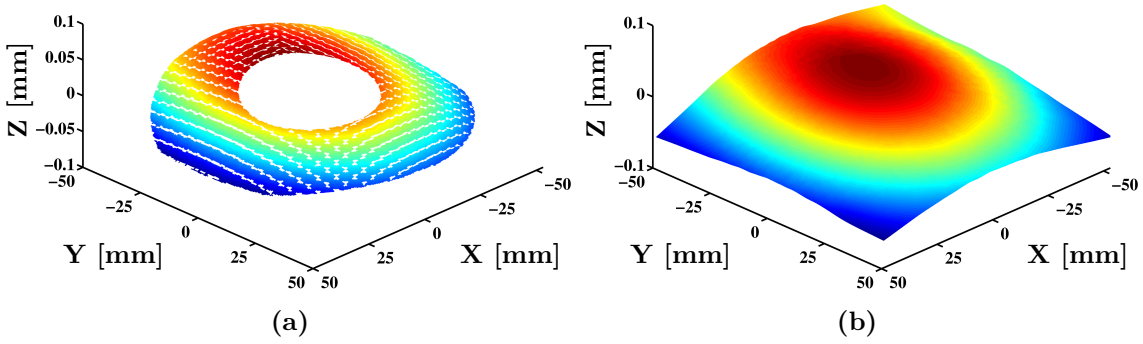

Figure 5.12: (a) Pure plate deformation excluding blister area as base for interpolation, (b) Interpolated pure plate deformation

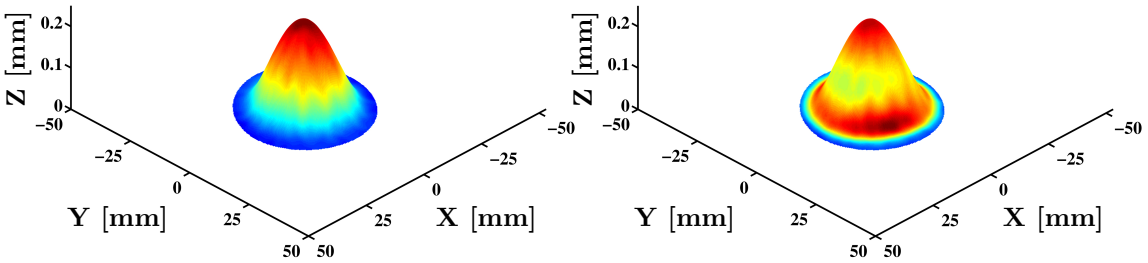

Figure 5.13: Pure blister deflection with superposed (a) principal strain ε_1 and (b) von Mises strain

lating the linear interpolation between the two sets of two known points in one coordinate direction. Subsequently, the two resulting interpolation points are the new set for the final interpolation in the second direction.

$$f(P_{I1}) = \frac{x_2 - x}{x_2 - x_1} f(P_{11}) + \frac{x - x_1}{x_2 - x_1} f(P_{21}) \tag{5.24}$$

$$f(P_{I2}) = \frac{x_2 - x}{x_2 - x_1} f(P_{12}) + \frac{x - x_1}{x_2 - x_1} f(P_{22}) \tag{5.25}$$

$$f(Q) = \frac{y_2 - y}{y_2 - y_1} f(P_{I1}) + \frac{y - y_1}{y_2 - y_1} f(P_{I2}) \tag{5.26}$$

This can be generalised for the total data set as a linear algebraic problem of the form

$$Ax = y \tag{5.27}$$

with $x \in \mathbb{R}^n$ being a vector with the length of the number of grid nodes n. The matrix $A \in \mathbb{R}^{m \times n}$ has the same number of columns, but with rows $m \geq n$ equivalent to the nodes supplied by the original data set and corresponding to the vector of the supplied data points $y \in \mathbb{R}^m$. The amount of unknown grid nodes was higher than the number of given data nodes, leading to an 'ill-posed' equation. This problem can be determined with the search for the minimum of the Euclidian norm $\|\cdot\|$, also known as the approximate solution of the least-squares problem [373].

Additionally a method was applied to control the 'stiffness' of the solution and with it the smoothness of the result. It is expressed in another linear equation:

$$Bx = 0 \tag{5.28}$$

Both, equation (5.27) and equation (5.28), were combined and scaled, so that the matrices A and B have a unit 1-norm. Equation (5.29) is a version of the Tikhonov regularisation [374, 375]. Tikhonov extended the least-squares problem with a penalised method by the addition of a 'stiffness' factor κ and a regularisation operator $B \in \mathbb{R}^{p \times n}, p \leq n$ [cf. 373, eq. 1.3]. Smaller κ values allow for larger gradients,

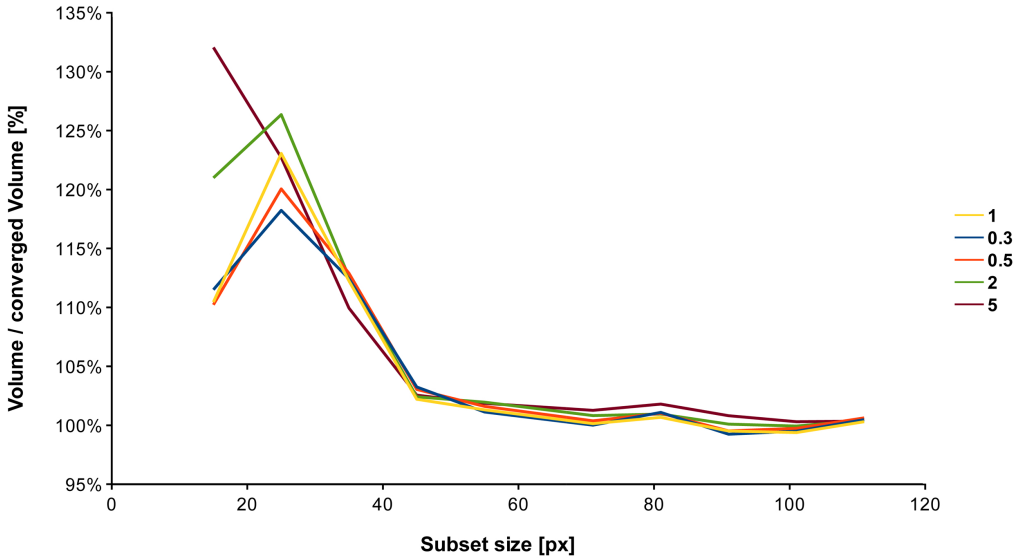

Figure 5.14: Change of volume by 'stiffness' κ variation of plate interpolation over subset size

i. e. the interpolation can follow smaller geometries, while larger κ yield a smoother surface. Deviating the 'stiffness' factor κ from the standard of 1 yields an increased difference in volume for smaller subset sizes as can be seen in figure (5.14). That is caused by a larger scatter of local deformations for calculations with smaller subsets.

$$\min_{x \in \mathbb{R}^n} \left\{ \|(Ax - y)\|^2 + \kappa \|Bx\|^2 \right\} \tag{5.29}$$

The selection of the subset size was carried out by evaluating the volume in regard to an increasing subset size (fig. 5.14). An image correlation with a small subset size contains more numerical inaccuracies [336] and therefore shows more artefacts and a rougher surface. This agrees with Pan et al. [376], who presented a similar approach to evaluate the ideal subset size based on the sum of squares of subset intensity gradients (SSSIG), and Sun and Pang [377], who introduced the concept of a subset entropy. Ultimately a subset size of 51×51 px was selected in this study.

The interpolated substrate deflection data was written in an x–y coordinate grid with strictly positive gradients in x- and y-coordinate direction. The spacing of the grid was obtained by averaging over each column or row for x- and y-coordinates respectively. Both x–y grids, the original DIC data and the interpolated, differed from each other. A triangular volume integration algorithm would have neglected the difference of position in the x–y plane between two corresponding nodes of pure deformation and pure plate bending. Thus, a computationally more expensive method was developed and applied to calculate the volume, as described in the following paragraphs.

Hexahedrons were build between the nodes of the blister and the virtual substrate surface, which sum up to the blister volume. A convex hexahedron with planar

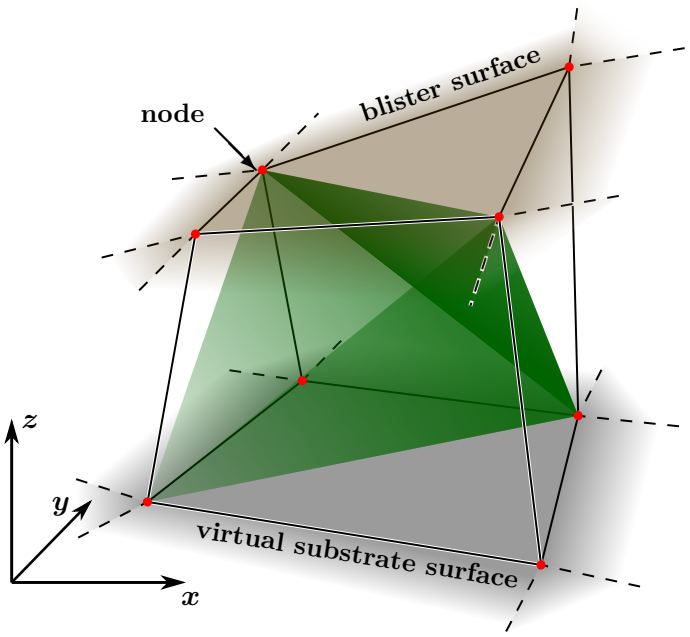

Figure 5.15: Hexahedron (*black wire frame*) spun between nodes on the two surfaces of blister and virtual substrate; one possible split for the 3D simplex (tetrahedron, *green*) shown inside

faces has an analytical and unique solution by splitting it up in five tetrahedrons as illustrated in figure (5.15). It is possible to split a hexahedron up in two different ways. If all faces are plane, the volumes of both possible splits are equal. However, the faces of the hexahedrons were not plane and the average of both splits had to be taken. The analytical solution for the volume of a 3-simplex (tetrahedron) can be written as

$$V = \frac{1}{6}\left|\det\left[\begin{pmatrix}\vec{a}\\ \vec{b}\\ \vec{c}\end{pmatrix}\right]\right| = \frac{1}{6}\left|(\vec{a}\times\vec{b})\cdot\vec{c}\right| \tag{5.30}$$

Hexahedrons can be self-intersecting or negative in volume around the edge of the blister. Being rather a numerical error than actual geometry the volumes of those hexahedrons were set to zero. In rare cases hexahedrons were concave, when the blister and virtual substrate surfaces were close to each other. Because equation (5.30) is limited to convex hexahedrons, a method had to be developed to generate convex out of concave hexahedrons. This method is presented for the 2D case in figure (5.16) and can be extended from concave tetragons to concave hexahedrons for 3D applications as described in the following paragraph.

In a first step the centre (P_{CG}) of all corner nodes (P_{C}) of the hexahedron was determined through the mean of all node coordinates.

$$P_{\mathrm{CG}} = \frac{\sum_{1}^{8} P_{\mathrm{C}}}{8} \tag{5.31}$$

The centre point was then made the centre of an auxiliary sphere, of which the radius

was larger than the maximum distance between the centre and the nodes. Naturally, every P_{C} of a hexahedron is linked through a vector with its three neighbouring P_{C}s. A vector addition of those three yields another vector, which was based on the P_{C} pointing away from the hexahedron towards the sphere. These vectors defined eight new nodes P_{S} on the sphere, so that every node P_{C} of the hexahedron has a mirrored node P_{S} on the sphere. Nodes from one hexahedron face combine for a new convex auxiliary hexahedron with their mirrored counter parts.

The mirrored nodes build a convex hexahedron themselves that encloses the concave and its auxiliary convex hexahedrons. The volumes of the enclosing and the auxiliary hexahedrons were obtained through the same process of splitting each hexahedron into its 3-simplex volumes as described in equation (5.30). Through the number of volume calculations alone, the computational effort was more than 8 times higher for a concave compared to a convex hexahedron. As only relatively few concave hexahedrons occurred, the additional total computation time was not substantially increased.

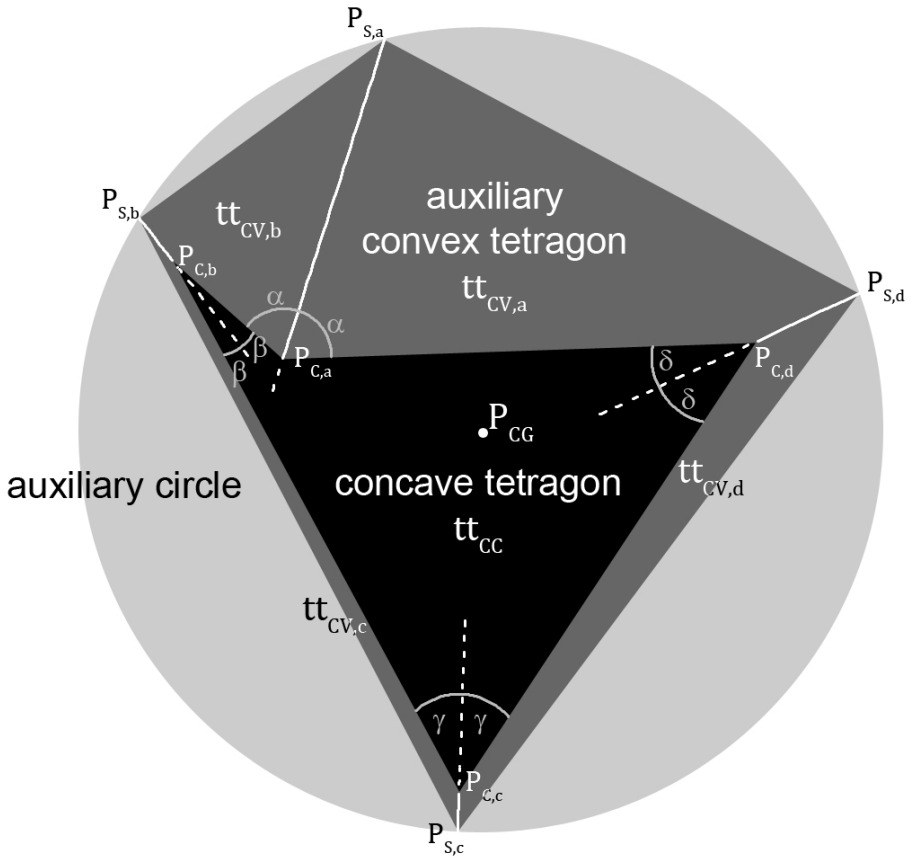

Figure 5.16: 2D illustration of the calculation of a concave ($_{\mathrm{CC}}$) tetragon tt_{CC} (*black tetragonal area*). Construction of four mirrored nodes $P_{\mathrm{S,a..d}}$ on auxiliary circle (*light grey circular area*), which become the nodes of one new enclosing, auxiliary, convex tetragon (*dark grey tetragonal area*), and construction of four auxiliar, convex ($_{\mathrm{CV}}$) tetragons $tt_{\mathrm{CV,a..d}}$ with two original nodes and two mirrored nodes each (e. g. $P_{\mathrm{C,a}}, P_{\mathrm{C,b}}, P_{\mathrm{S,a}}, P_{\mathrm{S,b}}$).

Subtracting the sum of volumes of the auxiliary hexahedrons (V_{aux}) from the volume of the enclosing hexahedrons (V_{enc}) resulted in the volume of the concave original hexahedron (V_{hex}) (5.32). All hexahedron volumes combined add up to the total blister volume (5.33).

$$V_{\text{hex}} = \sum V_{\text{enc}} - \sum V_{\text{aux}} \tag{5.32}$$

$$V_{\text{blister}} = \sum V_{\text{hex}} \tag{5.33}$$

5.7 DIC measurement results

The curve of the measured volume over the applied pressure, exemplary shown in figure (5.17), is in its shape analogue to stress-strain curves of brittle polymers like epoxy resins. A smaller and sharper plastic transition would be expected for a tensile test of composite materials. However, the larger plastic transition suggests that, as expected for a transversely loaded specimen, the matrix is dominant in the overall material behaviour in out-of-plane direction. A linear-elastic increase in volume is followed by a plastic transition until ultimately crack propagation occurs. The crack propagation itself was not recorded, because of the rapid and catastrophic nature of the propagation.

The point of crack propagation, marked with an '×', has proven to be less consistent throughout the range of tested specimens than the transition point between linear-elastic and plastic material behaviour. For this reason, the transition point

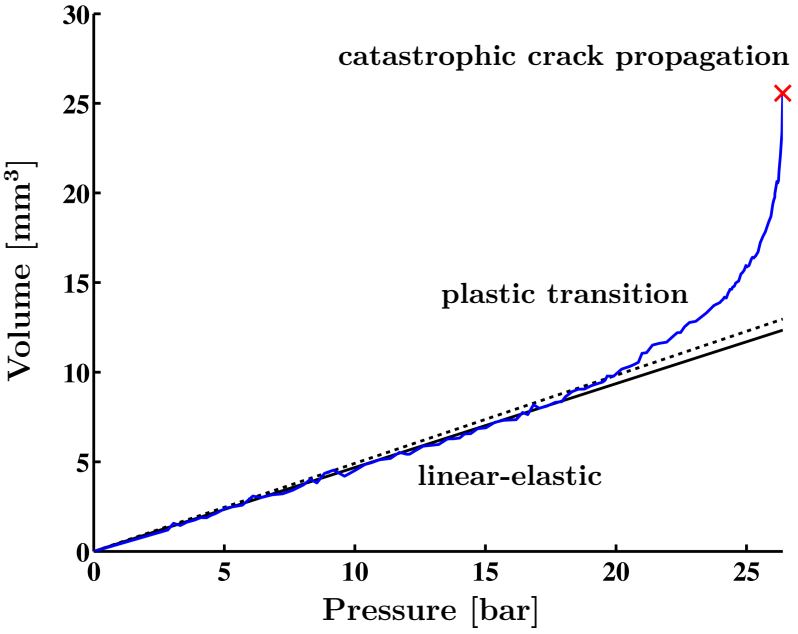

Figure 5.17: Measured blister volume for increasing pressure

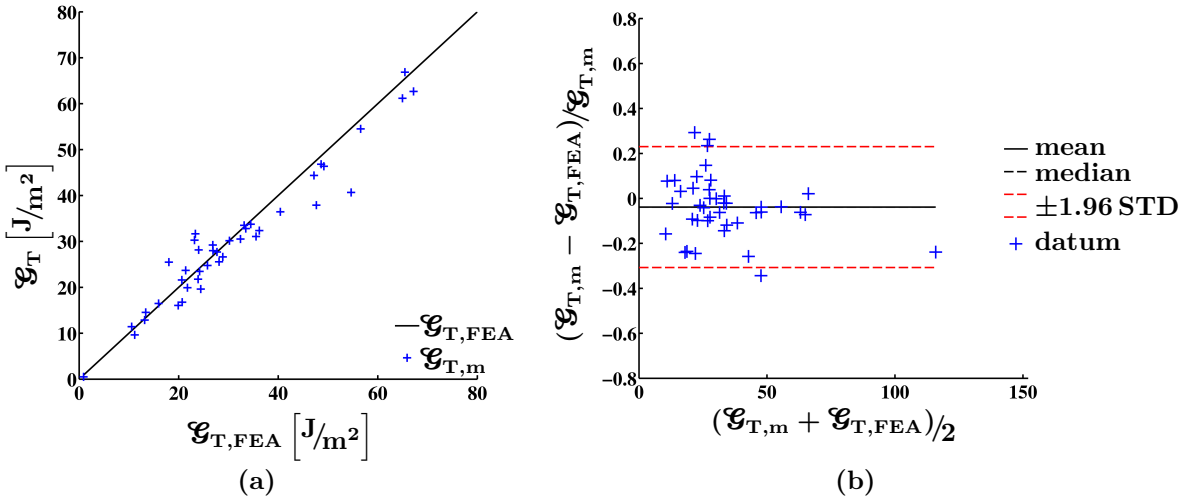

Figure 5.18: (a) Measured total ERR against the corresponding simulated ERR, (b) percentaged Bland-Altman plot: `STD=0.14, Kurt=3.33, Skw=0.23, Var=0.019`

was chosen as input for comparison with FEA simulations and analytical calculations. The transition point was determined by a search for the point, when the volume changed by more than 5 %. The linear interpolation line of the linear-elastic part and its 5 % deviation are plotted in figure (5.17) as solid and dotted lines respectively.

While the shown example of figure (5.17) was taken from the middle of all specimens in terms of generated volume, noise was more pronounced in measured curves of very small volumes. Smoothing algorithms, as described in chapter 5.5, were successfully applied on the correlation before the volume calculation for specimens with

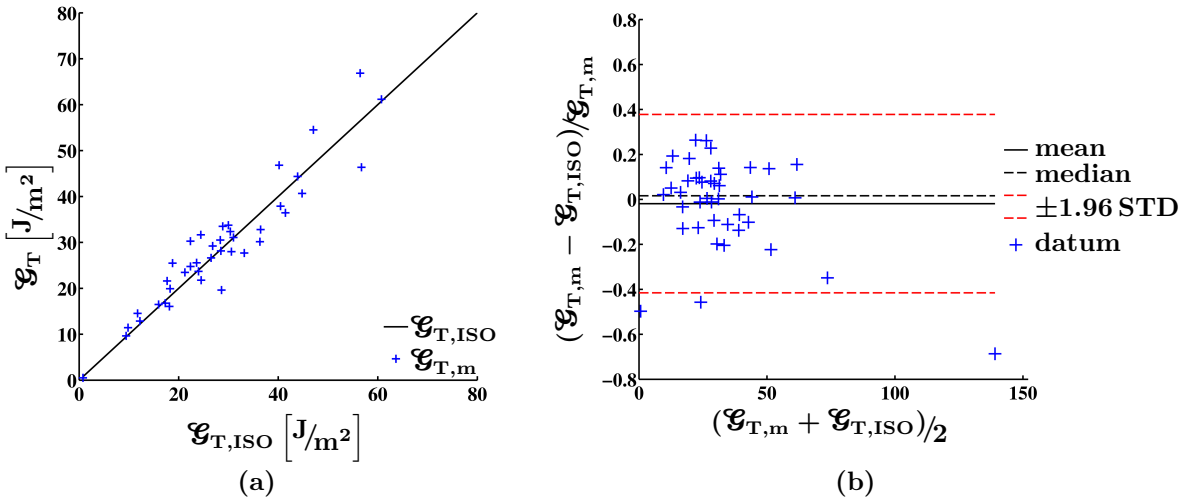

Figure 5.19: (a) Measured total ERR against the corresponding ERR from the standards solution, (b) percentaged Bland-Altman plot: `STD=0.20, Kurt=4.89, Skw=-1.33, Var=0.041`

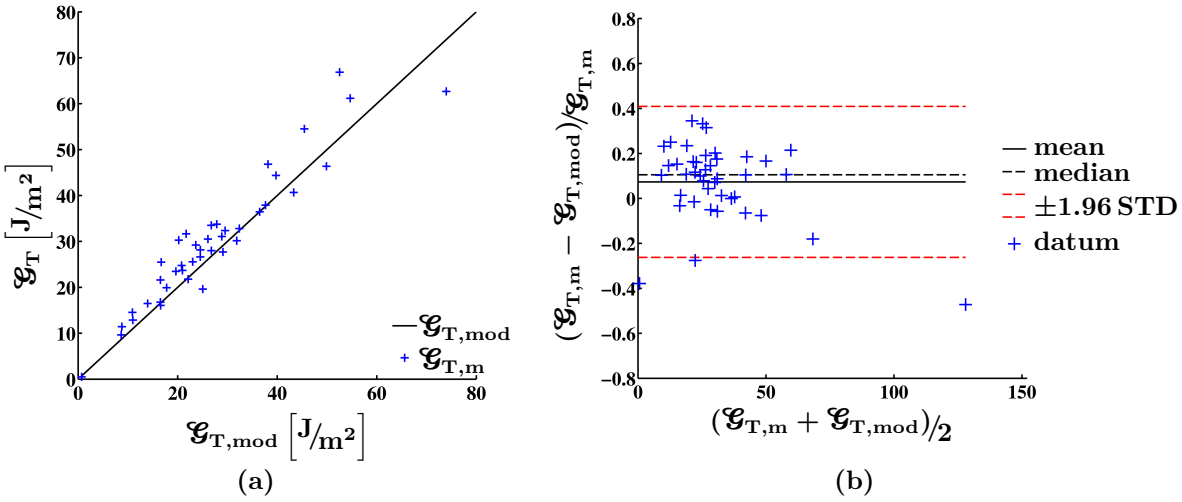

Figure 5.20: (a) Measured total ERR against the corresponding ERR from the modified standards solution, (b) percentaged Bland-Altman plot: `STD=0.17, Kurt=4.87, Skw=-1.22, Var=0.029`

a increased amount of noise. Typically, noise had to be erased from tests with small deformations as the noise to signal ratio on the measurement became too large.

The full set of data is plotted in the figures (5.18) to (5.20), each comparing the measured ERR to the FEA simulated or analytically obtained results. Figure (5.18a) displays the measured data plotted over its equivalent simulated result. The black diagonal line indicates an ideal fit and is therefore denoted as $\mathcal{G}_{T,FEA}$.

For further statistical analysis, the second diagram, figure (5.18b), shows a mean-difference plot, also known as Bland-Altman plot [378]. This type of plot is most practical to illustrate the difference between two measurement methods. Here, the

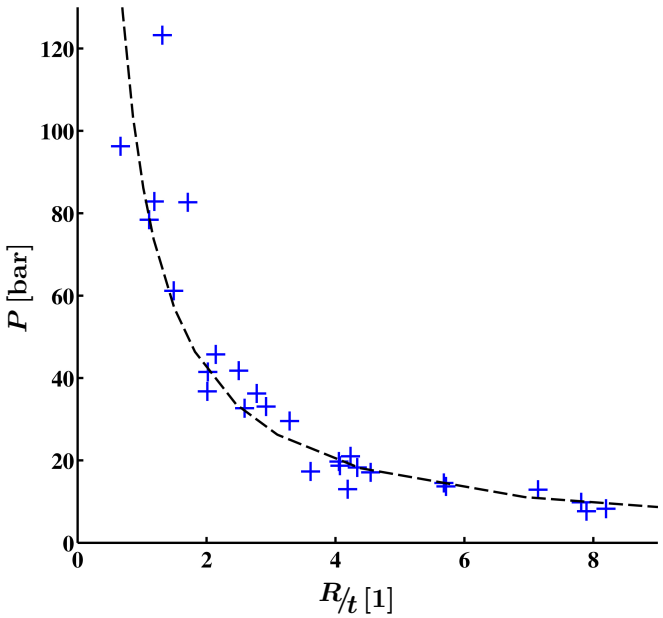

Figure 5.21: Measured critical pressure with respect to a change in geometry

plot type was modified to show instead the percentage of the difference being plotted over the mean. The modification implies that a y-axis value of 0.2 is equivalent to a 20 % difference between both methods. Bland-Altman plots are only valid for normal distributed data, which is true for all data sets presented, as can be understood from the mean and median being almost identical.

The comparison between the measured ERR and the total ERR from FEA simulation shows acceptable agreement. A linear correlation between both methods of ERR determination is found in figure (5.18a). Though the data is scattered, a normal distribution of the scatter is displayed in figure (5.18b) and the majority of data points lies within an approximately ±20 % difference with a standard deviation of about 0.137.

The results obtained through the analytical solutions from the standards and the modified solution appear similar as displayed in figures (5.19) and (5.20) respectively. Figure (5.19b) reveals that the analytical formulation from the standards yields the largest scatter with a standard deviation of about 0.202 with most data points lying within approximately ±30 %. Compared to the standards solution, the scatter is reduced for the modified standards solution to a standard deviation of about 0.171. However, the standard deviation from the FEA simulation, as presented in the paragraph above, is the smallest. Similarly, the variation for the modified standard lies in-between both. In contrast, the mean offset is larger than the other results.

The change of the measured critical pressure P_c is documented in figure (5.21)

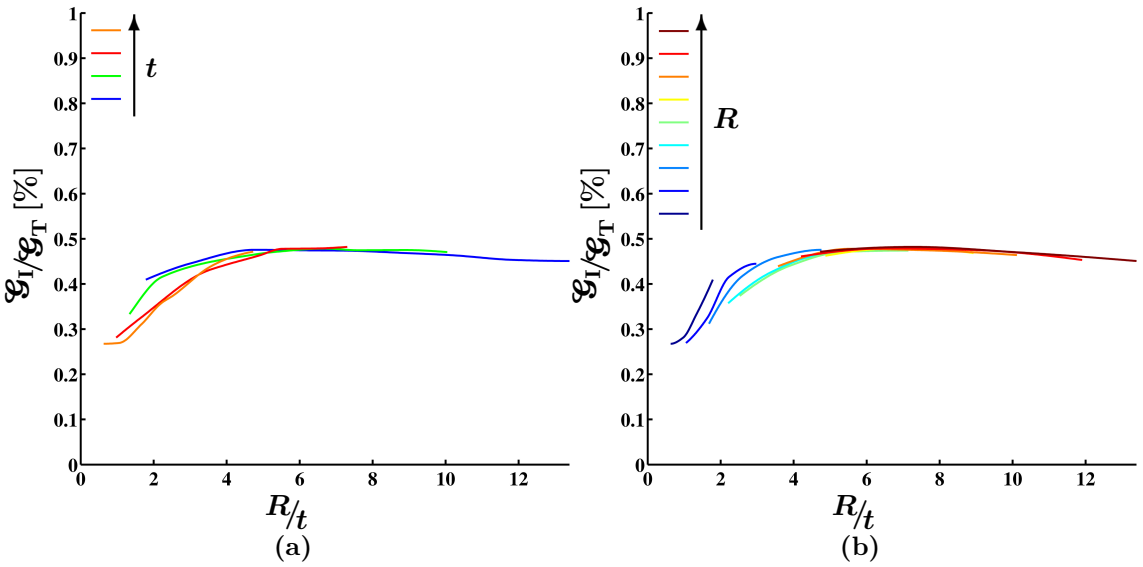

Figure 5.22: Influence of radius and thickness on the mode mix; Simulations undertaken with pressure calculated through the curve fitting function $f(R/t) = P_c$; Arrows indicate directions of increasing values

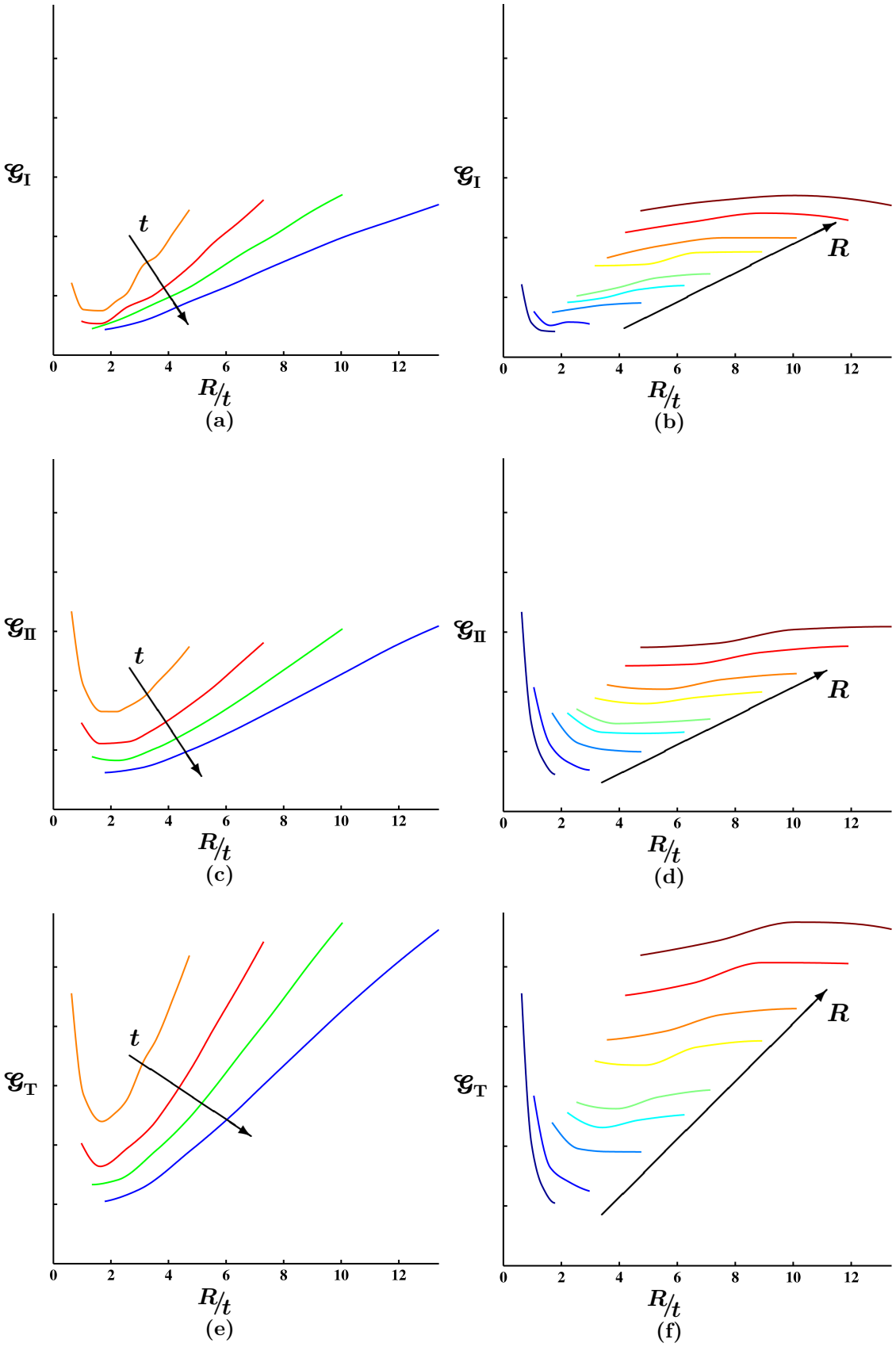

Figure 5.23: Influence of radius and thickness on $\mathcal{G}$; Simulations undertaken with pressure calculated through the curve fitting function $f(R/t) = P_{\mathrm{c}}$; Arrows indicate directions of increasing values

as a function of the geometry of the defect and repair. With smaller defect radius R or increasing repair thickness t the critical pressure increases hyperbolically. A curve fit of the function of the obtained data displayed in figure (5.21) was achieved through:

$$P_{\mathrm{c}}(R,t) = \left(95\left(\frac{R}{t}\right)^{-1.07} - 1.5\right)\,\mathrm{bar} \tag{5.34}$$

The mode-I and mode-II portion of the total ERR was obtained through a VCCT simulation displayed in figure (5.22). One set of material properties averaged from all quasi-isotropic glass fibre specimens was used for the simulation, which was run across a range of radii and thicknesses similar to those of the tested specimens. The failure pressure P_{c} was calculated with the function in equation (5.34). For larger R/t the mode mix converges at approximately 45 % of the total ERR for $\mathcal{G}_{\mathrm{I}}$.

The radius and the thickness impact the ERR in different ways. Figure (5.23) was derived from the same number of simulations presented in figure (5.22). It becomes clear that the change of the result is not going to be the same for an equivalent change of R or t. Therefore, different ERRs can be achieved for constant R/t.

5.8 DIC measurement discussion

In general, a measurement can be regarded as reasonable accurate, if the results are within about a ±15 % difference [379]. Aerospace applications, for instance, rely on a high reproducibility of the composite parts in terms of materials and manufacturing in order to achieve the desired material properties. In contrast to the highly controlled lab environments, which are needed to achieve high repeatability, composite repairs in the oil and gas industry have to be applied in the field under often harsh and demanding conditions. As a result, the usual requirements for such applications focus more on long-term reliability and easy manufacturing, but less on high-end, highly stiff and strong lightweight constructions. Surface preparation, fibre volume fractions, fibre orientations, pollution and matrix gas content are some of the factors that are important for a high quality composite part, which are difficult to control in a rough environment like oil and gas production. Therefore, a relatively high scatter in quality must be assumed and safety factors must be chosen accordingly. Some of the scatter can be recognised in the preceding section in figures containing measured data such as figure (5.21) on the variation of the critical pressure in comparison to the fitted curve.

The results presented from the DIC measurements, the FEA simulation and the two analytical solutions show acceptable agreement. As expected, the FEA simulations cohered closest with the measured data. The encountered scatter of ±20 % is reasonable for oil and gas composite parts. It proves that FEA simulations under

usage of the VCCT are valid, yet the boundary conditions need careful consideration. Consequentially, it is possible to obtain the ERR of a PBT through FEA without the need of analytical solutions. Additionally, VCCT simulations provide the ratio between the different fracture modes. It was shown in figure (5.22) that at least for $R/t > 3$ an approximated $\mathcal{G}_{\mathrm{I}}/\mathcal{G}_{\mathrm{T}} \approx 0.40\text{-}0.45$ can be assumed.

Simulating actual tests with FEA and the VCCT yields more accurate results than employing analytical equations. Yet, because the analytical solutions investigated agree with the measured ERR within the presented limits, it seems sensible to calculate the ERR analytically with an additional safety factor, to account for the inaccuracies of the analytical formulations and the fluctuation in repair quality.

Although the measured curves of the volume over pressure show a pronounced part of plastic deformation, the pressure increase throughout the plastic deformation is comparatively small. It appears to be a feasible option to simulate or calculate specimens with the recorded failure pressure, without the extra expenditure of a DIC measurement. An average reduction factor could be applied on the failure pressure to account for the plastic deformation.

Furthermore, it was shown in chapter 2.4 that the ERR formulation of the standards can be improved by correcting the shear term. In the standards the ERR formulation (2.102) is treated like a design criterion using $\mathcal{G}_{\mathrm{Tc}}$ against failure through interface fracture. The study of the influence of R and t on the ERRs indicates that the simple fracture criterion of a critical ERR, as proposed in the ASME and ISO standards and discussed in chapter 2.4, is not sufficient. In contrast to the failure pressure, it is impossible to find one curve describing the critical total ERR. The development of a criterion for one defined geometry could help to obtain a standardised ERR.

It can be concluded that digital image correlation is a feasible method to track the volume building underneath a blister. The ERR can be derived from the volume with a simple equation and yields results similar to those of the analytical solution and the VCCT, which proves the validity of all three independent methods. In future work, DIC measurements could be improved by implementing the recently presented approach by Zhou et al. [380] of using adaptive translational subset offsets. Benefiting from all subset points coinciding with full integer points in the image, induced errors from interpolations can be avoided. Another advancement would be the adoption of the development by Cofaru et al. [381] of a method for adaptive variable subset shapes, overcoming limitations imposed by constant rectangular shaped subsets used in current DIC software. Both, which are not yet implemented in the software used for this study, are going to offer lower measurement errors in later releases.

In the case that no precise information about the fracture mode mix is needed,

analytical solutions can be adopted, especially if a more complex measurement method like the DIC is assessed as too expensive. The VCCT increases the understanding with more accurate results and the added information about the different fracture modes at the cost of additional FEA simulation time.

Chapter 6. Comparison of SLBT, PBT and analytical solution

6.1 General summary

The study presented had the aim to improve the understanding of the interface fracture between composite repair and metal substrate in blister tests of repairs against leaking oil and gas pipes. The standards of ASME [2] and ISO [1] provide formulations and procedures for the evaluation of failure scenarios outlined above. These formulations and procedures were reviewed within this study and the investigations presented led to changes and new developments being proposed in order to improve the existing standards.

For this purpose, shaft- and pressure loaded blister test methods have been evaluated for their viability for the qualification of repair systems. Literature was found presenting research on typically unreinforced thin plates or membranes as top layers bonded on an infinitely stiff substrate, but a gap in research published was identified about thick plates and fibre-reinforced specimens. With composite repairs of pressured pipes as the application under investigation, this study focused on thick, fibre-reinforced laminates as top layers resembling composite repairs. Circular sharp-edged defects were assumed and primarily quasi-isotropic glass fibre-reinforced epoxies were used as repair material.

Accurate analytical solutions were established to provide cost and time efficient tools for the determination of energy release rates (ERR). The validity of existing and novel developed analytical expressions for shaft-loaded blister tests (SLBT) and pressure blister tests (PBT) was evaluated. As a consequence, the best formulation for a test with a hemispherical punch (SLBT-H) was identified, a new equation for the calculation of the ERR for a flat punch test (SLBT-F) was derived and the shear term of the ERR formulation of the standards for PBTs was corrected.

Two types of FEA simulations were performed for comparison with the analytical solutions. The first simulation employed was the new development of the pressure-volume method (PVM). It was designed as a simple method to simulate the ERR without the need to implement complex fracture simulations in the programme. The second and more sophisticated simulation method was the virtual crack closure technique (VCCT). Yet, the VCCT was the main simulation method used, because

of its advantages over the PVM in terms of universality of application and the capability of distinction of fracture modes. Both methods were explained in detail and a comprehensive review of alternative simulation techniques was presented.

Additionally, a programme was written in order to automate the generation of input files, the batch running of the FEA and the post-processing and evaluation of the data obtained. The automation allowed for a large number of simulations across an array of different variables to be performed. From this extensive data set it was possible to show the impact of shaft, repair and defect geometries on the resulting ERR.

To verify the FEA simulations, specimens were tested with SLBT-F, SLBT-H and PBT for various defect sizes, repair thicknesses and materials. A novel method was introduced, using digital image correlation, to measure and track the volume and pressure in a PBT. The data was subsequently used to calculate the ERR and, to the best of the author's knowledge, it represents the only published direct way of measuring the ERR with a PBT and is one of only few works published utilising digital image correlation (DIC) to measure a blister volume. A software programme was written for the numerical post-processing of the DIC data and the main procedures are described in detail in this thesis.

Based on the results of the measurements and the FEA simulations the methods of the ASME and ISO standards were revised. A discussion of all results, of the relation between the test methods investigated and of the implications on the standards derived from these findings can be found in the following chapter. As one consequence, an alternative procedure for the qualification and dimensioning of composite repairs was proposed. For this purpose, a derivative of the ERR was introduced that adjusts the ERR for the repair-defect geometry. As a result, the ERR can be fitted with a function of the variable 'defect radius over thickness'. Subsequently, a function for the critical pressure was derived that is dependent on the VERR. Because the units of the new value change to energy per volume, it was interpreted as the energy released in relation to the volume deformed and therefore the name volumetric energy release rate (VERR) was proposed.

6.2 Discussion of pressure and shaft-loaded blister test results

One question raised leading to the study presented was the compatibility between shaft-loaded and pressurised blister tests. The measured data from the tested specimens of the SLBTs in chapter 4 and the PBT tested specimens measured with DIC, described in chapter 5, are presented in figures (6.1) to (6.3). The equivalent critical 'pressure' of the SLBT specimens was calculated from the measured force on the shaft and the defect area. Plotting the critical pressure over the geometry

figure (6.1) shows that in terms of resulting strength no distinct difference between the three test methods can be found. Yet, it could be argued that a flat punch (SLBT-F) results in a load curve slightly higher than the pressurised specimens (PBT) and hemispherically capped punches (SBLT-H) yield a curve slightly below that of a PBT.

A more pronounced difference can be observed in figure (6.2), where the total ERR resulting from a hemispherical punch head is larger than the more similar PBT and SLBT-F. In chapter 4.5 the influence of different punch geometries and their comparison to blister tests using fluid pressure on the ERR and the mode mix was discussed and it was concluded that the three methods are not always interchangeable. While the mode mix is different between all three methods, the PBTs' load displacement curves (5.17) share more similarities with those of the SLBT-H (4.17). Additionally, the accuracy of the calculation for the SLBT-H is higher than for the SLBT-F, because the punch size is less critical, provided the radius is large enough to avoid major plastic deformation (i. e. matrix cracking at the contact). It was also shown that neither is comparable in the mode mix. However, taking the graphs presented in this chapter into account, which show the load and ERR over geometry, it must be concluded that SLBT-Fs are more suitable as alternative to PBTs. Yet, it has to be recommended to conduct PBTs, if knowledge about the ERR is required.

Within the scope of the study was the validation of the fracture criterion provided by the standards of ASME and ISO. In chapters 5.7 and 5.8 the ERR was demonstrated not to be simple in its interpretation as a fracture criterion, due to its dependence on the repair-defect geometry. Consequently, it was discussed that a fracture criterion as provided by the standards based on $\mathcal{G}_{\mathrm{Tc}}$ and treated like a $\mathcal{K}_{\mathrm{Ic}}$

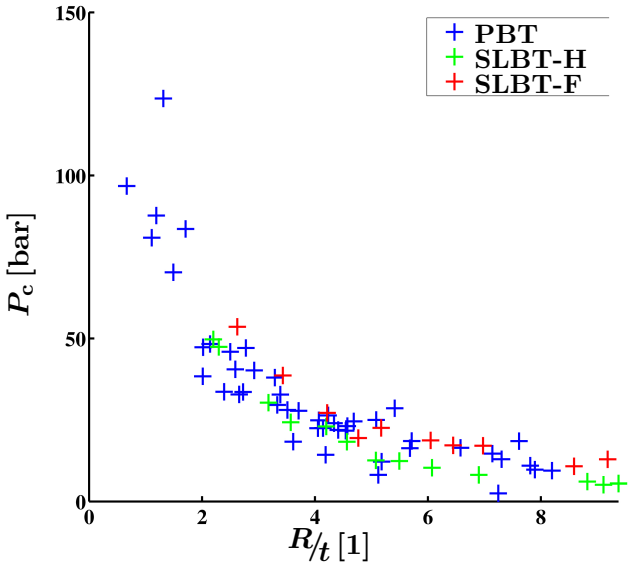

Figure 6.1: Measured critical pressure of all tested specimens plotted against the change in geometry

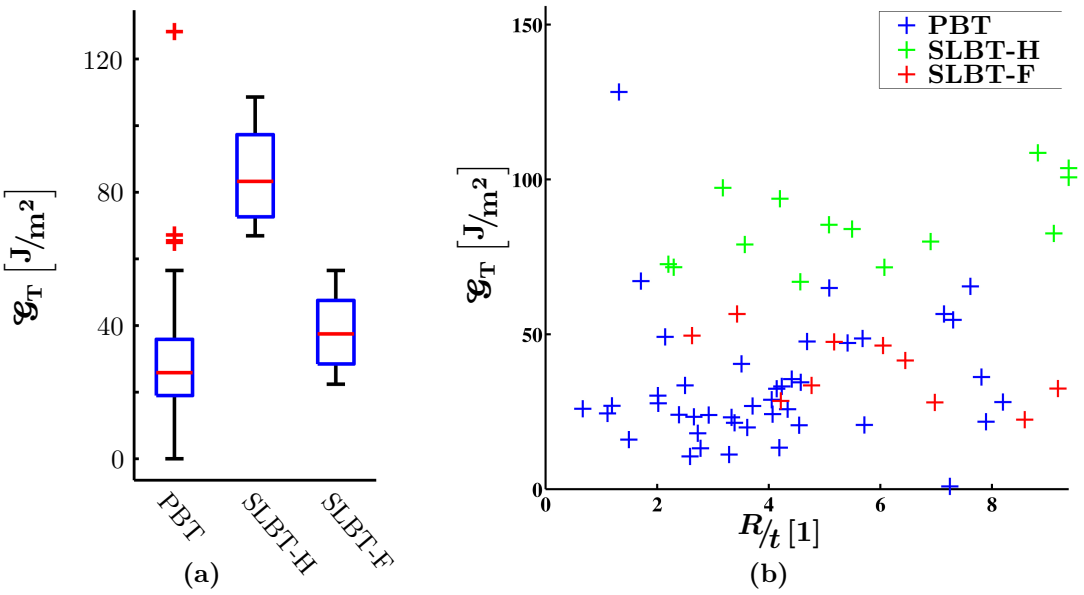

Figure 6.2: (a) The difference in distribution between the three different means of blister fracture testing; (b) The energy release rate of all tested specimens plotted against the change in geometry

criterion cannot be recommended.

In order to develop an alternative procedure for the qualification and dimensioning of a repair system, an ERR derivative independent of the geometry would be advantageous. To the best of the author's knowledge, no normalisation of the ERR against the geometry has been published to date, that preserves the inherent characteristics of the ERR. Wan [151] derived a normalisation of the ERR presented in equations (2.78) to (2.81). This approach ultimately removes every variable (F, w, R and π) from the formulation of the ERR. The conversion leads to a normalised

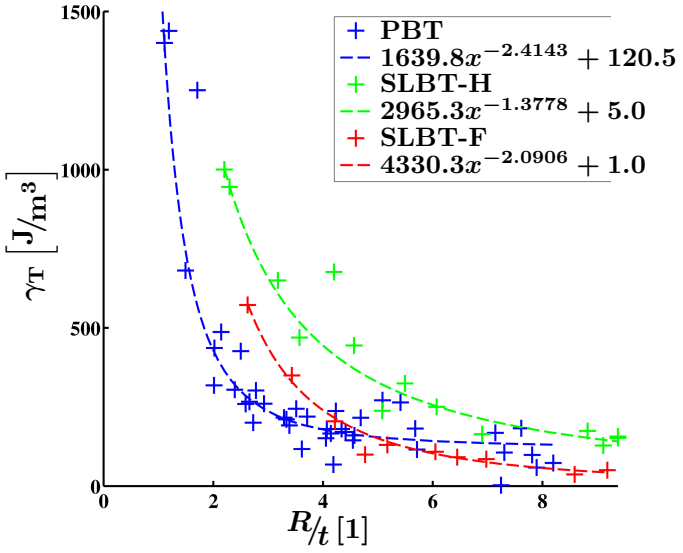

Figure 6.3: The VERR of all tested specimens plotted against the change in geometry

ERR for plates of $\chi_b = 0.5$ and for membranes of $\chi_m = 0.25$, which are the scalar factors in the respective ERR formulations.

From the results of this study an alternative normalisation based on the geometry was introduced, in which the ERR is multiplied by the thickness and divided through the defect area as written in equation (6.1). This normalisation by geometry leads to a change in units to energy per volume instead of area and could be interpreted as the energy released per material volume under deformation. Therefore, it is proposed to denominate γ as *volumetric energy release rate* (VERR). Relationships such as $\mathcal{G}_\mathrm{T} = \mathcal{G}_\mathrm{I} + \mathcal{G}_\mathrm{II} + \mathcal{G}_\mathrm{III}$ remain valid for the VERR.

$$\gamma = \mathcal{G}\frac{t}{A} = \frac{Pt}{2A}\frac{\mathrm{d}V}{\mathrm{d}A} \quad \left[\frac{\mathrm{J}}{\mathrm{m}^3}\right] \tag{6.1}$$

The ERR appears widely scattered along R/t in figure (6.2), but after normalisation the VERR falls on curves (6.3) comparable to the distribution observed with the critical pressure in figure (6.1). Both the data of the critical pressure P_c and the total VERR γ_T, can be fitted with a power law curve of the form $f(x) = ax^{-b} + c$. Figure (6.3) suggests that the three test methods investigated can be fitted with similar, yet different curves. Comparable to figure (6.2), total VERR results from loading with a flat punch appear to be closer to a PBT than those from a hemispherical punch. An evaluation of the 'ideal' simulated results shows that the different curves of figure (5.23) all become one curve in figure (6.4) verifying the normalisation proposed.

Both fitting curves presented in figure (6.6a) and figure (6.6b) were derived as a power law with R/t as variable and logically can be expressed as one function linking

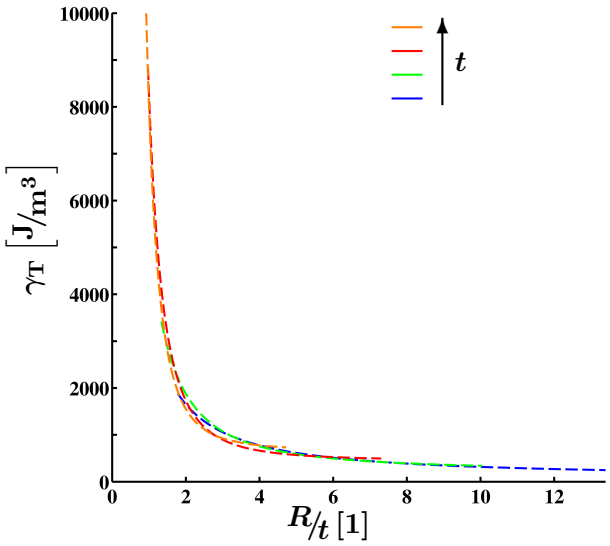

Figure 6.4: The VERR of the simulated results from the study presented in figures (5.22) to (5.23) plotted against the change in geometry

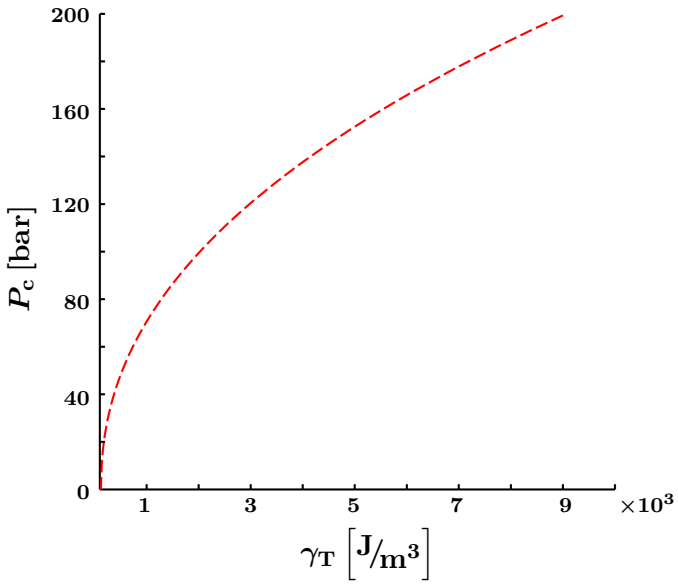

Figure 6.5: The critical pressure as function of the critical VERR

P and γ:

$$f(R/t) = P_c = a_P x^{-b_P} + c_p \quad , \quad g(R/t) = \gamma_T = a_\gamma x^{-b_\gamma} + c_\gamma \tag{6.2}$$

$$\Rightarrow \qquad P_c(\gamma) = a_P \left(\sqrt[-b_\gamma]{\frac{\gamma - c_\gamma}{a_\gamma}} \right)^{-b_P} + c_p \tag{6.3}$$

The critical pressure achievable can directly be read from the VERR in figure (6.5).

With the advantage of a 2D curve instead of a 3D surface (fig. 5.23) necessary to explain the ERR behaviour sufficiently, the safe/fail classification of a repair is simplified and described in the following paragraph. The steps of a possible procedure to qualify repair systems and to calculate the dimensioning required for a given repair scenario could be summarised as follows:

1. Assumption of the mode mix (cf. fig. 5.22) $\mathcal{G}_I/\mathcal{G}_T = \begin{cases} 0.45 & R/t \geq 4 \\ 0.05 R/t + 0.25 & R/t < 4 \end{cases}$

2. Determination of the critical energy release rate by:

   a) If the ratio $R/t \geq 4$ or is assumed to be constant in all repair scenarios, then it is sufficient to conduct one set of MMB tests for the specific R/t ratio. The SLB provides a ratio of $\mathcal{G}_I/\mathcal{G}_T \approx 0.6$ and consequently cannot be recommended.

   b) If different ratios $R/t < 4$ can be encountered it is necessary to determine a full fracture criterion, preferably B-K or power law (cf. sec. 2.1.3). A number of samples per data point have to be tested to measure $\mathcal{G}_{Ic}$ with DCB tests, $\mathcal{G}_{IIc}$ with ENF tests and SLB or MMB for supporting data

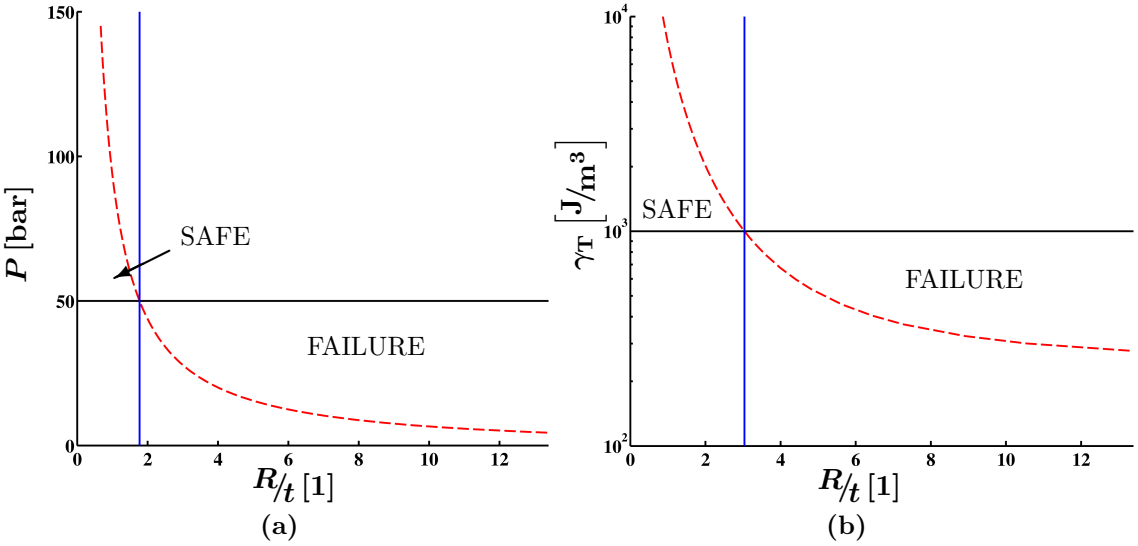

Figure 6.6: Determination of regions of safe operation for an arbitrary chosen critical $P_c = 50\text{bar}$ and $\gamma_T = 1000$ (n. b. the optional log scaling of γ)

points across different mode mixes to evaluate the formulation of the criterion as shown in figure (2.5).

3. A series of samples must be tested in a PBT for a range of probable R/t ratios to measure P_c and $\mathcal{G}_T$ and to calculate γ_T

4. Knowing the distribution of P_c and γ_T over R/t it is possible to fit a curve with a power law ($f(x) = ax^{-b} + c$)

5. The area of safe operation can be determined by the point on the fitted curves crossing the maximum working pressure or the critical VERR obtained in point 2 and by equation (6.1).

Following point 5, the regions of safe and unsafe operation were drawn in figure (6.6) exemplary for an arbitrary P_c and γ_{TC}. The outlined procedure would have to be conducted once for every repair system as part of its qualification. Subsequently, the obtained curves could be used in an actual repair scenario for the dimensioning of the repair or estimation of its residual safety.

For application on an already applied repair with a blister starting to form, the approximate delamination size would have to be measured in the field. Together with the known repair thickness, it can be evaluated whether the repair approaches its critical VERR. In the case of a new repair, the repair thickness necessary would be calculated based on the maximum working pressure and the expected defect size known from an NDT measurement [40, 382].

6.3 General conclusion

From the work presented the following conclusions can be drawn:

1. Analytical formulations exist for the calculation of the ERR for SLBTs and PBTs that yield satisfactory results. However, it was shown that specific formulations have to be employed depending on the type of loading and the geometries of punch, defect and repair. For 'thin plates' (ratio $R/t > 10$) in an SLBT-H the load based solution is most suitable for any punch radius. For the calculation of 'thicker' repair plates the near-point solution would be preferred under the assumption of a small punch-defect radius ratio ($R_{\text{pun}}/R_{\text{def}} < 0.3$). This assumption is true in the majority of cases as the contact zone of a hemispherical punch is small compared to its radius. The introduced annular line load solution was proven to be the most accurate option for SLBT-F. A correction of the shear term of the PBT formulations provided by the standards was proposed and demonstrated to improve the existing solution.

2. The PBT with DIC measurement was developed and proven to be a feasible method to measure the ERR. The corrected analytical solution and the VCCT simulation were validated by the DIC-PBT method to yield accurate results. Through the knowledge gained, the DIC does not have to be employed for additional tests. Instead the less expensive and complex methods of FEA and analytical formulations can be used. If no precise information about the mode mix is necessary the analytical solution is sufficient. The mode mix was investigated and graphs presented, which can be used to estimate the mode ratio. Otherwise, the VCCT is a feasible type of simulation for interface fracture and can be extended with the CZM for a crack propagation simulation along a predefined crack face for relatively small additional expense.

3. SLBTs behave differently for different punch geometries. The punch head radius of an SLBT-H is critical if too small, because of matrix cracking at the contact zone, but produces an almost constant ERR regardless of the size. In contrast, a flat punch SLBT-F yields changing ERRs and mode ratios for different punch radii and is less accurate when calculated with analytical solutions. Despite being less convenient, a flat punch would be recommended over an SLBT-H to mimic a PBT. However, the data presented suggests that neither is ideal enough as a substitute for PBTs, because of the distinct differences in the ERR and its mode ratios, although the measured failure loads of all three tests coincide.

4. Through the PBTs, it was found that the ERR is dependent on the radius of the defect and the thickness of the repair, but not via the relation R/t. The fracture

criterion provided in the standards effectively utilises $\mathcal{G}_{\mathrm{Tc}}$, which was shown by the data presented to be inadequate. A fracture criterion, such as B-K or power law, could not be derived, because the mode mix ratio is approximately constant at $\mathcal{G}_{\mathrm{I}}/\mathcal{G}_{\mathrm{T}} \approx 0.45$ for all $R/t > 4$. However, a volumetric energy release rate (VERR) was introduced that is the ERR adjusted for the repair-defect geometry. The VERR provides the advantage that the dependence on R and t for $h(R,t) = \mathcal{G}$ is converted to a dependence on R/t for $g(R/t) = \gamma$ comparable to the function of the critical pressure. Therefore, the critical pressure can be written as function of the VERR in the form $e(R/t) = P_c = f(\gamma)$.

5. The procedure proposed for the qualification and dimensioning of composite repairs extends the existing recommendation by the standards, as it improves the understanding of the impact of the repair-defect geometry on the crack propagation, ultimately making hydrocarbon production more safe. It may be possible to omit the evaluation of the ERR and, instead, to design a repair solely based on a fitting curve of the critical pressure, as demonstrated in figure (6.6a).

6.4 Future work

Further investigations are necessary to improve the understanding of the geometry not only of the repair but also of the defect, moving on from circular defects with sharp edges to different shapes. As corrosive or abrasive material deterioration causes defects of various shapes, this topic could be of interest for future research, while the study presented only investigated in circular 'sharp-edged' through defects. In particular, questions arise about thin remaining thicknesses of the substrate attached to the repair within what was regarded as defect area in the study presented. A large remaining thickness was already partly under investigation [383], although not from an interface fracture point of view. In this context, the standards [1, 2] classify a remaining thickness of 1 mm as a 'leak' that has to be repaired. Extending the work presented with an investigation of full pipe sections would link the research closer to the field application. The DIC test method presented could provide a powerful tool for the measurements of such pipe section tests. The development of an in-situ coupon-test could support the characterisation of an applied repair and increase safety against leakage. Additional research on the VERR would be needed to fully understand the relation between energy and volume as well as its physical implications.

Chapter 7. References

[1] *DD CEN ISO/TS 24817*, ISO International Organization for Standardization, BSI British Standards, 2011, Petroleum, petrochemical and natural gas industries — Composite repairs for pipework — Qualification and design, installation, testing and inspection.

[2] *ASME PCC-2: Repair of pressure equipment and piping*, The American Society of Mechanical Engineers, 2011, Nonmetallic and bonded repairs.

[3] J. Xia, P. K. Das, and D. Karunakaran, "A parametric design study for a semi/SCR system in northern north sea," *Ocean Engineering*, vol. 35, pp. 1686–1699, 2008.

[4] L. C. M. Meniconi, S. R. Reid, and P. D. Soden, "Preliminary design of composite riser stress joints," *Composites: Part A*, vol. 32, pp. 597–605, 2001.

[5] B. B. Mekha, "On the wave and VIV fatigue of steel catenary risers connected to floating structures," in *21st International Conference on Ocean, Offshore and Arctic Engineering*, vol. 1. ASME, 2002, pp. 57–63.

[6] G. L. Kuiper, J. Brugmans, and A. V. Metrikine, "Destabilization of deepwater risers by a heaving platform," *Journal of Sound and Vibration*, vol. 310, pp. 541–557, 2008.

[7] Z. J. Westgate, M. F. Randolph, D. J. White, and S. Li, "The influence of sea state on as-laid pipeline embedment: A case study," *Applied Ocean Research*, vol. 32, pp. 321–331, 2010.

[8] A. P. Moser and S. Folkman, *Buried pipe design*, 3rd ed. New York: McGraw-Hill, 2008.

[9] *Background Information*, Nord Stream AG, November 2013. [Online]. Available: http://www.nord-stream.com/

[10] B. Bruce, N. Porter, G. Ritter, M. Boring, M. Losev, I. Harris, B. Mohr, D. Harwig, R. Gordon, C. Neary, and M. Sullivan, "Internal repair of pipelines," Edison Welding Institute, 1250 Arthur E. Adams Drive, Columbus, OH 43221, 30-month technical progress report 46211GTH, 2005.

[11] O. O. Ochoa and M. M. Salama, "Offshore composites: Transition barriers to an enabling technology," *Composites Science and Technology*, vol. 65, pp. 2588–2596, 2005.

[12] "Composite repair clamp," JEC Paris Innovations Award Winner, Advanced Composite Structures Australia Pty. Ltd., 2014.

[13] *Pipe reinforcement & repair system*, Clock Spring, December 2012. [Online]. Available: http://www.clockspring.com/

[14] C. R. Alexander, "Development of a composite repair system for reinforcing offshore risers," Ph.D. dissertation, Texas A&M University, 2007.

[15] H. S. da Costa-Mattos, J. M. L. Reis, R. F. Sampaio, and V. A. Perrut, "An alternative methodology to repair localized corrosion damage in metallic pipelines with epoxy resins," *Materials and Design*, vol. 30, pp. 3581–3591, 2009.

[16] J. M. Duell, J. M. Wilson, and M. R. Kessler, "Analysis of a carbon composite overwrap pipeline repair system," *International Journal of Pressure Vessels and Piping*, vol. 85, pp. 782–788, 2008.

[17] A. R. Mableson, K. R. Dunn, N. Dodds, and A. G. Gibson, "Refurbishment of steel tubular pipes using composite materials," *Plastics, Rubber and Composites*, vol. 29, no. 10, pp. 782–788, 2000.

[18] C. R. Alexander and F. Worth, "Assessing the use of composite materials in repairing mechanical damage in transmission pipelines," in *Proceedings of IPC2006*, no. 10482, Calgary, Canada, 2006, p. 7, 6th International Pipeline Conference.

[19] J. A. Peck, G. Li, S.-S. Pang, and M. A. Stubblefield, "Light intensity effect on UV cured FRP coupled composite pipe joints," *Composite Structures*, vol. 64, pp. 539–546, 2004.

[20] L. E. Eiselstein and R. Huet, "Corrosion failure analysis with case histories," in *Uhlig's corrosion handbook*, R. W. Revie, Ed. John Wiley & Sons, 2011, ch. 1, pp. 3–14.

[21] S. F. Wika, "Pitting and crevice corrosion of stainless steel under offshore conditions," Ph.D. dissertation, NTNU – Trondheim, Norwegian University of Science and Technology, Department of Materials Science and Engineering, 2012.

[22] *ASTM G46 – 94*, The American Society for Testing and Materials, 2013, Standard guide for examination and evaluation of pitting corrosion.

[23] R. W. Staehle, "Lifetime prediction of materials in environments," in *Uhlig's corrosion handbook*, R. W. Revie, Ed. John Wiley & Sons, 2011, ch. 10, pp. 123–143.

[24] J. R. Galvele, "Tafel's law in pitting corrosion and crevice corrosion susceptibility," *Corrosion Science*, vol. 47, pp. 3053–3067, 2005.

[25] A. J. Betts and L. H. Boulton, "Crevice corrosion: review of mechanisms, modelling and mitigation," *Corrosion Engineering, Science and Technology*, vol. 28, no. 4, pp. 279–296, 1993.

[26] N. J. Laycock, J. Stewart, and R. C. Newman, "The initiation of crevice corrosion in stainless steel," *Corrosion Science*, vol. 39, no. 10-11, pp. 1791–1809, 1997.

[27] A. Shekhter, C. Loader, and B. R. Crawford, "Assessment of the effect of pitting corrosion on the safe life prediction of the p-3c," Defence Science and Technology Organisation, DSTO, Australian Government, Department of Defence, Air Vehicles Division, Tech. Rep. DSTO-TR2080, 2007.

[28] X. G. Zhang, "Galvanic corrosion," in *Uhlig's corrosion handbook*, R. W. Revie, Ed. John Wiley & Sons, 2011, ch. 10, pp. 123–143.

[29] API, "Crude oil category – category assessment document," The American Petroleum Institute, Petroleum HPV Testing Group, US EPA, Tech. Rep., 2011, High production volume (HPV) chemical challenge program.

[30] R. T. Gonçalves, G. F. Rosetti, A. L. C. Fujarra, and A. C. Oliveira, "Experimental study on vortex-induced motions of a semi-submersible platform with four square columns, Part I: Effects of current incidence angle and hull appendages," *Ocean Engineering*, vol. 54, pp. 150–169, 2012.

[31] C. Alexander and O. O. Ochoa, "Extending onshore pipeline repair to offshore steel risers with carbon-fibre reinforced composites," *Composite Structures*, vol. 92, pp. 499–507, 2010.

[32] P. Gundersen, K. Doynov, T. Andersen, and R. Haakonsen, "Methodology for determining remnant fatigue life of flexible risers subjected to slugging and irregular waves," in *31st International Conference on Ocean, Offshore and Arctic Engineering*, vol. 3. ASME, 2012, pp. 321–330.

[33] T. K. Sen, "Probability of fatigue failure in steel catenary risers in deep water," *ASCE, Journal of Engineering Mechanics*, vol. 132, no. 9, pp. 1686–1699, 2006.

[34] W. K. Goertzen and M. R. Kessler, "Creep behavior of carbon fibre/epoxy matrix composites," *Materials Science and Engineering*, vol. 421, pp. 217–225, 2006.

[35] L. Yuan and S. Kyriakides, "Liner wrinkling and collapse of bi-material pipe under bending," *International Journal of Solids and Structures*, vol. 51, no. 3-4, pp. 599–611, 2014.

[36] J. L. Otegui, S. Urquiza, A. Rivas, and A. Trunzo, "Local collapse of gas pipelines under sleeve repairs," *International Journal of Pressure Vessels and Piping*, vol. 77, pp. 555–566, 2000.

[37] J. H. Greenwood, "Very long term permeability testing of underground petrol pipework," *Polymer Testing*, vol. 20, pp. 383–388, 2001.

[38] R. MacDonald, L. Simon, K. Goerz, and M. Girgis, "Corrosion failure in a lined sour gas pipeline - Part 2: Role of methanol in corrosion behind liner," in *Proceedings of the NACE North Area Western Conference*. NACE International, 2010, pp. 1–17, Calgary.

[39] F. Rueda, J. L. Otegui, and P. Frontini, "Numerical tool to model collapse of polymeric liners in pipelines," *Engineering Failure Analysis*, vol. 20, pp. 25–34, 2012.

[40] S. Kariyawasam, P. Yeung, S. Clouston, and G. Hurd, "Overcoming technical limitations in identifying and characterizing critical complex corrosion," in *Proceedings of the 9th International Pipeline Conference*. The American Society of Mechanical Engineers, 2012, pp. 229–236, Vol. 2: Pipeline Integrity Management.

[41] J. Humpenöder, "Gas permeation of fibre reinforced plastics," *Cryogenics*, vol. 38, no. 1, pp. 143–147, 1998.

[42] M. S. Abdul Majid, T. A. Assaleh, A. G. Gibson, J. M. Hale, A. Fahrer, C. A. P. Rookus, and M. Hekman, "Ultimate elastic wall stress (UEWS) test of glass fibre reinforced epoxy (GRE) pipe," *Composites: Part A*, vol. 42, pp. 1500–1508, 2011.

[43] A. G. Gibson, M. S. Abdul Majid, T. A. Assaleh, J. M. Hale, A. Fahrer, C. A. P. Rookus, and M. Hekman, "Qualification and lifetime modelling of fibreglass pipe," *Plastics, Rubber and Composites*, vol. 40, pp. 80–85, 2011.

[44] A. T. Zhender, *Fracture Mechanics*, 1st ed. New York: Springer, 2012.

[45] D. Gross and T. Seelig, *Bruchmechanik*, 4th ed. Berlin: Springer, 2007.

[46] G. R. Irwin and J. A. Kies, "Critical energy rate analysis of fracture strength," *Welding Journal, Welding Research Supplement*, vol. 33, pp. 193–198, 1954.

[47] A. A. Griffith, "The phenomena of rupture and flow in solids," *Philosophical Transactions of the Royal Society of London, Series A, Containing Papers of a Mathematical of Physical Character*, vol. 221, pp. 163–198, 1921.

[48] J. W. Hutchinson and Z. Suo, "Mixed mode cracking in layered materials," *Advances in Applied Mechanics*, vol. 29, pp. 64–191, 1991.

[49] C. F. Shih, "Cracks on bimaterial interfaces: elasticity and plasticity aspects," *Materials Science and Engineering*, vol. 143, pp. 77–90, 1991.

[50] L. Banks-Sills, "50th anniversary article: Review on interface fracture and delamination of composites," *Strain*, vol. 50, no. 2, pp. 98–110, 2014.

[51] M. L. Williams, "On the stress distribution at the base of a stationary crack," *Journal of Applied Mechancis*, vol. 24, pp. 109–114, 1957.

[52] H. M. Westergaard, "Bearing pressures and cracks," *Journal of Applied Mechancis*, vol. 6, pp. 49–53, 1939.

[53] G. R. Irwin, "Analysis of stresses and strains near the end of a crack traversing a plate," *Journal of Applied Mechancis*, vol. 24, pp. 361–364, 1957.

[54] I. C. Sneddon, "The Distribution of Stress in the Neighbourhood of a Crack in an Elastic Solid," in *Proceedings of the Royal Society of London. Series A, Mathematical and Physical*, vol. 187(1009). The Royal Society, 1946, pp. 229–260.

[55] T. L. Anderson, *Fracture Mechanics, Fundamentals and Applications*, 3rd ed. London: Taylor & Francis, 2005.

[56] C. E. Inglis, "Stresses in a plate due to the presence of cracks and sharp corners," *Transactions of the Institute of Naval Architects*, vol. 55, pp. 219–241, 1913.

[57] J. Dodds, Robert H., T. L. Anderson, and M. T. Kirk, "A framework to correlate a/W ratio effects on elastic-plastic fracture toughness (J_c)," *International Journal of Fracture Mechanics*, vol. 48, pp. 1–22, 1991.

[58] D. S. Dugdale, "Yielding in steel sheets containing slits," *Journal of the Mechanics and Physics of Solids*, vol. 8, pp. 100–104, 1960.

[59] G. I. Barenblatt, "The mathematical theory of equilibrium cracks in brittle fracture," *Advances in Applied Mechanics*, vol. 7, pp. 55–129, 1962.

[60] M. L. Williams, "The stresses around a fault or crack in dissimular media," *Bulletin of the Seismological Society of America*, vol. 49, no. 2, pp. 199–204, 1959.

[61] G. P. Cherepanov, "The stress state in a heterogeneous plate with slits," *Izvestia AN SSSR, OTN, Mekhan. i Mashin*, vol. 1, pp. 131–137, 1962.

[62] J. R. Rice and G. C. Sih, "Plane problems of cracks in dissimilar media," *Journal of Applied Mechanics*, vol. 32, no. 2, pp. 418–423, 1965.

[63] F. Erdogan, "Stress distribution in bonded dissimilar materials with cracks," *Journal of Applied Mechanics*, vol. 32, no. 2, pp. 403–410, 1965.

[64] A. H. England, "A crack between dissimilar media," *Journal of Applied Mechanics*, vol. 32, no. 2, pp. 400–402, 1965.

[65] B. M. Malyshev and R. L. Salganik, "The strength of adhesive joints using the theory of cracks," *International Journal of Fracture Mechanics*, vol. 1, no. 2, pp. 114–128, 1965.

[66] M. Comninou, "The interface crack," *Journal of Applied Mechanics*, vol. 44, no. 4, pp. 631–636, 1977.

[67] M. Comninou and D. Schmueser, "The interface crack in a combined tension-compression and shear field," *Journal of Applied Mechanics*, vol. 46, no. 2, pp. 345–348, 1979.

[68] M. Comninou, "Interface crack with friction in the contact zone," *Journal of Applied Mechanics*, vol. 44, no. 4, pp. 780–781, 1977.

[69] A. K. Gautesen and J. Dundurs, "The interface crack under combined loading," *Journal of Applied Mechanics*, vol. 55, no. 3, pp. 580–586, 1988.

[70] J. Dundurs, "Discussion: 'Edge-bonded dissimilar rthogonal elastic wedges under normal and shear loading' (Bogy, D. B., 1968, ASME J. Appl. Mech., 35, pp. 460-466)," *Journal of Applied Mechanics*, vol. 36, no. 3, pp. 650–652, 1969.

[71] R. T. Shield, "Uniqueness for elastic crack and punch problems," *Journal of Applied Mechanics*, vol. 49, no. 3, pp. 516–518, 1982.

[72] R. T. Shield, "Variational principles for some nonstandard elastic problems," *Journal of Applied Mechanics*, vol. 54, no. 4, pp. 768–771, 1987.

[73] C. Atkinson, "On stress singularities and interfaces in linear elastic fracture mechanics," *International Journal of Fracture*, vol. 13, no. 6, pp. 807–820, 1977.

[74] N. Karkamkar, B. Bose, P. McLaughlin, and S. Santhanam, "The use of interlayers in modeling interface crack propagation," *Engineering Fracture Mechanics*, vol. 75, no. 18, pp. 5087–5100, 2008.

[75] N. Aravas and S. M. Sharma, "An elastoplastic analysis of the interface crack with contact zones," *Journal of the Mechanics and Physics of Solids*, vol. 39, no. 3, pp. 311–344, 1991.

[76] J. R. Rice, Z. Suo, and J.-S. Wang, "Mechanics and thermodynamics of brittle interfacial failure in bimaterial systems," *Metal-Ceramic Interfaces*, vol. 4, pp. 269–294, 1990, Acta-Scripta Metallurgica Proceedings Series.

[77] X. Deng, "General crack-tip fields for stationary and steadily growing interface cracks in anisotropic bimaterials," *Journal of Applied Mechanics*, vol. 60, no. 1, pp. 183–189, 1993.

[78] V. Boniface and L. Banks-Sills, "Stress intensity factors for finite interface cracks between a special pair of transversely isotropic materials," *Journal of Applied Mechanics*, vol. 69, no. 3, pp. 230–239, 2002.

[79] Z. Suo, "Singularities, interfaces and cracks in dissimilar anisotropic media," *Proceedings of the Royal Society of London. Series A, Mathematical and Physical Sciences*, vol. 427, no. 1873, pp. 331–358, 1990.

[80] K. C. Wu, "Stress intensity factor and energy release rate for interfacial cracks between dissimilar anisotropic materials," *Journal of Applied Mechanics*, vol. 57, no. 4, pp. 882–886, 1990.

[81] L. Banks-Sills and T. Ikeda, "Stress itnensity factors for interface cracks between orthotropic and monoclinic material," *International Journal of Fracture*, vol. 167, no. 1, pp. 47–56, 2011.

[82] I. Mohammed and K. M. Liechti, "The effect of corner angles in bimaterial structures," *International Journal of Solids and Structures*, vol. 38, no. 24-25, pp. 4375–4394, 2001.

[83] N. A. Fleck, J. W. Hutchinson, and Z. Suo, "Crack path selection in a brittle adhesive layer," *International Journal of Solids and Structures*, vol. 27, no. 13, pp. 1683–1703, 1991.

[84] C. F. Shih and R. J. Asaro, "Elastic-plastic and asymptotic fields of interface cracks," *International Journal of Fracture*, vol. 42, no. 2, pp. 101–116, 1990.

[85] J. R. Rice and G. F. Rosengren, "Plane strain deformation near a crack tip in a power-law hardening material," *Journal of the Mechanics and Physics of Solids*, vol. 16, no. 1, pp. 1–12, 1968.

[86] J. W. Hutchinson, "Singular behaviour at the end of a tensile crack in a hardening material," *Journal of the Mechanics and Physics of Solids*, vol. 16, no. 1, pp. 13–31, 1968.

[87] J. W. Hutchinson, "Plastic stress and strain fields at a crack tip," *Journal of the Mechanics and Physics of Solids*, vol. 16, no. 5, pp. 337–347, 1968.

[88] W.-X. Wang, T.-Y. Fan, and L.-X. Zhang, "Analytic study on angular fields of HRR solution," *Science in China – Series A: Mathematics*, vol. 41, no. 3, pp. 313–323, 1998.

[89] S. Yang, Y. J. Chao, and M. A. Sutton, "Complete theoretical analysis for higher order asymptotic terms and the HRR zone at a crack tip for moed I and mode II loading of a hardening material," *Acta Mechanica*, vol. 98, pp. 79–98, 1993.

[90] E. Østby, Z. L. Zhang, and C. Thaulow, "Constraint effect on the near tip stress fields due to difference in plastic work hardening for bi-material interface cracks in small scale yielding," *International Journal of Fracture*, vol. 111, no. 1, pp. 87–103, 2001.

[91] H. Y. Lee and Y. J. Kim, "Interfacial crack-tip constraints and J-integral for bi-materials with plastic hardening mismatch," *International Journal of Fracture*, vol. 143, no. 3, pp. 231–243, 2007.

[92] M. Belhouari, A. Amiri, A. Mehidi, K. Madani, and B. Bachir Bouiadjra, "Elastic–plastic analysis of interaction between an interface and crack in bi-materials," *International Journal of Damage Mechanics*, vol. 24, no. 3, pp. 299–326, 2014.

[93] J. L. Strom and J. P. Parmigiani, "Transition of crack path at bi-material interfaces," *Engineering Fracture Mechanics*, vol. 115, pp. 13–21, 2014.

[94] D. K. Yi, J. Zhuang, Z. M. Xiao, and S. K. Tan, "Elastic and plastic stress analysis of an interface crack between two dissimilar layers," *Acta Mechanica*, vol. 223, no. 11, pp. 2287–2301, 2012.

[95] D. K. Yi, Z. M. Xiao, and S. K. Tan, "An interface crack under biaxial loading with Dugdale plastic zone corrections in layered composite materials," *Engineering Fracture Mechanics*, vol. 109, no. 3, pp. 209–220, 2013.

[96] W. Becker and D. Gross, "About the Dugdale crack under mixed mode loading," *International Journal of Fracture*, vol. 37, no. 37, pp. 163–170, 1988.

[97] M. Fan, D. K. Yi, and Z. M. Xiao, "Elastic-plastic stress investigation for an arc-shaped interface crack in composite material," *International Journal of Mechanical Sciences*, vol. 83, pp. 104–111, 2014.

[98] A. N. Guz, I. A. Guz, and V. A. Men'shikov, "Three-dimensional problems in the dynamic fracture mechanics of materials with interface cracks (review)," *International Apllied Mechanics*, vol. 49, no. 1, pp. 1–61, 2013.

[99] G. R. Irwin, "Fracture dynamics," *Fracturing of Metals*, pp. 147–166, 1948.

[100] E. Orowan, "Fracture and strength of solids," *Reports on Progress in Physics*, vol. 12, p. 185, 1948.

[101] F. Erdogan and G. C. Sih, "On the crack extension in plates under plane loading and transverse shear," *Journal of Fluids Engineering*, vol. 85, no. 4, pp. 519–525, 1963.

[102] J. G. Williams and P. D. Ewing, "Fracture under complex stress – The angled crack problem," *International Journal of Fracture Mechanics*, vol. 8, no. 4, pp. 441–446, 1972.

[103] E. H. Yoffe, "The moving griffith crack," *Philosophical Magazine*, vol. 42, pp. 739–750, 1951.

[104] S. K. Maiti and R. A. Smith, "Theoretical and experimental studies on the extension of cracks subjected to concentrated loading near their faces to compare the criteria for mixed mode brittle fracture," *Journal of the Mechanics and Physics of Solids*, vol. 31, no. 5, pp. 389–403, 1983.

[105] S. K. Maiti and R. A. Smith, "Comparison of the criteria for mixed mode brittle fracture based on the preinstability stress-strain field part I: Slit and elliptical cracks under uniaxial tensile loading," *International Journal of Fracture*, vol. 23, no. 4, pp. 281–295, 1983.

[106] S. K. Maiti and R. A. Smith, "Comparison of the criteria for mixed mode brittle fracture based on the preinstability stress-strain field part II: Pure shear and uniaxial compressive loading," *International Journal of Fracture*, vol. 24, no. 1, pp. 5–22, 1984.

[107] H.-C. Wu, "Dual failure criterion for plain concrete," *Journal of the Engineering Mechanics Division*, vol. 100, no. 6, pp. 1167–1181, 1974.

[108] G. C. Sih, "Strain-energy-density factor applied to mixed mode crack problems," *International Journal of Fracture*, vol. 10, no. 3, pp. 305–321, 1974.

[109] P. S. Theocaris and P. D. Panagiotopoulos, "On the T- and S-criteria in fracture mechanics: new formulations and variational principles," *Acta Mechanica*, vol. 87, pp. 135–152, 1991.

[110] M. A. Hussain, S. L. Pu, and J. Underwood, "Strain energy release rate for a crack under combined mode I and mode II," *Fracture Analysis*, vol. ASTM STP 560, pp. 2–28, 1974.

[111] T.-C. Wang, C. F. Shih, and Z. Suo, "Crack extension and kinking in laminates and bicrystals," *International Journal of Solids and Structures*, vol. 29, no. 3, pp. 327–344, 1992.

[112] L. Banks-Sills and D. Ashkenazi, "A note on fracture criteria for interface fracture," *International Journal of Fracture*, vol. 103, no. 2, pp. 177–188, 2000.

[113] L. Banks-Sills, V. Boniface, and R. Eliasi, "Development of a methodology for determination of interface fracture toughness of laminate composites — the 0°/90°pair," *International Journal of Solids and Structures*, vol. 42, no. 2, pp. 663–680, 2005.

[114] L. Banks-Sills, "Fracture toughness of the +45°/-45°interface of a laminate composite," *International Journal of Fracture*, vol. 141, no. 1-2, pp. 195–210, 2006.

[115] J. C. Newman, Jr., "Fracture analysis of surface- and through-cracked sheets and plates," *Engineering Fracture Mechanics*, vol. 5, no. 3, pp. 667–689, 1973.

[116] D. Leguillon, "Strength or toughness? A criterion for crack onset at a notch," *European Journal of Mechanics – A/Solids*, vol. 21, no. 1, pp. 61–72, 2002.

[117] D. Leguillon and Z. Yosibash, "Crack onset at a v-notch. Influence of the notch tip radius," *International Journal of Fracture*, vol. 122, no. 1-2, pp. 1–21, 2003.

[118] A. Moradi, D. Leguillon, and N. Carrère, "Influence of the adhesive thickness on a debonding – An asymptotic model," *Engineering Fracture Mechanics*, vol. 114, pp. 55–68, 2013.

[119] Z. Hashin, "Finite thermoelastic fracture criterion with application to laminate cracking analysis," *Journal of the Mechanics and Physics of Solids*, vol. 44, no. 7, pp. 1129–1145, 1996.

[120] D. Taylor, P. Cornetti, and N. Pugno, "The fracture mechanics of finite crack extension," *Engineering Fracture Mechanics*, vol. 75, no. 7, pp. 1021–1038, 2005.

[121] P. Cornetti, N. Pugno, A. Carpinteri, and D. Taylor, "Finite fracture mechanics: A coupled stress and energy failure criterion," *Engineering Fracture Mechanics*, vol. 73, no. 14, pp. 2021–2033, 2006.

[122] D. Taylor, "Geometrical effects in fatigue: a unifying theoretical model," *International Journal of Fatigue*, vol. 21, no. 5, pp. 413–420, 1999.

[123] A. Seweryn, "A non-local stress and strain energy release rate mixed mode fracture initiation and propagation criteria," *Engineering Fracture Mechanics*, vol. 59, no. 6, pp. 737–760, 1998.

[124] P. Cornetti, V. Mantič, and A. Carpinteri, "Finite fracture mechanics at elastic interfaces," *Engineering Fracture Mechanics*, vol. 49, no. 7-8, pp. 1022–1032, 2012.

[125] P. Cornetti, A. Sapora, and A. Carpinteri, "Mode mixity and size effect in V-notched structures," *International Journal of Solids and Structures*, vol. 50, no. 10, pp. 1562–1582, 2013.

[126] P. Weißgräber and W. Becker, "Finite fracture mechanics model for mixed mode fracture in adhesive joints," *International Journal of Solids and Structures*, vol. 50, no. 14-15, pp. 2383–2394, 2013.

[127] M. Perelmuter, "Nonlocal criterion of bridged cracks growth: Weak interface," *Journal of the European Ceramic Society*, vol. 34, no. 11, pp. 2789–2798, 2014.

[128] M. Shahverdi, A. P. Vassilopoulos, and T. Keller, "Mixed-mode quasi-static failure criteria for adhesively-bonded pultruded GFRP joints," *Composites: Part A*, vol. 59, pp. 45–56, 2014.

[129] *ANSYS Mechanical APDL Structural Analysis Guide*, 14th ed., ANSYS Inc., 2012.

[130] J. R. Reeder, "A bilinear failure criterion for mixed-mode delamination," *Composite Materials: Testing and Design*, vol. 11, pp. 303–322, 1993, ASTM STP 1206.

[131] B. D. Davidson and W. Zhao, "An accurate mixed-mode delamination failure criterion for laminated fibrous composites requiring limited experimental input," *Journal of Composite Materials*, vol. 41, no. 6, pp. 679–702, 2007.

[132] H. T. Hahn and T. Johannesson, "A correlation between fracture energy and fracture morphology in mixed-mode fracture of composites," in *Mechanical Behaviour of Materials*, vol. 1. Stockholm, Sweden: Proceedings of the Fourth International Conference, Aug 1983, pp. 431–438.

[133] S. Hashemi, A. J. Kinloch, and G. Williams, "Mixed-mode fracture in fiber-polymer composite laminates," *Composite Materials: Fatigue and Fracture*, vol. 3, pp. 143–168, 1991, ASTM STP 1110.

[134] M. L. Benzeggagh and M. Kenane, "Measurement of mixed-mode delamination fracture toughness of unidirectional glass/epoxy composites with mixed-mode bending apparatus," *Composites Science and Technology*, vol. 56, no. 4, pp. 439–449, 1996.

[135] J. R. Reeder, "3D mixed-mode delamination fracture criteria – An experimentalist's perspective," in *21st Technical Conference of the American Society for Composites*, vol. 1. Dearborn, MI, USA: American Society for Composites, Sep 2006, pp. 129–145.

[136] R. Krüger, "Development and applications of benchmark examples for static delamination propagation predictions," in *28th Annual Technical Conference*. State College, Pennsylvania, USA: The American Society for Composites, Sep 2013, p. 21.

[137] J. D. Whitcomb, "Parametric analytical study of instability-related delamination growth," *Composite Science and Technology*, vol. 25, no. 1, pp. 19–48, 1986.

[138] *BS ISO 15024:2001*, British Standards Institution, 2002, Fibre-reinforced plastic composites — Determination of the mode I interlaminar fracture toughness, G_{IC}, for unidirectionally reinforced materials.

[139] *BS ISO 7991:2001*, British Standards Institution, 2001, Determination of the mode I adhesive fracture energy G_{IC} of structure adhesives using the double cantilever beam (DCB) and tapered double cantilever beam (TDCB) specimens.

[140] *ASTM D5528 – 01*, The American Society for Testing and Materials, 2009, Standard test method for mode I interlaminar fracture toughness of unidirectional fiber-reinforced polymer matrix composites.

[141] *ASTM D6115 – 97*, The American Society for Testing and Materials, 2011, Standard test method for mode I fatigue delamination growth onset of unidirectional fiber-reinforced polymer matrix composites.

[142] P. Davidson, A. M. Waas, and C. S. Yerramalli, "Experimental determination of validated, critical interfacial modes I and II energy release rates in a composite sandwich panel," *Composite Structures*, vol. 94, pp. 477–483, 2012.

[143] *BS ISO 15114:2014*, British Standards Institution, 2014, Fibre-reinforced plastic composites — Determination of the mode II fracture resistance for unidirectionally reinforced materials using the calibrated end-loaded split (C-ELS) test and an effective crack length approach.

[144] *ASTM D6671/D6671M – 06*, The American Society for Testing and Materials, 2006, Standard test method for mixed mode I – mode II interlaminar fracture toughness of unidirectional fiber reinforced polymer matrix composites.

[145] B. D. Davidson, R. Krüger, and M. König, "Three-dimensional analysis of center-delaminated unidirectional and multidirectional single-leg bending specimens," *Composite Science and Technology*, vol. 54, pp. 385–394, 1995.

[146] M. D. Thouless and H. M. Jensen, "Elastic fracture mechanics of the peel-test geometry," *Journal of Adhesion*, vol. 38, no. 3, pp. 185–197, 1992.

[147] A. J. Kinloch, C. C. Lau, and J. G. Williams, "The peeling of flexible laminates," *International Journal of Fracture*, vol. 66, pp. 45–70, 1994.

[148] H. Hertz, "Über die Berührung elastischer Körper (*on the contact of elastic solids*)," in *Miscellaneous Papers*, D. E. Jones and G. A. Schott, Eds. MacMillan & Co., 1881, ch. 5, pp. 146–163.

[149] I. N. Sneddon, "The relation between load and penetration in the axisymmetric boussinesq problem for a punch of arbitrary profile," *International Journal of Engineering Sciences*, vol. 3, pp. 47–57, 1965.

[150] E. P. O'Brien, S. Goldfarb, and C. C. White, "Influence of experimental setup and plastic deformation on the shaft-loaded blister test," *Journal of Adhesion*, vol. 81, no. 6, pp. 599–621, 2005.

[151] K.-T. Wan, "Fracture mechanics of a shaft-loaded blister test - Transition from a bending to a stretching membrane," *The Journal of Adhesion*, vol. 70, no. 3, pp. 209–219, 1999.

[152] J. G. Williams, "Energy release rates for the peeling of flexible membranes and the analysis of blister tests," *International Journal of Fracture*, vol. 87, pp. 265–288, 1997.

[153] M. Sheplak and J. Dugundji, "Large deflections of clamped circular plates under initial tension and transitions to membrane behavior," *Journal of Applied Mechancis*, vol. 65, no. 1, pp. 107–115, 1998.

[154] U. Komaragiri, M. R. Begley, and J. G. Simmonds, "The mechanical response of freestanding circular elastic films under point and pressure loads," *Journal of Applied Mechancis*, vol. 72, no. 2, pp. 203–212, 2005.

[155] A. A. K. Al-Maskari, "Composite repair systems for steel pipes," Ph.D. dissertation, Centre for Composite Materials Engineering, School of Mechanical & Systems Engineering, Newcastle University, 2009.

[156] W. C. Young and R. G. Budynas, *Roark's formulas for stress and strain*, 7th ed. Boston: Mc-Graw Hill, 2002.

[157] D. L. Holl, "Analysis of thin rectangular plates supported on opposite edges," *Iowa Eng. Exp. Sta.*, vol. 129, 1936, Iowa State College.

[158] A. M. Wahl, "Stresses and deflections in flat circular plates with central holes," *Trans. ASME Paper APM52-3*, vol. 52, no. 1, p. 29, 1930.

[159] E. Ventsel and T. Krauthammer, *Thin plates and shells: Theory, analysis and applications*, 1st ed. New York: Marcel Dekker, 2001.

[160] J. N. Reddy, *Mechanics of laminated composite plates and shells, Theory and analysis*, 2nd ed. Boca Raton: CRC Press, 2004.

[161] E. Reissner, "The effect of transverse shear deformation on the bending of elastic plates," *Journal of Applied Mechanics*, vol. 12, pp. A69–A77, 1945.

[162] E. Reissner, "On the theory of bending of elastic plates," *Journal of Applied Mechanics*, vol. 23, pp. 184–191, 1944.

[163] R. D. Mindlin, "Influence of rotary inertia and shear on flexural motions of iotropic, elastic plates," *Journal of Applied Mechanics*, vol. 18, pp. 1031–1036, 1951.

[164] C. M. Wang, G. T. Lim, J. N. Reddy, and K. H. Lee, "Relationships between bending solutions of Reissner and Mindlin plate theories," *Engineering Structures*, vol. 23, pp. 838–849, 2001.

[165] S. P. Timoshenko and S. Woinowsky-Krieger, *Theory of plates and shells*, 2nd ed. New York: McGraw-Hill, 1959.

[166] J. N. Reddy, *Theory and analysis of elastic plates and shells*, 2nd ed. Boca Raton: CRC Press, 2007.

[167] J. Dankert and H. Dankert, *Technische Mechanik: Statik, Festigkeitslehre, Kinematik/Kinetik*, 7th ed. Berlin: Springer Vieweg, 2013.

[168] A. A. Griffith, "The theory of rupture," in *Proceedings of the First International Congress of Applied Mechanics*, C. B. Biezeno and J. M. Burgers, Eds. J. Waltman Jr., 1924, pp. 55–63, Delft.

[169] E. Orowan, "Die mechanischen Festigkeitseigenschaften und die Realstruktur der Kristalle," *Zeitschrift für Kristallographie - Crystalline Materials*, vol. 89, no. 1, pp. 327–343, 1934.

[170] M. L. Williams, "The continuum interpretation for fracture and adhesion," *Journal of Applied Polymer Science*, vol. 13, pp. 29–40, 1969.

[171] C. F. Shih, B. Moran, and T. Nakamura, "Energy release rate along a three-dimensional crack front in a thermally stressed body," *International Journal of Fracture*, vol. 30, no. 2, pp. 79–102, 1986.

[172] I. S. Raju and K. N. Shivakumar, "An equivalent domain integral method in the two-dimensional analysis of mixed mode crack problems," *Engineering Fracture Mechanics*, vol. 37, no. 4, pp. 707–725, 1990.

[173] T. Nakamura, C. F. Shih, and L. B. Freund, "Computational methods based on an energy integral in dynamic fracture," *International Journal of Fracture*, vol. 27, no. 3-4, pp. 229–243, 1985.

[174] J. R. Rice, "A path independent integral and the approximate analysis of strain concentration by notches and cracks," *Journal of Applied Mechanics*, vol. 35, pp. 379–386, 1968.

[175] G. P. Nikishkov and S. N. Atluri, "An equivalent domain integral method for computing crack-tip integral parameters in non-elastic, thermo-mechanical fracture," *Engineering Fracture Mechanics*, vol. 26, no. 6, pp. 851–867, 1987.

[176] H. Okada and S. Ohata, "Three-dimensional J-integral evaluation for cracks with arbitrary curvatures and kinks based on domain integral method for quadratic tetrahedral finite element," *Engineering Fracture Mechanics*, vol. 109, pp. 58–77, 2013.

[177] F. H. K. Chen and R. T. Shield, "Conservation laws in elasticity of the J-integral type," *Zeitschrift für angewandte Mathematik und Physik ZAMP (Journal of Applied Mathematics and Physics)*, vol. 28, no. 1, pp. 1–22, 1977.

[178] M. Stern, E. B. Becker, and R. S. Dunham, "A contour integral computation of mixed-mode stress intensity factors," *International Journal of Fracture*, vol. 12, no. 3, pp. 359–368, 1976.

[179] J. F. Yau, S. S. Wang, and H. T. Corten, "A mixed-mode crack analysis of isotropic solids using conservation laws of elasticity," *Journal of Applied Mechanics*, vol. 47, no. 2, pp. 335–341, 1980.

[180] R. Daimon and H. Okada, "Mixed-mode stress intensity factor evaluation by interaction integral method for quadratic tetrahedral finite element with correction terms," *Engineering Fracture Mechanics*, vol. 115, pp. 22–42, 2014.

[181] M. C. Walters, G. H. Paulino, and R. H. Dodds, Jr., "Interaction integral procedures for 3-D curved cracks including surface tractions," *International Journal of Fracture*, vol. 72, pp. 1635–1663, 2005.

[182] T. Ikeda, M. Nagai, K. Yamanaga, and N. Miyazaki, "Stress intensity factor analyses of interface cracks between dissimilar anisotropic materials using the finite element method," *Engineering Fracture Mechanics*, vol. 73, no. 14, pp. 2067–2079, 2006.

[183] J. K. Knowles and E. Sternberg, "On a class of conservation laws in linearized and finite elastostatics," *Archive for Rational Mechanics and Analysis*, vol. 44, no. 3, pp. 187–211, 1972.

[184] Y. Z. Chen, "Analysis of L-integral and theory of the derivative stress field in plane elasticity," *International Journal of Solids and Structures*, vol. 40, no. 13-14, pp. 3589–3602, 2003.

[185] B. Budiansky and J. R. Rice, "Conservation Laws and Energy-Release Rates," *Journal of Applied Mechanics*, vol. 40, no. 1, pp. 201–203, 1973.

[186] A. Paluszny and R. W. Zimmerman, "Numerical simulation of multiple 3D fracture propagation using arbitrary meshes," *Computer Methods in Applied Mechanics and Engineering*, vol. 200, no. 9-12, pp. 953–966, 2011.

[187] D. M. Parks, "A stiffness derivative finite element technique for determination of crack tip stress intensity factors," *International Journal of Fracture*, vol. 10, no. 4, pp. 487–502, 1974.

[188] T. K. Hellen and W. S. Blackburn, "The calculation of stress intensity factors for combined tensile and shear loading," *International Journal for Fracture*, vol. 11, no. 4, pp. 605–617, 1975.

[189] D. M. Parks, "The virtual crack extension method for nonlinear material behaviour," *Computer Methods in Applied Mechanics and Engineering*, vol. 12, no. 3, pp. 353–364, 1977.

[190] T. K. Hellen, "Virtual crack extension methods for non-linear materials," *International Journal for Numerical Methods in Engineering*, vol. 40, no. 4, pp. 929–942, 1989.

[191] P. P. L. Matos, R. M. McMeeking, P. G. Charalambides, and M. D. Drory, "A method for calculating stress intensities in bimaterial fracture," *International Journal of Fracture*, vol. 40, no. 4, pp. 235–254, 1989.

[192] T. Belytschko and T. Black, "Elastic crack growth in finite elements with minimal remeshing," *International Journal for Numerical Methods in Engineering*, vol. 45, no. 5, pp. 601–620, 1999.

[193] N. Moës, J. Dolbow, and T. Belytschko, "A finite element method for crack growth without remeshing," *International Journal for Numerical Methods in Engineering*, vol. 46, no. 1, pp. 131–150, 1999.

[194] J. P. Crété, P. Longère, and J. M. Cadou, "Numerical modelling of crack propagation in ductile materials combining the GTN model and X-FEM," *Computer Methods in Applied Mechanics and Engineering*, vol. 275, pp. 204–233, 2014.

[195] N. Sukumar, D. L. Chopp, and B. Moran, "Extended finite element method and fast marching method for three-dimensional fatigue crack propagation," *Engineering Fracture Mechanics*, vol. 70, pp. 29–48, 2003.

[196] I. S. Raju and J. C. Newman, Jr., "Stress-intensity factors for a wide range of semi-elliptical surface cracks in finite-thickness plates," *Engineering Fracture Mechanics*, vol. 1, no. 4, pp. 817–829, 2005.

[197] N.-A. Noda and S. Miyoshi, "Variation of stress intensity factor and crack opening displacement of semi-elliptical surface crack," *International Journal of Fracture*, vol. 75, no. 1, pp. 19–48, 1996.

[198] S. K. Chan, I. S. Tuba, and W. K. Wilson, "On the finite element method in linear fracture mechanics," *Engineering Fracture Mechanics*, vol. 2, no. 1, pp. 1–17, 1970.

[199] J. Planas, M. Elices, G. V. Guinea, F. J. Gómez, D. A. Cendón, and I. Arbilla, "Generalizations and specializations of cohesive crack models," *Engineering Fracture Mechanics*, vol. 70, pp. 1759–1776, 2003.

[200] X.-P. Xu and A. Needleman, "Numerical simulations of fast crack growth in brittle solids," *Journal of the Mechanics and Physics of Solids*, vol. 42, no. 9, pp. 1397–1434, 1994.

[201] G. Alfano and M. A. Crisfield, "Finite element interface models for the delamination analysis of laminated composites: mechanical and computational issues," *International Journal for Numerical Methods in Engineering*, vol. 50, no. 7, pp. 1701–1736, 2001.

[202] K. S. Park and G. H. Paulino, "Cohesive zone models: A critical review of traction-separation relationships across fracture surfaces," *Applied Mechanics Reviews*, vol. 64, no. 060802, pp. 1–20, 2011, Transactions of the ASME.

[203] J. Mergheim, E. Kuhl, and P. Steinmann, "A finite element method for the computational modelling of cohesive cracks," *International Journal for Numerical Methods in Engineering*, vol. 63, no. 2, pp. 276–289, 2005.

[204] G. N. Wells and L. J. Sluys, "A new method for modelling cohesive cracks using finite elements," *International Journal for Numerical Methods in Engineering*, vol. 50, no. 12, pp. 2667–2682, 2001.

[205] R. de Borst, J. J. C. Remmers, and A. Needleman, "Mesh-independent discrete numerical representations of cohesive-zone models," *Engineering Fracture Mechanics*, vol. 73, pp. 160–177, 2006.

[206] T. N. Bittencourt, "Computer simulation of linear and nonlinear crack propagation in cementitious materials," PhD Thesis, Cornell University, May 1993.

[207] D. Xie and S. B. Biggers, Jr., "Progressive crack growth analysis using interface element based on the virtual crack closure technique," *Finite Elements in Analysis and Design*, vol. 42, pp. 977–984, 2006.

[208] D. Xie and S. B. Biggers, Jr., "Strain energy release rate calculation for a moving delamination front of arbitrary shape based on the virtual crack closure technique. Part I: Formulation and validation," *Engineering Fracture Mechanics*, vol. 73, no. 6, pp. 771–785, 2006.

[209] D. Xie and S. B. Biggers, Jr., "Strain energy release rate calculation for a moving delamination front of arbitrary shape based on the virtual crack closure technique. Part II: Sensitivity study on modeling details," *Engineering Fracture Mechanics*, vol. 73, no. 6, pp. 786–801, 2006.

[210] Y. J. Liu and Y. X. Li, "Revisit of the equivalence of the displacement discontinuity method and boundary element method for solving crack problems," *Engineering Analysis with Boundary Elements*, vol. 47, pp. 64–67, 2014.

[211] W.-T. Ang, *Hypersingular integral equations in fracture analysis*, 1st ed. Oxford: Woodhead Publishing, 2013.

[212] C.-H. Tu, J.-J. Dong, C.-S. Chen, C.-C. Ke, J.-Y. Jhan, and H. J. Yu, "Two-dimensional stress intensity factor analysis of cracks in anisotropic bimaterial," *Mathematical Problems in Engineering*, vol. 2013, no. 721656, pp. 1–14, 2013.

[213] X. Y. Zhuang, "Meshless methods: theory and application in 3D fracture modelling with level sets," PhD Thesis, Durham University, Oct 2010.

[214] M. B. Liu and G. R. Liu, "Smoothed particle hydrodynamics (SPH): an overview and recent developments," *Archives of Computational Methods in Engineering*, vol. 17, no. 1, pp. 25–76, 2010.

[215] W. K. Liu, S. Jun, and Y. F. Zhang, "Reproducing kernel particle methods," *International Journal for Numerical Methods in Engineering*, vol. 20, no. 8-9, pp. 1081–1106, 1995.

[216] C. A. Duarte and J. T. Oden, "An h-p adaptive method using clouds," *Composite Methods in Applied Mechanics and Engineering*, vol. 139, no. 1-4, pp. 237–262, 1996.

[217] S. N. Atluri and T. Zhu, "New concepts in meshless methods," *International Journal for Numerical Methods in Engineering*, vol. 47, no. 1-3, pp. 537–556, 2000.

[218] K. M. Liew, X. Zhao, and A. J. M. Ferreira, "A review of meshless methods for laminated and functionally graded plates and shells," *Composite Structures*, vol. 93, no. 8, pp. 2031–2041, 2011.

[219] J. Sladek, P. Stanak, Z.-D. Han, V. Sladek, and S. N. Atluri, "Applications of the MLPG method in engineering & sciences: A review," *Composite Modelling in Engineering & Sciences*, vol. 92, no. 4, pp. 423–475, 2013.

[220] J. M. Melenk and I. Babuška, "The partition of unity finite element method: Basic theory and applications," *Composite Methods in Applied Mechanics and Engineering*, vol. 139, no. 1-4, pp. 289–314, 1996.

[221] T. Belytschko, Y. Y. Lu, and L. Gu, "Crack propagation by element-free Galerkin methods," *Engineering Fracture Mechanics*, vol. 51, no. 2, pp. 295–315, 1995.

[222] T. Belytschko, Y. Krongauz, D. Organ, M. Fleming, and P. Krysl, "Meshless methods: An overview and recent developments," *Computer Methods in Applied Mechanics and Engineering*, vol. 139, no. 1-4, pp. 3–47, 1996.

[223] S. N. Atluri and T. Zhu, "A new meshless local Petrov-Galerkin (MLPG) approach in computational mechanics," *Computational Mechanics*, vol. 22, no. 2, pp. 117–127, 1998.

[224] P. Krysl and T. Belytschko, "Element-free Galerkin Method: convergence of the continuous and discontinuous shape functions," *Computer Methods in Applied Mechanics and Engineering*, vol. 148, no. 3-4, pp. 257–277, 1997.

[225] A. Huerta and S. Fernándes-Méndez, "Enrichment and coupling of the finite element and meshless methods," *International Journal for Numerical Methods in Engineering*, vol. 48, no. 11, pp. 1615–1636, 2000.

[226] S. A. Silling, "Reformulation of elasticity theory for discontinuities and long-range forces," *Journal of the Mechanics and Physics of Solids*, vol. 48, no. 1, pp. 175–209, 2000.

[227] B. Kilic, A. Agwai, and E. Madenci, "Peridynamic theory for progressive damage prediction in center-cracked composite laminates," *Composite Structures*, vol. 90, pp. 141–151, 2009.

[228] F. Bobaru and W. Hu, "The meaning, selection and use of the Peridynamic horizon and its relation to crack branching in brittle materials," *International Journal of Fracture*, vol. 176, no. 2, pp. 215–222, 2012.

[229] J. Xu, A. Askari, O. Weckner, and S. Silling, "Peridynamic analysis of impact damage in composite laminates," *Journal of Aerospace Engineering*, vol. 21, no. 3, pp. 187–194, 2008, Special Issue: Impact Mechanics of Composite Materials for Aerospace Application.

[230] W. Hu, Y. D. Ha, and F. Bobaru, "Peridynamic model for dynamic fracture in unidirectional fiber-reinforced composites," *Computer Methods in Applied Mechanics and engineering*, vol. 217-220, pp. 247–261, 2012.

[231] S. Osher and J. A. Sethian, "Fronts propagating with curvature-dependent speed: Algorithms based on Hamilton-Jacobi formulations," *Journal of Computational Physics*, vol. 79, no. 1, pp. 12–49, 1988.

[232] M. Stolarska, D. L. chopp, N. Moës, and T. Belytschko, "Modelling crack growth by level sets in the extended finite element method," *International Journal for Numerical Methods in Engineering*, vol. 51, no. 8, pp. 943–960, 2001.

[233] F. P. van der Meer, N. Moës, and L. J. Sluys, "A level set model for delamination – Modeling crack growth without cohesive zone or stress singularity," *Engineering Fracture Mechancis*, vol. 79, pp. 191–212, 2012.

[234] J. M. Linden, M. Köpple, D. Elder, and A. G. Gibson, "Fracture mechanics of crack propagation in composite repairs of steel pressure piping," *Journal of Reinforced Plastics and Composites*, vol. 33, no. 6, pp. 526–532, 2014, SI.

[235] *ANSYS Parametric Design Language Guide*, 14th ed., ANSYS Inc., 2012.

[236] *ANSYS Mechanical APDL Command Reference Guide*, 14th ed., ANSYS Inc., 2012.

[237] E. F. Rybicki and M. F. Kanninen, "A finite element calculation of stress intensity factors by a modified crack closure integral," *Engineering Fracture Mechanics*, vol. 9, no. 4, pp. 931–938, 1977.

[238] I. S. Raju, "Calculation of strain-energy release rates with higher order and singular finite elements," *Engineering Fracture Mechanics*, vol. 28, no. 3, pp. 251–274, 1987.

[239] R. Krüger, "Virtual crack closure technique: History, approach and applications," *Applied Mechanics Reviews*, vol. 57, no. 2, pp. 109–143, 2004.

[240] N. Muthu, S. K. Maiti, B. G. Falzon, and I. Guiamatsia, "A comparison of stress intensity factors obtained through crack closure integral and other approaches using eXtended element-free Galerkin method," *Computational Mechanics*, vol. 52, no. 3, pp. 587–605, 2013.

[241] R. Singh, B. J. Carter, P. A. Wawrzynek, and A. R. Ingraffea, "Universal crack closure integral for SIF estimation," *Engineering Fracture Mechanics*, vol. 60, no. 2, pp. 133–146, 1998.

[242] J. A. Nairn, "Generalized crack closure analysis for elements with arbitrarily-placed side nodes and consistent nodal forces," *International Journal of Fracture*, vol. 171, no. 1, pp. 11–22, 2011.

[243] R. S. Barsoum, "Triangular quarter-point elements as elastic and perfectly-plastic crack tip elements," *International Journal for Numerical Methods in Engineering*, vol. 11, no. 1, pp. 85–98, 1977.

[244] V. Murti and S. Valliappan, "A universal optimum quarter point element," *Engineering Fracture Mechanics*, vol. 25, no. 2, pp. 237–258, 1986.

[245] R. D. Narayana, B. Dattaguru, T. S. Ramamurthy, and K. Vijayakumar, "Modified crack closure integral using six-noded isoparametric quadrilateral singular elements," *Engineering Fracture Mechanics*, vol. 36, no. 6, pp. 945–955, 1990.

[246] A. B. Pereira, A. B. de Morais, and M. F. S. F. de Moura, "Design and analysis of a new six-point edge crack torsion (6ECT) specimen for mode III interlaminar fracture characterisation," *Composites: Part A*, vol. 42, no. 2, pp. 131–139, 2011.

[247] G. De Roeck and M. M. Abdel Wahab, "Strain energy release rate formulae for 3D finite element," *Engineering Fracture Mechanics*, vol. 50, no. 4, pp. 569–580, 1995.

[248] T.-C. Chiu and H.-C. Lin, "Analysis of stress intensity factors for three-dimensional interface crack problems in electronic packages using the virtual crack closure technique," *International Journal of Fracture*, vol. 156, no. 1, pp. 75–96, 2009.

[249] N. Muthu, B. G. Falzon, S. K. Maiti, and S. Khoddam, "Modified crack closure integral technique for extraction of SIFs in meshfree methods," *Finite Elements in Analysis and Design*, vol. 78, pp. 25–39, 2014.

[250] Y.-P. Liu, G.-Q. Li, and C.-Y. Chen, "Crack growth simulation for arbitrarily shaped cracks based on the virtual crack closure technique," *International Journal of Fracture*, vol. 185, no. 1-2, pp. 1–15, 2014.

[251] H. Okada, H. Kawai, and A. Kousuke, "A virtual crack closure-integral method (VCCM) to compute the energy release rates and stress intensity factors based on quadratic tetrahedral finite elements," *Engineering Fracture Mechanics*, vol. 75, no. 15, pp. 4466–4485, 2008.

[252] A. Agrawal and A. M. Karlsson, "Obtaining mode mixity for a bimaterial interface crack using the virtual crack closure technique," *International Journal of Fracture*, vol. 141, no. 1-2, pp. 75–98, 2006.

[253] K. S. Venkatesha, T. S. Ramamurthy, and B. Dattaguru, "Generalized modified crack closure integral (GMCCI) and its application to interface crack problems," *Computers & Structures*, vol. 60, no. 4, pp. 665–676, 1996.

[254] M. G. Manoharan and C. T. Sun, "Strain energy release rates of an interfacial crack between two anisotropic solids under uniform axial strain," *Composite Science and Technology*, vol. 39, no. 2, pp. 99–116, 1990.

[255] D. Bruno and F. Greco, "Mixed mode delamination in plates: a refined approach," *International Journal of Solids and Structures*, vol. 38, no. 50-51, pp. 9149–9177, 2001.

[256] D. Bruno, F. Greco, and P. Lonetti, "A 3D delamination modelling technique based on plate and interface theories for laminated structures," *European Journal of Mechanics — A/Solids*, vol. 24, no. 1, pp. 127–149, 2005.

[257] D. Bruno, R. Carpino, F. Greco, and P. Lonetti, "Energy release rate and mode partition for interlaminar crack in circular laminated beams," *International Journal of Solids and Structures*, vol. 43, no. 5, pp. 1201–1223, 2006.

[258] D. Bruno, R. Carpino, and F. Greco, "Modelling of mixed mode debonding in externally FRP reinforced beams," *Composites Science and Technology*, vol. 67, no. 7-8, pp. 1459–1474, 2007.

[259] A. Diaz Diaz, J.-F. Caron, and A. Ehrlacher, "Analytical determination of the modes I, II and III energy release rates in a delaminated laminate and validation of a delamination criterion," *Composite Structures*, vol. 78, no. 3, pp. 424–432, 2007.

[260] R. Krüger and P. J. Minguet, "Analysis of composite skin–stiffener debond specimens using a shell/3D modeling technique," *Composite Structures*, vol. 81, no. 1, pp. 41–59, 2007.

[261] E. Pietropaoli and A. Riccio, "Formulation and assessment of an enhanced finite element procedure for the analysis of delamination growth phenomena in composite structures," *Composite Science and Technology*, vol. 71, no. 6, pp. 836–846, 2011.

[262] N. T. Kattamis, M. S. Brown, and C. B. Arnold, "Finite element analysis of blister formation in laser-induced forward transfer," *Journal of Materials Research*, vol. 26, no. 18, pp. 2438–2449, 2011.

[263] S. Guo, K.-T. Wan, and D. A. Dillard, "A bending-to-stretching analysis of the blister test in the presence of tensile residual stress," *International Journal of Solids and Structures*, vol. 42, pp. 2771–2784, 2005.

[264] C. J. Jih and C. T. Sun, "Evaluation of a finite element based crack-closure method for calculating static and dynamic strain energy release rates," *Engineering Fracture Mechanics*, vol. 37, no. 2, pp. 313–322, 1990.

[265] D. Xie and S. B. Biggers, Jr., "Calculation of transient strain energy release rates under impact loading based on the virtual crack closure technique," *International Journal of Impact Engineering*, vol. 34, no. 6, pp. 313–322, 2007.

[266] K. N. Shivakumar, P. W. Tan, and J. C. Newman, Jr., "A virtual crack-closure technique for calculating stress intensity factors for cracked three dimensional bodies," *International Journal of Fracture*, vol. 36, no. 3, pp. R43–R50, 1988.

[267] *BS ISO 13586:2000*, British Standards Institution, 2003, Plastics — Determination of fatigue toughness (G_{IC} and K_{IC}) — Linear elastic fracture mechanics (LEFM) approach.

[268] *BS ISO 15850:2014*, British Standards Institution, 2014, Plastics — Determination of tension-tension fatigue crack propagation — Linear elastic fracture mechanics (LEFM) approach.

[269] *BS ISO 29221:2014*, British Standards Institution, 2014, Plastics — Determination of mode I plane-strain crack-arrest toughness.

[270] *BS ISO 17281:2002*, British Standards Institution, 2002, Plastics — Determination of fracture toughness (G_{IC} and K_{IC}) at moderately high loading rates (1 m/s).

[271] *BS ISO 19095:2014*, British Standards Institution, 2014, Adhesives — Evaluation of the adhesion interface performance in plastic-metal assemblies — Part 1–4.

[272] *BS ISO 25217:2009*, British Standards Institution, 2009, Adhesives — Determination of the mode 1 adhesive fracture energy of structural adhesive joints using double cantilever beam and tapered double cantilever beam specimens.

[273] E. P. O'Brien, T. C. Ward, S. Guo, and A. Dillard, "Strain energy release rates of a pressure sensitive adhesive measured by the shaft-loaded blister test," *The Journal of Adhesion*, vol. 79, no. 1, pp. 69–97, 2003.

[274] K. T. Wan and Y. W. Mai, "Fracture mechanics of a shaft-loaded blister of thin flexible membrane on rigid substrate," *International Journal of Fracture*, vol. 74, no. 2, pp. 181–197, 1995.

[275] K. Liao and K.-T. Wan, "Evaluation of film-substrate interface durability using a shaft-loaded blister test," *Journal of Composites Technology & Research*, vol. 23, no. 1, pp. 15–20, 2001.

[276] M.-H. Zhao, W.-L. Zheng, C.-Y. Fan, and E. Pan, "Nonlinear elastic mechanics of the ball-loaded blister test," *International Journal of Engineering Science*, vol. 49, pp. 839–855, 2011.

[277] O. Kozlova, M. Braccini, N. Eustathopoulos, M.-F. Devismes, and M. Dupeux, "Shaft loaded blister test for metal/ceramic brazing fracture," *Materials Letters*, vol. 62, pp. 3626–3628, 2008.

[278] M. T. Heitzmann, M. Hou, M. Veidt, and P. Falzon, "Influence of nonlinearities on the accuracy of the analytical solution for the shaft loaded blister test," *International Journal of Solids and Structures*, vol. 48, pp. 1424–1435, 2011.

[279] K. T. Wan and L. Kogut, "The coupling effect of interfacial adhesion and tensile residual stress on a thin membrane adhered to a flat punch," *Journal of Micromechanics and Microengineering*, vol. 15, pp. 778–784, 2005.

[280] M.-F. Wong and K.-T. Wan, "Adhesion-delamination mechanics of a prestressed circular film adhered onto a rigid substrate," *Journal of Adhesion*, vol. 83, pp. 67–83, 2007.

[281] L. H. Xiao, X. P. Su, J. H. Wang, and Z. Y. C., "A novel blister test to evaluate the interface strength between nickel coating and low carbon steel substrate," *Materials Science and Engineering*, vol. 501, pp. 235–241, 2009.

[282] M.-H. Zhao, W.-L. Zheng, and C.-Y. Fan, "Mechanics of shaft-loaded blister test for thin film suspended on compliant substrate," *International Journal of Solids and Structures*, vol. 47, pp. 2525–2532, 2010.

[283] M.-F. Wong, G. Duan, and K.-T. Wan, "Adhesion-delamination mechanics of a prestressed rectangular film adhered onto a rigid substrate," *Journal of Applied Physics*, vol. 101, pp. 1–7, 2007.

[284] K. T. Wan and J. Duan, "Adherence of a rectangular flat punch onto a clamped plate: Transition from a rigid plate to a flexible membrane," *Journal of Applied Mechanics*, vol. 69, no. 2, pp. 104–109, 2002.

[285] K. T. Wan and J. Duan, "Adherence of an axisymmetric flat punch onto a clamped plate: Transition from a rigid plate to a flexible membrane," *Journal of Applied Mechanics*, vol. 69, no. 2, pp. 110–116, 2002.

[286] Z. Sun, K.-T. Wan, and D. A. Dillard, "A theoretical and numerical study of thin film delamination using the pull-off test," *International Journal of Solids and Structures*, vol. 41, pp. 717–730, 2004.

[287] C. Jin and W. X. D., "A theoretical study of a thin-film delamination using shaft-loaded blister test: Constitutive relation without delamination," *Journal of the Mechanics and Physics of Solids*, vol. 56, pp. 2815–2831, 2008.

[288] C. Jin, "Theoretical study of mechanical behavior of thin circular film adhered to a flat punch," *International Journal of Mechanical Sciences*, vol. 51, pp. 481–489, 2009.

[289] M. R. Begley and T. J. Mackin, "Spherical indentation of freestanding circular thin films in the membrane regime," *Journal of Mechanics and Physics of Solids*, vol. 52, no. 9, pp. 2005–2023, 2004.

[290] H. H. Yu and J. W. Hutchinson, "Influence of substrate compliance on buckling delamination of thin films," *International Journal of Fracture*, vol. 113, no. 1, pp. 39–55, 2002.

[291] K. T. Wan and K. Liao, "Measuring mechanical properties of thin flexible films by a shaft-loaded blister test," *Thin Solid Films*, vol. 352, pp. 167–172, 1999.

[292] H. M. Jensen and M. D. Thouless, "Effects of residual stresses in the blister test," *International Journal of Solids and Structures*, vol. 30, no. 6, pp. 779–795, 1993.

[293] P. Nie, Y. Shen, Q.-L. Chen, and X. Cai, "Effects of residual stresses on interfacial adhesion measurement," *Mechanics of Materials*, vol. 41, pp. 545–552, 2009.

[294] B.-F. Ju, Y. Ju, M. Saka, K.-K. Liu, and K.-T. Wan, "A systematic method for characterizing the elastic properties and adhesion of a thin polymer membrane," *International Journal of Mechanical Sciences*, vol. 47, pp. 319–332, 2005.

[295] K.-K. Liu and B.-F. Ju, "A novel technique for mechanical characterization of thin elastomeric membrane," *Journal of Physics D: Applied Physics*, vol. 34, pp. 114–128, 2001, 15.

[296] H. Dannenberg, "Measurement of adhesion by a blister method," *Journal of Applied Polymer Science*, vol. 5, no. 14, pp. 125–134, 1961.

[297] M. L. Williams, "The fracture threshold for an adhesive interlayer," *Journal of Applied Polymer Science*, vol. 14, no. 5, pp. 1121–1126, 1970.

[298] M. L. Williams, "Cohesive-adhesive fracture in a pressurized double blister," *Journal of Adhesion*, vol. 5, no. 1, pp. 81–87, 1973.

[299] S. J. Bennett, K. L. Devries, and M. L. Williams, "Adhesive fracture mechanics," *Journal of Fracture*, vol. 10, no. 1, pp. 33–43, 1974.

[300] E. H. Andrews and A. Stevenson, "Fracture energy of epoxy resin under plane strain conditions," *Journal of Materials Science*, vol. 13, pp. 1680–1688, 1978.

[301] B. Cotterell and Z. Chen, "The blister test – Transition from plate to membrane behaviour for an elastic material," *International Journal of Fracture*, vol. 86, pp. 191–198, 1997.

[302] A. Arjun and K.-T. Wan, "Derivation of the strain energy release rate G from first principles for the pressurized blister test," *International Journal of Adhesion & Adhesives*, vol. 25, pp. 13–18, 2005.

[303] H. M. Jensen, "Analysis of mode mixity in blister tests," *International Journal of Fracture*, vol. 94, no. 1, pp. 79–88, 1998.

[304] O. A. Goussev, K. Zeman, and U. W. Suter, "Local bending moment as a measure of adhesion: The blister test," *The Journal of Adhesion*, vol. 56, no. 1, pp. 45–57, 1996.

[305] M. Heitzmann, "In-mould priming of fibre reinforced plastic helicopter composnents using thermoplastic polymers: Process integration, material selection and interface characterisation," Ph.D. dissertation, The University of Queensland, School of Mechanical and Mining Engineering, Australia, 2012.

[306] K. Hbaieb and Y. W. Zhang, "A parametric study of a pressurized blister test for an elastic-plastic film-rigid substrate system," *Materials Science and Engineering A*, vol. 390, pp. 385–392, 2005.

[307] K. Juss and P. Mertiny, "Assessment of adhesion between polyurethane liner and epoxy based substrate: Methodology and experiment," *Polymer Testing*, vol. 28, pp. 764–769, 2009.

[308] M. G. Allen and S. D. Senturia, "Application of the island blister test for thin film adhesion measurement," *Journal of Adhesion*, vol. 29, pp. 219–231, 1989.

[309] D. A. Dillard and Y. Bao, "The peninsula blister test: A high and constant strain energy release rate fracture specimen for adhesives," *Journal of Adhesion*, vol. 33, pp. 253–271, 1991.

[310] G. Margaritis, S. A. Sikorski, and F. J. McGarry, "Elastic-plastic finite element method analysis and application of the island blister test," *Journal of Adhesion, Science and Technology*, vol. 8, no. 3, pp. 273–287, 1994.

[311] H. M. Jensen and B. Cochelin, "Fracture analysis of the constrained blister test," *Journal of Adhesion*, vol. 47, no. 4, pp. 231–243, 1994.

[312] M. J. Napolitano, A. Chudnovsky, and A. Moet, "The constrained blister test for the energy of interfacial adhesion," *Journal of Adhesion Science and Technology*, vol. 2, no. 4, pp. 311–323, 1988.

[313] S. Roy, Y. Wang, S.-J. Park, X. Dewei, and K. M. Liechti, "A three-dimensional viscoelastic analysis of thin film delamination in a peninsula blister specimen," *Mechanics of Advanced Materials and Structures*, vol. 14, no. 5, pp. 379–390, 2007.

[314] K.-T. Wan and Y.-W. Mai, "Fracture mechanics of a new blister test with stable crack growth," *Acta Metallurgica et Materialia*, vol. 43, no. 11, pp. 4109–4115, 1995.

[315] Ł. Figiel and B. Lauke, "Interface fracture of polymer films: blister test experiments and modelling," *International Journal of Fracture*, vol. 139, pp. 71–89, 2006.

[316] A. Fedorov, W. P. Vellinga, and J. T. M. De Hosson, "Effects of tensile and compressive in-plane stress fields on adhesion in laser induced delamination experiments," *Journal of Applied Physics*, vol. 103, no. 10, pp. 103 523–1–7, 2008.

[317] P.-Y. Lin, "The in-situ measurement of mechanical properties of multi-layer coatings," Ph.D. dissertation, Massachusetts Institute of Technology, 1990.

[318] A. N. Gent and L. H. Lewandowski, "Blow-off pressures for adhering layers," *Journal of Applied Polymer Sciences*, vol. 33, pp. 1567–1577, 1987.

[319] B. J. Briscoe and S. S. Panesar, "The application of the blister test to an elastomeric adhesive," *Proceedings: Mathematical and Physical Sciences*, vol. 433, no. 1887, pp. 23–43, 1991.

[320] B. W. Hailesilassie and M. N. Partl, "Adhesive blister propagation under an orthotropic bituminous waterproofing membrane," *Construction and Building Materials*, vol. 48, pp. 1171–1178, 2013.

[321] J. R. Grohs, C. M. Siuta, E. Mieritz, S. W. Case, D. A. Dillard, and M. W. Ellis, "Using digital image correlation on pressure-loaded blister testing of PEM," in *Proceedings of the SEM Annual Conference*. Society of Experimental Mechanics, 2009, pp. 1–15.

[322] *BS EN ISO 8501*, British Standards Institution, 2007, Preparation of steel substrates before application of paints and related products.

[323] *SSPC–SP10/NACE No.2*, SSPC: The Society for Protective Coatings, NACE international: The National Association of Corrosion Engineers, 2000, Joint Surface Preparation Standard, Near-White Blast Cleaning.

[324] J. Aakkula and O. Saarela, "Silane based field level surface treatment methods for aluminium, titanium and steel bonding," *International Journal of Adhesion & Adhesives*, vol. 48, pp. 268–279, 2014.

[325] M. R. Tchoquessi Diodjo, L. Belec, E. Aragon, Y. Joliff, and L. Lanarde, "Silane coupling agent for attaching fusion-bonded epoxy to steel," *Applied Materials & Interfaces*, vol. 5, pp. 6751–6761, 2013.

[326] M. Honkanen, M. Hoikkanen, M. Vippola, J. Vuorinen, T. Lepistö, P. Jussila, H. Ali-Löytty, M. Lampimäki, and M. Valden, "Characterization of silane layers on modified stainless steel surfaces and related stainless steel-plastic hybrids," *Applied Surface Science*, vol. 257, pp. 9335–9346, 2011.

[327] M.-L. Abel, "Organosilanes: Adhesion promoters and primers," in *Handbook of adhesion technology*, L. F. M. da Silva, A. Öchsner, and R. D. Adams, Eds. Springer, 2011, ch. 11, pp. 237–258.

[328] E. M. Petrie, *Handbook of adhesives and sealants*, 2nd ed. McGraw-Hill, 2007.

[329] M. A. Sutton, W. Zhao, S. R. McNeill, J. D. Helm, R. S. Piascik, and W. T. Riddell, "Local crack closure measurements: Development of a measurement system using computer vision and a far-field microscope," *Advance in Fatigue Crack Closure Measurement and Analysis*, vol. 2, pp. 145–156, 1999, ASTM STP 1343.

[330] G. Stoilov, V. Kavardzhikov, and D. Pashkouleva, "A comparative study of random patterns for digital image correlation," *Journal of Theoretical and Applied Mechanics*, vol. 42, no. 2, pp. 55–66, 2012.

[331] J. Sicard and J. Sirohi, "Measurement of the deformation of an extremely flexible rotor blade using digital image correlation," *Measurement Science and Technology*, vol. 24, pp. 1–10, 2013.

[332] G. Crammond, S. W. Boyd, and J. M. Dulieu-Barton, "Speckle pattern quality assessment for digital image correlation," *Optics and Lasers in Engineering*, vol. 51, pp. 1368–1378, 2013.

[333] M. Fazzini, S. Mistou, L. Dalverny, and L. Robert, "Study of image characteristics on digital image correlation error assessment," *Optics and Lasers in Engineering*, vol. 48, pp. 335–339, 2010.

[334] Y. Q. Wang, M. A. Sutton, H. A. Bruck, and H. W. Schreier, "Quantitative error assessment in pattern matching: effects of intensity pattern noise, interpolation, strain and image contrast on motion measurements," *Strain*, vol. 45, no. 2, pp. 160–178, 2009.

[335] B. Pan, Z. Lu, and H. Xie, "Mean intensity gradient: An effective global parameter for quality assessment of speckle patterns used in digital image correlation," *Optics and Lasers in Engineering*, vol. 48, pp. 469–477, 2010.

[336] D. Lecompte, A. Smits, S. Bossuyt, H. Sol, J. Vantomme, D. van Hemelrijck, and A. M. Habraken, "Quality assessment of speckle patterns for digital image correlation," *Optics and Lasers in Engineering*, vol. 44, pp. 1132–1145, 2006.

[337] K. Triconnet, K. Derrien, F. Hild, and D. Babtiste, "Parameter choice for optimized digital image correlation," *Optics and Lasers in Engineering*, vol. 47, pp. 728–737, 2009.

[338] T. Hua, H. Xie, S. Wang, Z. Hu, P. Chen, and Q. Zhang, "Evaluation of the quality of a speckle pattern in the digital image correlation method by mean subset fluctuation," *Optics and Laser Technology*, vol. 43, pp. 9–13, 2011.

[339] H. Schürmann, *Konstruieren mit Faser-Kunststoff-Verbunden*, 2nd ed. Berlin: Springer, 2007.

[340] A. Puck and H. Schürmann, "Zur Beanspruchung und Verformung von GFK-Mehrschichtenverbund-Bauelementen. Teil 1. Grundlagen der Spannungs- und Verformungsanalyse," *Kunststoffe*, vol. 4, no. 57, pp. 284–293, 1982.

[341] R. Förster and W. Knappe, "Experimentelle und theoretische Untersuchungen zur Rißbildungsgrenze an zweischichtigen Wickelrohren aus Glasfaser/Kunststoff unter Innendruck," *Kunststoffe*, vol. 8, no. 61, pp. 583–588, 1971.

[342] R. L. Foye, "The transverse poisson's ratio of composites," *Journal of Composite Materials*, vol. 6, pp. 293–95, 1972.

[343] A. G. Gibson, "Through-thickness elastic constants of composite laminates," *Journal of Composite Materials*, vol. 47, no. 28, pp. 3487–3499, 2013.

[344] Correlated Solutions, "Digital Image Correlation: Overview of principles and software," 2009, Society for Experimental Mechanics, SEM 2009 Annual Conference & Exposition on Experimental & Applied Mechanics - Experimental Mechanics Applied to Failure, Workshop Presentation.

[345] A. Goshtasby and W. A. Gruver, "Design of a single-lens stereo camera system," *Pattern Recognition*, vol. 26, no. 6, pp. 923–937, 1993.

[346] *Pike Technical Manual V5.1.2*, Allied Vision Technologies GmbH, August 2012, Pike F-421B. [Online]. Available: http://www.alliedvisiontec.com/emea/products/cameras/firewire/pike/f-421bc.html

[347] *VIC-3D 2010 Testing Guide*, Correlated Solutions, http://www.correlatedsolutions.com, 2010.

[348] B. Pan, K. Qian, H. Xie, and A. Asundi, "Two-dimensional digital image correlation for in-plane displacement and strain measurement: a review," *Measurement Science and Technology*, vol. 20, pp. 1–17, 2009.

[349] B. Pan and Z. Wang, "Recent progress in digital image correlation," in *Proceedings of the SEM Annual Conference*. Society of Experimental Mechanics, 2010, pp. 317–326.

[350] M. A. Sutton, "Digital Image Correlation for Shape and Deformation Measurements," in *Springer Handbook of Experimental Solid Mechanics*, W. N. Sharpe, Jr., Ed. Springer, 2008, ch. 20, pp. 565–600.

[351] Z. Wang, S. Wang, and Z. Wang, "An analysis on computational load of DIC based on Newton-Raphson scheme," *Optics and Lasers in Engineering*, vol. 52, pp. 61–65, 2014.

[352] L. Luu, Z. Wang, M. Vo, T. Hoang, and J. Ma, "Accuracy enhancement of digital image correlation with B-spline interpolation," *Optics Letters*, vol. 36, no. 16, pp. 3070–3072, 2011.

[353] M. A. Sutton, J.-J. Orteu, and H. W. Schreier, *Image Correlation for Shape, Motion and Deformation Measurements*. Springer, 2009.

[354] B. Pan, "Bias error reduction of digital image correlation using Gaussian pre-filtering," *Optics and Lasers in Engineering*, vol. 51, pp. 1161–1167, 2013.

[355] J. Poissant and F. Barthelat, "A novel "subset splitting" procedure for digital image correlation on discontinuous displacement fields," *Experimental Mechanics*, vol. 50, no. 3, pp. 353–364, 2008.

[356] W. Tong, "An evaluation of digital image correlation criteria for strain mapping applications," *Strain*, vol. 41, no. 4, pp. 167–175, 2005.

[357] Z. Jian, Z. Dong, and Z. Zhe, "Assessment of gradient-based digital speckle correlation measurement errors," *Journal of the Optical Society of Korea*, vol. 16, no. 4, pp. 372–380, 2012.

[358] G. Vendroux and W. G. Knauss, "Submicron deformation field measurements: Part 2. Improved digital image correlation," *Experimental Mechanics*, vol. 38, no. 2, pp. 86–92, 1998.

[359] B. Pan, H.-M. Xie, B.-Q. Xu, and F.-L. Dai, "Performance of sub-pixel registration algorithms in digital image correlation," *Measurement Science and Technology*, vol. 17, pp. 1615–1621, 2006.

[360] C. Cofaru, W. Phillips, and W. van Paepegem, "Improved Newton-Raphson digital image correlation method for full-field displacement and strain calculation," *Applied Optics*, vol. 49, no. 33, pp. 6472–6484, 2010.

[361] Z.-F. Zhang, Y.-L. Kang, H.-W. Wang, Q.-H. Qin, Y. Qui, and X.-Q. Li, "A novel coarse-fine search scheme for digital image correlation method," *Measurement: Journal of the International Measurement Confederation*, vol. 39, no. 8, pp. 710–718, 2006.

[362] L. C. S. Nunes, D. A. Castello, P. A. M. dos Santos, and C. F. T. Matt, "Identification of material properties using full-field and non contact measurements," *Journal of the Brazilian Society of Mechanical Sciences and Engineering*, vol. 31, no. 3, pp. 167–172, 2009.

[363] P. Cheng, M. A. Sutton, H. W. Schreier, and S. R. McNeill, "Full-field speckle pattern image correlation with B-spline deformation function," *Experimental Mechanics*, vol. 42, no. 3, pp. 344–352, 2002.

[364] M. A. Sutton, C. Mingpi, W. Peters, and S. McNeill, "Application of an optimized digital correlation method to planar deformation analysis," *Measurement: Journal of the International Measurement Confederation*, vol. 4, no. 3, pp. 143–150, 1986.

[365] B. Pan, Z. Wang, and Z. Lu, "Genuine full-field deformation measurement of an object with complex shape using reliability-guided digital image correlation," *Optics Express*, vol. 18, no. 2, pp. 1011–1023, 2010.

[366] Y. Zhou and Y. Q. Chen, "Feature matching for automated and reliable initialization in three-dimensional digital image correlation," *Optics and Lasers in Engineering*, vol. 51, no. 3, pp. 213–223, 2013.

[367] P. Lava, S. Cooreman, S. Coppieters, M. de Strycker, and D. Debruyne, "Assessment of measuring errors in DIC using deformation fields generated by plastic FEA," *Optics and Lasers in Engineering*, vol. 47, pp. 747–753, 2009.

[368] H. W. Schreier and M. A. Sutton, "Systematic errors in digital image correlation due to undermatched subset shape functions," *Experimental Mechanics*, vol. 42, no. 3, pp. 303–310, 2002.

[369] M. A. Sutton, J. H. Yan, V. Tiwari, H. W. Schreier, and J. J. Orteu, "The effect of out-of-plane motion on 2D and 3D digital image correlation measurements," *Optics and Lasers in Engineering*, vol. 46, pp. 746–757, 2008.

[370] J. R. D'Errico, *Understanding Gridfit*, MatLab Central, woodchips**@**rochester.rr.com, 2006. [Online]. Available: http://uk.mathworks.com/matlabcentral/fileexchange/8998-surface-fitting-using-gridfit

[371] C. Hentschel, "Generic method for 2D image resizing with non-separable filters," in *ICIP*, vol. 3. IEEE, 2004, pp. 1653–1656.

[372] S.-C. Pei and I.-K. Tam, "Effective color inteprolation in CCD color filter arrays using signal correlation," *IEEE Transactions on Circuits and Systems for Video Technology*, vol. 13, no. 6, pp. 503–513, 2003.

[373] L. Reichel and A. Shyshkov, "A new zero-finder for Tikhonov regularization," *BIT Numerical Mathematics*, vol. 48, pp. 627–643, 2008.

[374] Y. Lin, L. Bao, and Y. Cao, "Augmented Arnoldi-Tikhonov regularization methods for solving large-scale linear ill-posed systems," *Mathematical Problems in Engineering*, vol. 2013, no. 548487, pp. 1–8, 2013.

[375] A. N. Tikhonov, A. V. Goncharsky, V. V. Stepanov, and A. G. Yagola, "Numerical methods for the solution of ill-posed problems," *Mathematics and its Applications*, vol. 328, 1995.

[376] B. Pan, Z. Wang, K. Qian, and W. Zhiyong, "Study on subset size selection in digital image correlation for speckle patterns," *Optics Express*, vol. 16, no. 10, pp. 7037–7048, 2008.

[377] Y. Sun and J. H. L. Pang, "Study of optimal subset size in digital image correlation of speckle pattern images," *Optics and Lasers in Engineering*, vol. 45, pp. 967–974, 2007.

[378] J. M. Bland and D. G. Altman, "Statistical methods for assessing agreement between two methods of clinical measurement," *The Lancet*, pp. 307–310, 1986.

[379] T. P. Philippidis, D. J. Lekou, and D. G. Aggelis, "Mechanical property distribution of CFRP filament wound composites," *Composite Structures*, vol. 45, no. 1, pp. 41–50, 1999.

[380] Y. Zhou, S. Chen, and C. Jubing, "Adaptive subset offset for systematic error reduction in incremental digital image correlation," *Optics and Lasers in Engineering*, vol. 55, pp. 5–11, 2014.

[381] C. Cofaru, W. Philips, and W. van Paepegem, "A novel speckle pattern — Adaptive digital image correlation approach with robust strain calculation," *Optics and Lasers in Engineering*, vol. 50, pp. 187–198, 2012.

[382] R. Carandente and P. Cawley, "A method to estimate the size of corrosion patches with guided waves in pipes," in *AIP Conference Proceedings*, vol. 1430. American Institute of Physics, 2012, pp. 1929–1936, Review of Progress in Quantitative Nondestructive Evaluation.

[383] J. L. F. Freire, R. D. Vieira, J. L. C. Diniz, and L. C. Meniconi, "Part 7: Effectiveness of composite repairs applied to damaged pipeline," *Experimental Techniques*, pp. 59–66, September/October 2007, Feature: A series on applications of experimental techniques in the field of pipeline integrity.